ATMOSPHERIC SURFACE AND BOUNDARY LAYERS OF THE AMAZON BASIN

Final Report

NASA Contract NCC1-95

Submitted to the

National Aeronautics and Space Administration
Langley Research Center
Hampton, VA

by

Michael Garstang
Principal Investigator

Department of Environmental Sciences
University of Virginia
Charlottesville, VA 22903

Date: 3/14/87

ATMOSPHERIC SURFACE AND BOUNDARY LAYERS OF THE AMAZON BASIN

Final Report

NASA Contract NCC1-95

Submitted to the

National Aeronautics and Space Administration
Langley Research Center
Hampton, VA

by

Michael Garstang
Principal Investigator

Department of Environmental Sciences
University of Virginia
Charlottesville, VA 22903

Date: 3/14/87

Abstract

Work completed under the NASA cooperative agreement NCC1-95 with the University of Virginia on the Amazon Boundary Layer Experiment, ABLE 2-A, is reported on in three phases: the design of the experiment, the execution of the field program and analysis of the results.

Three manuscripts and two abstracts of papers presented at national conferences sum up the scientific results.

1. Introduction

The research supported under this contract covered two years (January 1985-March 1987) and supported three distinct phases of work:

Phase 1: Design of and preparation for the Amazon Boundary Layer Experiment (ABLE 2-A) - January 1, 1985 - June 30, 1985

Phase 2: Execution of the ABLE 2-A field program - July 1, 1985 - August 15, 1985

Phase 3: Analysis of the ABLE 2-A - August 16, 1985 - March 14, 1987

The report that follows covers each of these phases with emphasis upon the research results generated in Phase 3.

2. Phase 1: Design and Preparation for ABLE 2-A

Three areas of experiment design were dealt with:

2.1 Surface based meteorological measurements
2.2 Aircraft missions: scientific considerations
2.3 Project meteorological support

2.1 Surface Based Meteorological Measurements

Considerable changes were made from the early conceptual field program design as outlined in the proposal for this work. For example, all resources were focussed upon a single land site, the Ducke Forest Reserve, 15 km NE of Manaus, with no activity planned on the river.

Two major measurement systems were designed for use at the Ducke Forest Reserve:

2.1.1 Tethered balloon system

A 76.3 m^3 (2500 ft^3) tethered balloon with associated ground support equipment consisting of a specially designed hydraulic winch and fairlead system was prepared for operations at the Ducke site. The tethered balloon was designed to obtain high vertical resolution (4 m) profiles of horizontal wind velocity, temperature, humidity and pressure from the surface to 1000 m.

Measurements were made by a custom-built sonde which telemetered the signal to a ground station. Signal processing converted the measurements into digital form. The digitized data was stored on magnetic tape. Real time displays served to monitor the observations and maintain quality control.

Soundings from the surface to 1000 m take 20 min to complete. A routine of 2 soundings per hour was planned over most daylight hours with approximately six, 24-hour operations planned.

The tethered system was also capable of carrying air sampling systems designed by the National Center for Atmospheric Research (NCAR) and the Oregon Graduate School. The air samplers carry 4 inflatable sampling bags which are filled by pumps and sealed by valves controlled by radio from the ground. Sampling is done between the surface and 1000 m.

2.1.2 Rawinsonde system

A rawinsonde system (RD-65) was prepared to track high resolution sondes (A.I.R.) between the surface and 400 mb (approximately 8000 m). The AIR sondes provide temperature, humidity and pressure at 25 m intervals. Radio tracking provides estimates of the horizontal wind velocity over the same vertical space interval.

A sounding routine was designed for intensive operations with soundings every three hours and standby days with a lower frequency of measurements.

2.2 Aircraft Missions: Scientific Considerations

Planning was carried out for the aircraft operations. Flights were designed to

2.2.1 Measure growing boundary layer under undisturbed conditions.

2.2.2 Measure structure of lower troposphere under nighttime conditions.

2.2.3 Measure circulations over the rivers.

2.2.4 Survey basin wide conditions.

2.2.5 Measure effect of convection: disturbed conditions.

Horizontal flight tracks, vertical profiling together with other sampling procedures were evaluated in terms of the scientific objectives of each mission.

3. Phase 2: Execution of the ABLE 2-A Field Program: Project Meteorological Support

The Principal Investigator (PI) servpd in the field as the Project Meteorologist. In this capacity the PI:

a) Established a Meteorological Forecast Center, monitoring the day-to-day weather and producing 24-hour forecasts.

b) Planned aircraft missions based upon the forecast.

c) Provided in-flight guidance onboard the Electra aircraft during the mission.

d) Provided a summary of weather conditions during ABLE 2-A. The summary is reproduced below.

3.1 Introduction

The week preceding the start of aircraft operations out of Manaus, i.e., 11-17 July 1985, was characterized by considerable activity over the Amazon basin. A high latitude frontal system had penetrated as an upper level trough as far equatorward as Belem. The resulting instability generated convective cloud complexes over and south of the Amazon, Solimões and Rio Negro rivers. One to two inches of rain occurred in the Manaus area every day from 12 to 16 July. Cloud clusters occurred both during daylight and nighttime hours with a number of nocturnal thunderstorms. This rainy period before the start of the aircraft operations out of Manaus is characteristic of wet season conditions.

Beginning 17/18 July, the region from Manaus eastwards and south of the Solimões and Amazon rivers became progressively under the domination of the subtropical anticyclone which gradually migrated equatorward to become centered in the vicinity of 20 to 25°S latitude and 35 to 45°W longitude dominating NE Brazil. This circulation persisted from 19th July to about 31 July when a relatively strong cold front migrated equatorward over the Andes eventually bringing unstable conditions over the border area near Tabatinga and westward to Manaus on 31 July, 1 and 2 August. On 2nd August, an equatorial vortex with an associated easterly wave extending from the mouth of the Amazon to 12°N advanced rapidly westwards. By the morning of 3rd August the vortex was north and just west of Manaus and dissipating.

Prior to the establishment of the subtropical high, the westerlies were as low as 8 km (1800Z, 17 July 1985) and precipitable water > 4 cm, θ_e in the midtroposphere was > 330°K and no marked midtropospheric inversions (i.e., no Trade Wind Inversion). Sounding at 0600Z on 18 July 1985 is an example of this period.

After the 20th of July, the easterlies became very deep (> 12 km), the atmosphere considerably drier, θ_e occasionally below 320°K and a persistent inversion (Trade Wind-like) was present at about 15,000 ft with weaker inversions below creating a multi-layered atmosphere. Precipitable water, under the dominance of the subtropical high, was below 4 cm with a low of 3.1 cm at 12Z on 31 July 1985.

In the documentation which follows the flights are grouped into:

1. Undisturbed Boundary Layer Day: 18, 19, 21 July
2. Survey Flight Manaus-Belem-Manaus: 23, 24 July
3. Night and River/Night Flights: 26, 31 July
4. Day/River Flights: 29 July
5. Disturbed Boundary Layer Flights: 2, 3 August

For each group of missions, a brief weather summary is given together with some supporting data.

3.2 Mission Types and Associated Weather

3.2.1 Undisturbed boundary layer day: Dates - 18, 19 and 21 July 1985

18 July 1985

Anticyclone is beginning to dominate NE Brazil but residual instability in Manaus region is still triggering daytime convection and associated showers and thundershowers. Sounding at 0600Z, 18 July 1985 shows large amount of moisture present (θ_e > 330°K) with 4.7 cm of precipitable water. Convective cloud growth is indicated by this sounding as soon as the surface starts to warm up from a θ_{es} of 350°K. Most of the flight was carried out under undisturbed conditions but the spiral at Ducke was carried out under a large upper level outflow > 14500 ft. Outflow had stabilized conditions in the vicinity of Ducke making this part of the flight representative of the wake conditions following a disturbance.

19 and 21 July 1985

Anticyclone established over NE Brazil. Precipitable water has decreased to 3.1 cm (which turns out to be the lowest we recorded during the experiment). Two well defined inversions are present with bases near 5000 and 1000 or 850 and 700 mb respectively. Moisture is low (θ_e minimum < 320°K). Growth of the new BL was well determined being intercepted at 500 ft at 0844 LST subsequently growing at a rate of $\sim$ 10 cm sec^{-1} to a depth of 5500 ft with small cumulus bases at about 5500 and tops at 6500 ft. The flight on 21 July took place under almost identical conditions except that the inversions are slightly elevated and the atmosphere wetter (precipitable water 4.3 cm). Over the flight sections of the mission, however, conditions were undisturbed duplicating the 19th of July. On the spiral down at Ducke there were TCu with tops above 18000 ft and scattered showers.

3.2.2 Survey flights: Manaus-Belem-Manaus: Dates - 23 and 24 July 1985

Anticyclone continues to dominate NE Brazil with cloud convection confined to the region north of the Amazon River. The upper level inversion produced by the subsiding air in the anticyclone remains through both legs of the mission with a weaker low level inversion around 7500 ft. Moisture content is moderate ($\leq$ 4 cm) so that a marked sea breeze front was present just west of Belem on arrival (23rd) and offshore on departure (24th). Convective build-ups were present along the track in the second half of the return flight.

3.2.3 Nighttime boundary layer and day and nighttime river flights: Dates - 26, 29, and 31 July 1985

A weak convective complex existed in the vicinity of Manaus for the nighttime BL flight on 26th July. Active thunderstorms lay to the N, W, and SW. The thunderstorms were avoided and the undisturbed region to the SE used in the daytime undisturbed BL flights was used to find undisturbed

conditions. The western and northern ends of the track were, however, under high outflow and close to precipitating systems early during the mission. The track was extended 15 min to the south to avoid these conditions. On return to Manaus the deep convection had propagated westward leaving a stratified multi-cloud layered atmosphere in the vicinity of Ducke and Manaus.

The 29th of July through the 31st of August exhibit extremely fair conditions for the entire northern Brazil with the only exception being the NW. No tropical or midlatitude influences over our region of interest during this period. Precipitable water remains below 4 cm (down to 3.2 cm, 1800Z on 30 July) with low θ_e ($\sim$ 320°K) and mid-level inversions near 10000 and 16000 ft. Over the river water temperatures were above 29°C, over the forest 22°C and over some of the shallow lakes > 32°C during the night. During the day the forest canopy approaches a maximum of $\sim$ 30°C so that water and forest temperatures are about the same. Turbulence is evident over the water at night and is suppressed over the water during the day.

3.2.4 Disturbed boundary layer flights: Dates - 2 and 3 August 1985

Both disturbed situations are complex perhaps because both cloud complexes were either stationary or slow moving. Because they were stationary or slow moving it is not obvious where the growth and decay is taking place and hence, where there is low level inflow and low level outflow. However, there is little doubt that we encountered both inflow and outflow at low levels and outflow at high levels on both days in both systems.

2 August 1985

The cloud complex worked on this day was the most active cloud cluster in the region. The complex lay to the west of Manaus over the Solimões and was triggered by high level cold dry air penetrating from the south as part of a dying cold front. The soundings at Manaus are in air east of the system and do not reflect the instability. Wind speed and direction (100°/20 kts) and the position of the complex placed the cloud cluster in the wake of the Manaus plume.

The system appeared to be growing most vigorously in the vicinity of point Able. Low level outflow should be expected here with mid-level inflow. At point Bravo we had entered the decaying point of the storm with a collapsed BL and upper level outflow coming down to the surface. This situation was even more pronounced in the vicinity of Delta with a new BL trying to grow and pronounced evaporation at the surface. On the leg Able-Charlie-Able we were in complex upper level outflow/inflow layers.

3 August 1985

Again the complex worked on this day was the most active in the region. The complex grew in the unstable region behind a rapidly moving equatorial vortex and associated easterly wave that was first detected 24 hours before the mission just west of Belem. The line which we worked was orientated nearly N-S almost due north of Manaus developing near 1000 LST and reaching its maximum growth around 1500 LST. The cloud cluster

was vigorous with tops probably exceeding 30-35000 ft and covering a large area with precipitation. We appeared to be in the wake of the system on the lines Able-Bravo-Able thus we should expect upper level air at low levels and outflow of BL air at high levels. The tracks Able-Charlie, Charlie-Able went past active growing convection as well as anvil outflow (particularly Charlie-Able). On the track Charlie-Delta at 16500 we were overflying the growing new convection ahead of the storm. Toward the northern end there was some upper level outflow but for most of Charlie-Delta section we should have been in largely undisturbed air. From Delta-Charlie at 500 ft we were skirting the rain showers of the leading edge of the disturbance. We could have been close enough to experience active low level outflow but no true gust front was evident. Slight variations in position relative to the rain and in altitude would put us in BL inflow into the storm. Interpretation is therefore complex.

4. Analysis of ABLE 2-A: Boundary Layer Structure and Processes

The primary goal of the research conducted under this cooperative agreement was to obtain a good description of the structure of the atmosphere immediately above the rain forest canopy (top of canopy to a few thousand meters), to describe this region during the growing daytime phase of the boundary layer and to examine the nighttime stratified state. At night particular interest centered upon the possibility of mesoscale circulations growing over the large rivers or water bodies.

A secondary objective was to examine the role that deep convective storms play in the vertical transport of heat, water vapor and other trace gases.

While significant progress has been made, much of the analysis remains to be done. In particular, work is in progress on the pronounced nocturnal stratified state and the associated high wind velocities observed in the lowest few hundred meters of the atmosphere. We can document winds up to 20 m s^{-1} within 200 m of the top of the canopy. Moisture pulses are observed with dry and wet episodes lasting up to 2 hours and extending to 1000 m. Analysis has produced a clear and in our opinion, entirely new description of the nocturnal boundary layer. We are in the process of developing an understanding of the observed nocturnal processes.

Similarly, we have documented but not yet understood, evidence of nocturnal circulations over the Rio Negro. Once again, work is still in progress on this topic.

Two major pieces of work have been completed:

a) Structure and Growth of the Mixing Layer over the Amazonian Rain Forest

and

b) Trace gas exchanges and convective transports over the Amazonian Rain Forest.

In each case, results have been reported to the scientific community in major conferences. The manuscripts submitted for publication and the papers presented at meetings are attached to this report.

Trace Gas Exchanges and Convective Transports over the Amazonian Rain Forest

Michael Garstang[1], John Scala[1], Steve Greco[1]
Robert Harriss[2], Sherwin Beck[2], Edward Browell[2], Glen Sachse[2],
Gerald Gregory[2], Gerald Hill[2], Joanne Simpson[3]
Wei-Kuo Tao[3] and Arnold Torres[4]

Short Title: Trace Gas Exchanges over Amazonian Rain Forest

---

[1]Department of Environmental Sciences, University of Virginia, Charlottesville, VA 22902.

[2]NASA/Langley Research Center, Hampton, VA 23665.

[3]NASA/Goddard Space Flight Center, Greenbelt, MD 20771.

[4]NASA/Wallops Flight Facility, Wallops Island, VA 23337.

Abstract

The NASA Amazon Boundary Layer Experiment (ABLE-2A) based in Manaus, Brazil in July and August, 1985 is used to examine meteorological processes responsible for the vertical and horizontal transport of biogenic and anthropogenic trace gases generated over the Amazon basin. Direct sampling of the surrounding environment of deep convective clouds shows marked changes in the vertical distribution of the lower and mid-troposphere of the concentration of O_3 and such surface derived species as CO, CO_2, and NO. Thermodynamic observations, together with two-dimensional cloud model simulations, confirm vertical transports within the convection and provide a basis to estimate the magnitude and efficiency of cloud up- and downward exchanges. A distinction is drawn between local changes due to convective up- and downdrafts and convective overturning as a net result of the storm processes. Marked variability is seen in trace gas concentrations along horizontal flight paths in the vicinity of the convection. Interpretation of simultaneously measured thermodynamic quantities and trace gas concentrations provide the information to infer the presence and direction of atmospheric transports and/or the presence of anthropogenic influences. The level of convective activity and the closely coupled Hadley and Walker circulations over the Amazon basin and its associated trace chemistry suggest the importance of this region to the global atmosphere.

1. Introduction

The Amazon basin not only contains the world's largest tropical rain forest but limbs of two major global wind systems, the Hadley and Walker circulations. Variations in the Southern Oscillation and Pacific and Atlantic warming events influence the intensity of the circulations over the basin and communicate effects of these circulations to the global atmosphere.

The forests and wetlands of the Amazon basin supply a wide range of trace gases in significant amounts to the atmosphere (Harriss et al., 1987). Some of these species are "greenhouse" gases, such as carbon dioxide and methane. Others, of the nitrogen and sulfur species, together with light and heavy hydrocarbons, interact to create ozone, elevated haze layers, and acid rain. Anthropogenic activities produce some of these trace gases in amounts comparable to their natural production and thus may markedly impact upon these processes.

Deep cumulus convection not only provides the link between sources and sinks of trace gases at the forest canopy and in the upper troposphere and lower stratosphere, but is indeed the unsteady yet essential mechanism that drives the vertical transport of heat, moisture, and momentum of the circulation systems themselves (Riehl and Simpson, 1979; Augstein et al., 1980). Understanding of the convective transports therefore serves a dual purpose by advancing our knowledge of chemical species transports and promoting an understanding of the larger scale circulations (Dickerson et al., 1987).

The Amazon Boundary Layer Experiment (ABLE-2A) focused primarily on biosphere-atmosphere interactions within the undisturbed troposphere over unmodified tropical rain forests and wetlands (Harriss et al., 1987).

However, organized cumulus convection occurring on two consecutive days near the conclusion of the experiment provided an opportunity to investigate boundary layer chemistry in the presence of relatively deep precipitating convection.

Convection over the central Amazon basin is influenced by at least two mechanisms: (1) high-latitude systems encroaching into the basin, and (2) tropical systems migrating zonally across the region. The cloud complexes which developed during the two day period were distinctly different and exhibited both kinds of forcing. We present in this paper the results of two aircraft missions which form part of a sustained effort to understand deep convective transports of chemical species utilizing direct and indirect measurements and numerical modeling of cumulus convection. By coupling the chemistry with numerical simulations of the convection, a reasonable picture of how cumulus convection mixes and distributes atmospheric constituents begins to emerge.

2. Measurement and Approach

The NASA Wallops Electra aircraft equipped with a range of chemical and meteorological instrumentation (Gregory et al., 1986, 1987) investigated deep convection on August 2 and 3, 1985 within the shaded regions of Figure 1. The objective of the aircraft flights was to measure and characterize chemical species in the lowest 5 km of the troposphere in the presence of active cumulus convection over a relatively pristine tropical forest. Of primary interest in this study are the measurements of ozone (O_3), carbon monoxide (CO), carbon dioxide (CO_2), nitric oxide (NO), dry-bulb temperature, and water vapor. An airborne ultraviolet differential absorption (UV-DIAL) system was used to remotely sense ozone and aerosol content (Browell et al., 1987).

Aerosols along the lidar path sensed with a spatial resolution of 15 m in the vertical and 20 m in the horizontal were used to determine the structure of the atmosphere (Browell et al., 1983). Two separate, in situ, measurements of O_3 were made by C_2H_4 chemiluminescence and UV absorption (Gregory et al., 1983, 1984). The in situ measurements on the aircraft profiles can be compared with previously remotely obtained UV-DIAL O_3 measurements. The O_3 measurements are accurate to 5 parts per billion by volume (ppbv) or 5%, whichever is greater.

A modified Beckman Industrial model 865 nondispersive infrared analyzer was used for CO_2 measurements. The details of the instrument and calibration procedures are given in Wofsy et al. (1987). Carbon monoxide was measured in situ using the differential absorption carbon monoxide (DACOM) instrument which utilizes a tunable diode laser detection technique (Sachse et al., 1987). The precision is 1.5% or $\pm$ 0.6 ppbv with a time response of 1 sec. Nitric oxide was measured by a chemiluminescence technique with an accuracy of better than 20% resulting in a precision of 3 pptv for a 30 sec integration (Torres et al., 1987).

Total air temperature was measured with a standard aircraft platinum resistance sensor (Rosemount Model 102AU1AP). This sensor and its signal conditioning amplifier were calibrated over the designed operating range of $\pm$ 50°C and demonstrated a worse case error of 0.15°C. Static air temperature was derived from the total air temperature sensor, aircraft Mach number, and temperature sensor recovery factors. For normal flight conditions, the estimated accuracy of derived static air temperature over the range of $\pm$ 50°C is $\pm$ 0.5°C.

Dew point temperature was primarily obtained from a commercial dew point hygrometer (EG&G Model 300) adapted for use on the NASA aircraft. A standard aircraft dew point hygrometer (EG&G Model 137) was also flown both for intercomparison purposes at depression values less than 25°C and as a back-up sensor. The stated accuracy of the Model 300 is $\pm$ 0.2°C and $\pm$ 0.06°C sensitivity to dew point changes for flow rates from 0.25 to 2.5 l/min over the designed operating range of $\pm$ 75°C.

Inflight horizontal wind velocity was obtained from the aircraft's Omega navigation and true air speed computer systems. At wind speeds above 5 m/sec the worse case accuracy is estimated to be $\pm$ 2.5 m/sec and $\pm$ 5 degrees for wind speed and direction, respectively. For wind speeds below 2.5 m/sec the computed wind direction was unreliable.

Ground-based atmospheric soundings were made from the surface to 400 mb every three hours from 1200 GMT to 2100 GMT at Ducke Reserve, located 150 km southeast of the August 3 sampling location. Additional soundings were made from the surface to 50 mb every six hours at Ponte Palata, located 165 km southeast of the August 3 sampling location.

The aircraft flights attempted to enclose the area of disturbance in a box by a series of approximately parallel flight tracks at altitudes of 150 m and 5000 m linked by spirals at the corners. Figures 2(a-b) illustrate the flight procedures with important dimensions noted. On both days, flight altitudes were kept constant within 10 m, altitude being determined by both radar and pressure altimeters. Initial aircraft soundings (spirals) and traverses were made prior to encountering cloudy air permitting comparison with the surface based soundings in the undisturbed environment.

GOES (Geostationary Orbiting Environmental Satellite) imagery was used to locate the cloud systems and to determine their movement and

general organization. The convection on August 2 developed in a dry, suppressed region to the north of a high latitude frontal zone. The migrating baroclinic zone provided the forcing to trigger convection over the southwest part of the Amazon basin. By 1701 GMT (Figure 3a), the cloud complex consisted of three distinctly glaciated convective areas adjacent to a broad region of cloudiness associated with the migrating frontal zone. A southerly extension in the equatorial trough activity is evident in the northern part of the basin. The leading edge of the largest areas of convection associated with instability generated by the high latitude system moved WNW at an approximate rate of 37 km/hr.

Satellite imagery for August 3 (Figure 3b) showed the cloud system examined on that day was likely the result of both tropical (southern extension of equatorial trough activity) and mid-latitude (remnants of the frontal zone) forcing. A line of convection developed southward of the Intertropical Convergence Zone (ITCZ) and parallel to the advancing front. When sampled, the cloud complex consisted of a 500 km north-south line with east-west organized elements embedded within. The leading edge of the convection migrated WSW at approximately 28 km/hr.

3. Model Calculations

A multi-dimensional, time-dependent, dynamic and microphysical numerical cloud model described by Soong and Ogura (1980), Soong and Tao (1984) and Tao and Soong (1986) is used to examine the two cloud systems. The model is non-hydrostatic and anelastic. Model variables include horizontal and vertical velocities, potential temperature and the mixing ratio of water vapor. In addition to a Kessler-type (1969) of two-category liquid water (cloud water and rain) parameterized microphysics, a sophisticated three-category ice phase (cloud ice, snow, and

graupel) scheme is included (Lin et al., 1983). The particles comprising the cloud water and cloud ice fields are each assumed to be monodisperse. The rain, snow, and graupel particles are distributed in size according to an inverse exponential distribution (Marshall and Palmer, 1948). The cloud water and cloud ice are assumed to advect with the airflow, having no appreciable terminal velocities of their own. Rain, snow, and graupel, while moving with the horizontal wind, also fall relative to the updraft with their respective terminal velocities. More than 27 different microphysical processes are included in association with the growth and transfer rates among the hydrometeors. Derivation of individual microphysical processes and other details may be found in Lin et al. (1983).

Initial conditions of temperature, mixing ratio, and the vertical distribution of the horizontal wind were obtained from ground-launched rawinsondes at Ducke Reserve and Ponte Palata (prior to the development of convection). The thermodynamic stratification on both days is conditionally unstable. Both cloud complexes exhibited a linear structure as can be seen in Figure 3, but Case I, August 2, 1985 (Figure 3a) developed a more cellular structure towards the end of the mission while Case II, August 3, 1985, remained linear throughout the mission. The two-dimensional version of the cloud model is best applied to true linear structure. The two-dimensional form was, however, used for both cases primarily because of the much greater cost in computer time of the three-dimensional version. The x-direction of the model is chosen to be perpendicular to the cloud lines in both numerical experiments. A steady-state mesoscale circulation in which the lines developed is also added. This circulation was sustained by a mesoscale convergence field. The observed cloud tops were never higher than 9 km for cloud 1 (August 2nd),

but they reached heights between 10.5 and 12 km for cloud 2 (August 3rd). In order to simulate these observed features by the model, two different magnitudes of mesoscale lifting forcing will be used for these two cases.

A stretched vertical coordinate is used to give fine resolution in lower levels, where clouds start to form, and coarse resolution in the upper levels of the model (Anthes, 1970). The grid interval is about 200 m near the ground and about 1000 m at the highest level, producing a domain depth of 16 km with 30 grid points. The two-dimensional version of the model has 128 grid points in the horizontal, with a grid spacing of 500 m. A leap frog time integration and a second-order space derivative scheme were used. To avoid the problem of time splitting, a time smoother (Robert, 1966) is adopted. The smoothing coefficient is set to 0.1 using a time interval of 10 sec.

4. Results

Figure 4 shows the equivalent potential temperature (EPT) field with height for the model-generated convection at the simulated time closest to cloud maturity. Maturity is defined as the time when the simulated cloud motions in the x,z plane are comprised of up- and downdrafts of equal magnitude (as suggested by the velocity vectors) prior to reduction in maximum cloud top height. The u-w velocity field confirms the downward extension of the low mid-tropospheric values of EPT while the upward motion coincides with higher surface EPT values extending upwards. The model output for August 2 at 36 min after initialization (Figure 4a) suggests that the convection was neither very deep nor particularly vigorous. The inferred draft circulations did not persist in the model calculations and the maximum height reached by the model cloud was about 8 km corresponding to the cloud top height

derived from photogrammetry.

The model generated cloud for August 3 at 40 min after initialization (Figure 4b) suggests well-developed and organized up- and downdrafts. A weak vertical circulation developed in the wake of the convection and remained active for the remainder of the simulation (60 min). The model cloud top height reached 12 km with suggested pressure perturbations attributable to the convection near 14 km. Photogrammatic calculations based upon airborne images place the maximum observed cloud top at 13 km. Table 1 compares environmental observations and model simulation results for the two days (cases).

The case comparison afforded by Table 1 confirms the greater convective development of the cloud complex on August 3 depicted in Figure 4. By combining the model simulation with the observations, we consider Figure 4 to be a useful guide. For Case II, the u-w vectors suggest inflow and upward motion on the western side of the line responding to the gust front (Figure 4b). Downward motions originating near 3.5 km penetrate to the surface from the east. The eastern side of the storm would thus represent the wake of the storm while the western side consists largely of undisturbed conditions near the surface but modified air in the middle troposphere ($\sim$ 650 mb).

For Case I, the well-defined up- and downward motions described for August 3 are missing. The model cloud motion fields do not support an efficient inflow-outflow couplet and thus suggest a convective situation of limited strength and potential future growth. The GOES imagery indicates that at the time of maximum cloud top height, the convection had lost some of its linear structure with other cells developing around the original line (Figure 4a).

The aircraft soundings flown at the corners of the enclosed convection (Figures 2a-b) document the state of the disturbed atmosphere during the lifetime of the convection (each mission required nearly six hours of flying). The vertical profiles of EPT were computed using an approximation developed by Bolton (1980). For the two cases, a mean undisturbed (non-precipitating) sounding calculated from over 25 aircraft profiles is presented in Figure 5 along with the first and last sounding flown for Case I (Figure 5a) and Case II (Figure 5b). In each case, approximately four hours separates the first and last soundings.

The drying observed at 3750 m on August 2 (Figure 5a) in the late morning can be found at 3500 m in the late afternoon. During the time of sampling, the lowest 1250 m warmed considerably with a maximum of 10 degrees K associated with an inversion. The afternoon sounding is generally warmer and contains more moisture below 3 km than the undisturbed mean.

Two distinct drying levels are evident in the morning sounding of August 3 (Figure 5b) centered at 4250 m and 2750 m. The afternoon observations indicate the convection removed the steep gradient in moisture at these levels and warmed the lowest 1750 m. Rapid fluctuations near the forest canopy in the early sounding are also smoothed. The afternoon profile is generally warmer than the undisturbed mean. Clearly, major thermodynamic reversals in the vicinity of the August 3 convection are reflected in the vertical distribution of EPT.

In addition to the aircraft soundings of EPT, the aerosol and O_3 profiles produced by the UV-DIAL along the flight tracks are also useful in documenting the evolving structure of the disturbed atmosphere. Figures 6-7 display the aerosol and ozone profiles below the upper flight tracks for August 2 and August 3.

Through examination of the aerosol profiles it is possible to subjectively determine cloud top and mixed layer heights directly below the aircraft and along the flight track. Mixed layer (ML) and cloud top heights were determined from the aerosol profiles by visual inspection of the aerosol concentrations and concentration gradients. A detailed description of this process is given by Browell et al. (1987) and comparisons between UV-DIAL and tethered balloon determinations of ML heights are given in Martin et al. (1987). The heights determined from Figures 6-7 make it possible to not only document the evolution of the convection and mixed layer, but also to illustrate the horizontal variability in convection and mixed-layer structure at different locations in the study area.

From Figure 6a it can be seen that on August 2 from 1600-1624 GMT, the mixed layer heights across the northern flight track (Figure 2a) increased from 500 m AGL (above ground level) in the northeast (Point A) to 800 m AGL before decreasing to near 0 m AGL in the northwest (Point B). Satellite imagery for 1601 GMT (not shown) indicates that the major portion of the convection was over the northwest corner. However, these convective clouds were already glaciated with cloud motions probably dominated by downdrafts. These prevailing downward motions in the NW provide a reasonable explanation for the suppression and destruction of the mixed layer at Point B at 1624 GMT. The model predicted vertical velocity fields suggests descending air on the northern side of the cloud field (Figure 4a). While the NW corner was glaciated, the 1601 GMT satellite imagery shows that several growing cumulus existed in the northeast (Point A). This is documented in the aerosol profile in Figure 6a which shows cloud tops above 3800 m AGL and mixed layer heights near 500-800 m AGL.

By 1800 GMT, almost all of the convection in the study area was glaciated. The only part of the study area not completely covered by clouds was the southern edge, which was still characterized by typical, undisturbed daytime conditions with a deep mixed layer and few well-developed convective clouds. This is documented in the aerosol profile of Figure 6b which shows few clouds and mixed layer heights of 900 m over most of the distance between Point C and Point D. The only exception is the northwest corner (Point D) where growing cloud tops reach 3000 m AGL. One feature which is particularly persistent in these images (Figures 6a-b) is the high aerosol concentration located between 1.5 and 2.0 km. This concentration of aerosols suggests an elevated haze layer due to regional burning during the previous day (Andreae et al., 1987).

As noted in the discussion of cloud model results (see Table 1), the convection on August 3 was characterized by more vigorous development. Satellite imagery for 1501 GMT (not shown) shows the early stages of a line of convection over the eastern half of the study region (Figure 2b).

The eastern flight track (Figure 2b) apparently traversed the wake of the storm complex as evidenced by the model-derived vertical velocity fields (Figure 4b) and supported by the presence of a suppressed mixed layer (Figure 7a). The apparent decline from 900 to 400 m in mixed layer heights between 1459 GMT and 1523 GMT along the flight track may represent the migration of the center of convection away from the eastern boundary.

By 1701 GMT, GOES imagery (Figure 3b) shows the organized line was nearly coincident with the western boundary of the study area (Figure 2b). The model-derived velocity fields for the western boundary are characterized by upward motion (Figure 4b). The mixed layer heights average about 1.0 km on this side of the storm (Figure 7b), and the distribution of cloud top heights between Point C and Point D further

emphasize vigorous convection in an inflow region.

We will describe in the sections which follow, the degree to which the vertical and horizontal distributions of O_3, CO, CO_2, NO, and water vapor can be observed by aircraft in the vicinity of convective clouds and understood using the two-dimensional model. The mean vertical profiles of individual trace gases along the active sides of the cloud system will be described first, followed by an examination of the horizontal variability of the observed gases at the two flight altitudes. Finally, we will estimate the vertical transports of given species by convective up- and downdrafts and by the convective cloud complex as a whole.

4.1 Mean Vertical Profiles of Individual Trace Gases

Vertically averaged values of O_3, CO, CO_2, and NO concentrations for the northern and southern sides of the August 2 and for the eastern and western sides of the August 3 cloud complexes are shown in Figures 8-11. The vertical profiles are obtained from the aircraft spirals on the corners of the box on either side of the storm complex. An additional measure of the vertical distribution of O_3 is obtained from the UV-DIAL measurements as shown in Figures 6 and 7. Average values of O_3 can be obtained at about 200 meter height intervals with a horizontal resolution of about 7 km in the cloud free areas below the aircraft. Ozone values and associated statistics which represent a sectional mean can be compared to the in situ means obtained from the aircraft spirals as shown in Figure 8. Local measurements taken during the aircraft spirals are representative of the north and south and east and west sides of the two storms as reflected by the sectional means and standard deviations. The weaker transports occurring on the August 2 compared to the stronger transports of O_3 on August 3 are evident over the entire

flight section. The details of local enhancement-demunition are not seen in the aircraft profiles but are clearly identifiable on the UV-DIAL O_3 sections. Considerable O_3 enhancement is seen between 1 and 3 km, especially on the eastern side of the August 3 storm with centers of maxima in O_3 exceeding 50 ppbv (Figure 7a). Ozone values at altitudes between 2.5 and 2.8 km on the eastern side for Case II (Figures 7a and 8b) are enhanced above any level observed in the lowest 5 km of the mean undisturbed troposphere. This suggests that the enhanced ozone values may not be due only to downward transports of mid- to upper-tropospheric ozone but may also be due to anthropogenic production. Model-derived EPT values observed between the same levels (Figure 4b) suggest that air descends from levels no higher than 3.5 km at maturity (40 min simulation time).

Ozone concentrations between 1.5 and 3.0 km in Case II (Figure 8b) are nearly doubled (compared to the undisturbed profile) and between 3.5 and 4.0 km nearly halved. This suggests an overturning of the lower troposphere effected by the storm. While in Case I (Figure 8a) enhancement of O_3 is seen between 1 and 3 km, the demunition noted in Case II between 3 and 4 km is not nearly as pronounced. This difference between the two convective cases is in accordance with the evidence cited earlier that Case II is the stronger, more active storm. Substantial depletion of O_3 values below 1 km and above 3.5 km is observed on both days.

Vertically averaged CO concentrations obtained from the aircraft spirals (Figure 9) exhibit a maximum between 1.5 and 2.0 km coincident with the lidar observed haze layers (Figures 6a and 7a). A pronounced peak in CO at 1.8 km occurs on August 2 when the presence of pollution is more evident than on August 3. The values on the north side of the August 2 storm complex were as much as 60 ppbv greater than the south at 1.8 km. Above 2 km, CO concentrations show much closer agreement on

either side of the complex. On August 3 (Figure 9b), CO values are similar on both sides of the disturbance. The largest variation between sides occurs near 5 km with east values exceeding west by less than 15 ppbv. Near surface or higher concentrations of CO on either side of the storm below 2 km suggests vertical turbulent mixing in the boundary layer rather than mixing due to cloud drafts.

A comparison of vertically averaged CO_2 concentrations observed on the disturbed days (Figure 10) shows a complete reversal in values in the lowest 1 km. Major CO_2 enhancement is evident below 1 km on August 2 (Figure 10a) with a maximum of 350 ppm observed at 400 m. In direct contrast, extensive CO_2 depletion is seen below 1 km on August 3 (Figure 10b) with values approaching 336 ppm at 200 m. Two elevated peaks of 348 ppm are observed at 2.3 and 3.7 km in the west profile on August 3. While low values of CO_2 might be expected in surface (canopy) air during the middle of the day (Figure 13, west side), the source of high values of CO_2 in the first 4 km of the atmosphere during the early afternoon is not obvious.

Vertically averaged profiles of NO concentrations for August 2 (Figure 11a) exhibit a pronounced maximum at 1.8 km on the north side of the storm coincident with the maximum observed CO values. The lowest NO values observed in any of the profiles occur at 4.2 km on the south side of the August 2 storm. No obvious trend in NO concentration is evident in the profiles on August 3 (August 11b). Both sides of the storm system exhibit a negative vertical gradient.

4.2 Horizontal Variability in θ_e, O_3, CO, and NO

Figures 12 and 13 show values of θ_e, O_3, CO, and NO along the upper (5 km) and lower (150 m) flight tracks enclosing the two convective cloud complexes shown in Figure 2. Simultaneous display of water

vapor (θ_e) and the three trace gases provides an opportunity to examine both the horizontal variability and the possible causes of observed changes in concentrations.

Model calculations (Figure 4) suggest that for Case I (Figure 12) descending motion predominates on the north side of the cloud system while ascending motions are concentrated on the south side. For Case II (Figure 13), ascending motion prevails on the western side, descending motion on the eastern side. As indicated above and in Table 1, Case I is considerably less vigorous than Case II.

Large and systematic excursions of θ_e are seen for both cloud systems at both levels. Major excursions in θ_e are, in most instances, accompanied by large amplitude variations in the other three trace gases. Aircraft sampling on the north side of the storm complex on August 2 occurred between 1600 GMT and 1720 GMT (Figures 12a-b). As noted in Section 4, satellite imagery, aerosol profiles and model results suggested the region around Point B was dominated by downward motions. This is supported by Figure 12b which shows a sharp decline in θ_e values coincident with a rapid increase in O_3 concentration near the surface.

Ordinarily, prevailing downdrafts would not result in an increase in CO concentration near the surface, however, the downdrafts in the vicinity of Point B are passing through a well defined haze layer between 1.5 and 2.5 km (Figure 6a) and this may be responsible for the observed CO values. Despite the apparent lack of a decline in θ_e values near Point B at the upper level (Figure 12a), downward motion is suggested by the rise in O_3 and drop in CO concentration. This paradox may be solved by consulting the model output for August 2 (Figure 4a) which indicates little if any gradient in θ_e between 3 and 6 km.

Significant variability in θ_e and the trace gases is also seen along the southern boundary of the storm complex of August 2. Figure 12c exhibits large oscillations in O_3, CO, and θ_e between 125 and 200 km characterized by concurrent increases (decreases) in θ_e and O_3, and a decrease (increase) in CO. Satellite imagery for this period and remotely sensed aerosol concentrations indicate the southern boundary consisted of a few growing cumulus within a developing mixed layer. The θ_e values further suggest active convective overturning. Sufficient time elapsed between the upper and lower traverses that the horizontal variability along the lower southern boundary (Figure 12d) reflected changes in the cloud field which were inconsistent with the upper level observations.

Horizontal fluctuations in θ_e and trace gas concentrations are also observed on August 3 (Figures 13a-d). Sampling along the eastern boundary of the study area (Figures 13c-d) occurred early in the lifetime of the storm complex. Satellite imagery shows the developing disturbance was located in the eastern half of the study region. The influence of convective overturning is demonstrated by the horizontal fluctuation in trace gases and θ_e along the upper level (Figure 13c). North of 80 km, increases (decreases) in θ_e and CO occur coincidently with a decrease (increase) in O_3.

The lower traverse (1543 GMT) was initiated nearly 1 hour after the start of the upper sampling, placing the aircraft within a developing outflow region. Despite this location, the measured values still indicate the presence of contaminated surface air.

Satellite imagery taken over the lifetime of the storm confirms a westward migration for the developing disturbance. The upper sampling (1656-1720 GMT) revealed coincidental horizontal fluctuations in θ_e and trace gas concentrations (Figure 13a). The simultaneous lidar pro-

file also documents active convection by illustrating areas of high mixed layer heights and cumulus clouds (Figure 7b). The low level traverse (Figure 13b) further supports convective activity along the western border by showing two areas of elevated θ_e values, suggesting upward motion. This trend is exhibited well by the surface derived trace gas, CO.

General guidance from the model estimates appears to be supported by simultaneous measurement of a suite of trace gases. No simple net result of upward and downward transport emerges from in situ sampling along aircraft tracks at different levels. Transports in both directions are evident in regions where model estimates might suggest transport mainly in one direction. Major vertical displacements are, however, evident and the intensity of one system (Case I) versus the other (Case II) is detected. We attempt in the next two sections to obtain some quantitative estimates of the vertical transports.

4.3 Convective Draft Transports

The time and space dependent nature of convective draft transports can be approximated by assuming that the model generated two-dimensional time-dependent fields are a reasonable representation of the real atmosphere. Under these circumstances a specific aircraft sounding may correspond to a given model location and time. The location of the aircraft sounding in model time and space can be determined in a general sense from supporting data such as the satellite visible images and aircraft photogrammetry. More precise location of the aircraft soundings was achieved by seeking the best correspondence between the vertical sounding of θ_e and the model predicted values of θ_e. Table 2 shows four such comparative examples. Soundings 1611 and 1720 on August 3 are discussed first. Sounding 1611 on August 3 corresponds to grid point 85 at 36 min

of the model calculation. The location of this sounding is at AA' in Figure 2b. The model computed θ_e field at 36 min is shown in Figure 14 together with the location of the sounding.

Figure 15 shows the vertical profiles of O_3 for sounding 1611 compared to the mean undisturbed O_3 profile together with the model calculated vertical (w) and horizontal (u) velocity fields. The model shows this sounding to be located in a region of downward motion. Model derived time evolution of the vertical velocity fields about this time (36 min) show these fields to be changing relatively quickly. Figure 16 illustrates 3 profiles of vertical and horizontal velocity for 34 min, 36 min, and 38 min. The vertical motion remains downward over this 4 min period but the changing profile reflects the convective draft nature of the motion.

Calculation of downward mixing of a volume of air located between 4 and 5 km with a mean undisturbed concentration of O_3 of 38 ppbv to a level between 2 and 3 km can be carried out assuming no entrainment on the descent and no significant production or destruction of O_3 over the short time period involved. Simple mixing of air with a concentration of 38 ppbv with an equal volume of air with a concentration of 22 ppbv yields a value of 30 ppbv. Given a mean model estimated vertical velocity of 2.5 m sec^{-1} over a distance of 2 km yields a time of 800 sec or approximately 13 min. The time period is consistent with the lifetime of convective scale downdrafts. Observed concentrations are greater than 30 ppbv at the 2 to 3 km level but exhibit a sudden discontinuous increase near 3 km not inconsistent with undilute (no entrainment) downward transports. Observations and model estimates appear to be entirely consistent with undilute convective downdraft transport.

Figure 17 shows the vertical profile of O_3 for sounding 1720 compared to the mean undisturbed O_3 profile, together with the model calculated vertical velocity profiles at 36, 38, and 40 min bracketing the time of best fit (38 min) for the location of best fit in model space. The model vertical velocities show both up- and downward motions with maximum velocities about one third the magnitude of the 1611 downward motions. The O_3 profile shows increased concentrations in the lower troposphere (between 1.0 and 2.8 km) and decreased concentrations in the layer between about 2.8 and 5.0 km. The observed O_3 distribution is indicative of convective overturning of these layers reflecting perhaps the net integrated result of the up- and downward transports of the storm complex at this location.

Soundings 1625 and 1919 (Table 2) on August 2 correspond to very weak model estimated vertical velocity fields (maximum value less than 0.5 m sec^{-1}). Similarly, the observed vertical profiles of O_3 at these times and locations show only weak departures from the mean but do exhibit the same tendency for convective overturning as described above.

Marked convective overturning producing local changes in concentrations of trace gases in the vicinity of convection would suggest possible changes in the radiative heating rates of these layers. It is unlikely that such changes could produce anything but very small changes in vertical temperature gradients and consequently buoyancy. However, the sense of the above overturning of O_3 in the lowest 5 km of the atmosphere is to destablize the column. We will ascertain whether such a process could help in maintaining a daytime convective system.

4.4 Mean Convective Complex Transports

The horizontal velocity fields around each convective cloud complex at two levels (5 km and 150 m) over a period of 6 hours was measured

by the aircraft. Streamline fields at each level were constructed assuming that the large scale velocity fields remained stationary. These streamline fields together with the velocity divergence, are shown in Figures 18 and 19.

The vertical velocity fields derived from Figures 18 and 19 and shown in Figures 20a-b suggest net upward transport over the entire storm complex over the 6 hour time frame. Decreases in O_3 concentrations shown in Figure 8 above 3 km would reflect upward transport. However, the increases in O_3 concentrations below 3 km (Figure 8) must be a consequence of downward motion. We must conclude that the smoothed horizontal velocity fields do not adequately reflect the up- and downward convective draft transports but may provide an estimate of storm complex scale vertical motion.

5. Conclusions

The interpretation of trace gas chemistry in the vicinity of deep convection can benefit from

a) the measurement of other thermodynamic quantities, particularly quantities with quasi-conservative characteristics such as θ_e.

b) cloud model simulations which can provide a framework for the interpretation of the observations.

c) Conversely, chemical species provide tracers which can help in the interpretation and validation of cloud model calculations.

Aircraft measurements along a horizontal track in the vicinity of deep convection exhibit very large changes in specie concentrations, doubling or halving concentrations over distances as short as 50 km. Simultaneous measurements of a number of species including temperature

and humidity, permit interpretation of at least the larger fluctuations. Distinction can be made between natural changes due to atmospheric motions (upward and downward transports) and anthropogenic changes due to such causes as biomass burning.

The interpretation of the chemical observations is greatly aided by the simultaneous use of a convective cloud model. Cloud models must ultimately incorporate chemical production and destruction. Caution must be exercised when interpreting observations made over a number of hours in the vicinity of convection where major vertical displacements of air can occur in a time frame of minutes to a few tens of minutes. However, careful use of model and observations would seem to serve to distinguish between the process (up- and downdrafts) and the net result. Thus, near instantaneous observations of the consequences of down- and updrafts can be detected in specie concentrations as well as convective overturning of the lower troposphere as a net overall result of the convective processes embedded in the storm.

The two convective cloud systems presented in this paper display substantial dynamical differences yet the observed differences in specie distribution and concentrations are relatively subtle. Observations of the trace gases were confined to the region between the surface and 5 km. We suspect that considerably greater differences between the two cloud systems would have been detected if the sampling could have been extended upwards above 5 km to nearer 13 km.

Acknowledgments

We wish to acknowledge the broad support of NASA in the GTE-ABLE program. We particularly wish to recognize the contributions of the NASA Electra aircrew and technicians. The work done at the University of Virginia was supported under funding from NASA. We also wish to thank Mrs. Deborah Martin for the drafting of the figures and Ms. Mary Morris for the preparation of the manuscript.

REFERENCES

Andreae, M.O., E.V. Browell, P.L. Silva Dias, M. Garstang, G.L. Gregory, R.C. Harriss, G.F. Hill, D.J. Jacob, M.C. Pereira, G.W. Sachse, A.W. Setzer, R.W. Talbot, A.L. Torres, and S. C. Wofsy, Biomass burning emissions and associated haze layers over Amazonia, submitted to J. Geophys. Res., 1986.

Anthes, R.A., Numerical experiments with a two-dimensional horizontal variable grid, Mon. Wea. Rev., 98, 810-822, 1970.

Augstein, E., M. Garstang, and G.D. Emmitt, Vertical mass and energy transports by cumulus clouds in the tropics, Deep Sea Res., Spec. Vol., 9-21, 1980.

Bolton, D., The computation of equivalent potential temperature, Mon. Wea. Rev., 108, 1046-1053, 1980.

Browell, E.V., A.F. Carter, S.T. Shipley, R.J. Allen, C.F. Butler, M.N. Mayo, J.H. Siviter, Jr., and W.M. Hall, NASA multipurpose airborne DIAL system and measurement of ozone and aerosol profiles, Appl. Opt., 22, 522-534, 1983.

Browell, E.V., G.L. Gregory, R.C. Harriss, and V.W.J. Kirchhoff, Tropospheric O_3 and aerosol distributions across the Amazon basin, to be published J. Geophys. Res., 1987.

Dickerson, R.R., G.J. Huffman, W.T. Luke, L.J. Nunnermacker, K.E. Pickering, A.C.D. Leslie, C.G. Lindsey, W.G.N. Slinn, T.J. Kelly, P.H. Daum, A.C. Delany, J.P. Greenberg, P.R. Zimmerman, J.F. Boatman, J.D. Ray, and D.H. Stedman, Thunderstorms: an important mechanism in the transport of air pollutants, Sci., 23, 460-465, 1987.

Gregory, G.L., C.H. Hudgins, and R.A. Edahl, Jr., Laboratory evaluation of an airborne ozone instrument which compensates for altitude/sensitivity effects, Envir. Sci. and Tech., 17, 100-103, 1983.

Gregory, G.L., S.M. Beck, and J.A. Williams, Measurements of free tropospheric ozone: An aircraft survey from 44 north to 46 south latitude, J. Geophys. Res., 89, 9642-9648, 1984.

Gregory, G.L., R.C. Harriss, R.W. Talbot, R.A. Rasmussen, M. Garstang, M.O. Andreae, R.R. Hinton, E.V. Browell, S.M. Beck, D.I. Sebacher, M.A.K. Khalil, R.J. Ferek, and S.V. Harriss, Air chemistry over the tropical forest of Guyana, J. Geophys. Res., 91, 8603-8612, 1986.

Gregory, G.L., E.V. Browell, and L.S. Gohan, Boundary layer ozone: an airborne survey across the Amazon basin, to be published J. Geophys. Res., 1987.

Harriss, R.C., S.C. Wofsy, M. Garstang, L.C.B. Molion, R.S. McNeal, J.M. Hoell, R.J. Bendura, S.M. Beck, R.L. Navarro, J.T. Riley, and R.C. Shell, The Amazon Boundary Layer Experiment, to be published J. Geophys. Res., 1987.

Kessler, E., On the distribution and continuity of water substance in atmospheric circulation, Meteor. Monogr., No. 32, Amer. Meteor. Soc., 84 pp., 1969.

Lin, Y.-H., R.D. Farley, and H.D. Orville, Bulk parameterization of the snow field in a cloud model, J. Clim Appl. Meteor., 22, 1065-1092, 1983.

Marshall, J.S., and W. Mck. Palmer, The distribution of raindrops with size, J. Meteor., 5, 165-166, 1948.

Martin, C.L., D.R. Fitzjarrald, M. Garstang, A.P. Oliveira, S. Greco, and E.V. Browell, Structure and growth of the mixing layers over the Amazon rain forest, to be published J. Geophys. Res., 1987.

Riehl, H., and J.S. Simpson, The balance of the equatorial trough zone, revisited, Contrib. Atmos. Phys. Beit. Physik Atmos., 52, 287-304 1979.

Robert, A.J., The integration of a low order spectral form of the primitive meteorological equations, J. Meteor. Soc., Japan, 44, 237-245, 1966.

Sachse, G.W., G.F. Hill, L.O. Wade, and M.G. Perry, Fast response, high precision carbon monoxide sensor using a tunable diode laser absorption technique, to be published J. Geophys. Res., 1987.

Soong, S.-T., and Y. Ogura, Response of a trade-wind cumuli to large-scale processes, J. Atmos. Sci., 37, 2035-2050, 1980.

Soong, S.-T., and W.-K. Tao, A numerical study of the vertical transport of momentum in a tropical rainband, J. Atmos. Sci., 41, 1049-1061, 1984.

Tao, W.-K., and S.-T. Soong, The study of the response of deep tropical clouds to mesoscale processes: three-dimensional numerical experiments, J. Atmos. Sci., 43, 2653-2676, 1986.

Torres, A.L., and H. Buchan, Tropospheric nitric oxide measurements over the Amazon basin, to be published J. Geophys. Res., 1987.

Wofsy, S.C., R.C. Harriss, and W.A. Kaplan, Carbon dioxide in the atmosphere over the Amazon basin, to be published in J. Geophys. Res., 1987.

Authors' Address List

Michael Garstang, Steve Greco, and John Scala
University of Virginia
Department of Environmental Sciences
Clark Hall
Charlottesville, VA 22903

Sherwin Beck, Edward Browell, Robert Harriss, Glen Sachse and Gerald Hill
NASA/Langley Research Center
Hampton, VA 23665

Joanne Simpson and Wei-Kuo Tao
Laboratory for Atmospheres
NASA/Goddard Space Flight Center
Greenbelt, MD 20771

Arnold Torres
NASA/Wallops Flight Facility
Wallops Island, VA 23337

FIGURE CAPTIONS

Fig. 1. Study area over the central Amazon basin (see insert for location) together with flight tracks of the ABLE-2A missions. The regions of disturbed weather described in this paper are within the shaded areas to the north and south of the Rio Negro.

Fig. 2. Flight tracks and vertical soundings around the convection for both days. The upper level tracks A to B and C to D were flown at about 5 km, the lower level tracks B' and C' and D' to C' at 150 m. (a) The convection on August 2 migrated WNW through the open end of the box. (b) A distinct line of convection with identifiable cells extended northward out of the open end on August 3.

Fig. 3. GOES satellite imagery, full disc visible. The closed circle contains the convective area of study and the arrow points to the leading edge of the frontal boundary. (a) 1701 GMT, August 2. (b) 1701 GMT, August 3.

Fig. 4. Two-dimensional cloud model output. Equivalent potential temperature contours in degrees K are shown with superimposed heavy dashed lines approximating major u-w vectors. The two compass directions defined by the plane of the model output are included. (a) August 2 simulation at 36 min after initialization. (b) August 3 simulation at 40 min after initialization.

Fig. 5. Aircraft-derived vertical profiles of computed equivalent potential temperature. Three soundings corresponding to the late morning (solid), late afternoon (dashed), and mean aircraft (dots) profiles are plotted. (a) August 2 using 1534 GMT and 1919 GMT soundings. (b) August 3 using 1405 GMT and 1807 GMT soundings.

Fig. 6. UV-DIAL determined aerosol and O_3 profiles for August 2, 1985. (a) North side flight track from Point A to Point B. (b) South side flight track from Point C to Point D.

Fig. 7. UV-DIAL determined aerosol and O_3 profiles for August 3, 1985. (a) East side flight track from Point A to Point B. (b) West side flight track from Point C to Point D.

Fig. 8. Vertically averaged concentration of O_3 along the principle sides (Fig. 2) of the two storm complexes. (a) August 2, Mission 12. (b) August 3, Mission 13. The mean undisturbed profile (dashed) of O_3 is obtained from flights in undisturbed weather. Sectional average values together with 1 standard deviation bars show the mean values for O_3 from the UV-DIAL with the symbols identifying the location.

Fig. 9. Vertically averaged concentrations of CO along the principle sides of the two cloud complexes. (a) August 2, Mission 12. (b) August 3, Mission 13.

Fig. 10. Vertically averaged concentrations of CO_2 along the principle sides of the two cloud complexes. (a) August 2, Mission 12. (b) August 3, Mission 13.

Fig. 11. Vertically averaged concentrations of NO along the principle sides of the two cloud complexes. (a) August 2, Mission 12. (b) August 3, Mission 13.

Fig. 12. Values of O_3, CO, NO, and θ_e along each traverse of the flight box around the cloud complex of August 2, 1985. (a) Upper traverse on the northern side. (b) Lower traverse on the northern side. (c) Upper traverse on the southern side. (d) Lower traverse on the southern side.

Fig. 13. Values of O_3, CO, NO, and θ_e along each traverse of the flight box around the cloud complex of August 3, 1985. (a) Upper traverse on the western side. (b) Lower traverse on the western side. (c) Upper traverse on the eastern side. (d) Lower traverse on the eastern side.

Fig. 14. Model computed θ_e field at 36 min simulation time. The location of the 1611 sounding from August 3, 1985 is designated by the vertical line at A-A'.

Fig. 15. Aircraft derived vertical profile of O_3 for sounding 1611 on August 3, 1985, and model calculated vertical velocity (w) and horizontal velocity (u) fields at 36 min simulation time.

Fig. 16. Time evolution of the vertical velocity and horizontal fields computed by the model at A-A' corresponding to the location of aircraft sounding 1611.

Fig. 17. Aircraft derived vertical profile of O_3 for sounding 1720 on August 3, 1985 and time evolution of the vertical velocity field as computed by the model corresponding to the location of the aircraft sounding. The subscripts associated with the velocity profiles reflect the model simulation time.

Fig. 18. Interpolated streamline fields together with calculated horizontal divergence. (a) Using upper level winds on August 2, 1985. (b) Using lower level winds on August 2, 1985.

Fig. 19. Interpolated streamline fields together with calculated horizontal divergence. (a) Using upper level winds on August 3, 1985. (b) Using lower level winds on August 3, 1985.

Fig. 20. Mean vertical velocity derived from the streamline fields and horizontal divergence. (a) August 2, 1985. (b) August 3, 1985.

TABLE 1. Case Comparison of the Two Disturbed Days Utilizing Environmental Observations and Model Simulation Results.

	Case I: August 2, 1985	Case II: August 3, 1985
ENVIRONMENTAL OBSERVATIONS		
Maximum observed cloud top height	25,000 ft	42,000 ft
Low level wind	Northeasterly	Northwesterly
MODEL OUTPUT		
Maximum height of pressure perturbation	330 mb	130 mb
Maximum rainwater	5.0 g kg	5.0 g kg
Maximum vertical velocity	14.0 m s	16.0 m s

TABLE 2. Comparison Between Aircraft Derived Vertical Sounding of θ_e and the Model Predicted Values of θ_e.

Height (km)	Aircraft August 2, 1985 1625	Model 26 min	Aircraft August 2, 1985 1919	Model 28 min	Aircraft August 3, 1985 1611	Model 36 min	Aircraft August 3, 1985 1720	Model 38 min
5.0	331	325	321	327	329	332	329	328
4.5	328	325	325	325	323	329	329	327
4.0	327	325	324	326	326	329	329	328
3.5	326	324	323	327	326	327	329	326
3.0	325	324	324	327	317	326	328	325
2.5	328	325	327	328	316	328	321	328
2.0	329	327	330	327	326	332	330	333
1.5	334	338	334	335	331	336	333	335
1.0	335	340	339	341	339	338	337	338
0.5	338	339	343	346	344	341	339	342

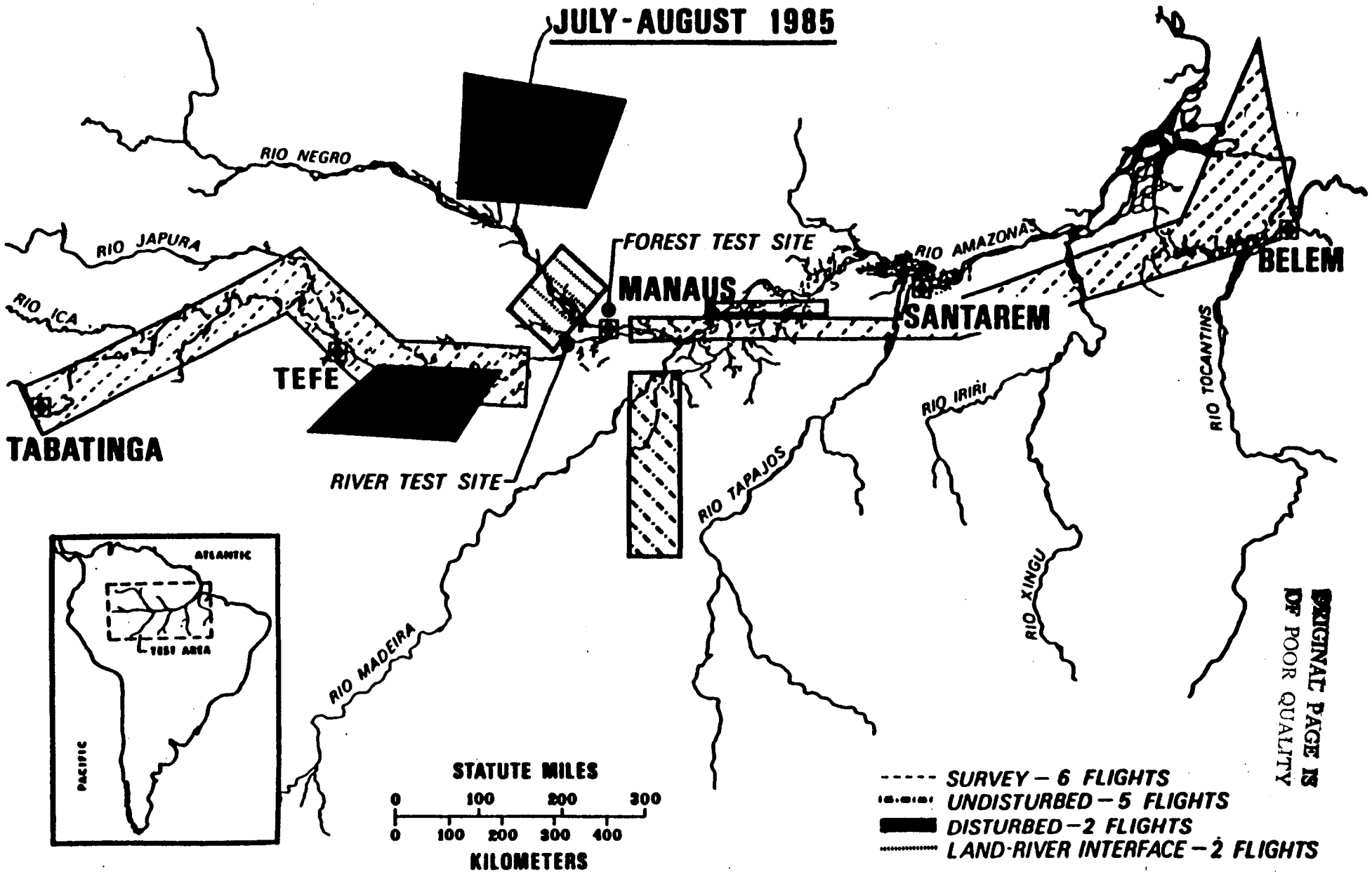

fig 1

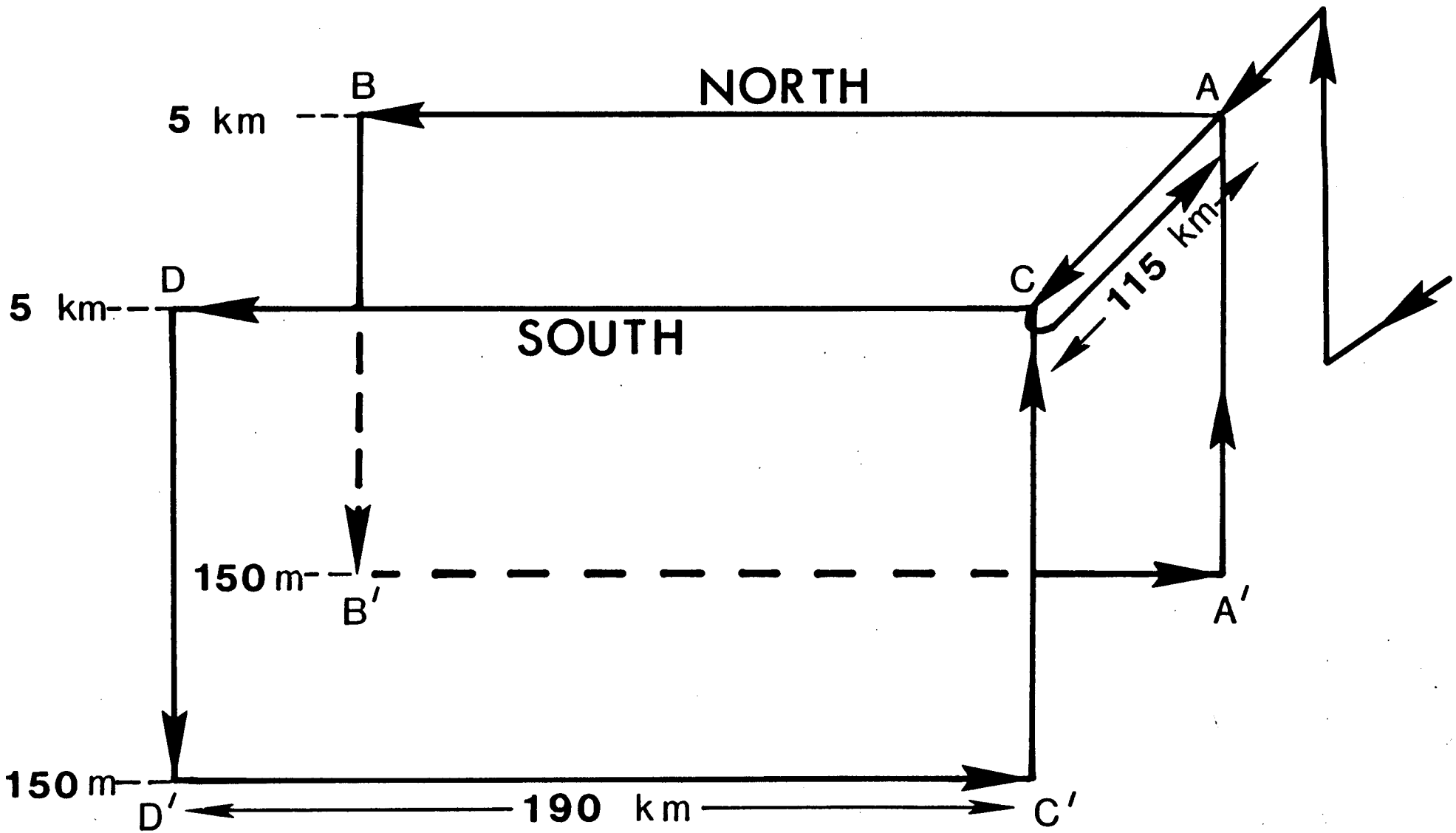

fig 2a

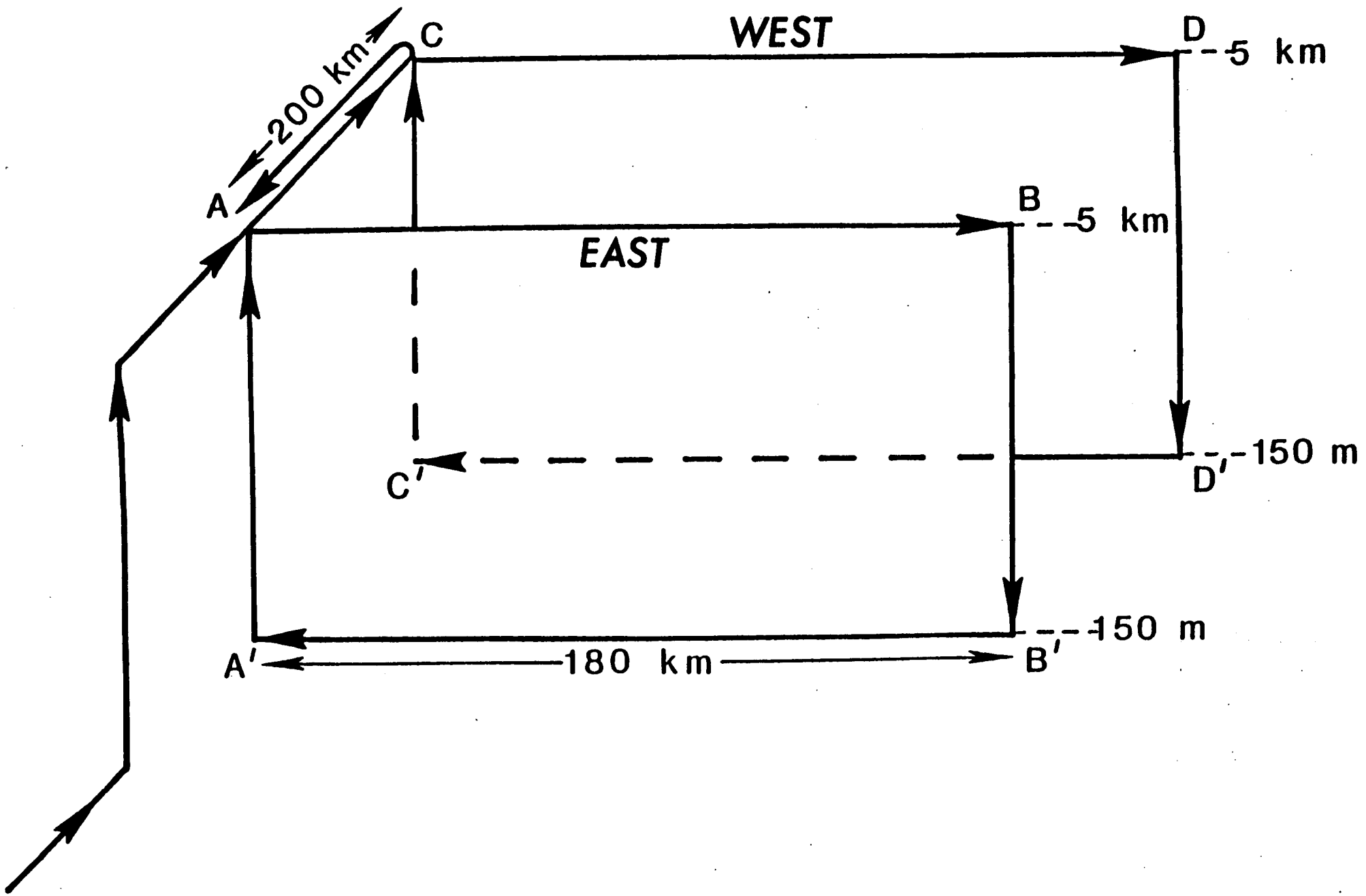

Fig 26

1701 02AU85 38A-4 00101 19111 WC1

Fig 36

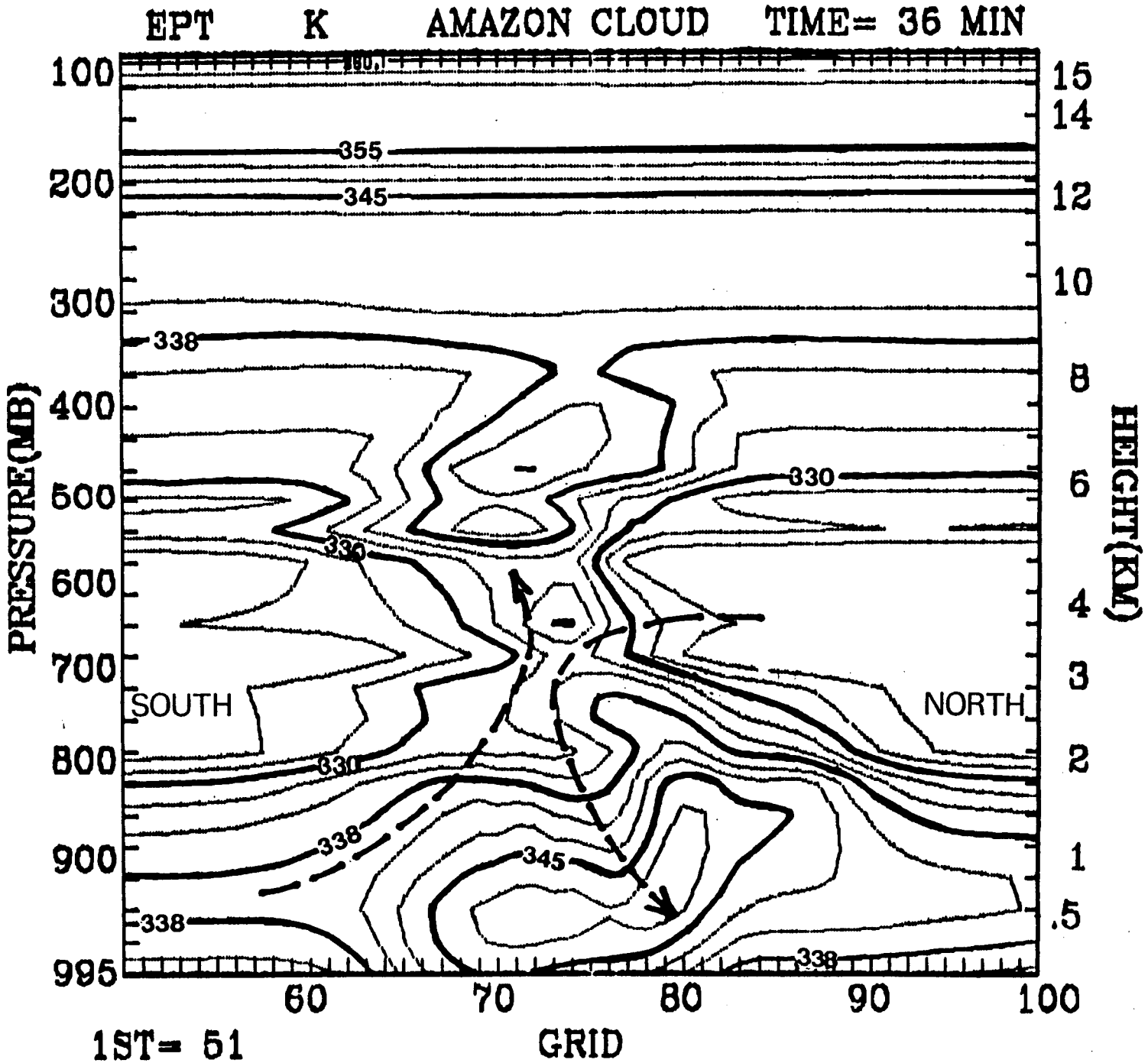
EPT K AMAZON CLOUD TIME= 36 MIN
PRESSURE(MB)
HEIGHT(KM)
100
200
300
400
500
600
700
800
900
995
15
14
12
10
8
6
4
3
2
1
.5
360
355
345
338
330
330
630
338
345
338
338
SOUTH
NORTH
60
70
80
90
100
1ST= 51
GRID

Fig 4a

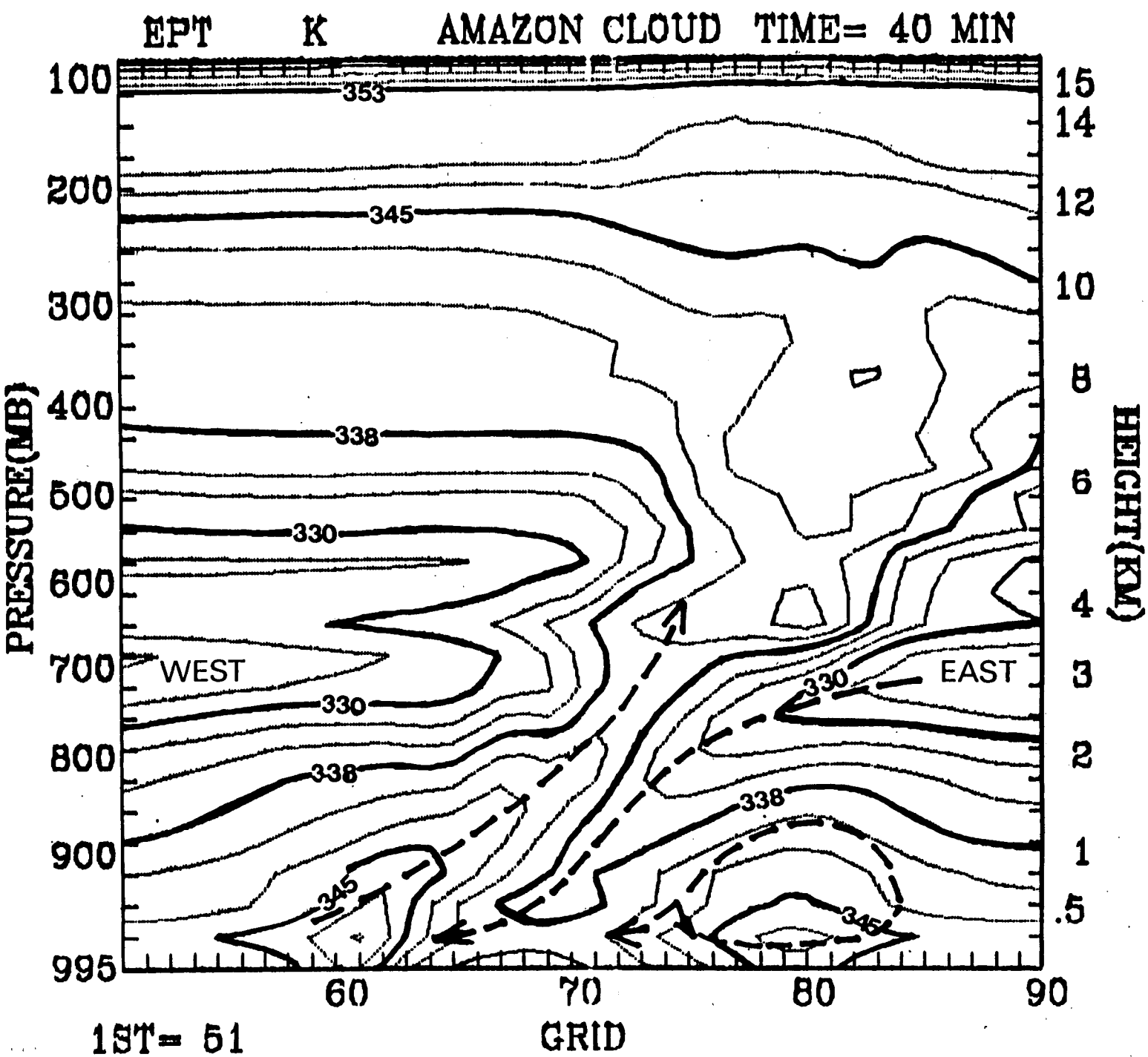
EPT K AMAZON CLOUD TIME= 40 MIN
PRESSURE(MB)
HEIGHT(KM)
100
200
300
400
500
600
700
800
900
995
15
14
12
10
8
6
4
3
2
1
.5
353
345
338
330
330
338
338
345
345
WEST
EAST
60
70
80
90
IST= 51
GRID

Fig 4b

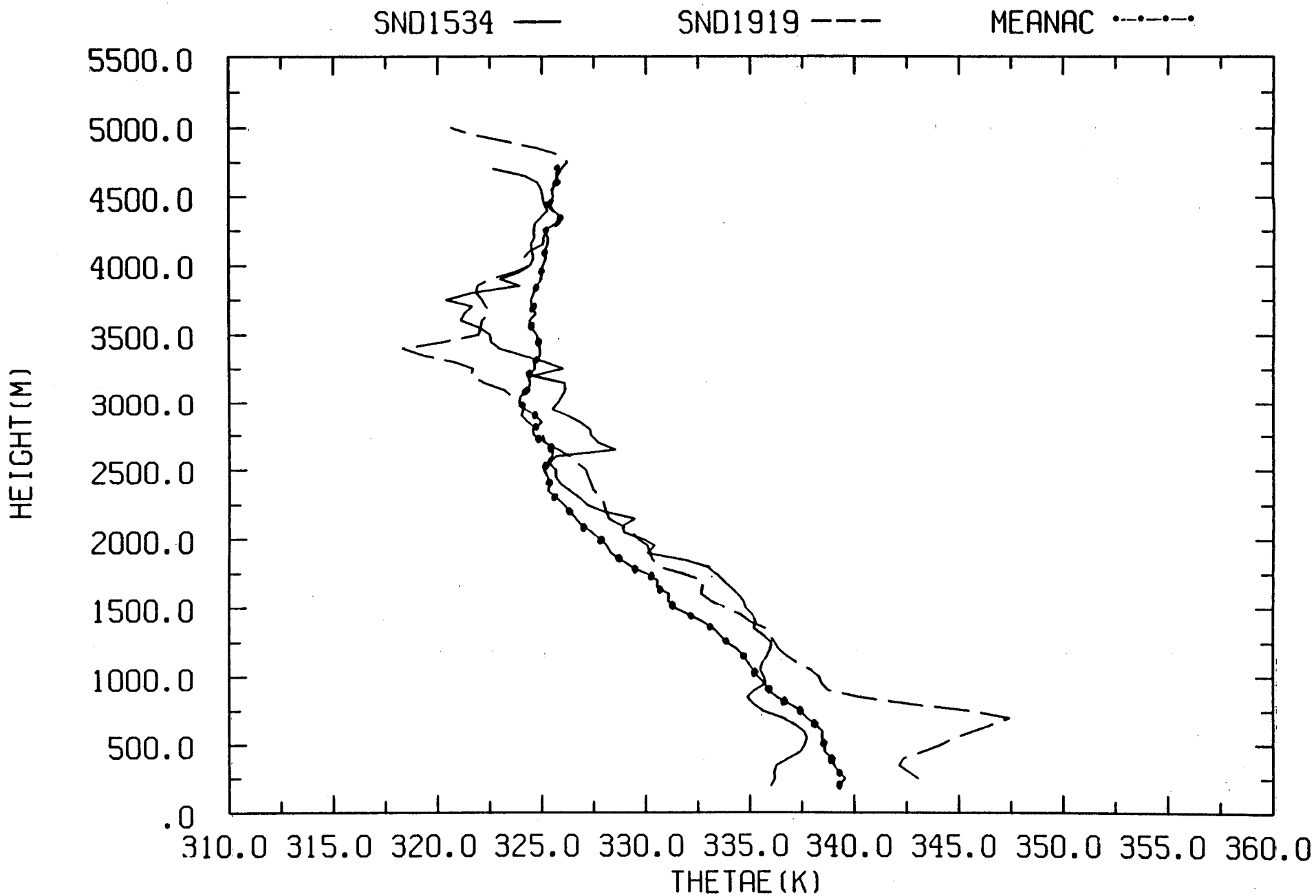
SND1534
SND1919
MEANAC
5500.0
5000.0
4500.0
4000.0
3500.0
3000.0
2500.0
2000.0
1500.0
1000.0
500.0
.0
HEIGHT(M)
310.0 315.0 320.0 325.0 330.0 335.0 340.0 345.0 350.0 355.0 360.0
THETAE(K)

Fig 5a

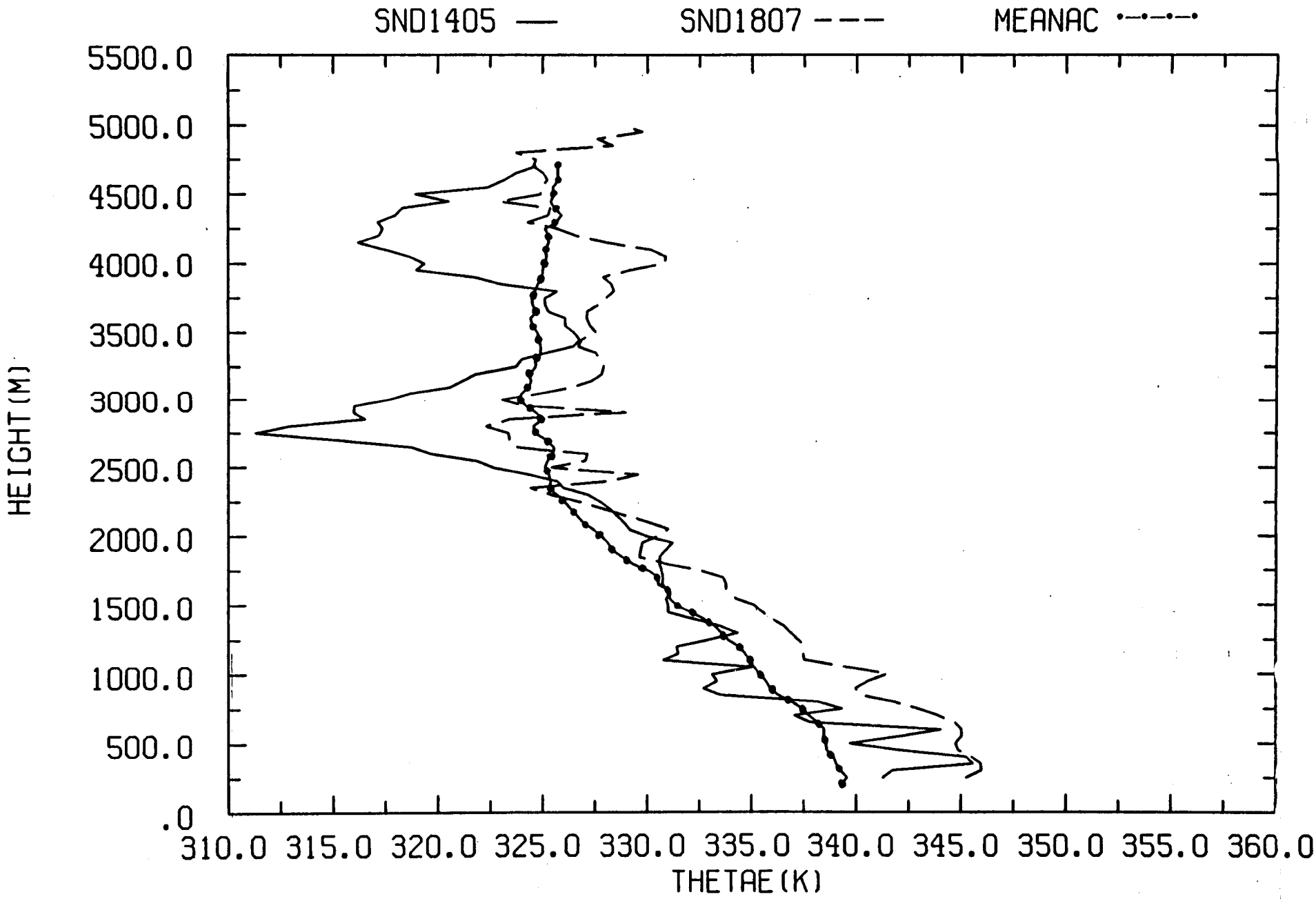
SND1405
SND1807
MEANAC
5500.0
5000.0
4500.0
4000.0
3500.0
3000.0
2500.0
2000.0
1500.0
1000.0
500.0
.0
HEIGHT(M)
310.0 315.0 320.0 325.0 330.0 335.0 340.0 345.0 350.0 355.0 360.0
THETAE(K)

Fig 5b

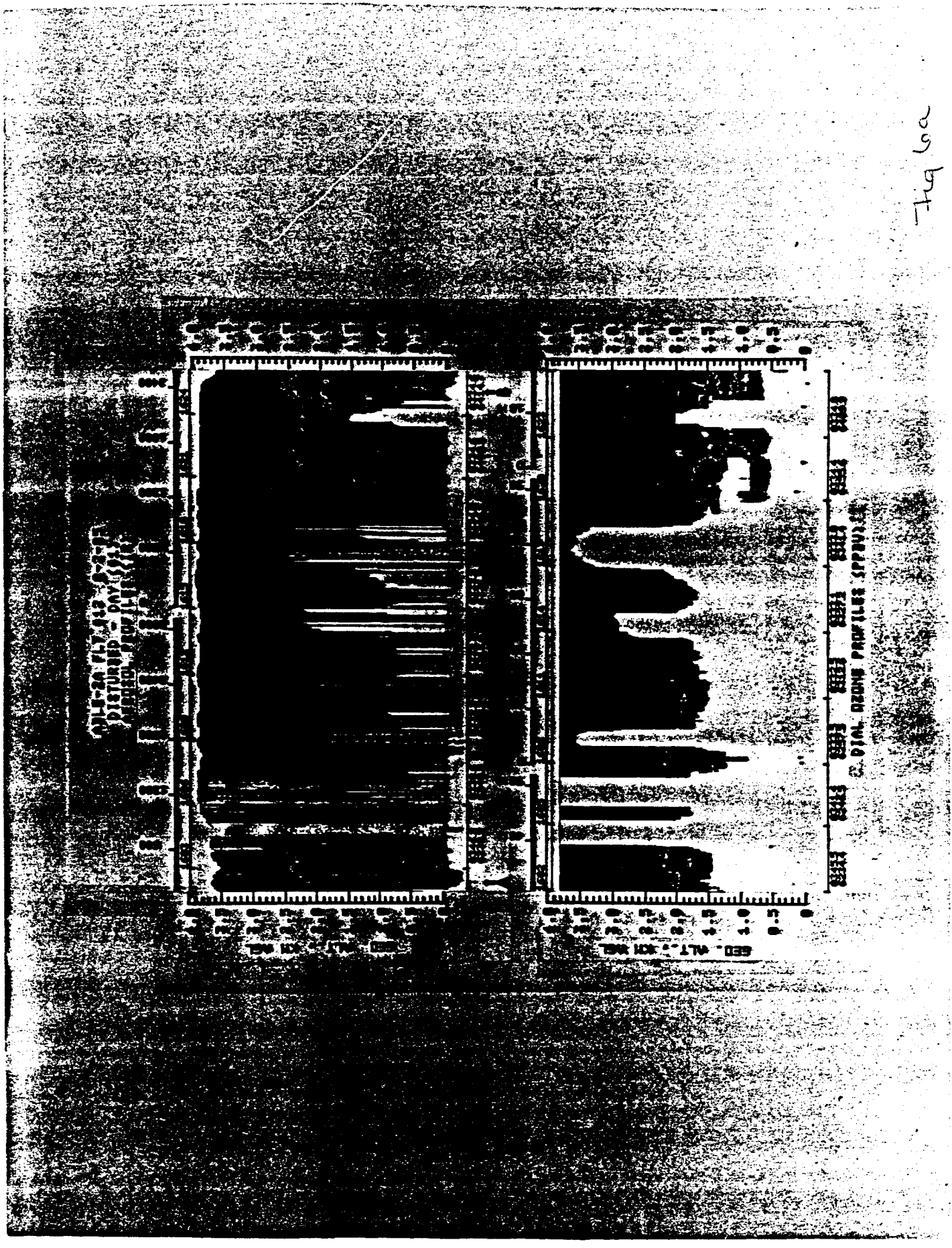

Fig 6a

NASA
L-86-4333

NASA
L-86-4336

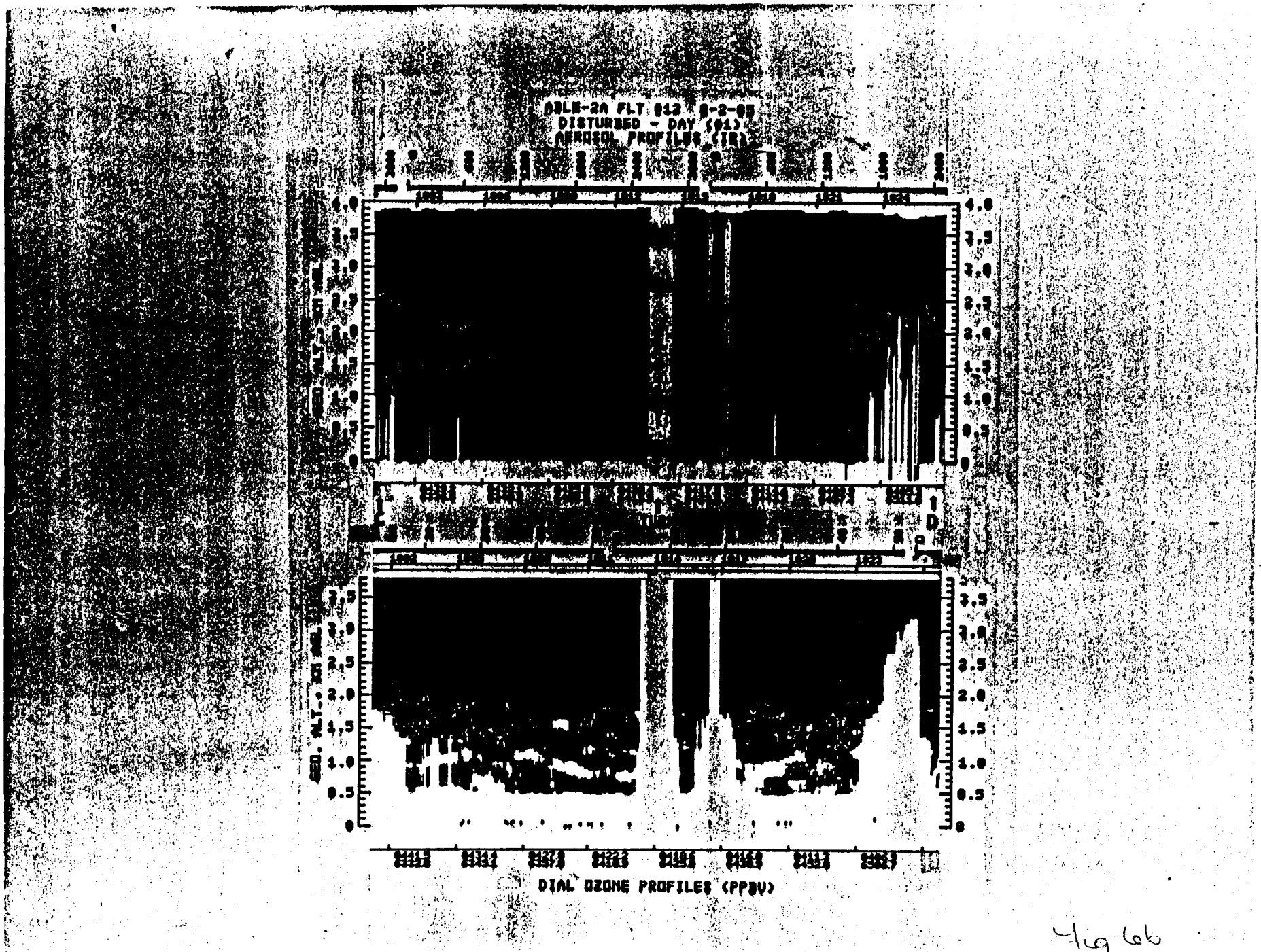

4/29 Lab

ORIGINAL PAGE IS
OF POOR QUALITY

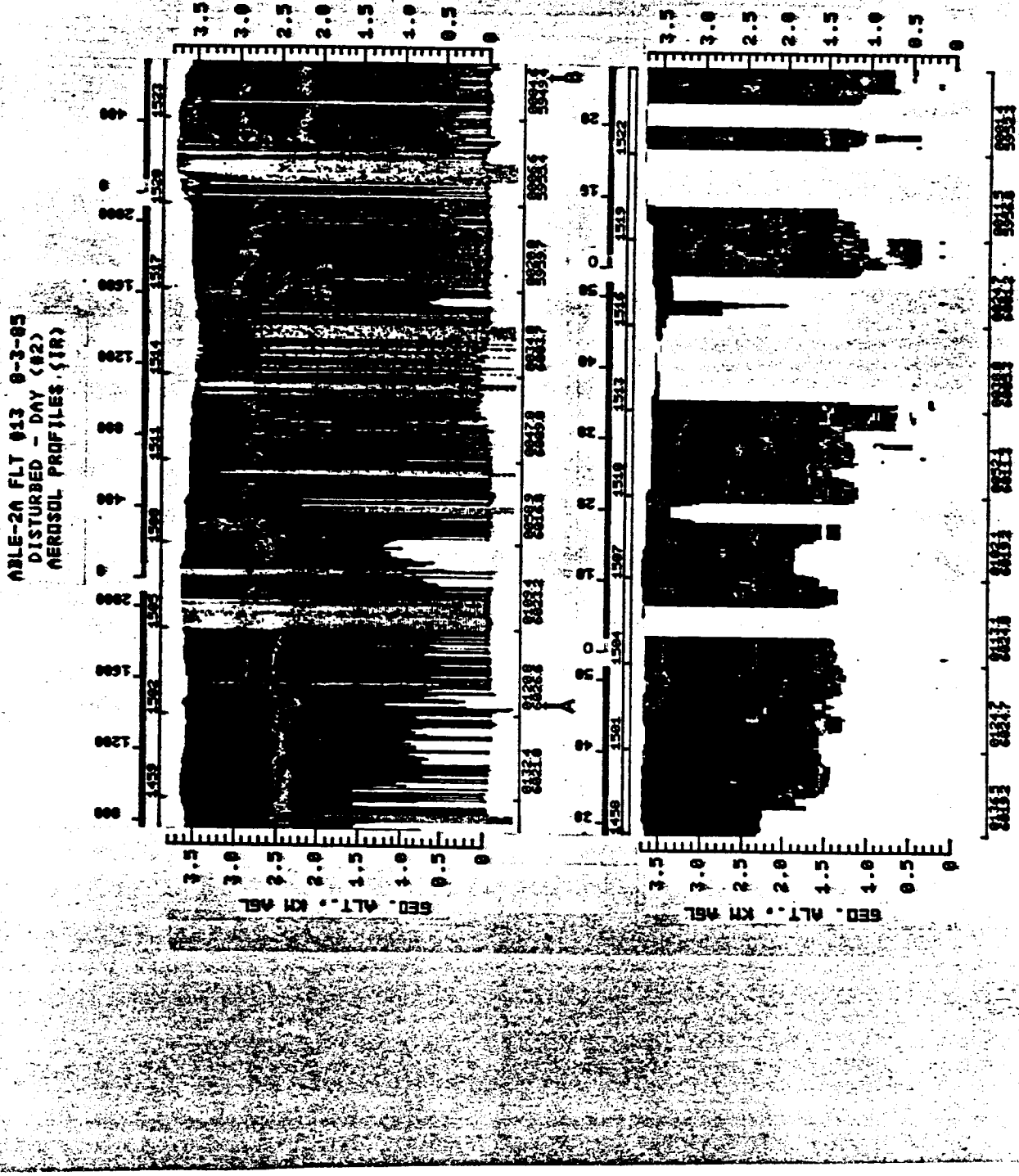

NASA
L-86-3083

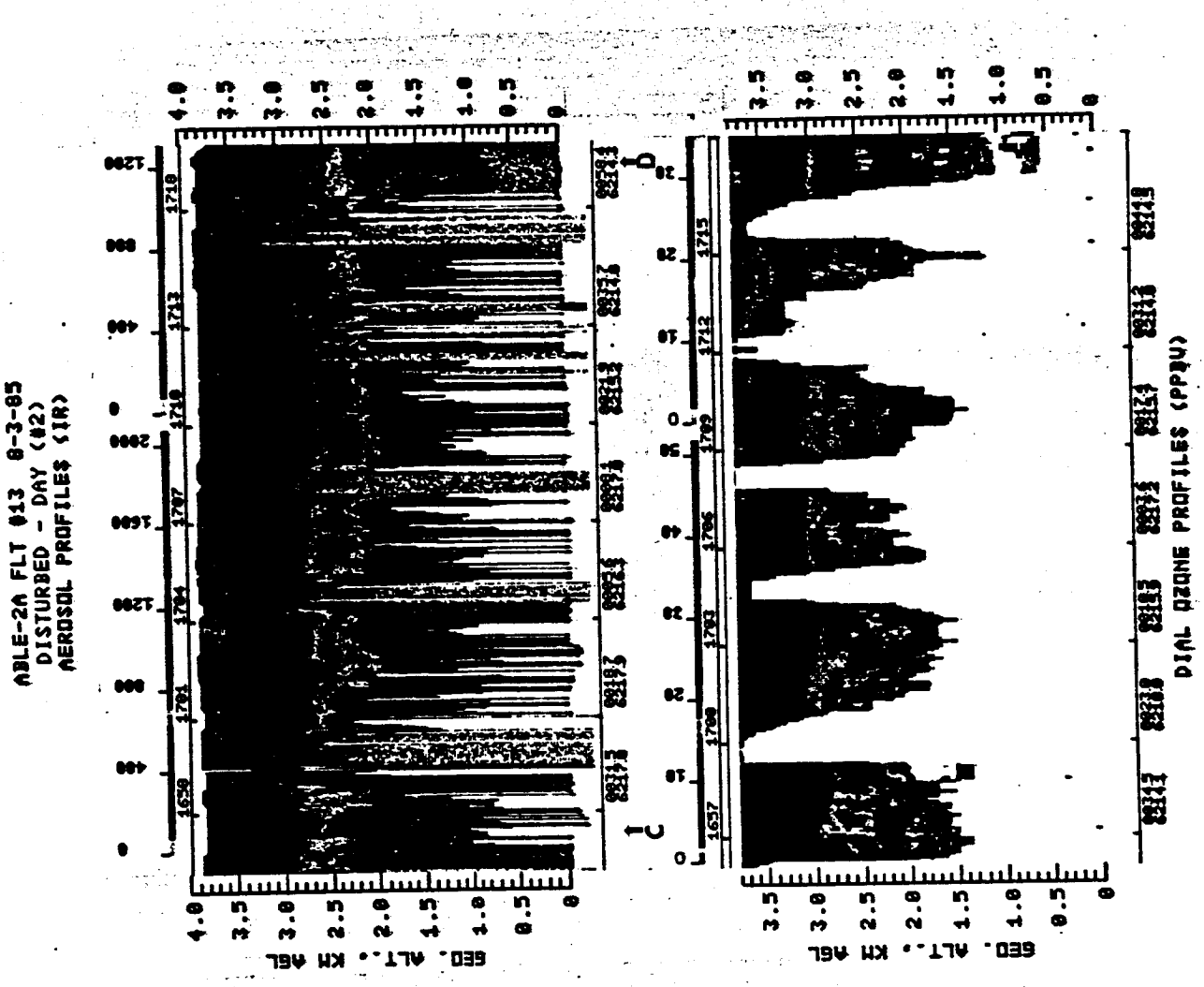

Fig 7b.

NASA
L-86-3086

MISSION 12

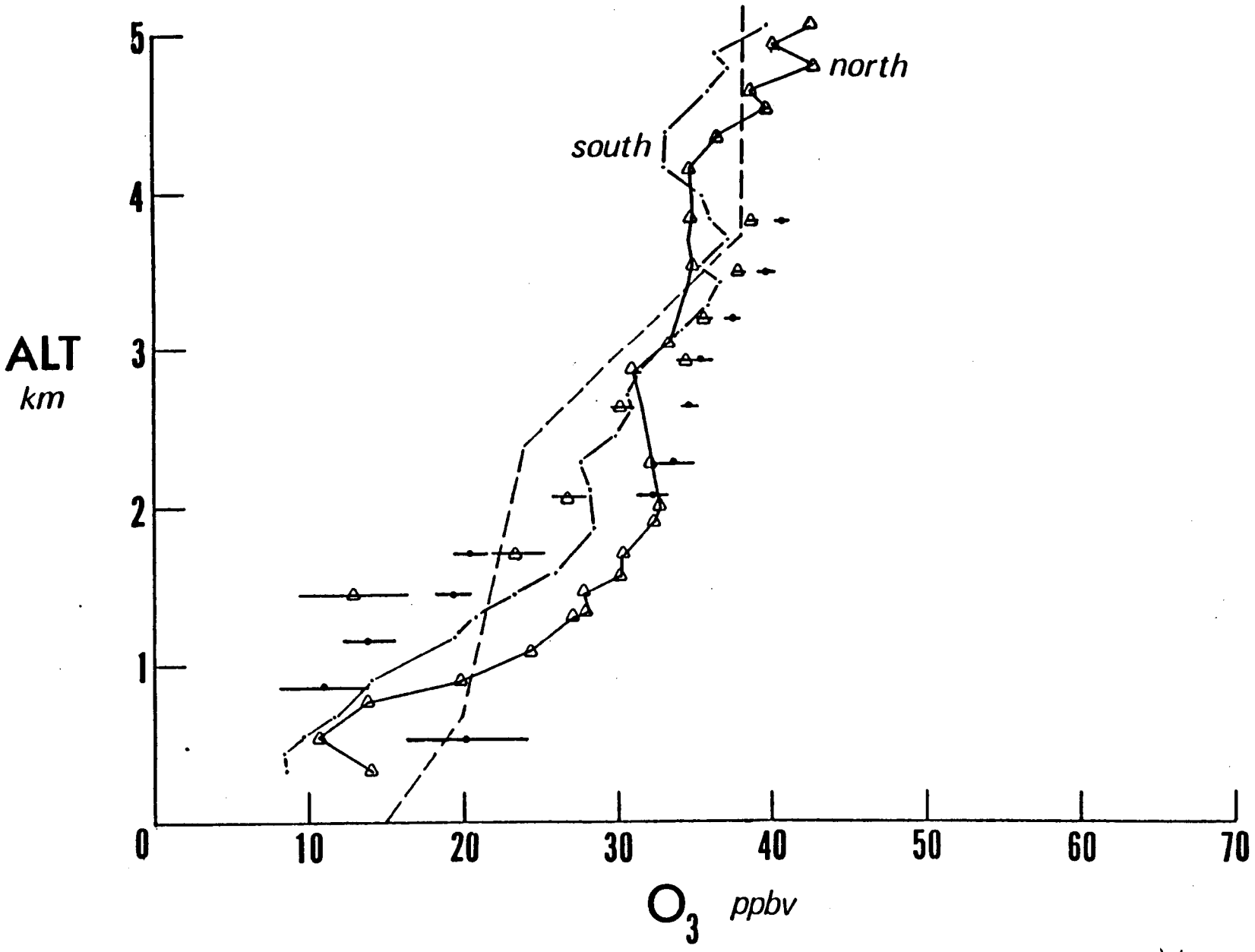

Fig 8a

MISSION 13

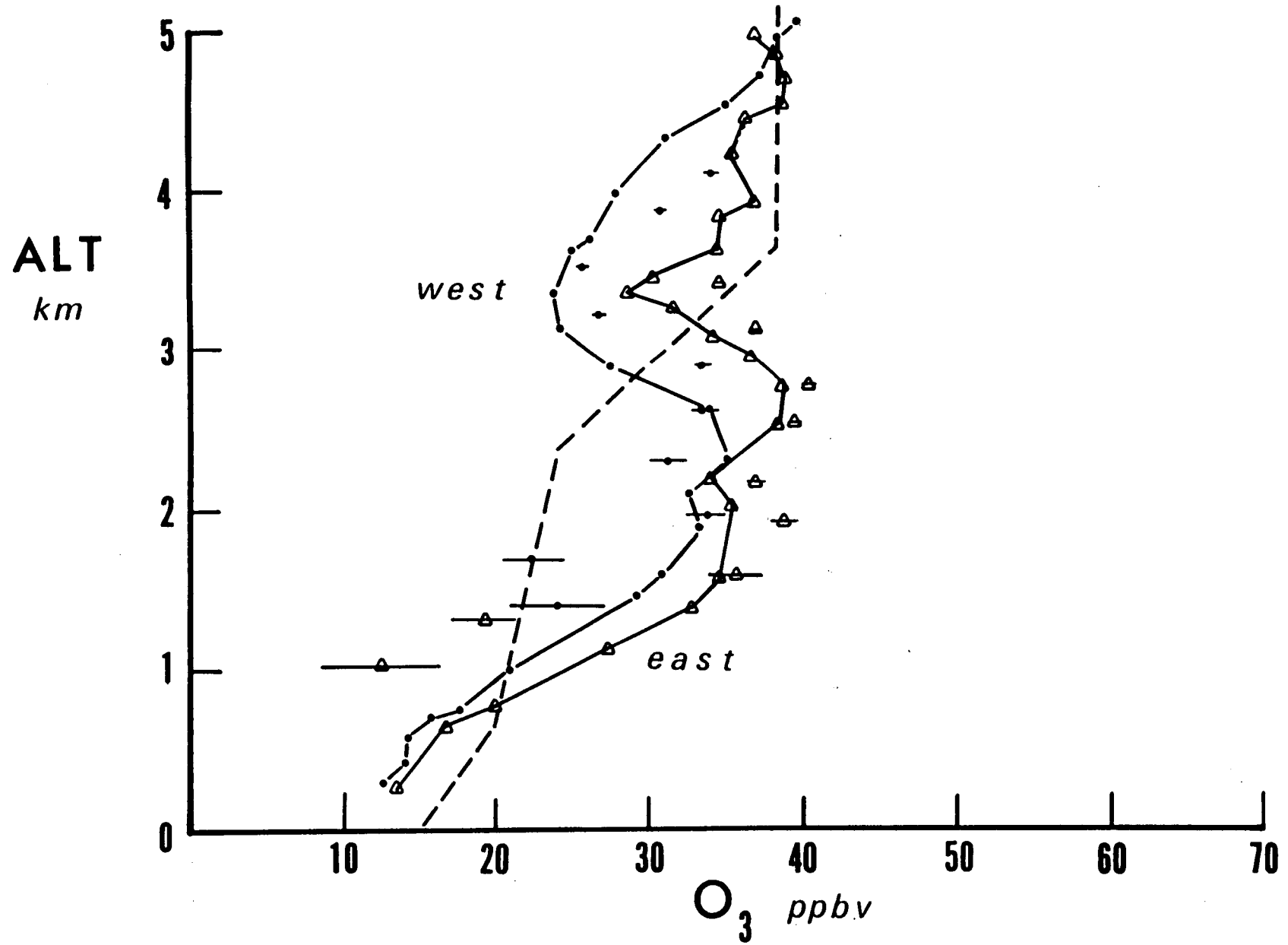

4/9 86

MISSION 12

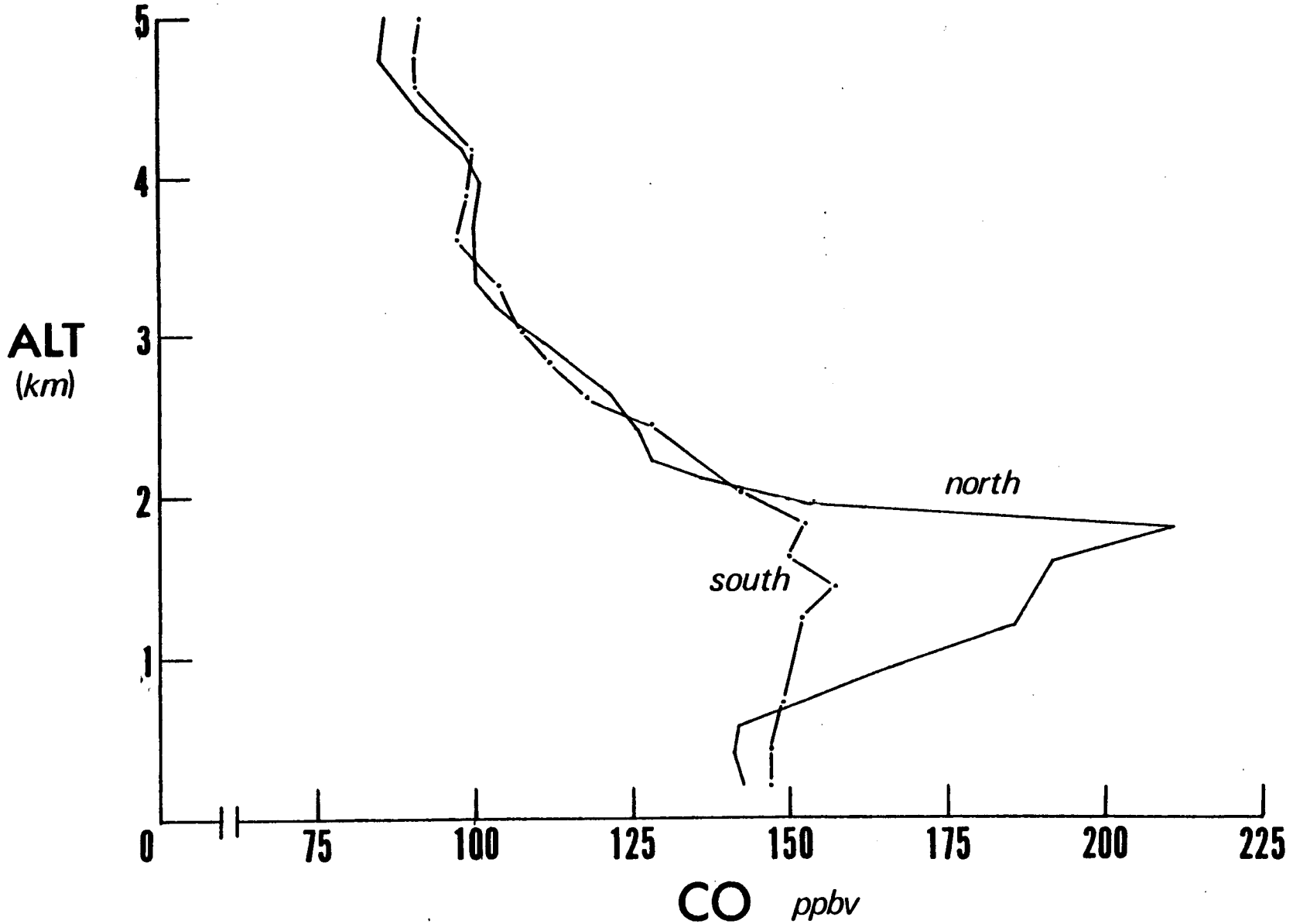

Fig 9a

MISSION 13

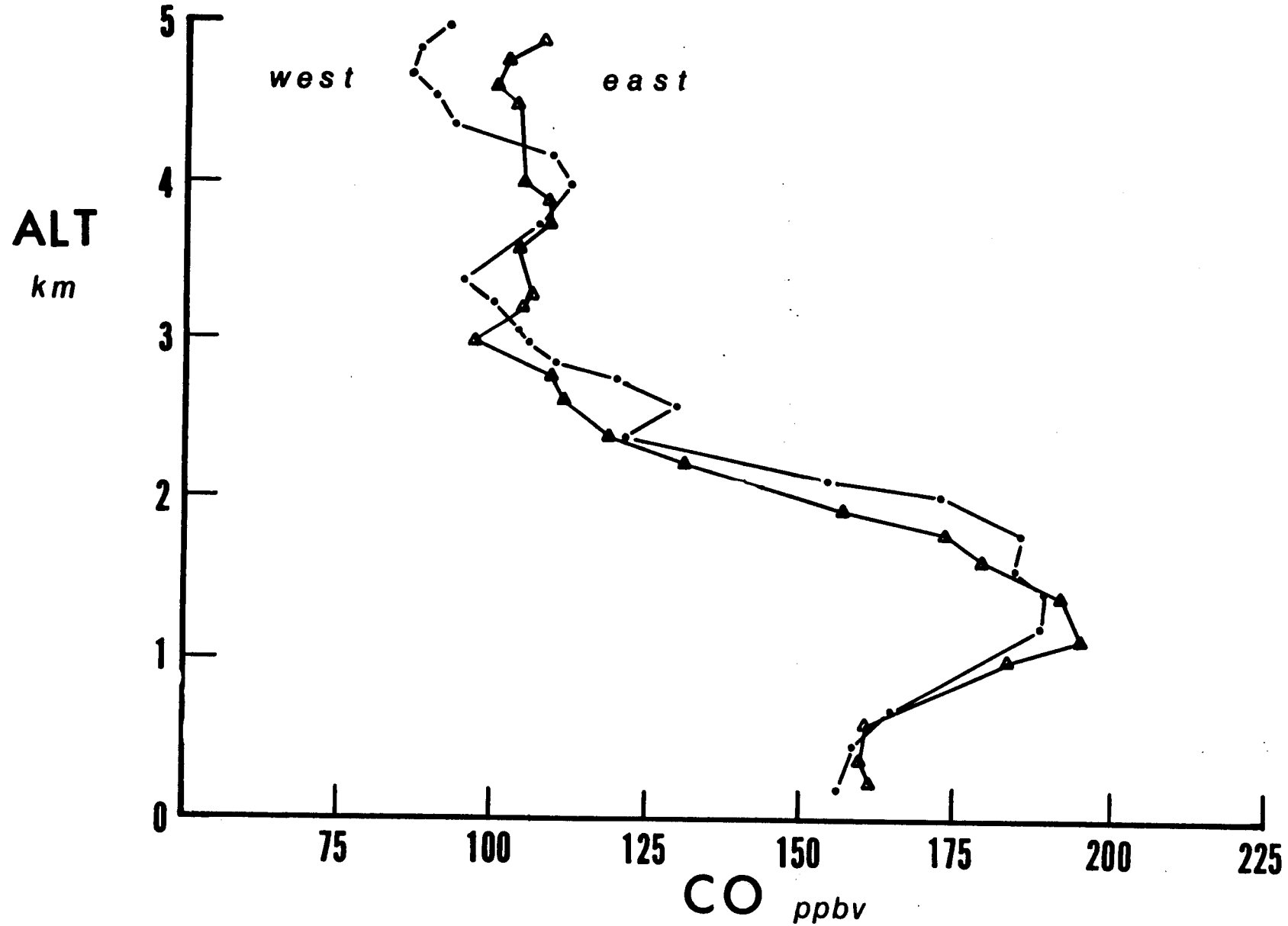

Fig 9b

MISSION 12

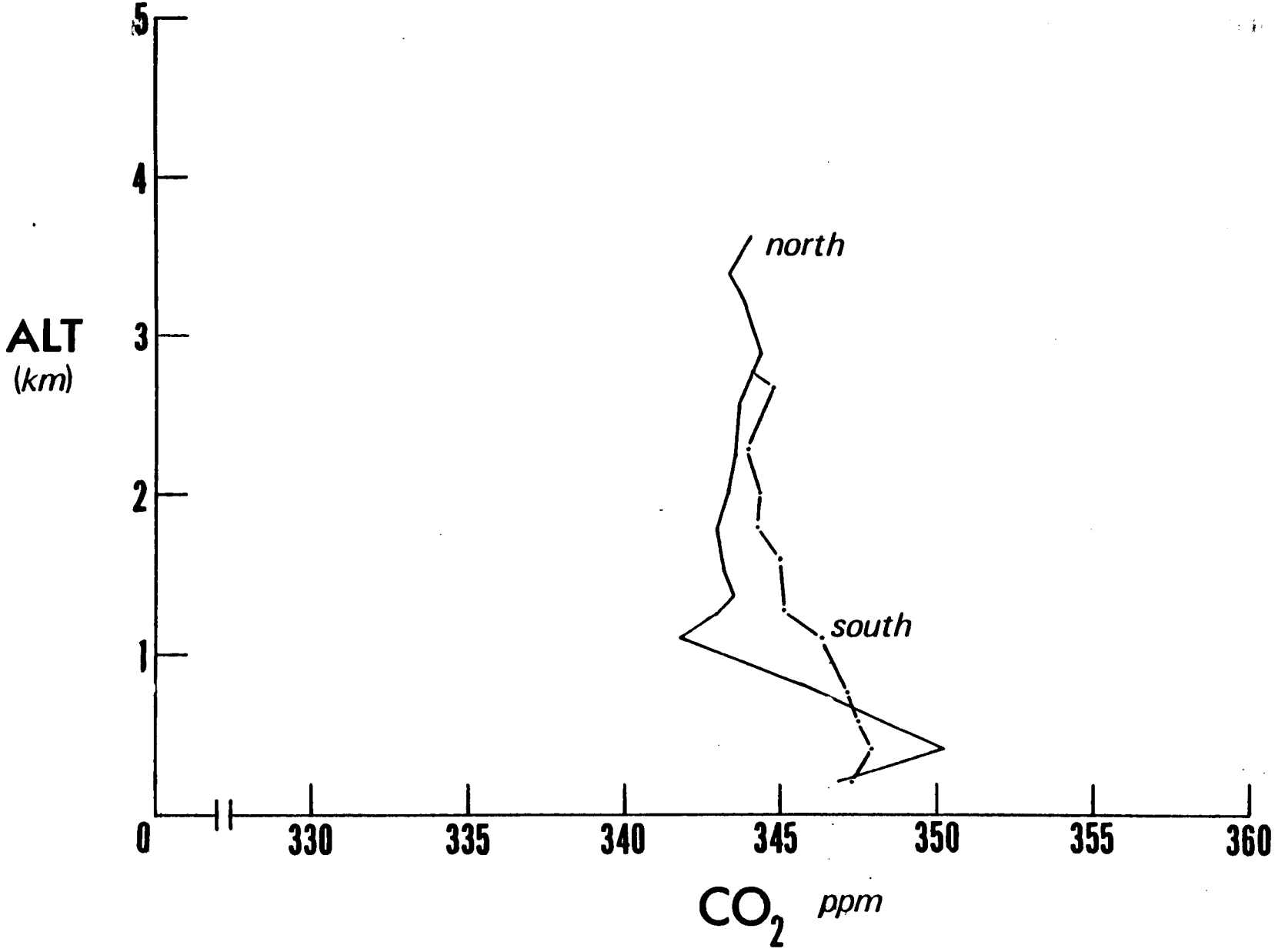

Fig 10a

MISSION 13

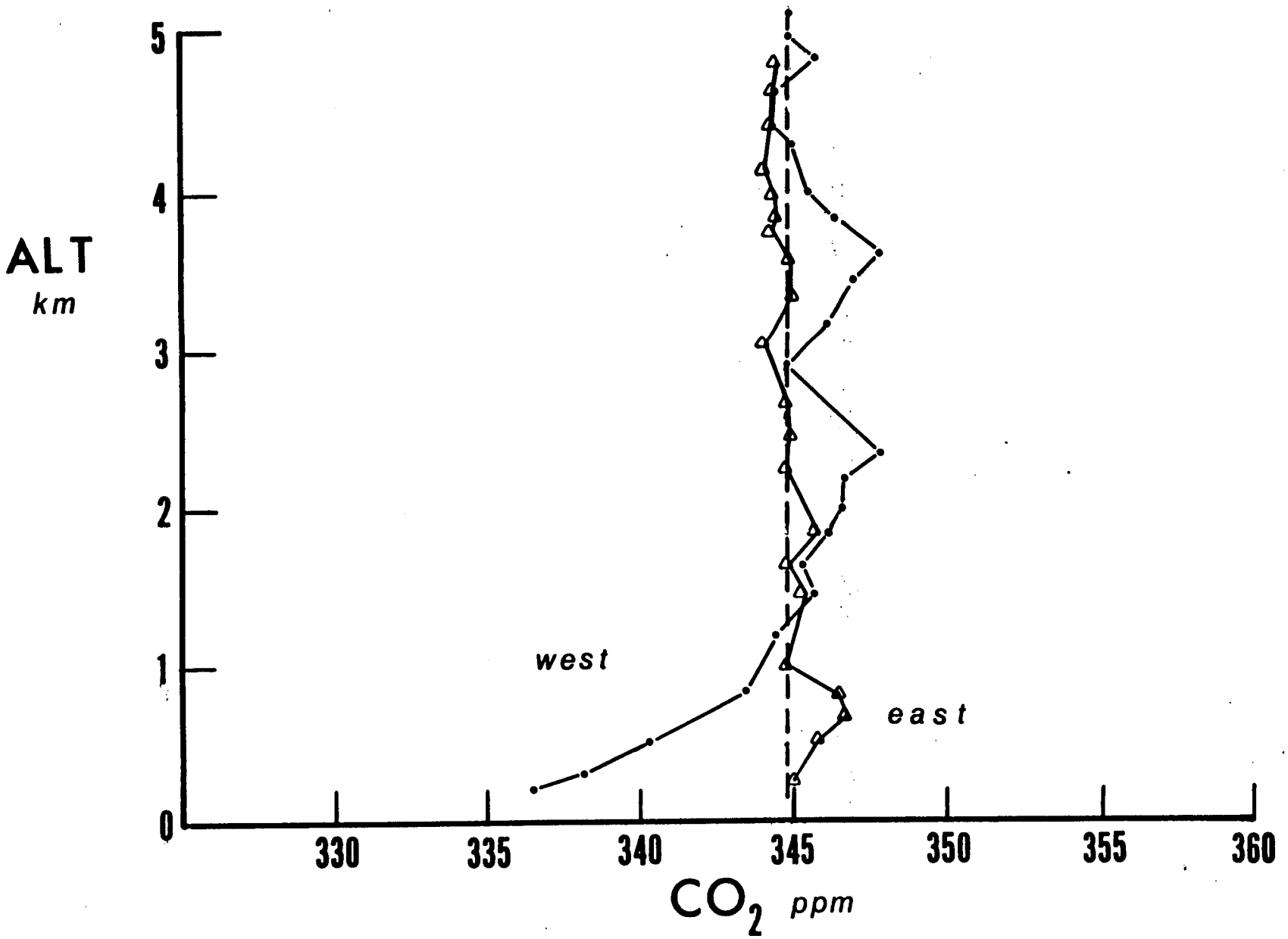

Fig 10b

MISSION 12

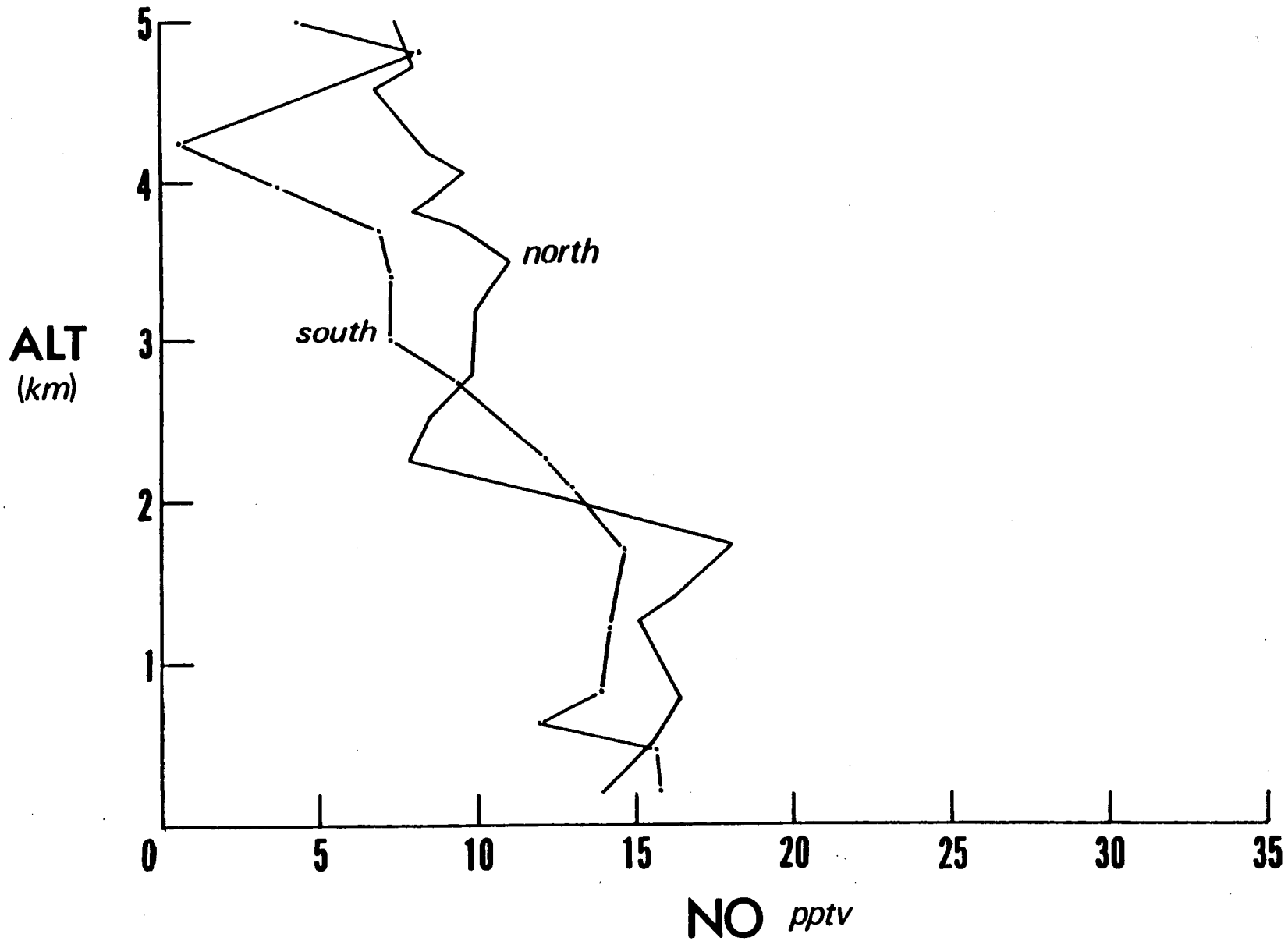

Fig 11a

MISSION 13

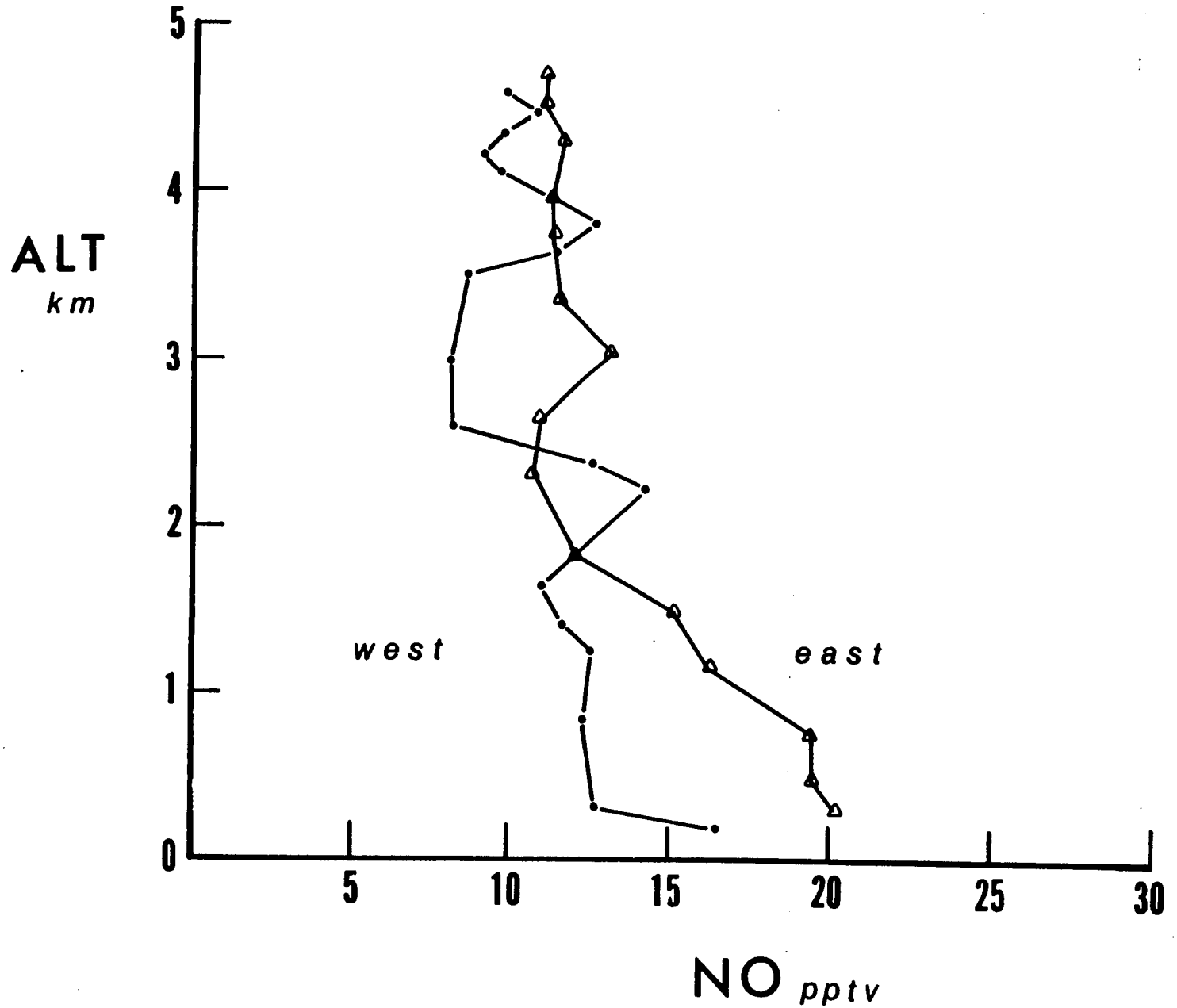

Fig 11b

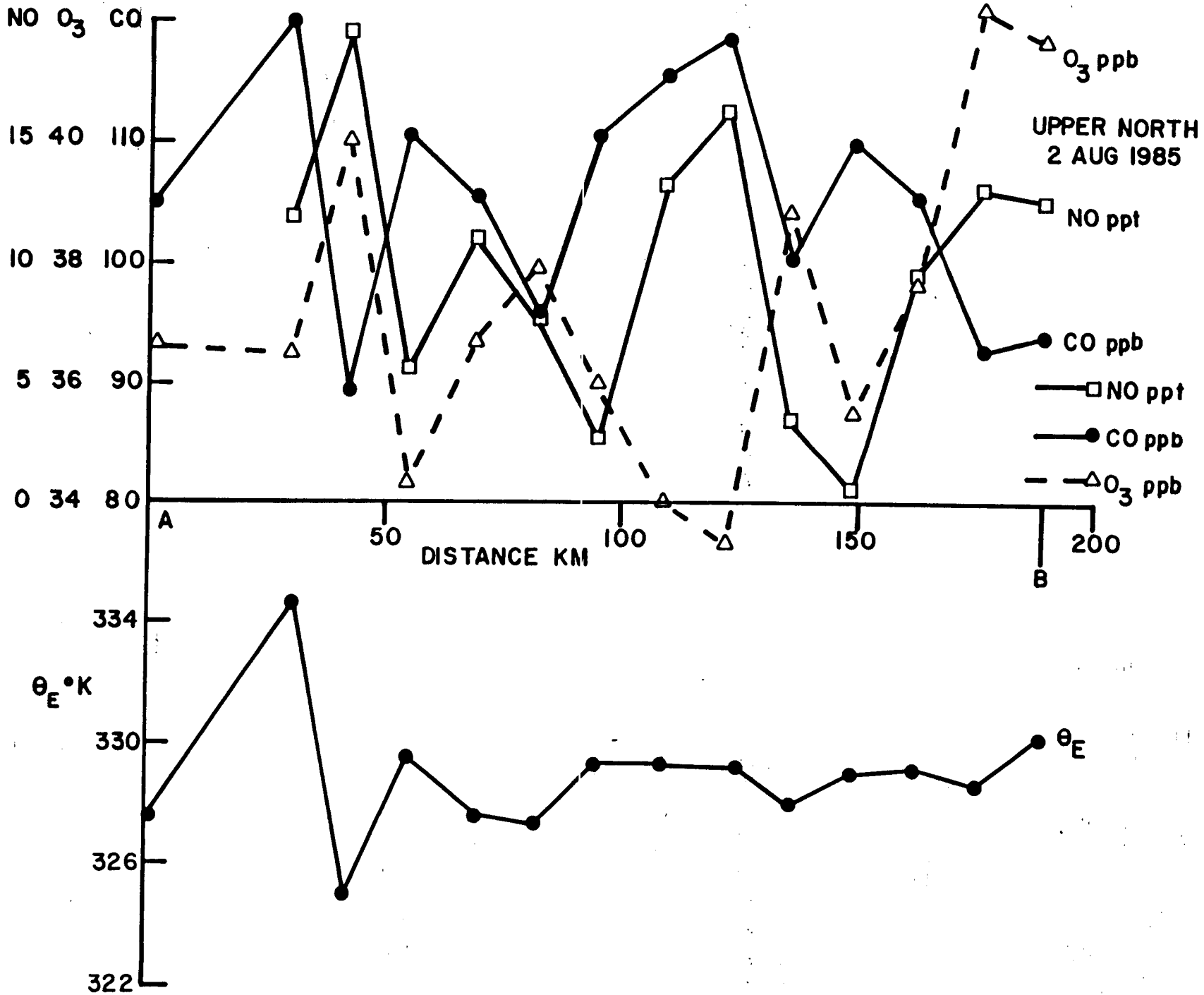
NO
O_3
CO
15
40
110
10
38
100
5
36
90
0
34
80
A
50
100
150
200
B
DISTANCE KM
O_3 ppb
UPPER NORTH
2 AUG 1985
NO ppt
CO ppb
NO ppt
CO ppb
O_3 ppb
θ_E °K
334
330
326
322
θ_E

Fig 12a

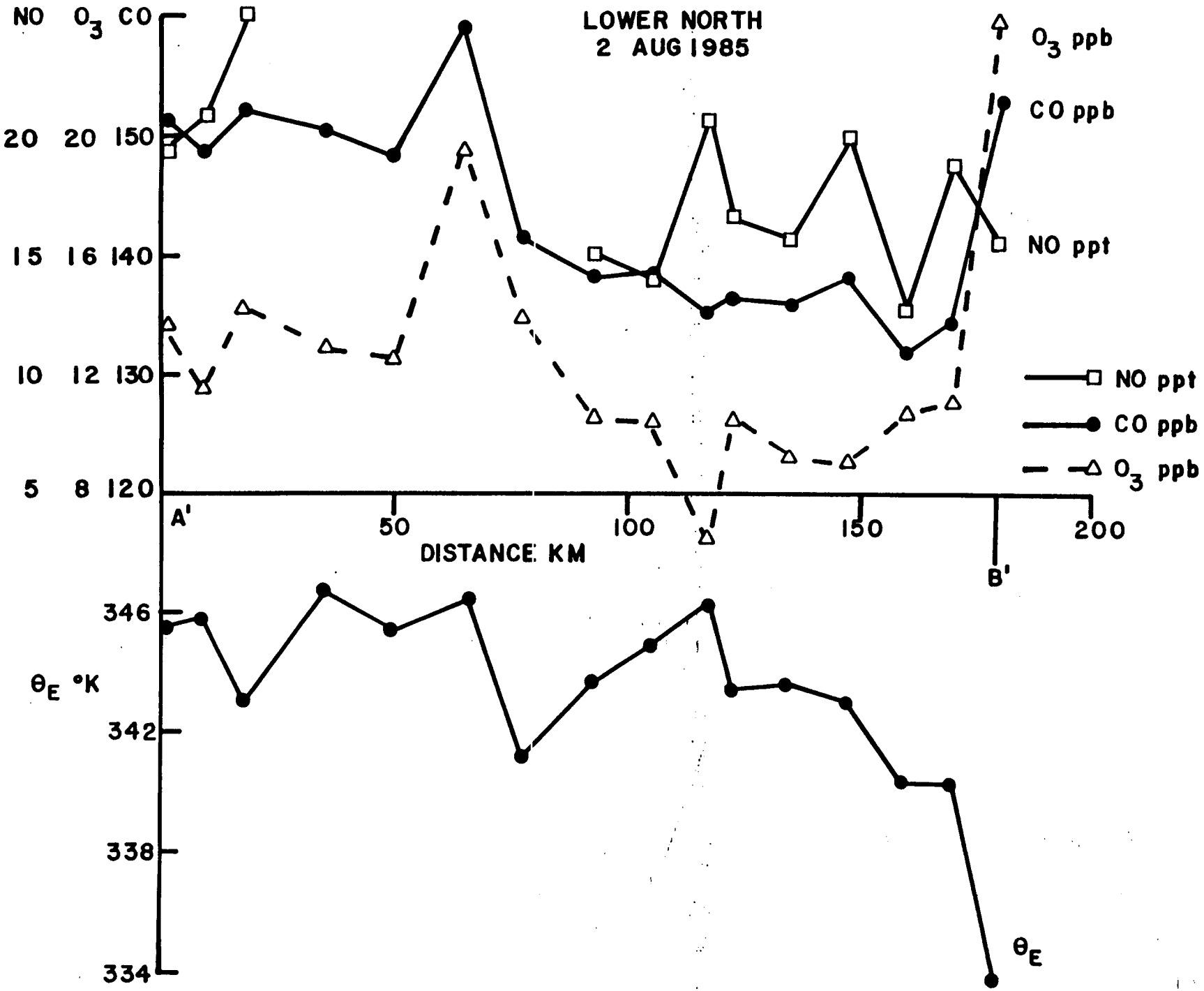
NO O3 CO
LOWER NORTH
2 AUG 1985
O3 ppb
CO ppb
NO ppt
20 20 150
15 16 140
10 12 130
5 8 120
NO ppt
CO ppb
O3 ppb
A'
50
100
150
200
B'
DISTANCE KM
346
θE °K
342
338
334
θE

Fig 12b

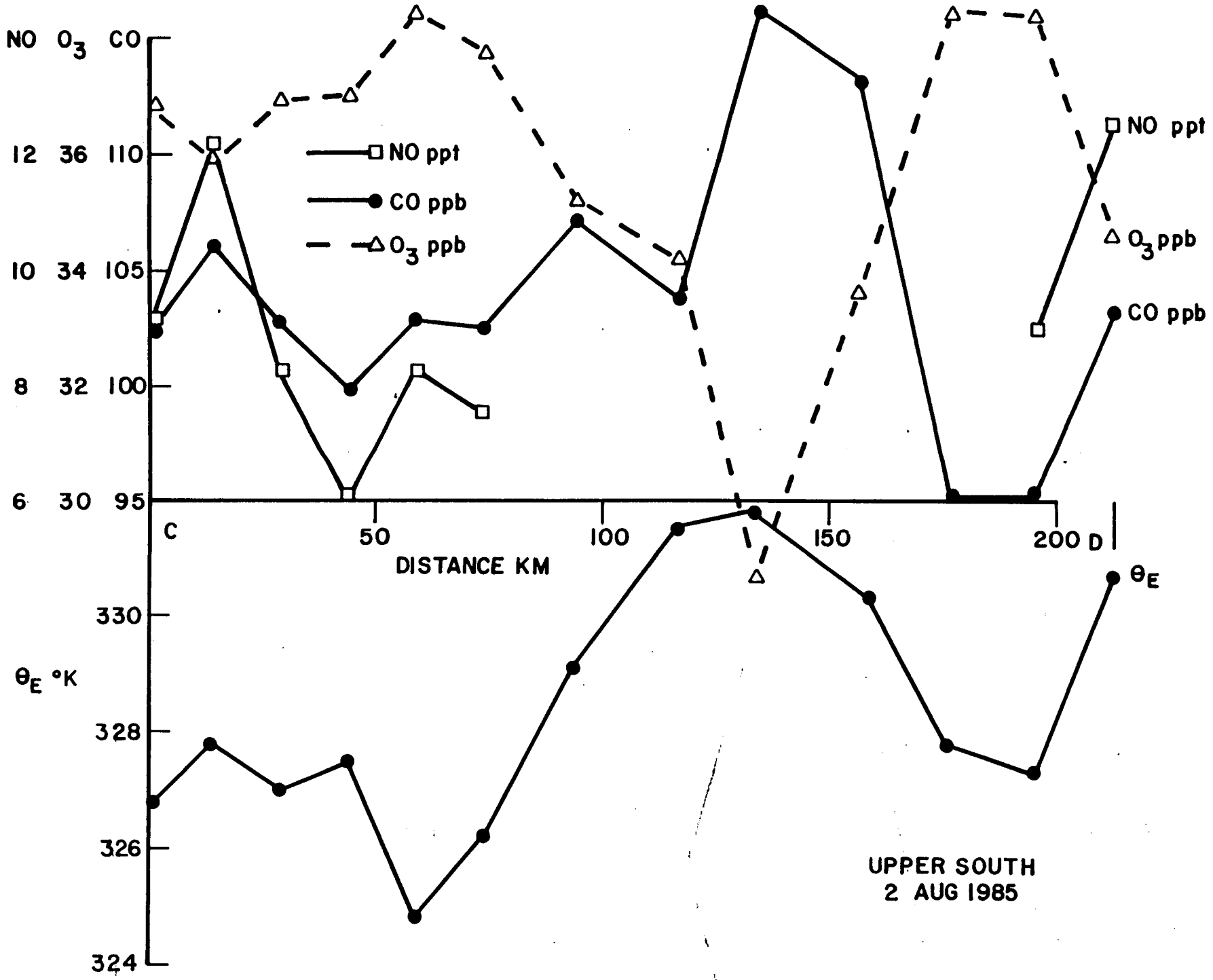
NO O_3 CO
12 36 110
10 34 105
8 32 100
6 30 95
NO ppt
CO ppb
O_3 ppb
C
50
100
150
200 D
DISTANCE KM
θ_E
θ_E °K
330
328
326
324
UPPER SOUTH
2 AUG 1985

Fig 12c

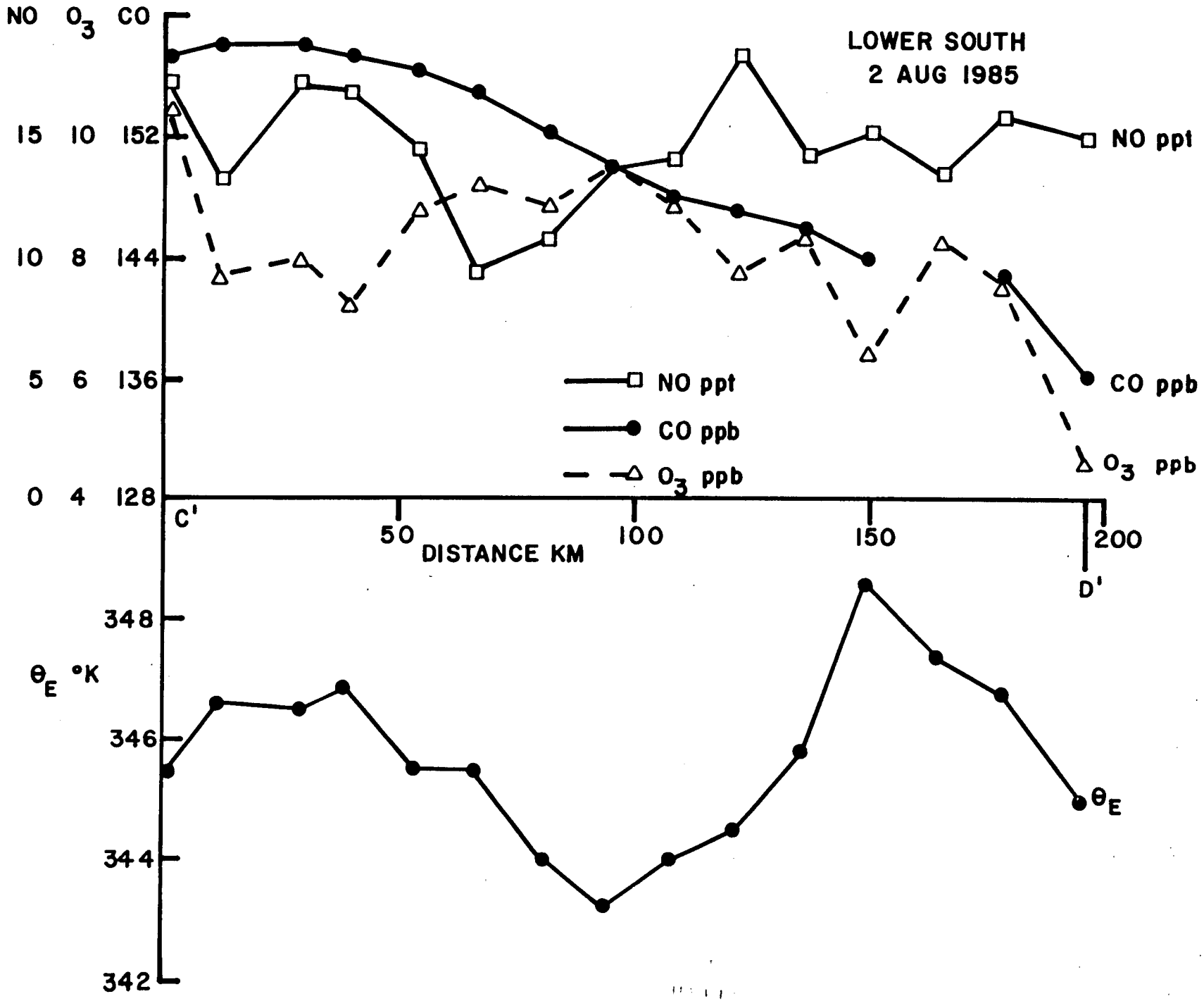
NO
O3
CO
LOWER SOUTH
2 AUG 1985
15
10
152
10
8
144
5
6
136
0
4
128
NO ppt
CO ppb
O3 ppb
C'
50
100
150
200
D'
DISTANCE KM
θE °K
348
346
344
342
θE

Fig 12d

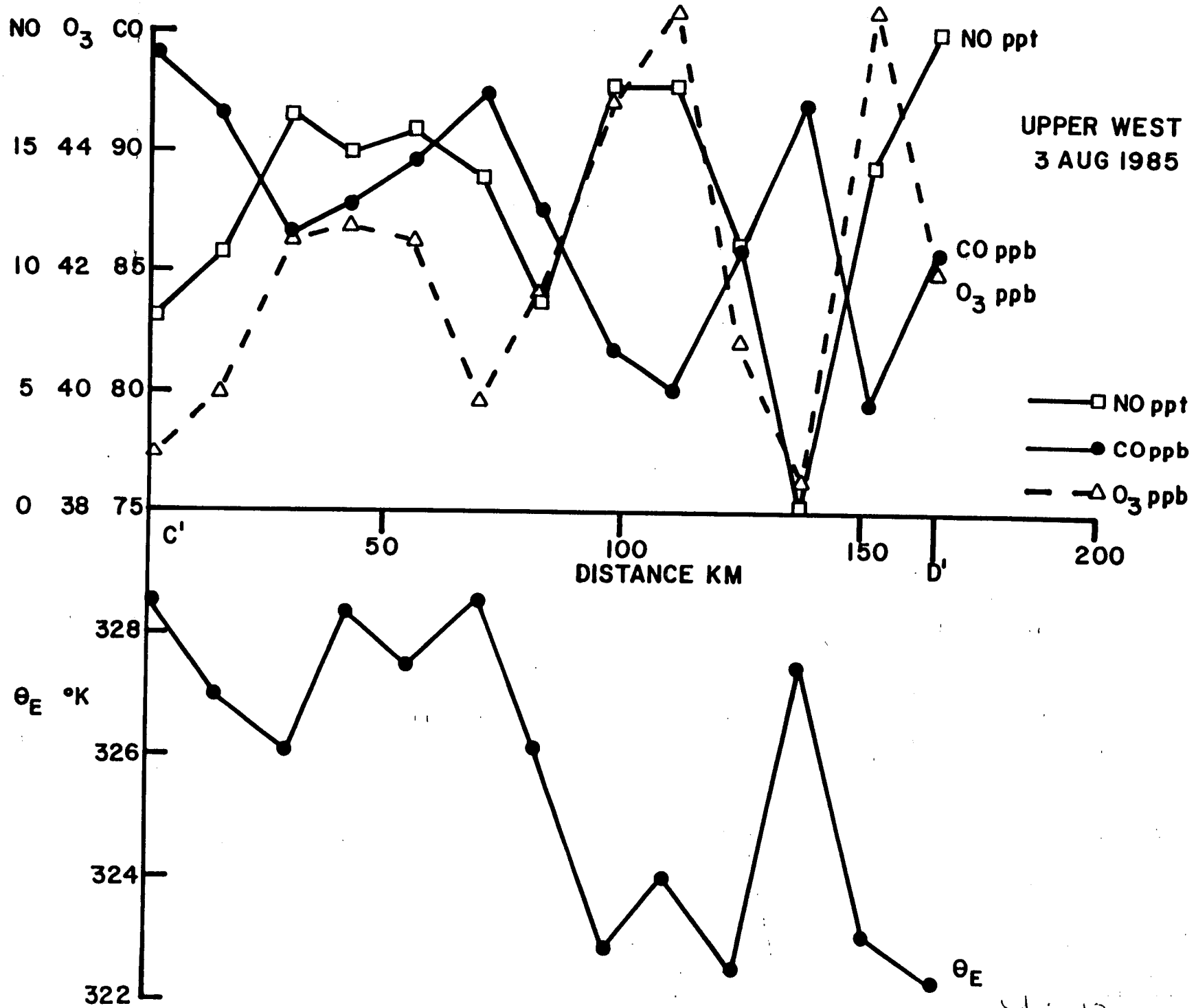
NO O_3 CO
15 44 90
10 42 85
5 40 80
0 38 75
NO ppt
CO ppb
O_3 ppb
UPPER WEST
3 AUG 1985
NO ppt
CO ppb
O_3 ppb
C'
50
100
150
D'
200
DISTANCE KM
328
θ_E °K
326
324
322
θ_E

Fig 13a

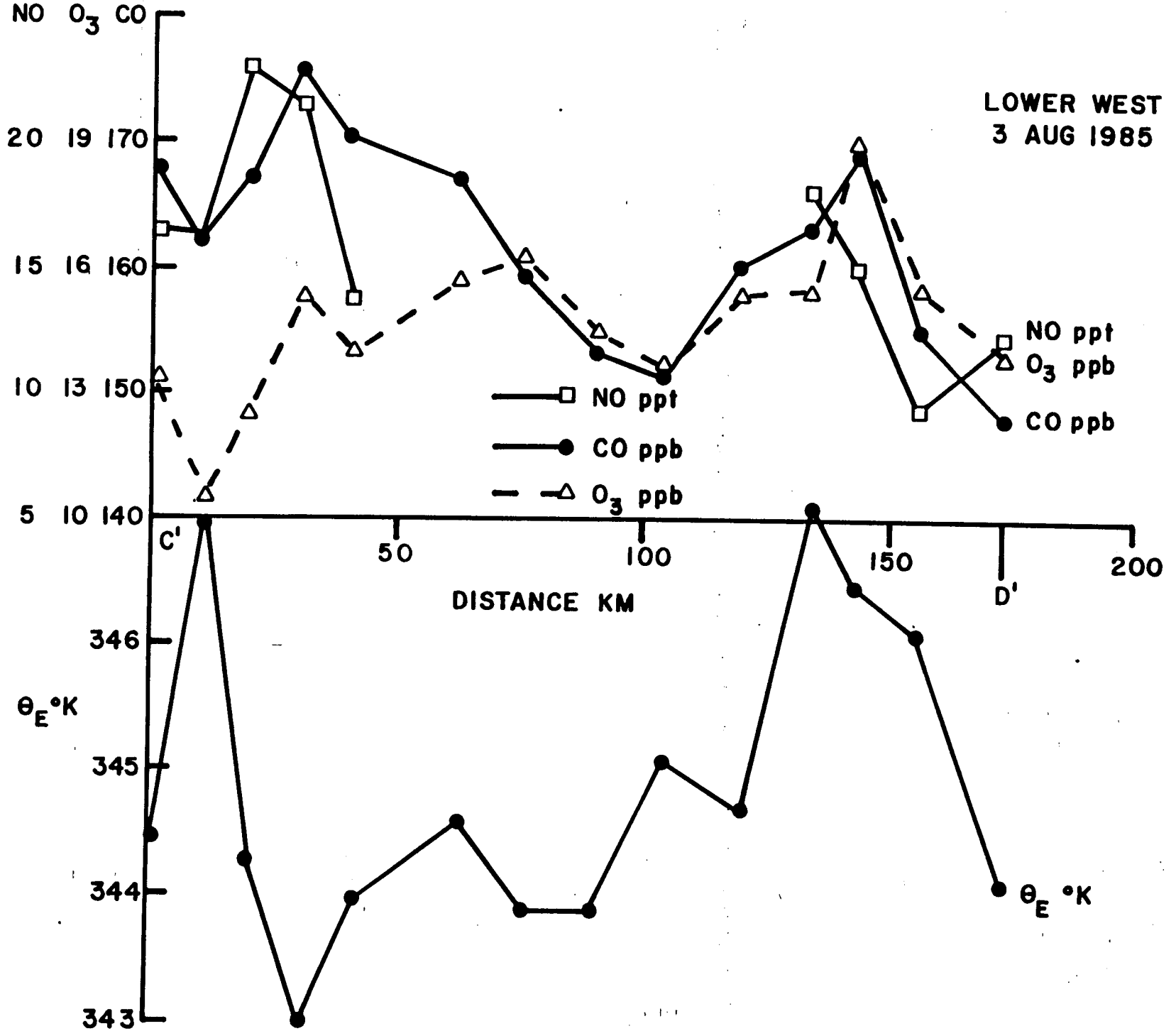
NO O_3 CO
20 19 170
15 16 160
10 13 150
5 10 140
LOWER WEST
3 AUG 1985
NO ppt
O_3 ppb
CO ppb
C'
50
100
150
200
D'
DISTANCE KM
346
345
344
343
θ_E °K

Fig 136

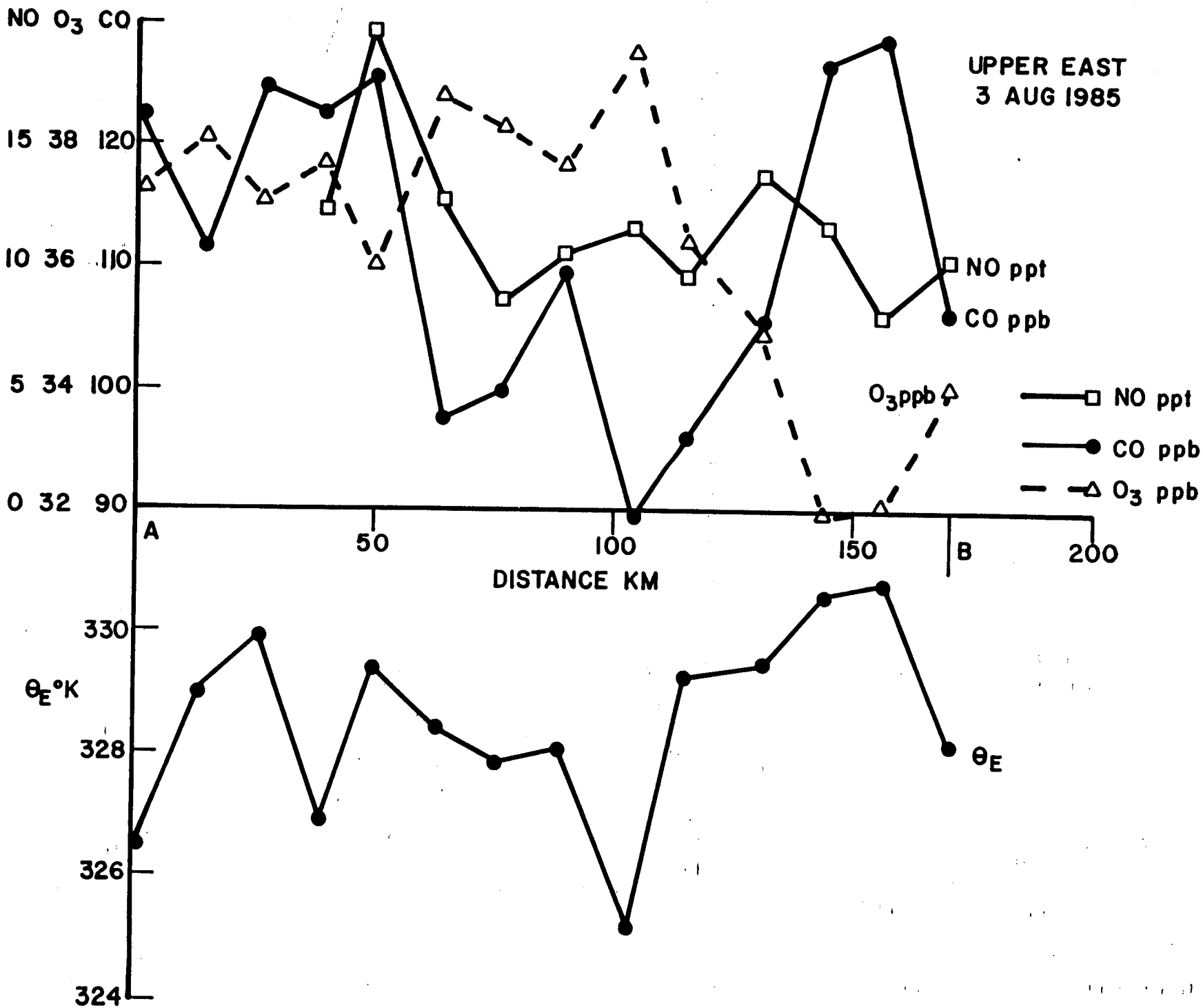
NO O3 CO
15 38 120
10 36 110
5 34 100
0 32 90
UPPER EAST
3 AUG 1985
NO ppt
CO ppb
O3ppb
NO ppt
CO ppb
O3 ppb
A
50
100
150
B
200
DISTANCE KM
330
328
326
324
θE°K
θE

Fig 13c

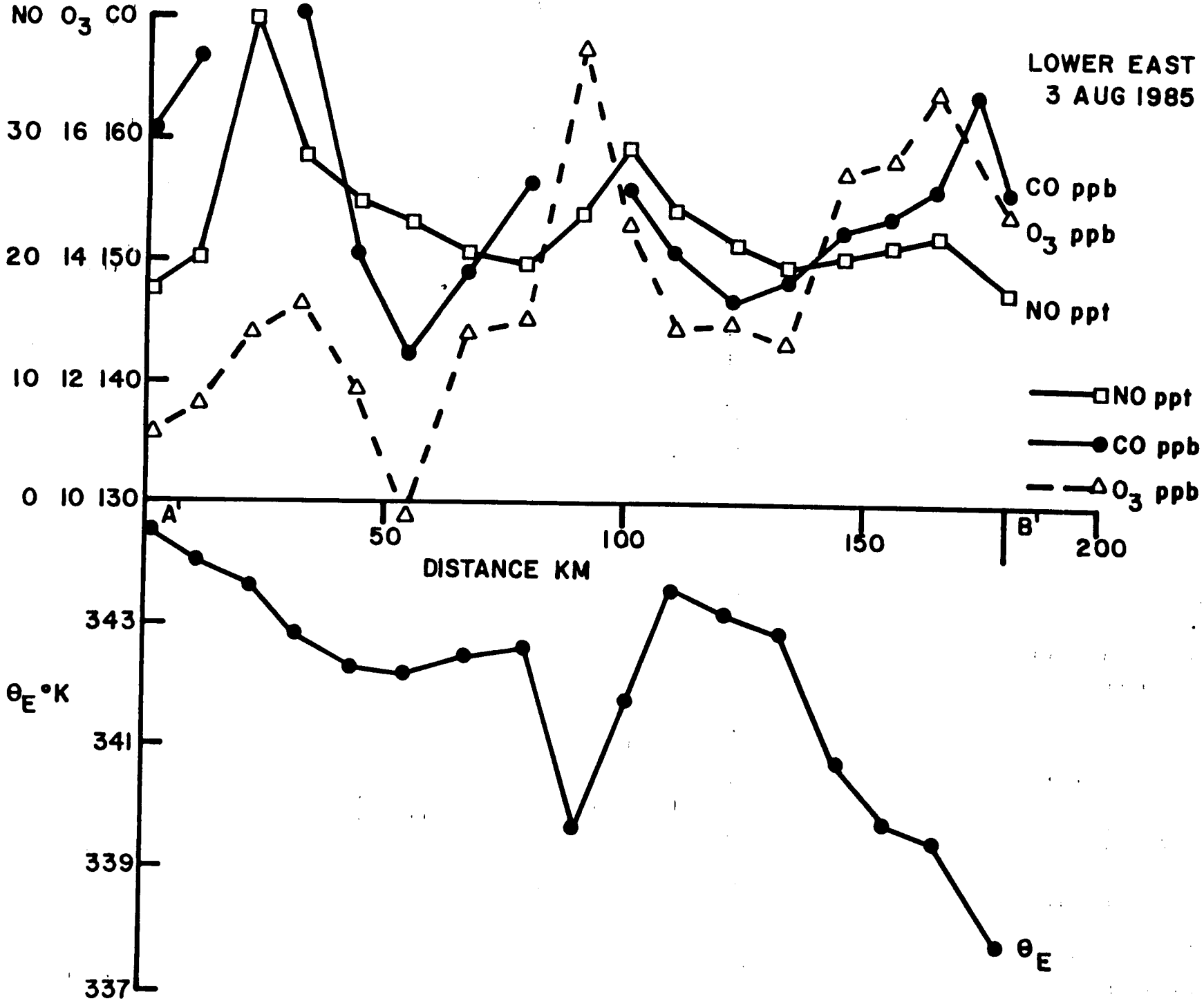
NO O_3 CO
30 16 160
20 14 150
10 12 140
0 10 130
LOWER EAST
3 AUG 1985
CO ppb
O_3 ppb
NO ppt
NO ppt
CO ppb
O_3 ppb
A'
50
100
150
B'
200
DISTANCE KM
343
θ_E °K
341
339
337
θ_E

Fig 13d

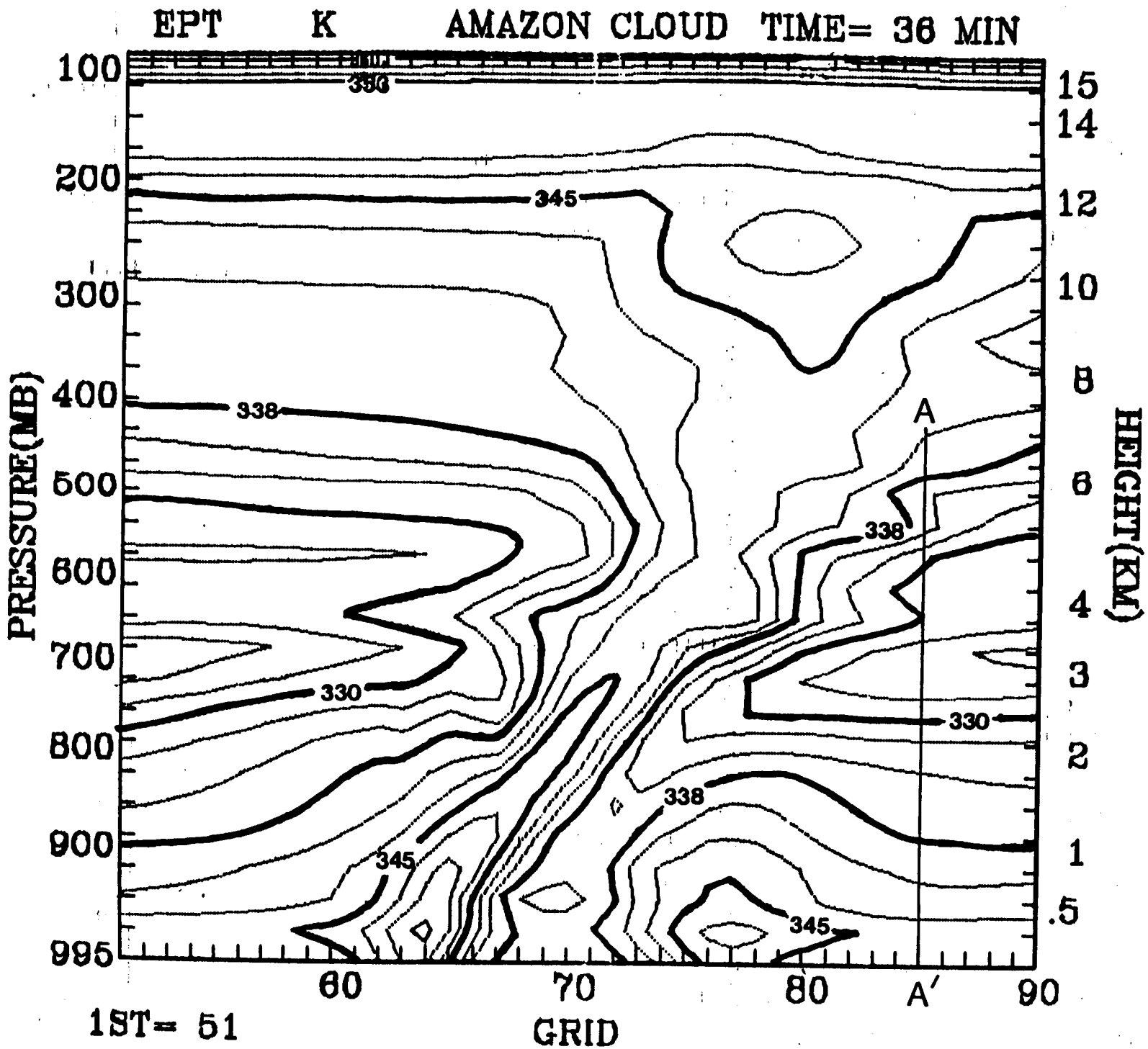
EPT K AMAZON CLOUD TIME= 36 MIN
PRESSURE(MB)
HEIGHT(KM)
100
200
300
400
500
600
700
800
900
995
15
14
12
10
8
6
4
3
2
1
.5
350
345
338
330
A
A'
60
70
80
90
1ST= 51
GRID

Fig 14

MISSION 13

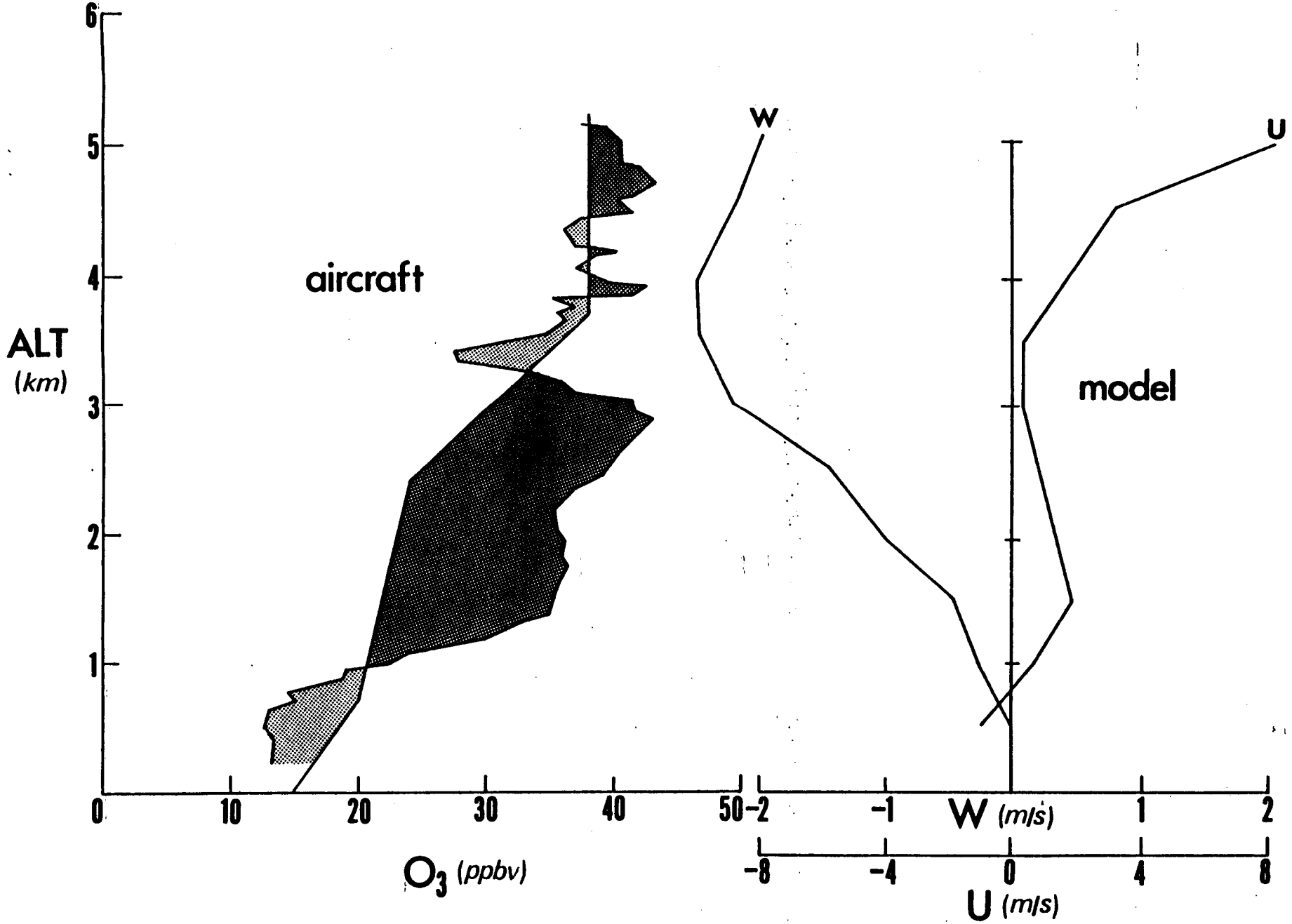

Fig. 15

MISSION 13

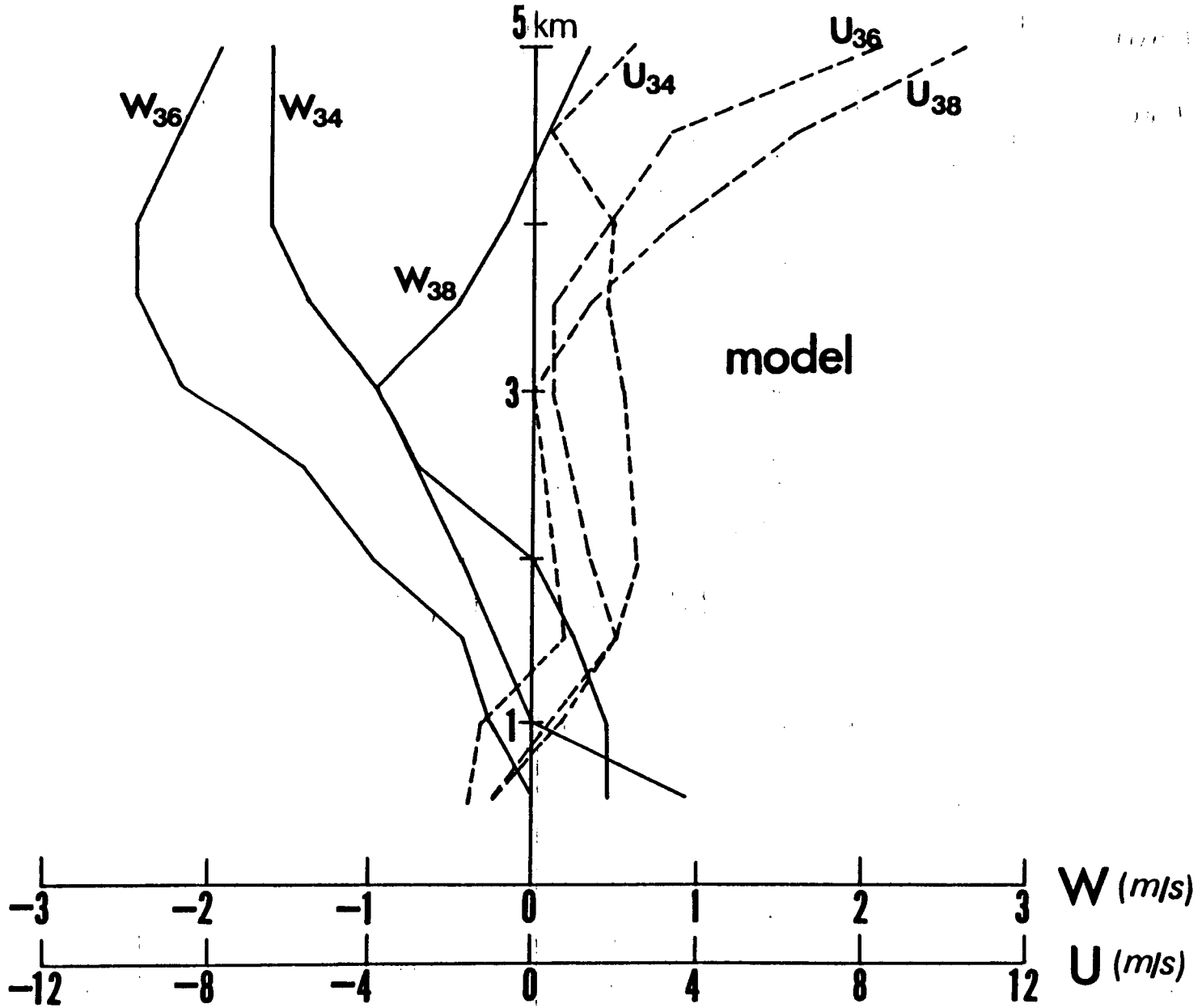

Fig 16

MISSION 13

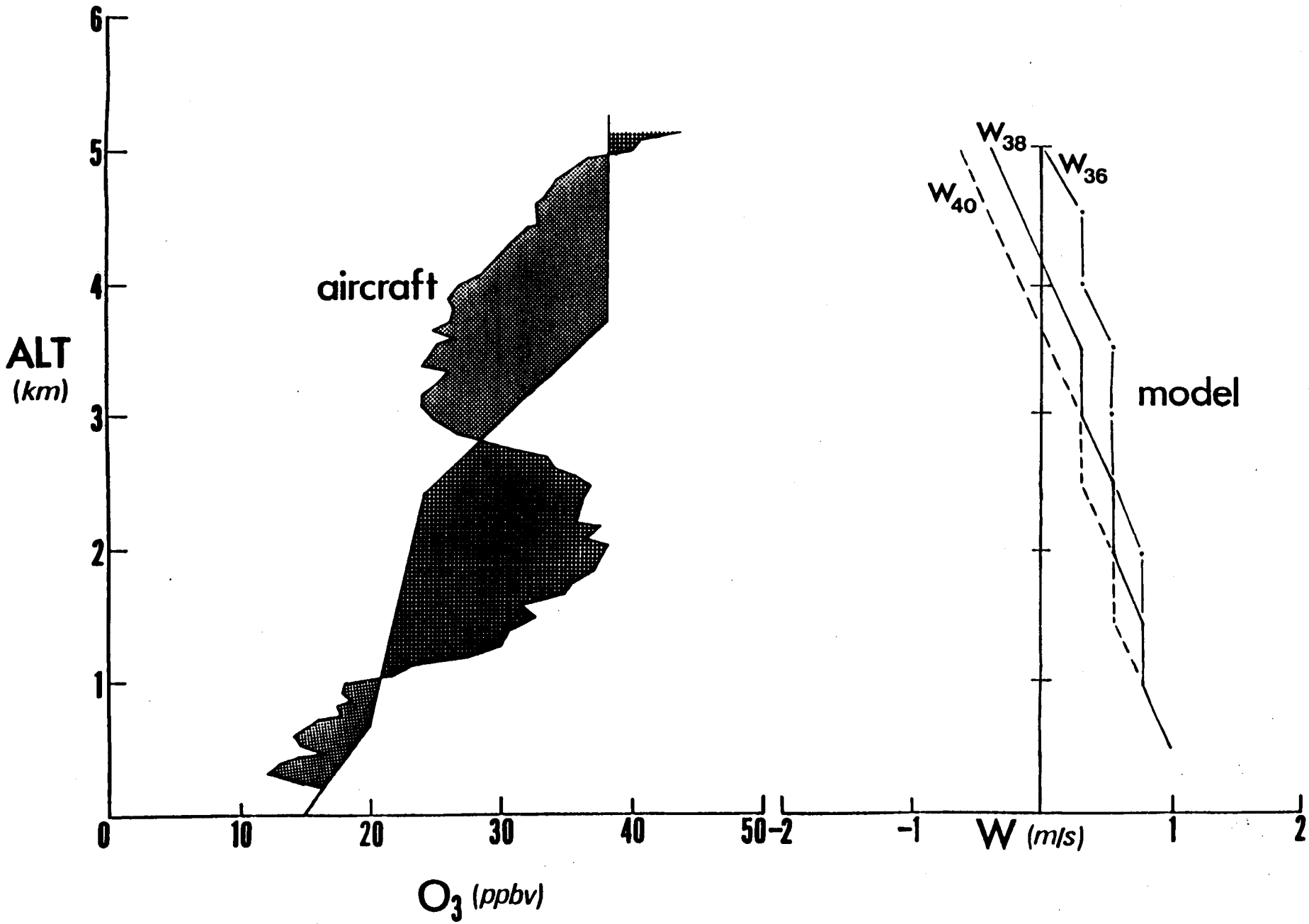
ALT
(km)
6
5
4
3
2
1
0
10
20
30
40
50
O3 (ppbv)
aircraft
W38
W36
W40
model
-2
-1
W (m/s)
1
2

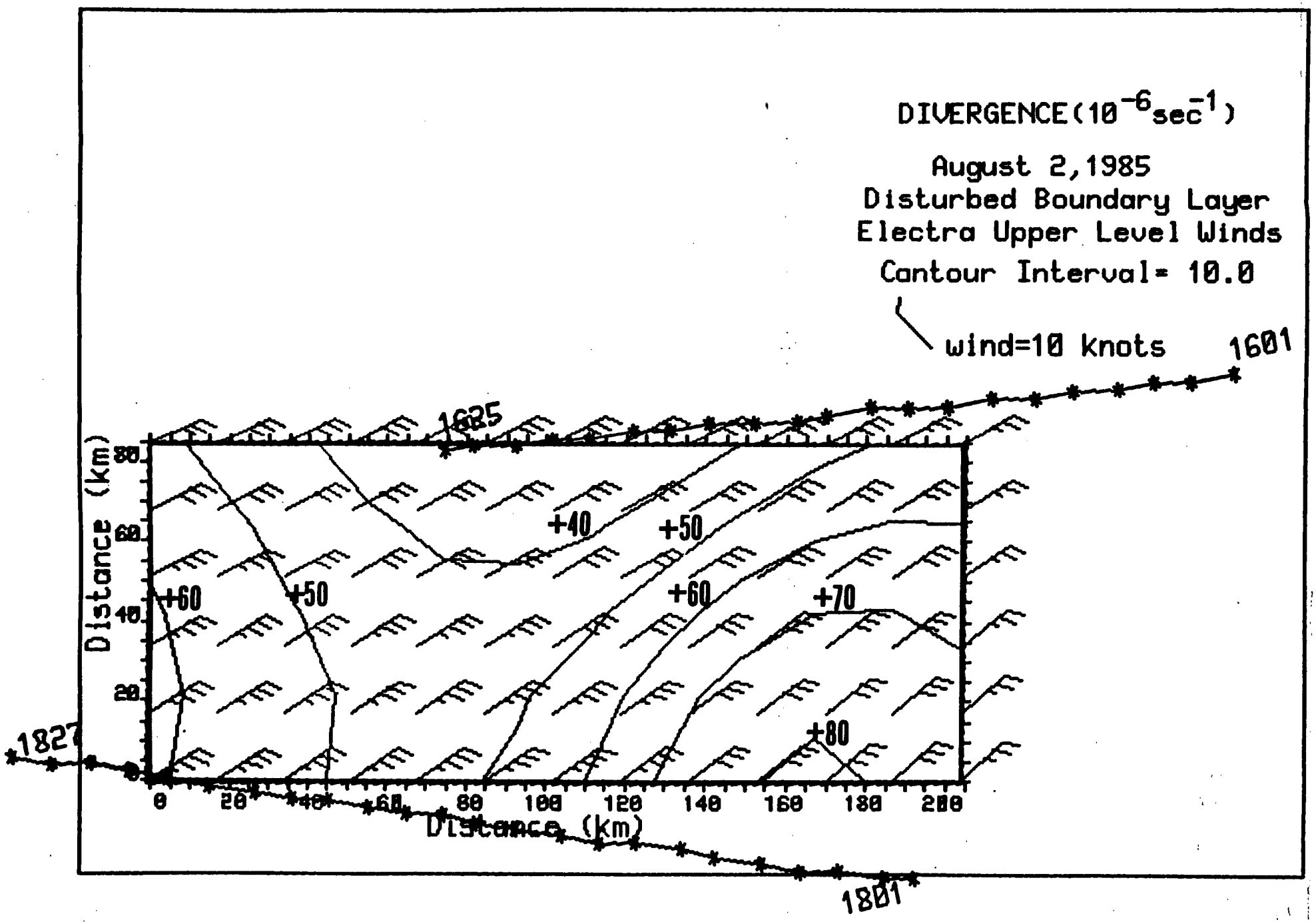
DIVERGENCE(10^{-6} sec^{-1})
August 2,1985
Disturbed Boundary Layer
Electra Upper Level Winds
Contour Interval= 10.0
wind=10 knots
1601
1625
1827
1801
Distance (km)
Distance (km)
0
20
40
60
80
100
120
140
160
180
200
+40
+50
+60
+50
+60
+70
+80

Fig 18a

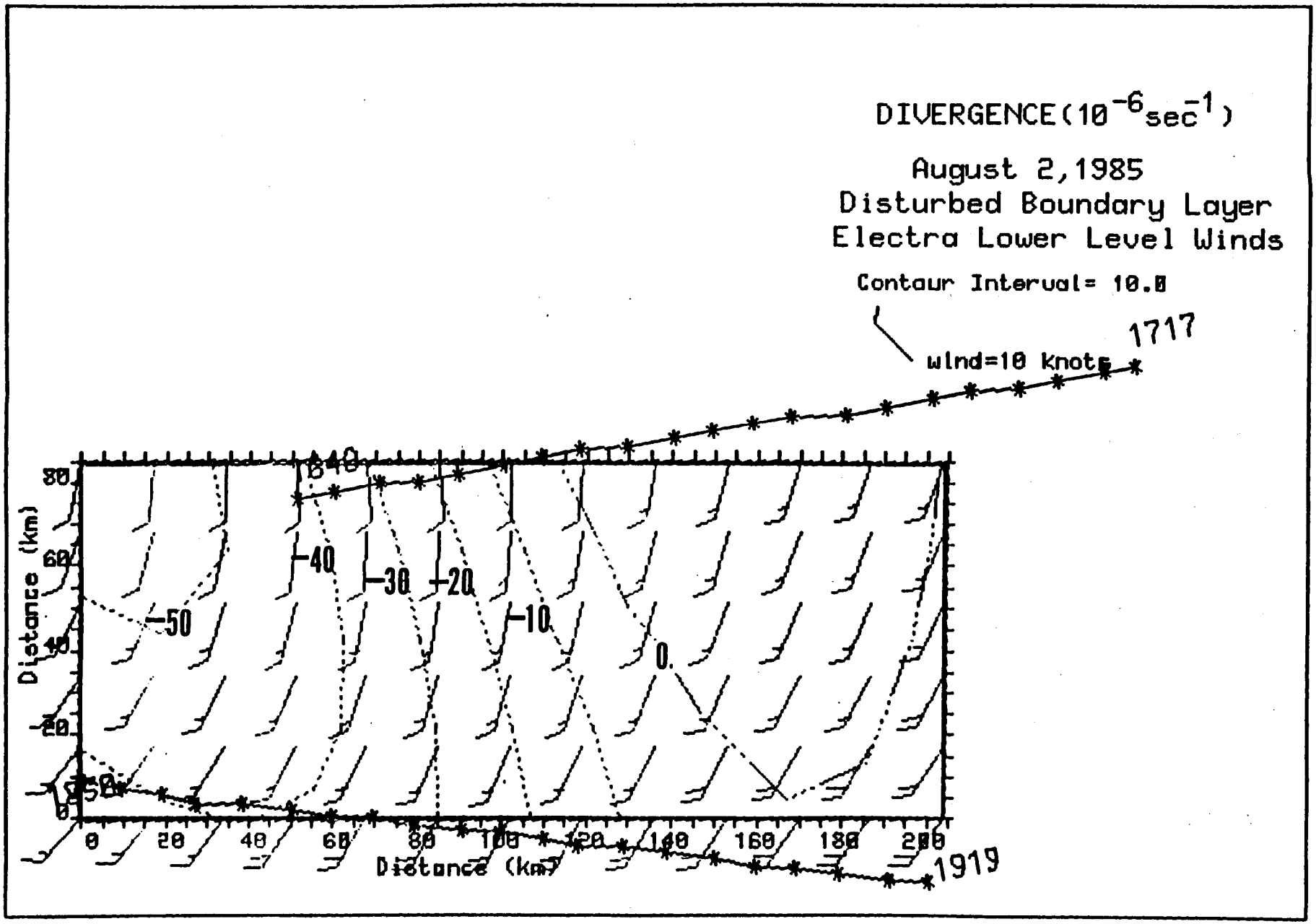
DIVERGENCE(10^{-6} sec^{-1})
August 2,1985
Disturbed Boundary Layer
Electra Lower Level Winds
Contour Interval= 10.0
1717
wind=10 knots
-40
-30
-20
-50
-10
0
Distance (km)
Distance (km)
1919

Fig 18b

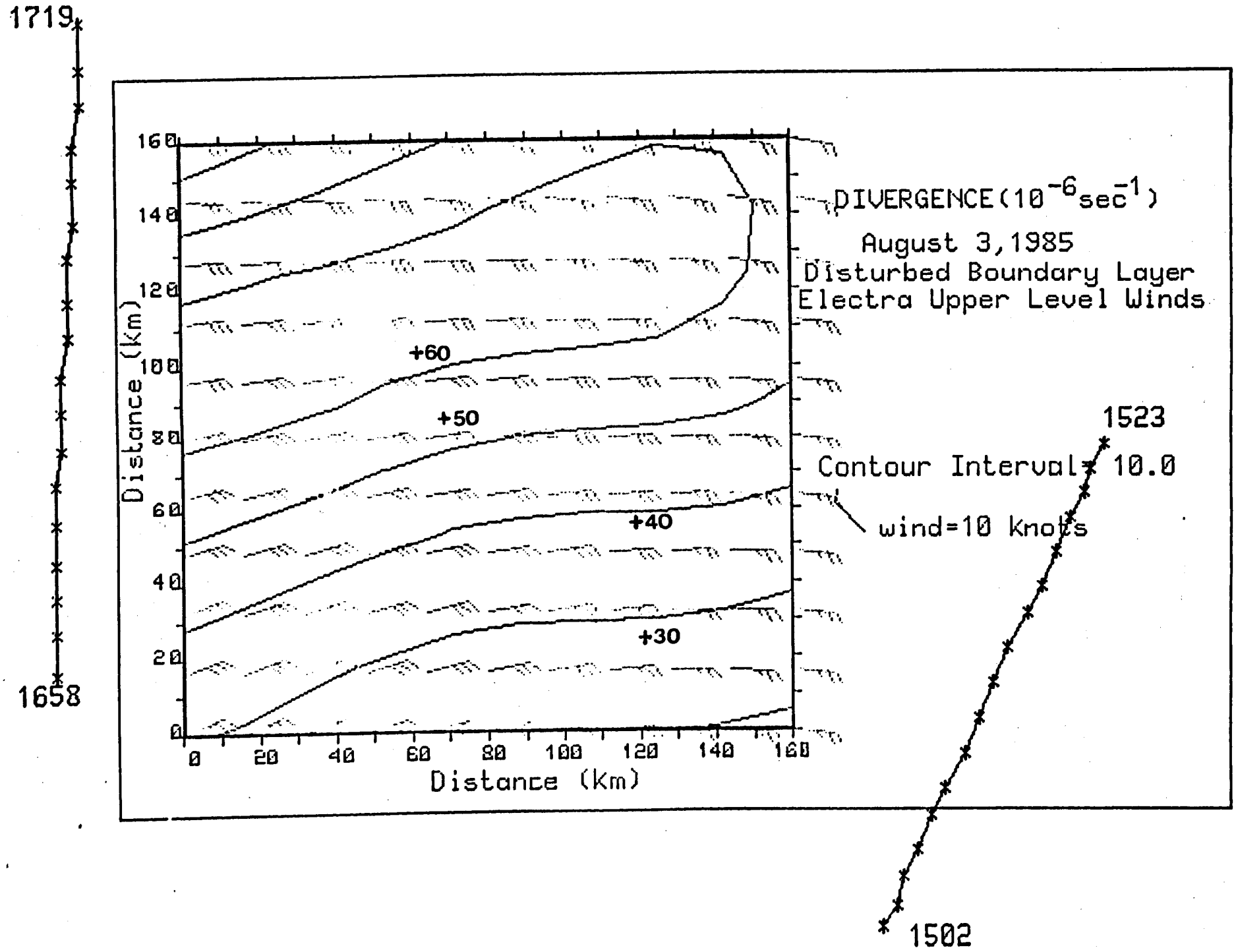
1719
1658
DIVERGENCE(10^{-6} sec^{-1})
August 3, 1985
Disturbed Boundary Layer
Electra Upper Level Winds
+60
+50
+40
+30
Contour Interval= 10.0
wind=10 knots
1523
1502
Distance (km)
Distance (km)
0
20
40
60
80
100
120
140
160

Fig 19a

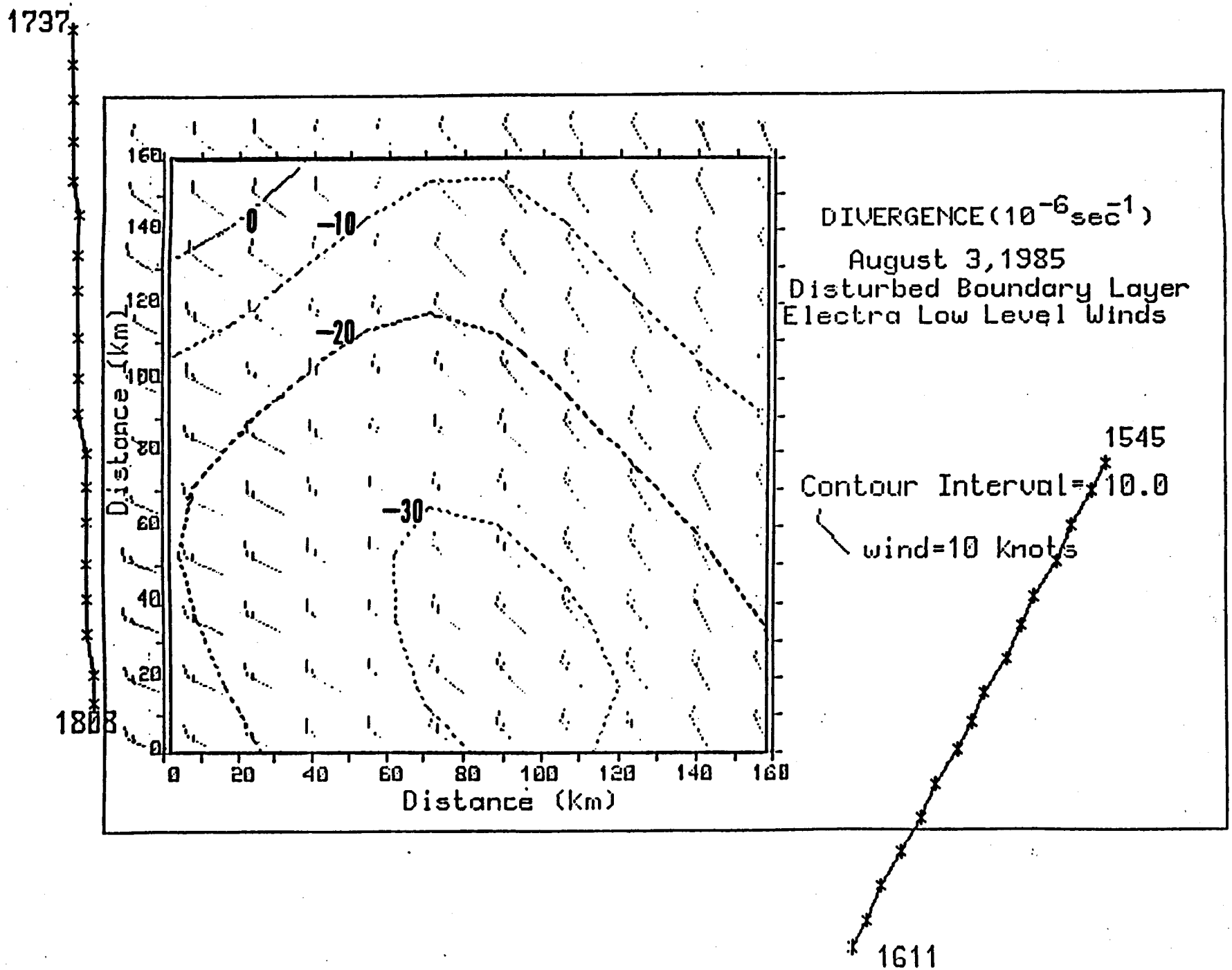
1737
1808
0
-10
-20
-30
Distance (km)
Distance (km)
0
20
40
60
80
100
120
140
160
DIVERGENCE (10^{-6} sec^{-1})
August 3, 1985
Disturbed Boundary Layer
Electra Low Level Winds
1545
Contour Interval= 10.0
wind=10 knots
1611

Fig 196

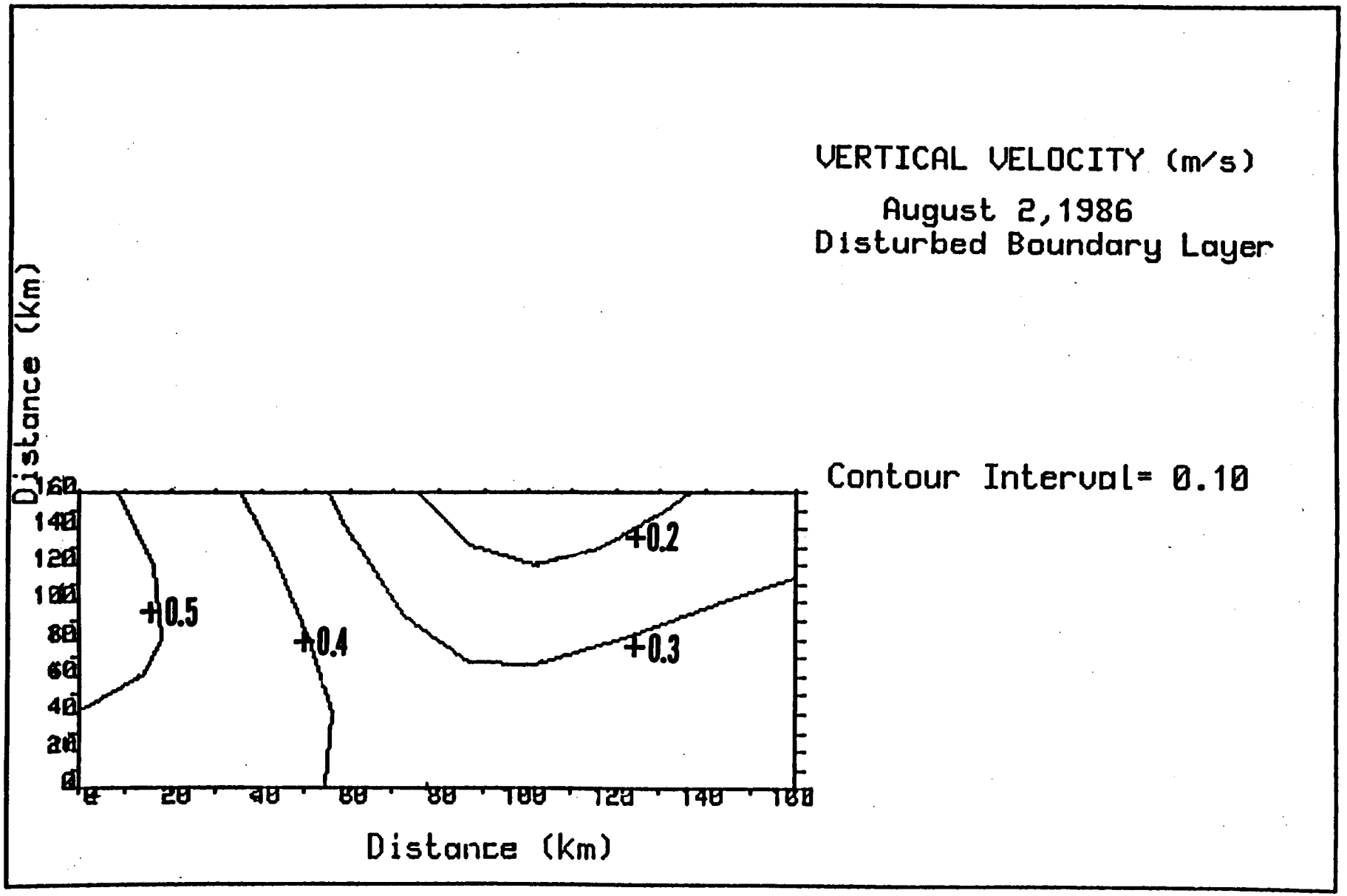
VERTICAL VELOCITY (m/s)
August 2,1986
Disturbed Boundary Layer
Contour Interval= 0.10
Distance (km)
+0.5
+0.4
+0.3
+0.2
Distance (km)

Fig 20a

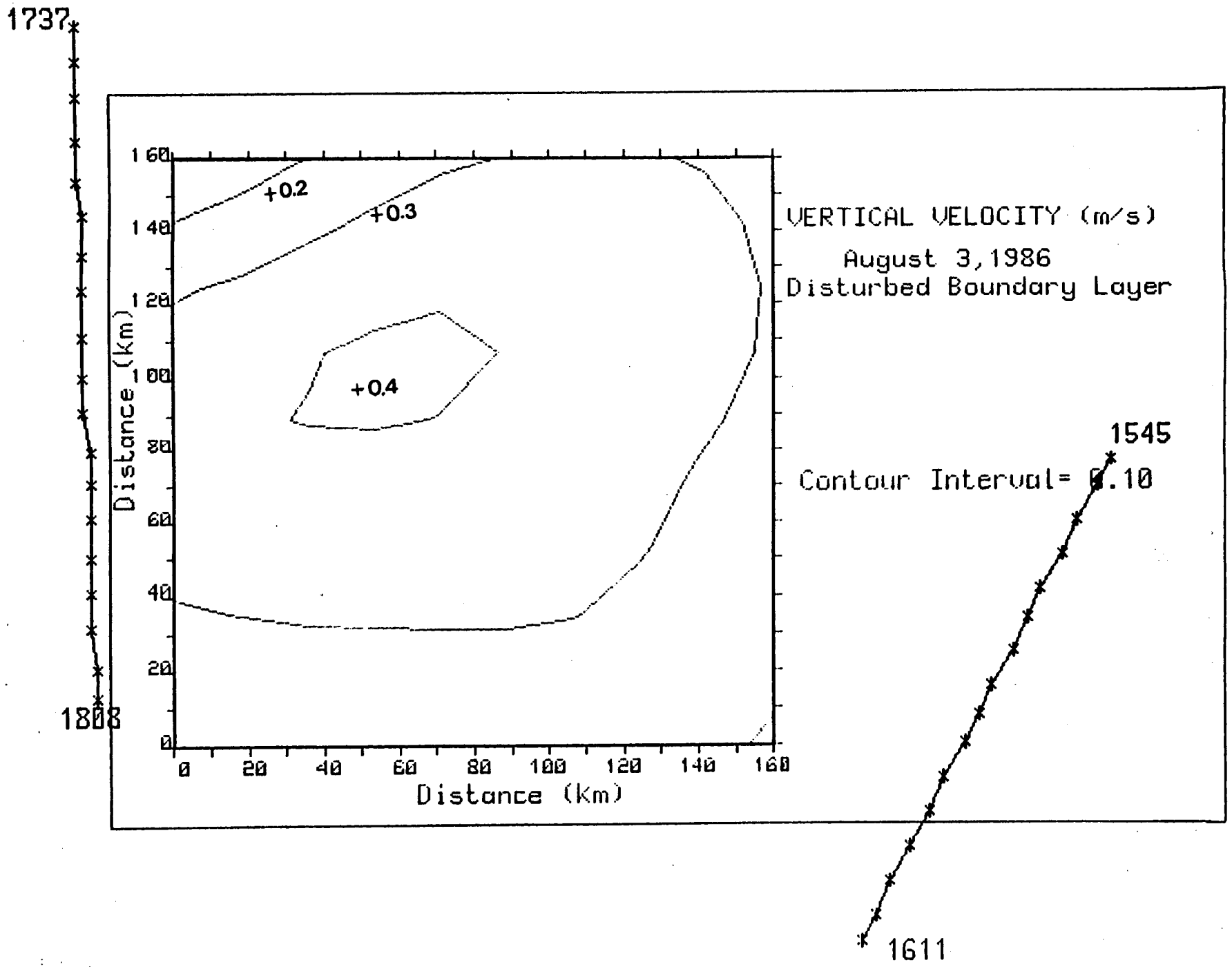
1737
1808
160
140
120
100
80
60
40
20
0
Distance (km)
0
20
40
60
80
100
120
140
160
Distance (km)
+0.2
+0.3
+0.4
VERTICAL VELOCITY (m/s)
August 3, 1986
Disturbed Boundary Layer
Contour Interval= 0.10
1545
1611

Fig 206

4.1.1 Paper presented at the Spring Meeting of the American Geophysical Union.

The Influence of Convection on Tropospheric Chemistry in the Central Amazon

MICHAEL GARSTANG (Department of Environmental Sciences, University of Virginia, Charlottesville, VA 22903)
SHERWIN BECK and EDWARD BROWELL (NASA/Langley Research Center, Hampton, VA 23665)
PEDRO DIAS (University of Sao Paulo, Sao Paulo, Brazil)
GERALD GREGORY, ROBERT HARRISS, GERALD HILL and GLEN SACHSE (NASA/Langley Research Center, Hampton, VA 23665)

Meteorological and chemical measurements made on and from the NASA Electra aircraft around two convective cloud complexes are examined. Ozone concentrations in the middle and lower troposphere are significantly different from the non-convective state. Enhancement and diminution of O_3 and CO in the atmospheric boundary layer and in the middle troposphere can be explained in terms of measured velocity, temperature and moisture fields surrounding the cloud.

The findings stress the importance of convective cloud transports in a region of particular significance to global trace chemistry and the general circulation of the atmosphere.

Structure and Growth of the Mixing Layer over the Amazonian Rain Forest

Charles Martin[1], David Fitzjarrald[2], Michael Garstang[3], Amauri P. Oliveira[4], Steve Greco[3], and Edward Browell[5]

Short title: Amazonian Rain Forest Mixed Layer Structure and Growth

[1]Simpson Weather Associates, Inc., Charlottesville, VA 22902.

[2]Atmospheric Sciences Research Center, State University of New York, Albany, NY 12205.

[3]Department of Environmental Sciences, University of Virginia, Charlottesville, VA 22903.

[4]Departamento de Meteorologia, Instituto Astrônomico e Geofísico, Universidade de São Paulo, Brasil

[5]NASA/Langley Research Center, Hampton, VA 23665.

Abstract

Measurements carried out over the rain forest of central Amazonia during the NASA Amazon Boundary Layer Experiment (ABLE-2A) are used to examine the structure and growth of the atmospheric mixed layer. Fluxes of sensible and latent heat were measured at the top of the canopy and measurements of temperature, moisture, and horizontal wind were made in and above the mixed layer by means of a tethered balloon, rawinsonde, and aircraft. Airborne lidar measurements provided an estimate of the depth of the mixed layer over large distances. The mixed layer is found to be very shallow at night, frequently just above the canopy, growing rapidly at 5-8 cm s^{-1} soon after sunrise to a maximum height of 1800 m by 1300 local standard time (LST). Mixed layer heights above 1000 m between 1000 LST and 1600 LST are common during undisturbed conditions. Fossil mixed layers, well mixed but no longer mixing, were found to 2000 m and at all times of the day and night.

The simple jump model, when initialized with an early morning sounding, and forced with observed buoyancy fluxes, is compared with observations. The model over-predicts the depth of mixed layer. The role of meso- to synoptic-scale subsidence on the order of 2 cm s^{-1} due to large cloud systems, removed by 1 to 200 km from the local site, are called upon to explain the observed differences.

Model estimates and observations of moisture entrainment fluxes across the top of the mixed layer both reach 1000 W m^{-2} while fluxes across the top of the canopy reach 400 W m^{-2} during the day time. Flux divergence in the mixed layer leads to drying which is observed at the top of the canopy. No horizontal inhomogeneities in the mixed layer structure or depth were found over large distances suggesting that point

measurements under undisturbed conditions can be used to obtain estimates of mixed layer structure and fluxes over large areas of the Amazon basin.

1. Introduction

The Amazon rain forest has been recognized as a major source region of atmospheric trace gases and aerosols (NAS 1984, Fishman et al., 1986; Logan and Kirchhoff, 1986). Species that are produced or consumed in the forest are transported between forest and the troposphere through the atmospheric boundary layer. During the day, there is a dry convective boundary layer coupling the canopy to the deeper atmosphere through turbulent mixing. In this paper, we refer to this region as the mixed layer. The behavior of this layer is critical in determining the transport of species to the deeper atmosphere and their concentrations there. Very little data is available to describe the structure and processes of the atmospheric mixed layer over such a vast and inaccessible region as the Amazon basin. The few rawinsonde stations which do carry out one or two operational soundings per day in the basin provide infrequent sampling and the vertical resolution of the operational rawinsonde is not good enough to describe the structure of the mixed layer.

A major purpose of the NASA Amazon Boundary Layer Experiment (ABLE-2A) was to obtain a quantitative description of the mixed layer at a single forest location and to obtain estimates of the spatial homogeneity or inhomogeneity of the mixed layer away from this location by means of a research aircraft. The field program was designed to obtain high time and space resolution measurements over a period of about three weeks during the mainly undisturbed weather of the dry season in July and August 1985.

The description of the structure and growth of the mixed layer over the tropical rain forest is directed at gaining an understanding of how

a large suite of important chemical species and aerosols (Harriss et al., 1987) generated in the soils, in the forest canopy and above the canopy are communicated between the canopy and the deeper atmosphere. These findings have significant implications since deep convection in the equatorial trough plays a fundamental role in balancing the heat and moisture budgets of the global atmosphere (Riehl and Simpson, 1979; Augstein et al., 1980). There is substantial and increasing evidence of transport of chemical species and aerosols via major teleconnections between the tropical oceanic and continental circulations of mid- and higher latitudes in both hemispheres (Rasmussen and Carpenter, 1982; van Loon, 1984). Silva Dias et al. (1987) demonstrates that large, transient convective episodes over the Amazon basin provoke waves that influence the midlatitudes.

To achieve an understanding of the chemical transports, the behavior of the atmosphere immediately above the forest canopy must be described on time and space scales which will depict systematic changes such as day-to-night variations as well as short-lived transient phenomena such as convective cloud in- and outflows. We present in this paper the diurnal sequence of the thermodynamic structure of the convective boundary layer together with estimates of entrainment fluxes across the top of the mixed layer. Most of our findings are based upon local measurements at a single site. We use aircraft measurements to demonstrate that the local measurement, under undisturbed conditions (little or no shower activity), is representative of large areas (400-500 km in linear distance). The more difficult question of vertical and horizontal transports of quantities in the atmosphere under transient disturbed (raining) conditions is addressed elsewhere (Garstang et al., 1987) and

is the main focus of the next field experiment, ABLE 2B, scheduled for April-May 1987.

2. Field Measurements

ABLE-2A, described by Harriss et al. (1987), was based on Manaus (2^{o}S,60^{o}W) in central Amazonia (Figure 1). Measurements were made from July 15, 1985 to August 7, 1985 under weather conditions characteristic of the early dry season. Thus, while showers (25 to 55 mm rain per day) occurred on the first few days of the experiment in the Manaus region, dry conditions characteristic of the subtropical anticyclone became increasingly common from July 17 onwards. Convective activity in the form of large cloud complexes, continued to occur to the west of Manaus throughout the experiment. Manaus often lay just inside the fair weather region (Figure 2), on the boundary between the suppressed conditions of the anticyclone and active convection to the west of Manaus.

Ground-based measurements were made from the Ducke Forest Reserve located about 20 km northeast of Manaus (Figure 1). Since ground elevations in the reserve averaged 90 m above mean sea level (MSL), the height of the forest canopy is about 35 m. Thus the top of the canopy is approximately 125 m above MSL. In this paper all elevations are referenced to sea level unless otherwise noted.

Heat, water, and momentum fluxes were calculated at two levels, 5 and 10 m, above the top of the forest canopy using fast-response measurements from instrumentation mounted on top of a micrometeorological tower. These measurements are described by Fitzjarrald et al. (1987). An automatic weather station on the same tower provided

mean values of temperature, moisture, and horizontal wind velocity (Shuttleworth et al., 1984).

Temperature, humidity, pressure, and horizontal wind speed and direction were measured by a tethered balloon borne sonde profiling at the rate of 1 m s^{-1} between 10 and 1100 m above the ground. Measurements were made every 10 sec providing a vertical resolution of 10 m. Each sounding between the surface and 1000 m took approximately 20 min and 2 soundings per hour were made during most daylight hours. On six occasions the above sounding routine was carried out through the night. The general characteristics of the tethered balloon system are described by Emmitt (1978) and Wylie and Ropelewski (1980). Details of the sonde used and the measurements made are presented in Table 1.

Rawinsonde measurements were made from the Ducke Forest Reserve station and from the Brazilian Air Force station at Ponte Pelada, 20 km to the southwest of the Ducke Reserve. At Ducke, soundings were made at 3 h intervals during all operations. When operations were confined to daylight hours soundings were made between 0800 and 1700 (60^{o}W) LST. The Ducke soundings were made to an average height of 450 mb using a high resolution Atmospheric Instrumentation Research (AIR) sonde and digital recording and processing system (Table 2) providing measurements every 25 m. At Ponte Pelada, 4 soundings per day were made from the surface to an average height of 100 mb. Soundings were made at the synoptic hours (00, 06, 12, and 18 geomagnetic time (GMT)) using operational Vaisala equipment. Comparisons between these three sounding systems as well as the aircraft measurements, indicate that the AIR sondes systematically overestimated the mixing ratio by 2 g kg below 700 mb. A correction of this order was applied to the Ducke rawinsoundings.

The NASA Electra aircraft made meteorological and chemical measurements along the flight track and in spirals between 150 m and 5 km above the surface. An airborne ultraviolet differential absorption lidar (UV-DIAL), described by Browell et al. (1987), provided measurements of aerosol and ozone concentrations in the vertical column below the aircraft. The vertical and horizontal resolution of the aerosol measurement (15 m and 20 m) is sufficient to define such features as the average top of the mixing layer and the base of any well defined inversion over distances of about 7 km. Over-flights and spirals were carried out over the Ducke ground station. Extended horizontal flights covering hundreds of kilometers (Harriss et al., 1987) and up to 6 h of flying time covered a significant fraction of the Amazon basin. The aircraft cruised at about 110 m s^{-1} (400 kph).

Table 3 lists the times for which data is available from the systems described above. Prior to analysis, quality control checks were made on the data, corrections made for tethered balloon motion, and interpolation using a cubic spline (Reinsch, 1976) carried out where appropriate. The balloon motion correction for wind speed began with selecting pairs of ascending and descending profiles assumed to be made during stationary conditions. The mean of the two profiles was assumed to represent the true wind speed, and a bivariate regression provided a relation for the difference between observed and true wind speed as a function of altitude and observed wind speed. A separate relationship was determined for ascending and descending profiles, and applied to the observations to determine true wind speed.

The eddy flux measurements were edited to remove periods of bad data, which were known to occur when sensors failed (Fitzjarrald et al.,

1987). These problems were not common, and the data return for the eddy flux measurements was approximately 77%. The upper and lower levels of the eddy flux data were observed to be very similar (Fitzjarrald et al., 1987). In the following calculations, data was used from the lower level at 39 m, approximately 5 m above the canopy.

Sample tethered ballon profiles are shown in Figures 3 and 7 for daytime and nighttime regimes. Both sequences of profiles show (Figures 3 and 7) mixed layer development. The stable layer into which the mixed layer grows is well described by the 0414 LST sounding on July 31 (Figure 7a). This nighttime profile is a classic example of the strong nocturnal stratification which was typical of the measurement period. The generation of the mixed layer is traced by the morning and early afternoon soundings, where the virtual potential temperature, θ_v, wind speed, and specific humidity are well mixed up to 800 m by 0948 (Figure 7e) and above 1200 m by 1158 (Figure 7f). In addition, note that the variability of the wind speed with height, especially in the u-component, also indicates the vertical extent of active turbulent mixing.

Objective methods have been developed and applied to determining mixed layer height over the open ocean from tethered balloon profiles (Fitzjarrald and Garstang, 1981a). The ABLE profiles are significantly more complex so that a subjective technique was chosen for determining the mixed layer height. This consisted of visually defining the height in the profile where there was a discontinuity in moisture, virtual potential temperature and wind speed, and below which mixing appeared to be fairly complete (see for example Figures 3a, 3b, 7a, 7b, 7c). In particular the variability, in the vertical, of the wind speed was

useful in determining the region of active turbulent mixing. In addition, other factors were considered, such as the time of day, the general trend within a series of profiles, and the local weather observations. All profiles were examined, and in most cases a reliable mixed layer height could be determined. In a number of afternoon cases, the mixed layer rose above the maximum tethered balloon level (1100 m) to which measurements could be made (see for example Figures 3c, 3d, and 3e). Radiosonde and aircraft measurements could be used to define these deeper mixed layers. We also identify residual mixed layers resulting from previous mixing. Such residual or fossil mixed layers are identified observationally as regions of no or weak vertical gradients in moisture and temperature without marked variability in horizontal wind velocity.

The above procedures for determining the top of the mixing layer are used to infer the depth of the mixed layer as described in the remainder of this paper.

3. Case Studies with Model Application

Three stages of boundary layer growth on undisturbed days are (Tennekes, 1973; Caughey, 1982): a) surface heating causes erosion of a strong inversion that develops overnight. At this time there is relatively little coupling with the environment above the convectively mixed layer. Since this layer is relatively shallow, we expect changes in surface fluxes to result in relatively large changes in concentration at this stage; b) rapid rise of the convectively mixed layer, with attendant entrainment flux of air from above becoming important; c) gradual decay of dry convective mixing as the surface buoyancy flux

changes sign (Nieuwstadt and Brost, 1986). We consider the undisturbed state to be one in which convective activity and advection effects are minimal. A disturbed day is one in which convective features are likely to interact with the mixed layer behavior through downdrafts, between-cloud subsidence, rain showers, or interruption of insolation. We can also identify disturbed days by surface observations, rainfall records, and the lidar measurements. On days which include important effects of storm outflows or rainfall, the sequence of events may be restarted, with a new, shallower convective boundary layer appearing in the wake region (Fitzjarrald and Garstang, 1981a, 1981b). According to this idealization, a mixed layer only grows upward, entraining and energizing a relatively quiescent fluid. When the layer becomes decoupled from the surface, there is no reason for the layer, originally mixed by buoyant elements rising from the surface, to form strong gradients of nonreacting species. In this circumstance, we expect to discover fossil mixed layers that are mixed but no longer mixing. We test this conceptual model with reference to two cases observed during this experiment.

We will use the simple "jump" model of mixed layer growth (Tennekes, 1973; Betts, 1973) to allow us to estimate the entrainment fluxes. This model assumes zero gradients of virtual potential temperature (θ_v), water vapor mixing ratio (q), and concentrations of trace substances in a mixed layer, with a finite jump in each quantity at the mixed layer top. Thus the mixed layer mean for any of these quantities X_m is:

$$dX_m/dt = (F_{Xo} - F_{Xh})/h \qquad (1)$$

where h is the mixed layer thickness, F_{Xo} is the surface flux of

quantity and F_{Xh} is the entrainment flux of X into the mixed layer at the top. F_{Xo} is obtained from measurements. Entrainment at h is related to the "jump" in X at h,

$$F_{Xh} = (X_h - X_m)w_{en}, \tag{2}$$

with w_{en}, the entrainment velocity, given as $dh/dt - w_h$. Environmental subsidence is given by w_h. When the mixed layer grows into a layer exhibiting vertical gradient Γ_X, X_h changes according to:

$$dX_h/dt = \Gamma_X w_{en}. \tag{3}$$

We apply the standard closure assumption:

$$F_{\theta v,h} = -0.25\ F_{\theta,o} \tag{4}$$

(Betts, 1973).

Our aim is to estimate the maximum thickness a mixed layer can achieve given observed stratification and the observed surface fluxes. We hypothesize that the entrainment flux of any other constituent during the morning growth phase could similarly be estimated, given surface fluxes of the constituent and buoyancy along with a time series of the mixed layer heights.

Driedonks (1982) presented a series of comparisons of predictions of this model with more complex entrainment parameterizations. He found that the simple model yielded acceptable predictions of mixed layer height, and noted that increasing the complexity of the entrainment parameterization did not noticably improve the prediction.

We will now use two case studies, July 25 and July 31, to examine mixed layer behavior and apply some of these ideas. The sequence of soundings (Figure 3) on July 25, 1985 illustrates the hypothesized

stages of growth for the first case. With the onset of surface heating at about 0700 LST, a shallow mixed layer forms. By 0745 (Figure 3a) this mixed layer is about 200 m thick, capped by a jump of more than $4^{o}K$ in θ_v. Note that the wind component profiles show higher variability below this stable cap, giving indirect evidence that convective turbulence is present. By 1202, the jump in stability at mixed layer top is smaller, and there is mixing evident to about 850 m. The soundings at 1316 (Figure 3c) place the mixed layer at approximately 1000 m.

Figure 4 presents a combination of contoured θ_v values in the mixing layer and mixing layer heights, along with the surface fluxes and meteorological parameters measured at the micrometeorological tower. During the night, mechanical mixing promotes weak negative turbulent heat flux and positive moisture flux. After sunrise, heat and moisture fluxes become positive, and the stable layer erodes, becoming a shallow well mixed layer. Note that the specific humidity measured at the micrometeorological tower reached a local maximum between 0800 and 0900, after which it dropped until midday. This feature was observed on many days, and we interpret the humidity variation according to the conceptual model described above in which moisture flux initially converges into a shallow mixed layer in the hours immediately after sunrise. Strong stability above this layer inhibits diluting entrainment fluxes. Since the layer is still shallow, the layer mean humidity increases, and this is evidenced even at the canopy top.

There is an apparent and anomalous "drop" in the mixed layer between 1316 and 1345 as seen in the tethered balloon profiles (Figures 3c, 3d). At this time the sensible heat flux dropped to near zero, and

hourly-averaged incident solar radiation decreased (Figure 4). Variability in the wind profile increases below the new inversion at 500 m, indicating that this new layer is again convective (Figure 3d). We interpret the change in mixed layer height to be the net result of a storm outflow. Betts (1976) and Fitzjarrald and Garstang (1981a, 1981b), among others, have shown that shallow cool layers are left in the wake of storm downdrafts. Observations show that the surface heat flux recovers by 1400 (Figure 4) and we hypothesize that this new mixed layer grows from its interrupted level until the surface heat flux changes sign after 1600. Abrupt changes in the boundary layer occur when the surface heat flux becomes negative. Comparing the soundings at 1630 and 1643 (Figures 3e, 3f), we note that variability in the horizontal wind profile is diminished at the later time, and this is accompanied by static stability throughout the column to 700 m. The layer between 700 and 1100 m dries approximately 2 g kg^{-1} between these two soundings. It may be that this moisture change was accomplished by decaying convective eddies in the upper part of the decaying boundary layer, as Nieuwstadt and Brost (1986) have demonstrated in model simulations. They showed that there is an increase in the turbulent convective energy in the upper half of the old boundary layer when surface buoyancy fluxes are cut off abruptly. It is possible that this energy was sufficient to mix in the drier air above. A stable boundary layer approximately 150 m thick was evident in the 1806 sounding (not shown).

Some of the features of mixed layer growth on this day may be understood by reference to the jump model. The environmental stability was assumed to be described by a linear fit to the observed values of θ_v

above the mixing layer. We assumed that above this layer, no significant environmental change occurred during the morning. We take the θ_v profile at 0745 (Figure 3a) as the initial condition, using the observed buoyancy fluxes (Figure 4) as the lower boundary condition to simulate conditions on July 25.

Results for the model estimated mixed layer growth (Figure 5a, dashed line labeled H_1) show that the model cannot simulate the rapid observed initial growth of the mixed layer to 800 m by 1000 LST. The model does not complete erosion of the stable layer until approximately 1100, and this is both because of the strong inversion as seen in the initial condition and because of the small and intermittent observed buoyancy fluxes (Figure 4). Photographs (Figure 6) indicate that July 25 was quite cloudy, and, although no rain was observed at the balloon or tower sites, it is quite likely that there were showers in the vicinity. As a result, we can expect there to have been horizontal inhomogeneities in the surface fluxes and in the mixed layer thickness. We found that earlier model onset time of the rapid mixed layer rise (1100 in Figure 5a) could be induced by reducing the initial "jump" in θ_v.

The mixed layer height from the original simulation grows above 1800 m (Figure 5a), much higher than was ever observed. Johnson (1977) has also found that this model predicted excessive mixed layer thickness in his simulations of cloud development over south Florida. His model results indicated that cloud-induced subsidence as large as 9 cm s^{-1} are necessary to explain the limit to mixed layer growth. However, his result was obtained with an assumed sinusoidal surface flux formulation independent of cloud formation. Here we see that even when using the

intermittent observed surface fluxes, there is excessive growth. We do not dispute that cloud-induced subsidence may be modifying mixed layer growth over the Amazon, but events between 1300 and 1400 on July 25 clearly represent another type of phenomenon. The tethered balloon sounding at 1345 (Figure 3f) is cooler than the sounding at 1316 (Figure 3e), indicating that a new mixed layer formed in cooler drier air deposited by cloud downdrafts. We restarted the simulation using the 1345 sounding and found that there was sufficient surface buoyancy flux observed after that time to grow the mixed layer back to 1000 m by 1600 (Figure 5a, solid line labeled H_2).

Observed values of $\theta_{v,m}$ and $\theta_{v,h}$ (Figure 5b) indicate that the inversion probably was filled in between 0900 and 1100. In later hours the data show that the jump in θ_v was maintained. There are several points where the model shows qualitative agreement. As expected, model predicted $\theta_{v,m}$ approaches $\theta_{v,h}$, although at a slower rate than was observed. After rapid mixed layer growth begins at approximately 1100, the model predicted jump in θ_v is similar to the observed jump (Figure 5b).

As with θ_v, the model produces qualitative agreement with the observations of the mixing ratio (Figure 5c). A slight increase in q_m after 0800 followed by significant drying after 1100 are seen both in the data and the model results. Because of the excessive growth of the mixed layer as predicted by the model, simulated q_m and q_h continue to decrease until the buoyancy flux stops and the mixed layer growth ceases. The observations show an increase in q_m and q_h after 1300, consistent with the idea of downdrafts forming a new shallow mixed layer

which now behaves as in the morning, by moistening due to the moisture flux convergence in this thinner layer.

A case study for July 31 is presented next. Photographs (Figure 6) show there to have been shallow clouds only in the late morning hours with few clouds seen in the afternoon, a reflection of the drier, more subsident synoptic conditions observed during the last days of July and the first week in August. Figure 2 illustrates the large scale conditions prevailing on July 31 and referred to earlier. We wish to make particular note of the fact that the fair conditions in the vicinity of Manaus are seen to be within approximately 200 km of significant cloud complexes to the west.

The tethered balloon profiles for July 31 are shown in Figure 7. The 0414 LST sounding (Figure 7a) exhibits the strong nocturnal inversion, and a large wind shear from the surface to the inversion. A well mixed profile of q below the inversion suggests that shear induced mechanical mixing is active. At 0729 (Figure 7c) the surface θ_v has warmed by $2^{o}K$, but the region of mixing has remained below the inversion. By 0846 (Figure 7d) the rapid growth has begun, with the mixed layer height having grown 300 m (from 200 m to 500 m) in 1.25 h (5-6 cm s^{-1}). Rapid growth continues, and by 1158 (Figure 7f) the mixed layer is above 1100 m.

One pronounced feature of these suppressed days at the end of the experiment is a mid-morning maximum in q, as measured at the top of the forest canopy, followed by drying throughout the day (Figure 8). This drying starts before the nocturnal stable layer is completely eroded (approximately 1030), and continues until nocturnal cooling reestablishes a shallow mixed layer (approximately 1830). Concurrently,

however, significant (approximately 400 W m^{-2}) fluxes of water vapor are occurring across the top of the forest canopy. Entrainment fluxes across the top of the mixed layer must therefore be large for drying in the mixed layer, as measured at the top of the canopy to occur over the time period 1000-1800 LST. Clearly the entrainment moisture flux must be appreciable later if it is to overcome the very large moisture flux observed above the forest canopy and lead to drying within the layer.

The jump model was applied to the July 31 case, being initialized with the 0846 sounding (Figure 7d) and forced by the surface fluxes. Several parameters were adjusted in an attempt to produce more realistic results. The simulation again leads to excessive mixed layer thickness (Figure 9a, h1), unless we arbitrarily double the environmental θ_v lapse rate (Figure 9a, h2) or include appreciable environmental subsidence (0.02 m s^{-1}, Figure 9a, h3).

Estimates of the large scale environmental sinking, based upon changes in the heights of the mixing ratio contours at night between about 100 and 500 m above the surface, show subsidence on the order of 300 m in 12 h or close to 0.75 cm sec^{-1}. Time series of the predicted mixed layer mixing ratio (Figure 9c) exhibit the observed midmorning maximum for all simulations except the one with the enhanced stability. Note that changing environmental stability or subsidence has little effect on mixed layer virtual potential temperature (Figure 9b). Based on these results, we submit that subsidence, at least on the order of 2.0 cm s^{-1}, probably occurred during this period. Subsidence of this magnitude cannot be ascribed to the large scale sinking of the subtropical anticyclone. Nor can conventional between-cloud subsidence be called upon, since no clouds were observed. Instead, we submit that

meso- to synoptic-scale subsidence is occurring on the scale of the cloud complexes observed 100-200 km west of Manaus as shown in Figure 2. In this context the "dry" conditions are defined in spatial rather than temporal terms.

The entrainment moisture flux across the top of the mixed layer flux must be enormous as noted above to lead to drying above the Amazon forest canopy. While similar drying by entrainment has been observed close to the tropical ocean during transient periods (Fitzjarrald and Garstang, 1981a), it appears to be a normal occurrence over the "dry season" rain forest. The observed values of specific humidity q, the depth of the mixed layer h, and the surface moisture flux can be used with Eq. (1) to make a direct estimate of the entrainment moisture flux. In this case, q measured at the micrometerological tower was taken to represent average value in the mixing layer. $F_{q,h}$ computed in this manner can then be compared to the model derived value (Figure 10). The agreement is good, both methods clearly demonstrating that the entrainment moisture flux across the top of the mixed layer must exceed 1000 W m^{-2} to produce realistic mixed layer drying rates. The significance of this finding is enhanced by the fact that the observed entrainment depends primarily upon knowledge of the mixed layer depth. As will be shown later, both the mixed layer depth as well as its spatial and temporal behavior can be determined across the Amazon basin by the Airborne UV-DIAL (UltraViolet-DIfferential Absorption Lidar) system. Thus estimates of entrainment fluxes were made over large distances.

Two points follow: 1) if the difference in concentration between the mixed layer and the environment above is large enough, entrainment fluxes will dominate the balance even in the presence of very large

surface fluxes, and 2) estimated fluxes into the deeper atmosphere will depend on not only the measured surface flux and concentration of a quantity, but upon mixed layer depth and rate of growth.

Many of the features described for the two case studies were seen on other days. A sample of other days (Figure 11), shows that the association between mixed layer top rise and surface drying occurred on July 26 (Figure 11a), and August 2 and 5 (Figures 11c and d). The normal course of mixed layer rise was apparently interrupted by storm outflows on July 27 (Figure 11b). On days when the outflows interrupted convective boundary layer growth, it is possible for a mixed, but not actively mixing, layer to be left in the atmosphere. The fact that the same, predictable features appear in the time sequences of tethered balloon soundings, coupled with the evidence from the several aircraft flights to be shown below, leads us to conclude that we have observed phenomena characteristic of conditions over the rain forest over wide areas of the Amazon basin.

Fitzjarrald et al. (1987) remarked on the frequent periods with small, positive or even negative, sensible heat fluxes observed during the daytime over the Amazon forest. We have seen here that even with such periods, the convective boundary layer tends to grow above 1000 m, well above the 500 m thickness typically seen over tropical oceans. The net effect of these periods of transient stability on estimates of average transport over large areas is not easy to determine. However, we hypothesize that one consequence is that there must be modulation of the mixing intensity of turbulence in the convective boundary layer, as estimated by the characteristic mixing velocity w^* and mixing time h/w^*. This modulation may be important in interpreting the budget of chemical

species whose reaction time is comparable to the turbulent mixing time. This effect has been noted for atmospheric turbulence in the surface layer (Lenschow, 1982; Fitzjarrald and Lenschow, 1983) for the ozone-nitrogen oxide smog reaction and may be important in the boundary layer for other species. Characteristic mixing times together with extreme daytime values are shown in Table 4.

4. Composite Analysis

The case studies presented above serve to illustrate the mechanisms of mixed layer behavior above the Amazon forest. A description of the average daily conditions observed during the experiment is presented next.

Figure 12 shows the mixed layer heights for all days of the experiment as a function of local standard time. A large variation in the height over the course of the 24 hours is seen. On average the mixed layer growth rate is 5-8 cm s^{-1} during the vigorous heating of midmorning. In individual cases the growth rate could be as rapid as 10 cm s^{-1}, whereas under certain conditions, such as extensive cloud cover, the mixed layer growth occurred at rates much lower than the average.

Figure 12 also shows plots of average daily values of θ_v and the surface layer values of temperature, heat flux, specific humidity, moisture flux, incident solar radiation and net radiation. While general characteristics of the case studies such as the deflection in specific humidity is reflected in the mean values, detailed mechanistic processes are lost.

During the night, the negative net radiation has been cooling the surface, and a small but persistent negative sensible heat flux is

cooling the mixed layer. A uniform moisture profile below the shallow nocturnal stable layer is maintained at night. By sunrise, 0600 LST, a pronounced stable layer has formed, with warming of $3^{o}C$ from the surface to 100 m above canopy level. As the solar heating intensifies after dawn, the heat flux begins to climb rapidly and becomes positive after 0800. Between 0800 and 1000, moisture and heat are being entrained into the stable layer. While the heat flux is warming the stable layer, the specific humidity reaches a maximum and then begins to decrease when the mixing layer begins to expand more rapidly into the less stable layer above the previous inversion height. The concentration of q after sunrise followed by dilution several hours later reflected in the mean are described in the case studies of July 25 and 31.

During midday the mixing layer continues to grow, on the average reaching heights above 1200 m by 1200 LST. The composite of θ_v shows the deepening adiabatic layer which is indicative of well mixed conditions. Average mixing layer height for the late afternoon can be above the height of the tethered balloon, but rawinsonde and lidar measurements suggest that at times it has extended to 1600 m as will be shown below.

After the heating stops in late afternoon, the heat flux once again turns negative, quickly reestablishing the surface stable layer. This decouples the surface fluxes from the existing well mixed layer, and a new layer must form which is only mixed by mechanical means. In many of the individual cases, a rise in humidity is often seen in late afternoon or early evening which could be due to moisture convergence in this shallow stable layer. The shallow layer may be the result of late afternoon convective outflows, nocturnal cooling, or both. The

frequently observed increase in humidity is not discernable in the mean. Radiational cooling produces a pronounced temperature inversion during the night. At 0400 the lapse rate of θ_v between the surface and 300 m is 17.5 $^{o}K\ km^{-1}$.

5. Time and Space Variations in Mixed Layer Depth

The frequency and vertical height resolution of the tethered balloon measurements of mixed layer depth provide the best local measurement of the depth of the mixed layer. Figures 12 and 13 show mixed layer depths determined subjectively according to the definitions stated in Section 1 for a) all days (Figure 12), b) disturbed days (Figure 13a), and c) undisturbed days (Figure 13b).

The disturbed day mixed layer heights (Figure 13a) show greater variability than the undisturbed day heights (Figure 13b). The difference in heights between the two classes of days is not, however, pronounced primarily because the level of convective activity in the Manaus region in the dry season is low. When measurements are made in the immediate vicinity of clouds by the aircraft, as is shown below, the mixed layer heights show large variation.

The rawinsonde measurements made at Ducke and the aircraft and UV-DIAL soundings provide measurements of the mixed layer to its maximum depths. We wish to verify that other measurement techniques used to detect the depth of the mixed layer compare favorably with the tethered balloon method for two reasons: a) to establish that mixed layer heights above 1100 m did indeed occur, obtain an estimate of these heights, and determine the time of day at which they occurred; and

b) to show that the local behavior of the mixed layer is reproduced over a wide region of near uniform rain forest.

Figure 14 shows that there is good agreement between the mixed layer height determination by tethered sonde and radiosonde under both disturbed (Figure 14a) and undisturbed (Figure 14b) conditions, with correlation coefficients of 0.86 and 0.73 respectively. With relatively few exceptions, the determinations of mixed layer height from the two systems is well within 200 m. UV-DIAL versus aircraft spiral soundings for undisturbed conditions are shown in Figure 15. Except for a slight tendency (less than 100 m on average) to overestimate the mixed layer height from the lidar, the agreement is excellent (correlation coefficient of 0.96). UV-DIAL versus the tethered sonde and radiosonde for undisturbed conditions is shown in Figure 16. Wider scatter is observed here (correlation coefficient of 0.79) primarily because the aircraft could not operate in the vicinity of the tethered balloon with the balloon flying. Nor were the aircraft measurements coincident with the radiosonde launches. Thus, these observations are frequently separated in time by as much as 1 h. Since mixed layer heights change by as much as 360 m in 1 h, larger scatter may be expected. We conclude from the preceding that the special radiosonde and the aircraft in situ and remote (UV-DIAL) methods represent viable tools for examining the behavior of the mixed layer height in time and space.

Figure 17 shows the height of the mixed layer as determined from the radiosonde time series at Ducke. New growing mixed layer heights, when observed with a system which is sampling heights every 3 h, are not frequently observed above 1000 m. Active mixing is seen to near 1800 m only once by the rawinsonde system. On the other hand such infrequent

sampling detects evidence of previous mixed layers or fossil mixed layers with considerable frequency above 1000 m up to a maximum height of 2000 m. Fossil mixed layers may extend above the active mixed layer height by small but continued growth on the order of 200 m.

Figure 18a shows mixed layer heights as determined from the aircraft spiral soundings taken over many different locations (see Harris et al., 1987) as a function of time of day. Mixed layer heights are seen frequently above 1000 m (close to but below 1800 m) during the late morning and early afternoon. While the mixed layer height is well behaved on undisturbed days (Figure 18b), on disturbed flights (Figure 18c) there is very large variation with no dependence upon the limited time span sampled. This observation is important when compared to the results in Figure 17 for it dramatically illustrates the variability of the mixed layer height when the observation is taken in close proximity to convective clouds. Conversely, the observations show that away from clouds, mixed layer growth is well behaved.

Mixed layer heights determined by lidar on undisturbed days are well behaved in the growing phase (Figure 19). Here lidar estimates of the depth of the mixed layer have been taken from all flights on undisturbed days over a wide region of tropical rain forest. The maximum average rate of growth occurs between 1000 and 1200 LST approaching 5 cm sec^{-1}, in agreement with the findings based on in situ measurements. Lidar measurements under disturbed conditions (not shown) are limited to a short period of about 4 h centered on 1300 LST. They show large scatter which is in agreement with the aircraft spiral soundings.

Agreement between the lidar measurements of mixed layer height and measurements made by more conventional systems under undisturbed weather

conditions, suggests that under these conditions the lidar might be used to extend the point measurements of balloons to space measurements over a much larger domain. Figure 20 shows lidar observations on an undisturbed day (August 21, 1985) which cover a large region (see Figure 1 for flight track) of tropical rain forest. Measurements begin at 0916 LST (1316 GMT) and continue to 1223 LST (1623 GMT) thus covering the time of maximum mixed layer growth. Figure 20a starting at 0916 LST shows a mixed layer is evident to 250 m near point A and is growing along the flight track to 500 m near point B at 0946 LST. By the next high level pass (Figure 20b) starting at 1140 LST, the mixed layer has grown to 1100 m near point B (growth rate of 8.8 cm sec^{-1}) after which it slowly rises to about 1200 m at 1206 near point A (growth rate 9.3 cm sec^{-1}). The mixed layer has about the same depth until convective activity increases during the final leg near Ducke (Figure 20c). Successive lidar measurements under undisturbed conditions show the same behavior of the mixed layer. There is no evidence that, over the vast regions of rain forest around Manaus, the growth rate of the mixed layer shows any major spatial variations due to subtle changes in the underlying surface. The onset of rapid growth of the mixed layer is influenced by underlying conditions as evidenced by Figure 20a. Other changes observed in mixed layer depth could be directly associated with convective cloud activity. The very rapid growth of the mixed layer exhibited in the early growth phase as observed by lidar agrees with the growth rates based upon in situ measurements. The marked flux divergences, illustrated earlier by Figure 10 associated with mixed layer growth and deep mixed layers, can be expected where such conditions are observed by the aircraft. Since rapid growth and deep mixed

layers were observed over wide areas of rain forest by the aircraft we conclude that vertical exchanges across the top of the mixed layer on the order of those calculated locally are occurring over the entire Amazon basin.

6. Conclusions

The observations of ABLE-2A provide an initial description of the structure and growth of the atmospheric mixed layer over an equatorial rain forest under "dry" season conditions. The dry season state depends on the subsidence intensity and is seen to vary both temporally and spatially across the region. Thus, while undisturbed conditions prevailed for much of the experiment, disturbed conditions coexisted but were spatially displaced. On occasion these perturbations did influence local measurements.

Radiative cooling of the forest canopy results in a marked surface inversion limiting mixing to a layer which is often within a few meters of the forest canopy. Stratified conditions develop very rapidly at or before sunset. Sensible heat fluxes are usually negative an hour before sunset and remain negative throughout the night. Mixed layer growth begins soon after sunrise as the surface sensible heat flux goes positive. Maximum rates of growth of up to 10 cm s^{-1} are reached within two hours of sunrise. The mixed layer under undisturbed conditions typically reaches 1000 m by 1000 LST, remaining above this altitude until 1600 LST. Thus, mean mixed layer growth rates lie between 5 and 8 cm s^{-1}. Maximum depth of the mixed layer is reached by 1300 LST and is observed to reach a maximum height of just below 1800 m.

Convective cloud outflows in the mixed layer interrupt mixed layer growth but regrowth in the wake of the cloud occurs at a rate comparable to growth rates in a cloud free atmosphere. When cumulus convection is present, mixed layer depth is generally limited to 1000 m or less, responding not only to near surface cloud outflows but to between cloud induced subsidence. Fossil mixed layers, which are mixed but no longer mixing, were detected to elevations of 2000 m at all hours of the day or night.

No horizontal discontinuities were noted in the mixed layer depth over distances of 300-400 km under undisturbed conditions. Growth rates and the general behavior of the mixed layer as determined locally were duplicated over a very large region of rain forest around Manaus. This would suggest that if the daytime evaporative fluxes measured locally (400 W m^{-2}) are typical of the region then entrainment fluxes at the top of the mixed layer are also typical (1000 W m^{-2}). Conditions over the rain forest can thus be contrasted with those over the open ocean where the evaporative flux is about 25% of the daytime forest flux and the mixed layer is one-half to one-third the depth but each persist for 24 h, while the forest counterpart operates for less than 12 hours. Thus the diurnal pulse is enormous over the rain forests but absent over the tropical oceans.

The model overpredicted the height of the mixed layer in the cases analyzed. We suggest that the observed mixed layer height is a result of between cloud subsidence. Absence of local clouds and the presence of large cloud complexes, 100 to 200 km from the observation site, lead us to believe that subsidence on the order of 2 cm s^{-1} is derived from

meso- to synoptic scale sinking affecting large areas around these pervasive cloud complexes.

A frequent drying during the day in the surface layer above the canopy in the face of substantial vapor flux (approx. 16 g s^{-1} m^{-2}) suggests a large entrainment flux across the top of the mixed layer. Estimates of the entrainment flux based upon observations of the depth of the mixed layer, the surface fluxes and an estimate of the mixed layer specific humidity agree with model estimates of the entrainment flux. Latent heat fluxes across the top of the mixed layer reach 1000 W m^{-2}.

We conclude that if the difference between the concentrations in the mixed layer and above the mixed layer is large enough, entrainment fluxes across the top of the mixed layer will dominate the balance in the mixed layer even in the presence of large surface layer fluxes. This conclusion implies that any estimate of the fluxes across the top of the mixed layer will depend critically upon knowledge of the growth and depth of the mixed layer.

Fluxes of water vapor across the canopy under undisturbed conditions appear to be relatively well behaved. Thus, estimates of water vapor fluxes across the mixed layer top will depend primarily upon knowledge of the mixed layer depth and the profile of the water vapor. The UV-DIAL aerosol measurements supply estimates of the depth of the mixed layer. Concurrent measurement of the water vapor profile would provide an estimate of the vapor flux across the top of the mixed layer. Such measurements could be made over large areas under undisturbed conditions.

The ABLE-2A findings suggest that we can now make reliable estimates of water vapor and sensible heat fluxes over wide areas of the Amazon basin under undisturbed conditions. These estimates can be made with the greatest certainty for those times and places where the aircraft measurements were made. Greater uncertainties would appear if these estimates were applied to the fair weather regions of the basin as a whole. We believe, however, that this would represent a substantial improvement in our current knowledge of boundary layer structure and process over this important region. Extending these findings to encompass the disturbed conditions of the wet season is the next major task.

Acknowledgments

The work presented in this paper was funded by grants awarded by NASA to Simpson Weather Associates, the University of Virginia, and the Atmospheric Sciences Research Center. Manuscript preparation was performed by Mary Morris and Karen Emmitt. Data processing was provided by Jay Boisseau, and drafting and proofing by Debby Martin. Data from the automatic weather station were processed by researchers at the Institute of Hydrology, United Kingdom, and provided by G. Fisch at the National Institute for Amazon Studies (INPA), Manaus. A. P. Oliveira acknowledges support from the Fundação de Amparo a Pesquisa do Estado de São Paulo (FAPESP), Processo 86/1263-6, for graduate studies at the State University of New York, Albany.

The authors wish to express their deep appreciation for all of the above mentioned assistance, and to each of the participants in ABLE-2A, all of whom contributed to the success of the experiment.

REFERENCES

Augstein, E., M. Garstang, and G. D. Emmitt, Vertical mass and energy transports by cumulus clouds in the tropics, Deep Sea Res., Spec. Vol., 9-21, 1980.

Betts, A. K., Non-precipitating cumulus convection and its parameterization, Quart. J. Roy. Meteor. Soc., 99, 178-196, 1973.

Betts, A. K., The thermodynamic transformation of the tropical subcloud layer by precipitation and downdrafts, J. Atmos. Sci., 33, 1008-1020, 1976.

Browell, E. V., G. L. Gregory, R. C. Harriss, and V. W. J. Kirchhoff, Tropospheric O_3 and aerosol distributions across the Amazon basin, to be published J. Geophys. Res., 1987.

Caughey, S. J., Observed characteristics of the atmospheric boundary layer, in Atmospheric Turbulence and Air Pollution Modelling, edited by F. T. M. Nieuwstadt and H. van Dop, pp. 107-138. D. Reidel, Hingham, Mass., 1982.

Driedonks, A. G. M., Models and observations of the growth of the boundary layer, Bound.-Layer Meteor., 23, 283-306, 1982.

Emmitt, G. D., Tropical cumulus interaction with and modification of the subcloud layer, J. Atmos. Sci., 35, 1485-1502, 1978.

Fishman, J., P. Minnis, and H. G. Reichle, Jr., Use of satellite data to study tropospheric ozone in the tropics, J. Geophys. Res., 91, 14451-14465, 1986.

Fitzjarrald, D. R. and M. Garstang, Vertical structure of the tropical boundary layer, Mon. Wea. Rev., 109, 1512-1526, 1981a.

Fitzjarrald, D. R. and M. Garstang, Boundary-layer growth over the tropical ocean, Mon. Wea. Rev., 109, 1762-1772, 1981b.

Fitzjarrald, D. R. and D. H. Lenschow, Mean concentration and flux profiles for chemically reactive species in the atmospheric surface layer, Atmos. Environ, 17, 2505-2512, 1983.

Fitzjarrald, D. R., B. L. Stormwind, G. Fisch, and D. M. R. Cabral, Turbulent transport observed just above the Amazon forest, to be published J. Geophys. Res., 1987.

Garstang, M., J. Scala, S. Greco, R. Harriss, S. Beck, E. Browell, G. Sachse, G. Gregory, G. Hill, J. Simpson, W.-K. Tao, and A. Torres, Trace gas exchanges and convective transports over the Amazonian rain forest, to be published J. Geophys. Res., 1987.

Harriss, R. C., S. C. Wofsy, M. Garstang, L. C. B. Molion, R. S. McNeal, J. M. Hoell, R. J. Bendura, S. M. Beck, R. L. Navarro, J. T. Riley, and R. C. Shell, The Amazon Boundary Layer Experiment, to be published J. Geophys. Res., 1987.

Johnson, R. H., Effects of cumulus convection on the structure and growth of the mixed layer over south Florida, Mon. Wea. Rev., 105, 713-724, 1977.

Lenschow, D. H., R. Pearson, Jr., and B. B. Stankor, Measurements of ozone vertical flux to ocean and forest, J. Geophys. Res., 87, 8833-8837, 1982.

Logan, J. A., and V. W. J. H. Kirchhoff, Seasonal variations of tropospheric ozone at Natal, Brazil, J. Geophys. Res., 91, 7875-7882, 1986.

National Academy of Sciences, Global Tropospheric Chemistry, National Academy Press, Washington, D.C., 194 pp, 1984.

Nieuwstadt, F. T. M. and R. A. Brost, The decay of convective turbulence, J. Atmos. Sci., 43, 532-546, 1986.

Rasmusson, E. M. and T. H. Carpenter, Variations in tropical sea surface temperature and surface wind fields associated with the Southern Oscillation/El Niño, Mon. Wea. Rev., 110, 354-384, 1982.

Reinsch, C. H., Smoothing by spline functions, Numerishe Mathe., 10, 177-183, 1976.

Riehl, H., and J. S. Simpson, The balance of the equatorial trough zone, revisited, Contrib. Atmos. Phys. Beit. Physik Atmos., 52, 287-304, 1979.

Shuttleworth, W. J., J. H. C. Gash, C. R. Lloyd, C. J. Moore, J. Roberts, A. DeO. M. Filho, G. Fisch, V. DeP. S. Filho, M. DeN. G. Ribeiro, L. C. B. Molion, L. D. DeA. Sa, J. C. A. Nobre, O. M. R. Cabral, S. R. Patel, J. C. DeMoraes, Eddy correlation measurements of energy partition for Amazonian forest, Quart. J. Roy. Meteor. Soc., 110, 1143-1162, 1984.

Silva Dias, P. L., W. H. Schubert, and M. DeMaria, Large-scale response of the tropical atmosphere to transient convection, J. Atmos. Sci., 40, 2689-2707, 1987.

Tennekes, H., A model for the dynamics of the inversion above a convective boundary layer, J. Atmos. Sci., 30, 558-567, 1973.

van Loon, H., The Southern Oscillation. Part III: Associations with the trades and with the trough in the westerlies of the South Pacific Ocean, Mon. Wea. Rev., 112, 947-954, 1984.

Wylie, D. P., and C. F. Ropelewski, The GATE Boundary Layer Instrumentation System (BLIS), Bull. Amer. Meteor. Soc., 61, 1002-1011, 1980.

Authors' Address List

Charles L. Martin
Simpson Weather Associates, Inc.
809 E. Jefferson Street
Charlottesville, VA 22902

David Fitzjarrald and Amauri P. Oliveira
Atmospheric Sciences Research Center
State University of New York
100 Fuller Road
Albany, NY 12205

Michael Garstang and Steve Greco
Department of Environmental Sciences
University of Virginia
Charlottesville, VA 22903

Edward Browell
NASA/Langley Research Center
Hampton, VA 23665

FIGURE CAPTIONS

Fig. 1. Location of the ABLE-2A experiment. Ground based measurements were made at Reserva Ducke, shown in inset box. The 100 m ground elevation contour and stream courses are given for the area southeast of highway AM10. Flight track for Mission 5 is shown south of Manaus ·—·.

Fig. 2. Infrared GOES image at 1800 Z, July 31, 1985 showing the large clear region of the subtropical anticyclone over northeastern Brazil and the characteristic cloud complexes to the northwest, west and southwest of Manaus (3^{o}S, 60^{o}W, see Figure 2)

Fig. 3. Tethered balloon profiles made on July 25, 1985. (a) 0745 LST. (b) 1202 LST. (c) 1316 LST. (d) 1345 LST. (e) 1630 LST. (f) 1643 LST.

Fig. 4. Data from July 25. The upper plot shows contours of virtual potential temperature, θ_v, as measured by the tethered balloon. Observed mixed layer heights are marked with + from the tethered balloon and • from the rawin sounding. The lower three graphs show time series of the buoyancy flux $\overline{w'\theta'}$, temperature T, moisture flux $\overline{w'q'}$, specific humidity q, incoming solar radiation flux R_s, net radiation flux R_n and rainfall, all measured at the micrometeorological tower. $\overline{w'\theta'}$ and $\overline{w'q'}$ were measured at the 40 m level; the other parameters were measured at the 45 m level. SR and SS are approximate sunrise and sunset.

Fig. 5. Application of the jump model for July 25. Simulated mixed layer heights H_1 and H_2 are shown in (a) with corresponding profiles of θ_v measured by the tethered balloon. Ascending and descending tethered balloon profiles are marked A and D respectively. Values of $\theta_{v,m}$, $\theta_{v,h}$, $q_{v,m}$ and $q_{v,h}$ for the H_1 simulation are shown with the corresponding

observations from the tethered balloon are shown in (b) and (c) respectively.

Fig. 6. Photographs taken from the micrometeorological tower. (a) Taken at 0937, July 25, showing convective activity early in the day. (b) Taken at 1430, July 31, and is typical of the fair weather conditions which prevailed on that day.

Fig. 7. Tethered balloon profiles made on July 31. (a) 0414 LST. (b) 0656 LST. (c) 0729 LST. (d) 0846 LST. (e) 0948 LST. (f) 1158 LST.

Fig. 8. As in Figure 4, for July 31.

Fig. 9. Application of the jump model for July 31. Three different boundary conditions were prescribed: a) $\Gamma\theta_v = .0011^{\circ}K/m$, $w_h = 0$ (——), b) $\Gamma\theta_v = .0022^{\circ}K/m$, $w_h = 0$ (---), and c) $\Gamma\theta_v = .0012^{\circ}K/m$, $w_h = -0.02$ m/s (. . .). Predicted mixed layer height h, $\theta_{v,m}$ and q_m are shown, along with the corresponding values measured by the tethered balloon.

Fig. 10. Model derived moisture entrainment flux and the observed moisture entrainment flux calculated from measured values of h, q and F_{qo}. The lower graph shows the observed values of h, q and Fq_o (= w'q').

Fig. 11. As in Figure 4, but for July 26, July 27, August 2 and August 5.

Fig. 12. As in Figure 4, but averaged over 24 hours, for data between July 21 and August 5. Individual mixed layer heights are denoted by +, or * when the mixed layer extended above the top of the tethered balloon profile.

Fig. 13. Tethered balloon determinations of mixed layer heights. (a) Disturbed days. (b) Undisturbed days. All occasions on which the

height of the mixed layer was above the sampling height of the tethered balloon (1100 m) are indicated by X at 1200 m.

Fig. 14. Comparison of radiosonde (H_R) and tethered balloon (H_T) determinations of mixed layer height. (a) Disturbed days. (b) Undisturbed days.

Fig. 15. Comparison of aircraft (H_A) and UV-DIAL (H_U) determinations of mixed layer height.

Fig. 16. Comparison of tethered balloon (H_T, ●), radiosonde (H_R, ▲), and UV-DIAL (H_U) determination of mixed layer heights.

Fig. 17. Mixed layer heights determined by radiosonde for all days. Explicit mixed layer heights as defined in text are shown as X, previous day or fossil mixed layer tops are shown as O.

Fig. 18. Mixed layer height as determined by the aircraft (H_A). (a) All days. (b) Undisturbed days. (c) Disturbed days.

Fig. 19. Mixed layer heights as determined from the UV-DIAL (H_U) on undisturbed days only.

Fig. 20. UV-DIAL measurements made during undisturbed conditions on July 21. Time (GMT) appears above the color trace. The color bars above the time provide a key to UV-DIAL values. Latitude and longitude are shown below the color trace. (a) 1316-1346 Z. (b) 1541-1605 Z. (c) 1600-1623 Z.

TABLE 1. Tethersonde Sensor Characteristics

Measurand	Transducer	Range	Precision
wind speed	cup anemometer	0 to 20 m/s	+/-0.2 m/s
wind direction	magnetic compass	0 to 360°	+/-5°
dry bulb temperature	thermistor	-80 to 50°C	+/-0.2°C
wet bulb temperature	thermistor	-80 to 50°C	+/-0.2°C
dry and wet bulb match		-20 to 35°C	+/-0.1°C
pressure	aneroid	600 to 1050 mb	+/- 1.0 mb

Sample rate: 10 seconds

TABLE 2. Radiosonde Sensor Specifications.

Measurand	Transducer	Range	Precision
dry bulb temperature	thermistor	-70°C to 50°C	0.5°C for -40°C to 40°C
humidity	carbon hygristor	10% to 100% RH	5% RH for -40°C to 40°C
pressure	aneroid	1050 mb to 250 mb	3 mb

Sample rate: 5 seconds

TABLE 3. Summary of the Data Set. Y = observations; N = no observations

Date	Tethered Balloon Night Operations	Tethered Balloon Profiles	Ducke Rawin Soundings	Aircraft Flight	Tower Flux Measurements	Tower Weather Station
Jul 15		13	3		N	Y
Jul 16		18	4		N	Y
Jul 17		13	4		N	Y
Jul 18		14	4	Day	N	Y
Jul 19		21	4	Day	N	Y
Jul 20		7	4		N	Y
Jul 21		15	4	Day	N	Y
Jul 22		22	4		Y	Y
Jul 23		13	4	Day	Y	Y
Jul 24		15	3	Day	Y	Y
Jul 25	Y	20	6		Y	Y
Jul 26	Y	24	8	Night	Y	Y
Jul 27		21	6	Night	Y	Y
Jul 28					Y	Y
Jul 29		12	3		Y	Y
Jul 30	Y	9	2	Day	Y	Y
Jul 31	Y	49	9	Day	Y	Y
Aug 01	Y	20	8		Y	Y
Aug 02	Y	44	8	Day	Y	Y
Aug 03		30	5	Day	Y	Y
Aug 04		24	4		Y	Y
Aug 05		27	2	Day	Y	Y

TABLE 4. Characteristic mixing times $t = h/w^*$, where w^* is the mixing velocity and h is the mixed layer depth. The reference temperature θ_{vo} is taken to be 300°K. w^* is given by:

$$w^* = \left(\frac{g\ \overline{w'\theta_v'}\ h}{\theta_{vo}}\right)^{1/3}$$

Date	Time (LST)	h(m)	$\overline{w'\theta'_v}$ (w m^{-2})	w^* (m s^{-1})	t (min)
July 25	0951	650	100	1.19	9.1
July 25	1215	840	100	1.30	10.7
July 25	1325	440	180	1.27	5.8
July 31	0856	430	60	0.88	8.1
July 31	1045	1090	120	1.50	12.1
July 31	1544	1890	80	1.23	12.1

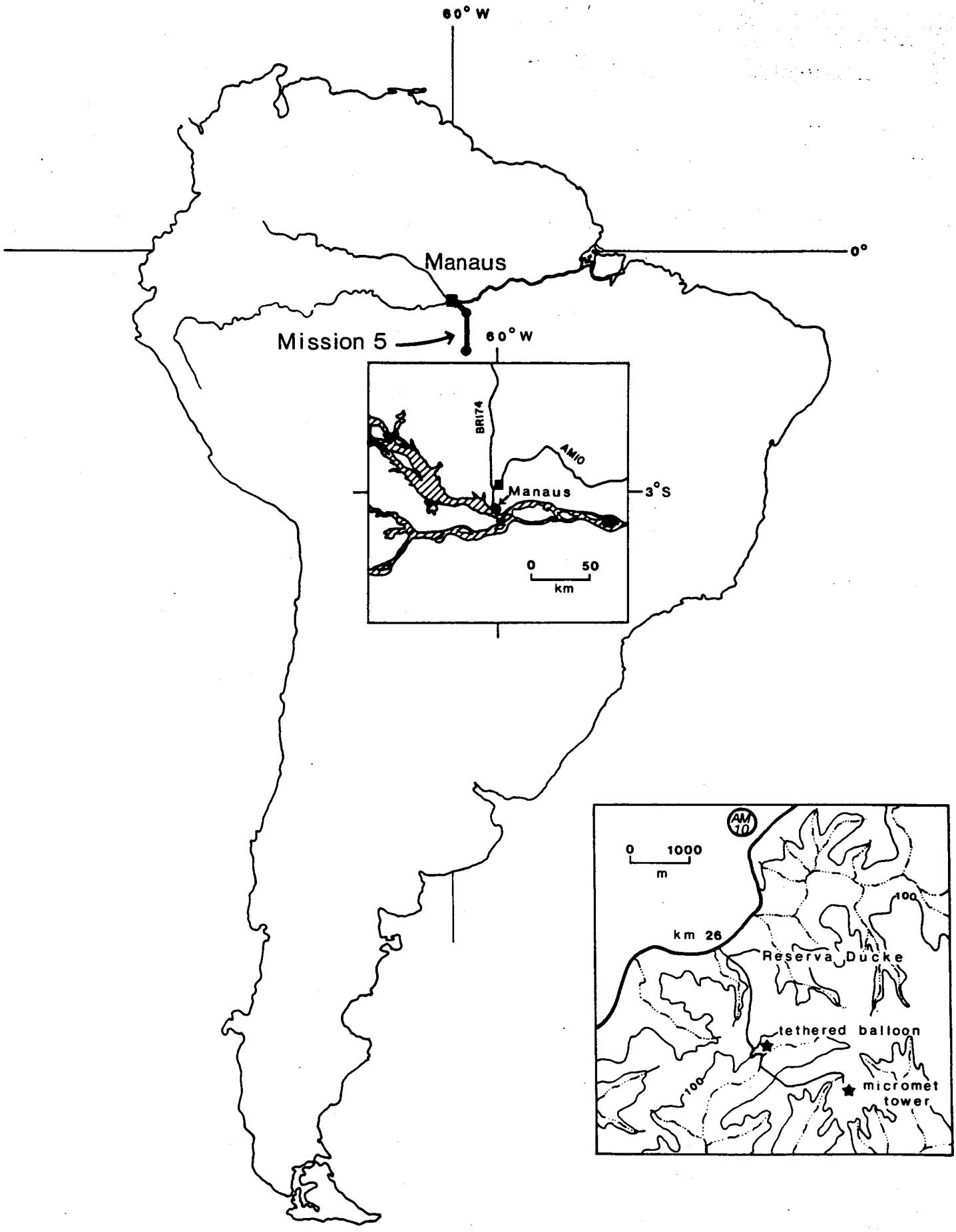
60° W
0°
Manaus
Mission 5
60° W
BR174
AM10
Manaus
3°S
0
50
km
AM 10
0
1000
m
100
km 26
Reserva Ducke
tethered balloon
100
micromet
tower

Fig 1

Fig 2

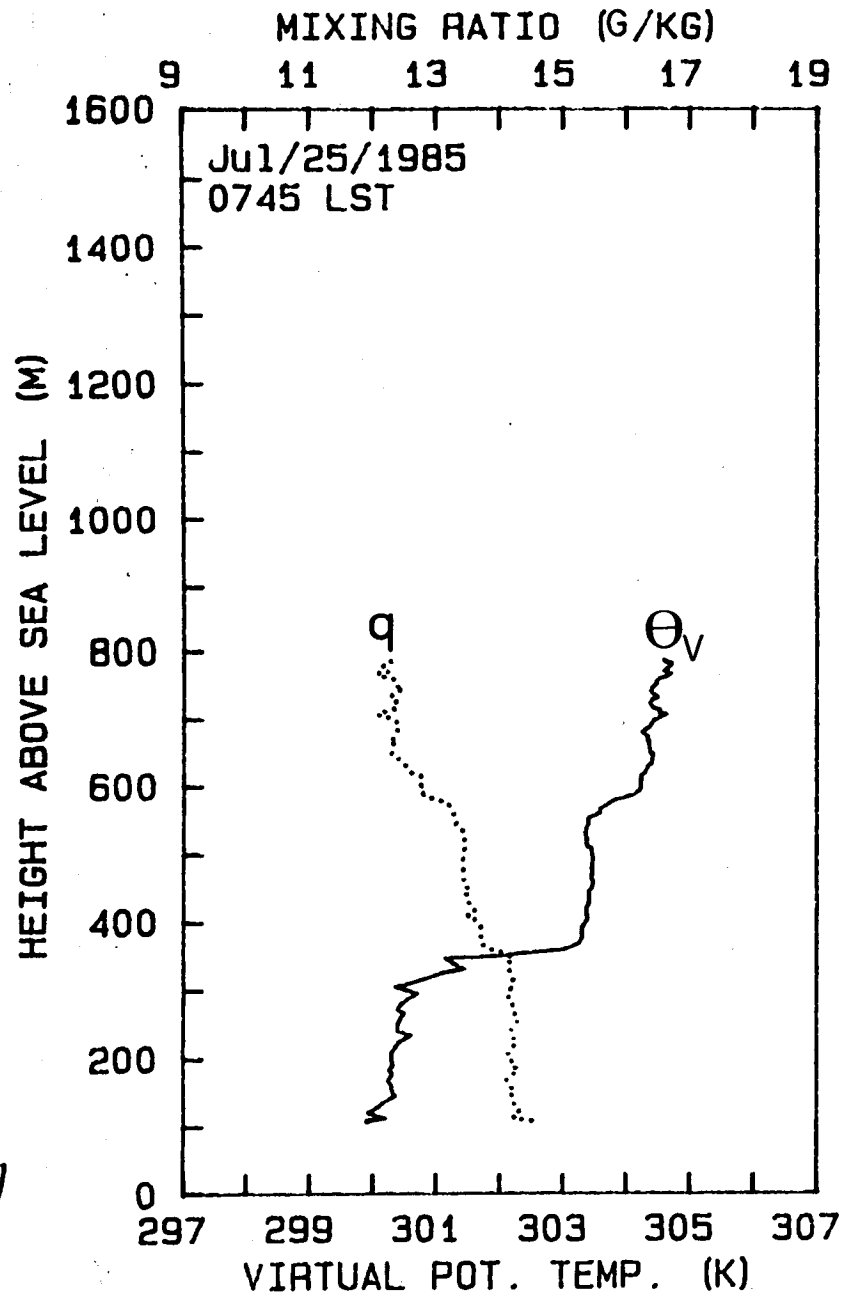
MIXING RATIO (G/KG)
9
11
13
15
17
19
Jul/25/1985
0745 LST
q
Θ_V
HEIGHT ABOVE SEA LEVEL (M)
1600
1400
1200
1000
800
600
400
200
0
297
299
301
303
305
307
VIRTUAL POT. TEMP. (K)

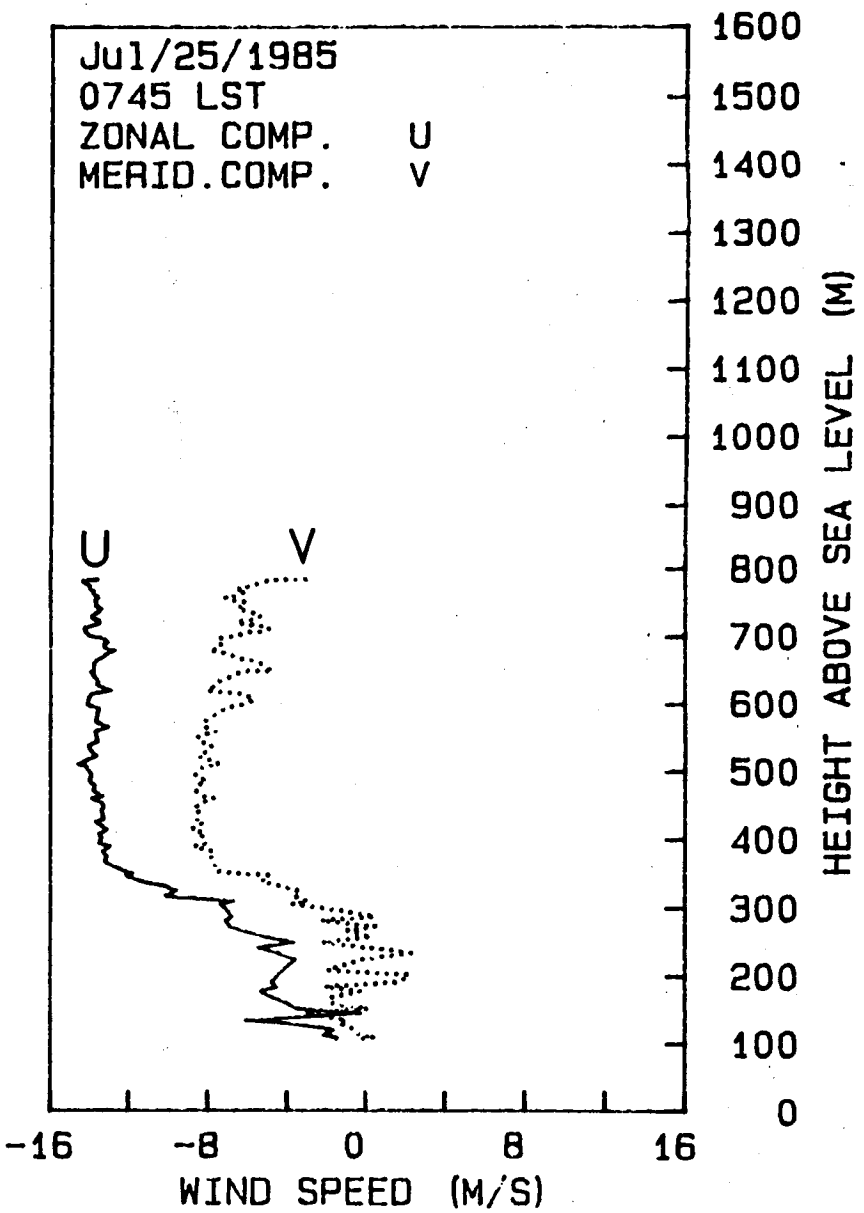
Jul/25/1985
0745 LST
ZONAL COMP. U
MERID.COMP. V
U
V
1600
1500
1400
1300
1200
1100
1000
900
800
700
600
500
400
300
200
100
0
HEIGHT ABOVE SEA LEVEL (M)
-16
-8
0
8
16
WIND SPEED (M/S)

Fig 3a

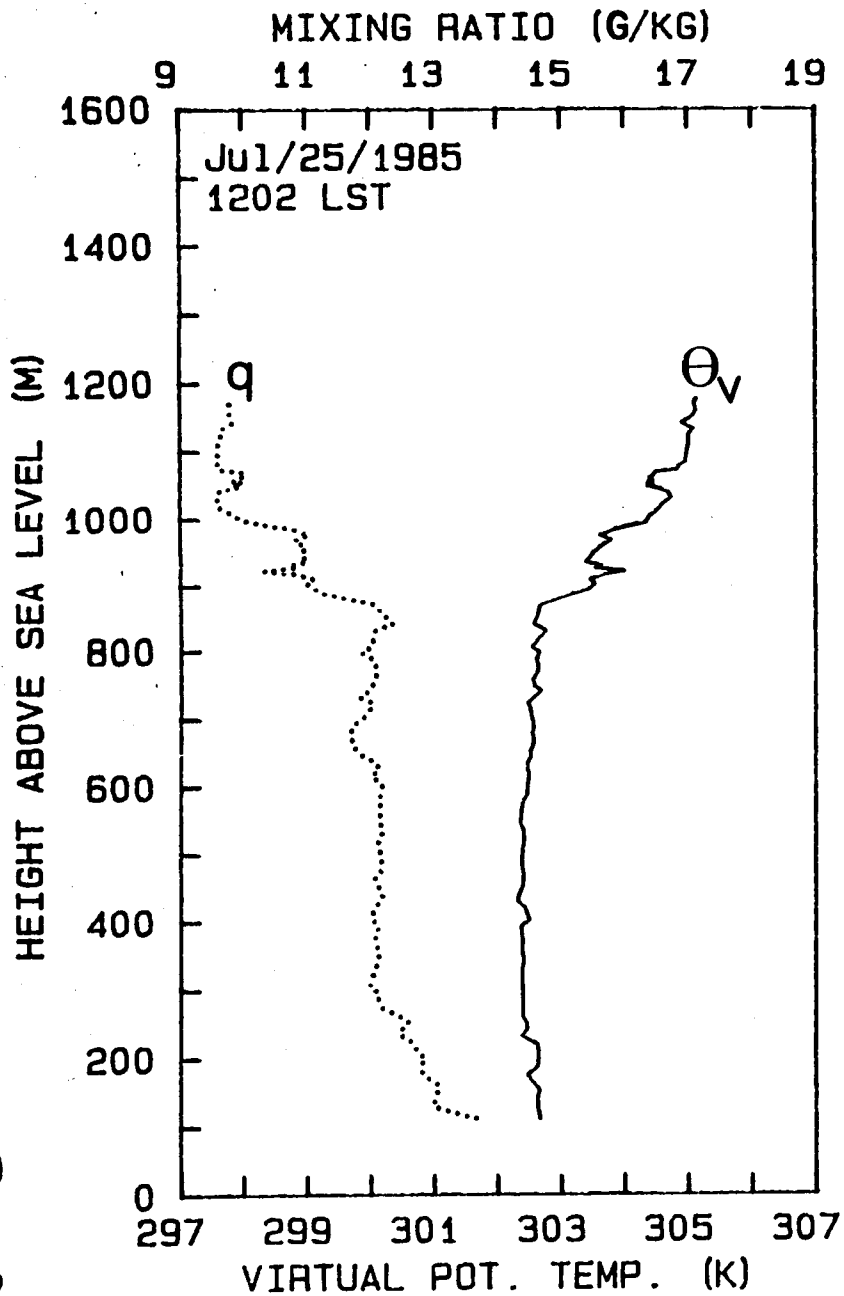
MIXING RATIO (G/KG)
9
11
13
15
17
19
Jul/25/1985
1202 LST
q
θ_v
HEIGHT ABOVE SEA LEVEL (M)
1600
1400
1200
1000
800
600
400
200
0
297
299
301
303
305
307
VIRTUAL POT. TEMP. (K)

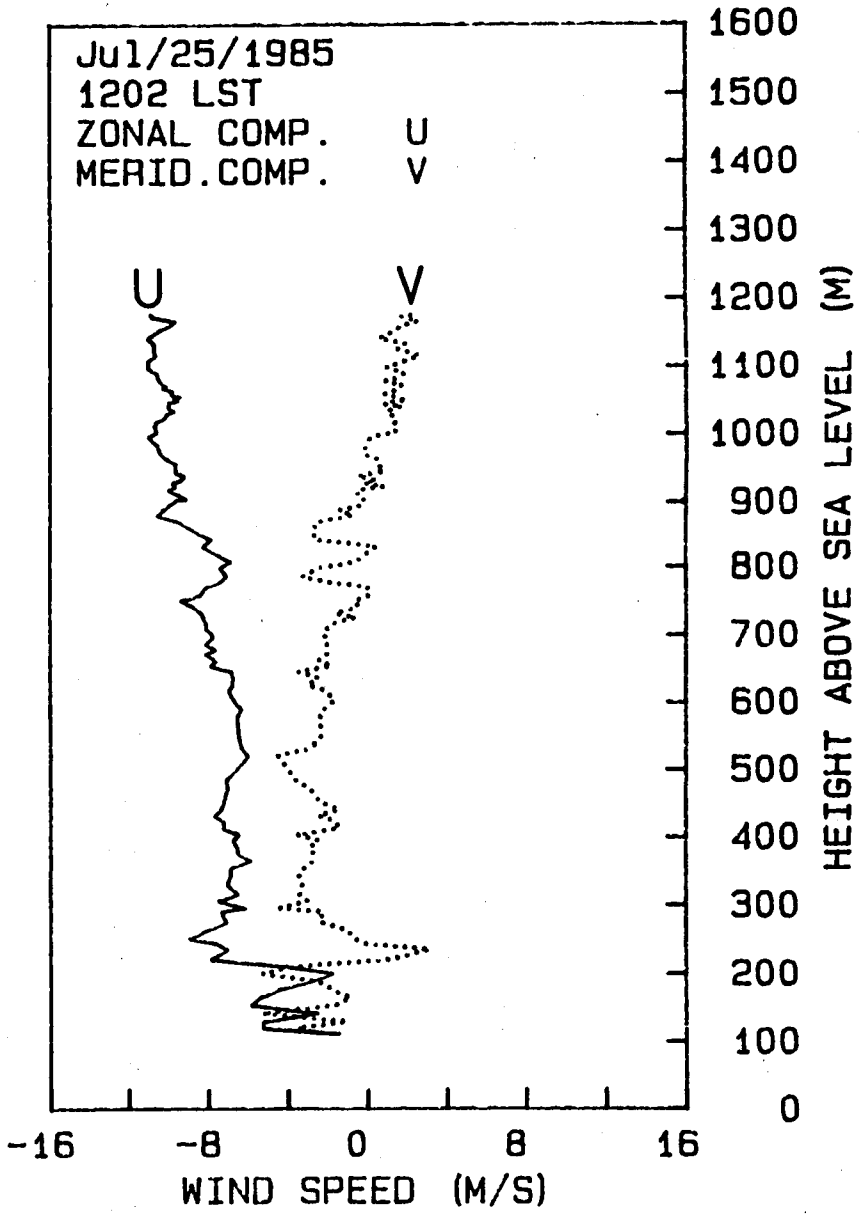
Jul/25/1985
1202 LST
ZONAL COMP. U
MERID.COMP. V
U
V
1600
1500
1400
1300
1200
1100
1000
900
800
700
600
500
400
300
200
100
0
HEIGHT ABOVE SEA LEVEL (M)
-16
-8
0
8
16
WIND SPEED (M/S)

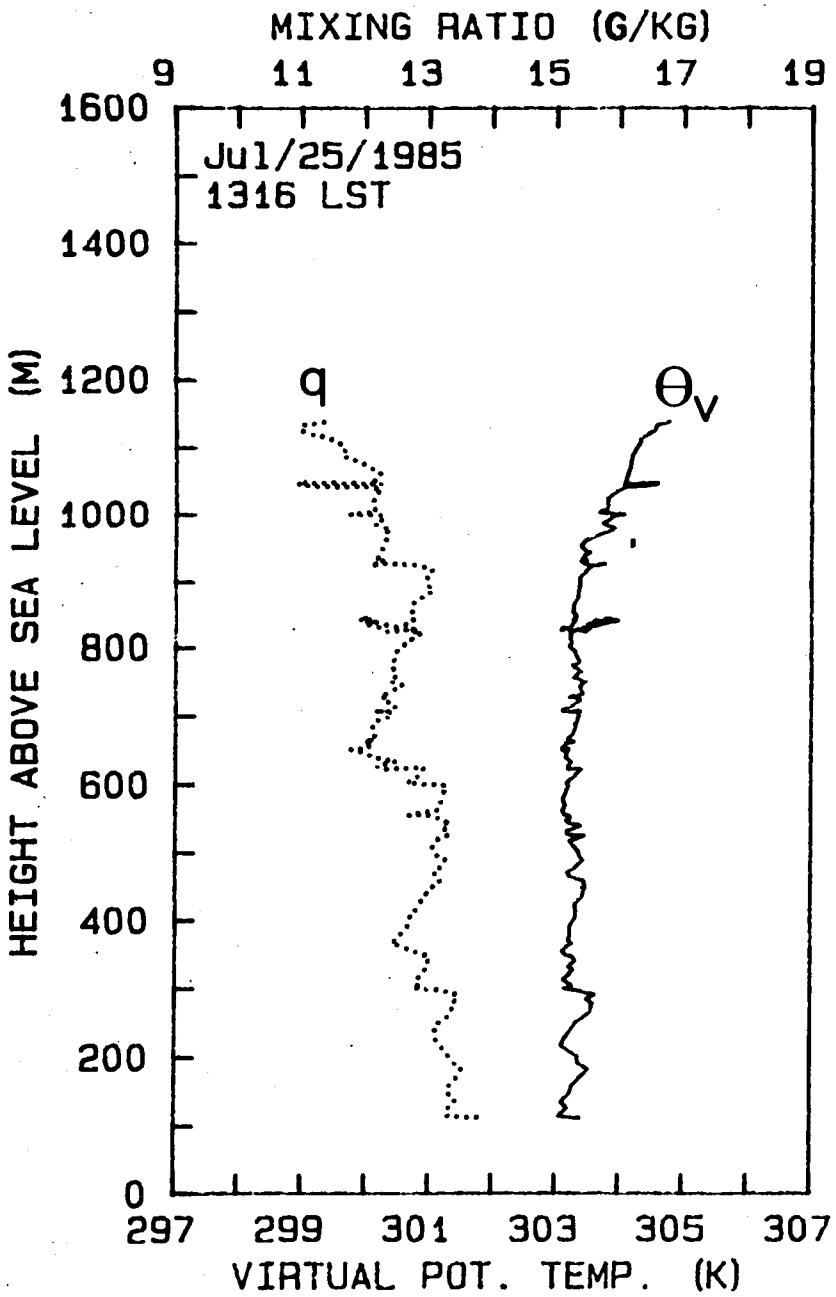
MIXING RATIO (G/KG)
9
11
13
15
17
19
Jul/25/1985
1316 LST
q
θ_v
HEIGHT ABOVE SEA LEVEL (M)
1600
1400
1200
1000
800
600
400
200
0
297
299
301
303
305
307
VIRTUAL POT. TEMP. (K)

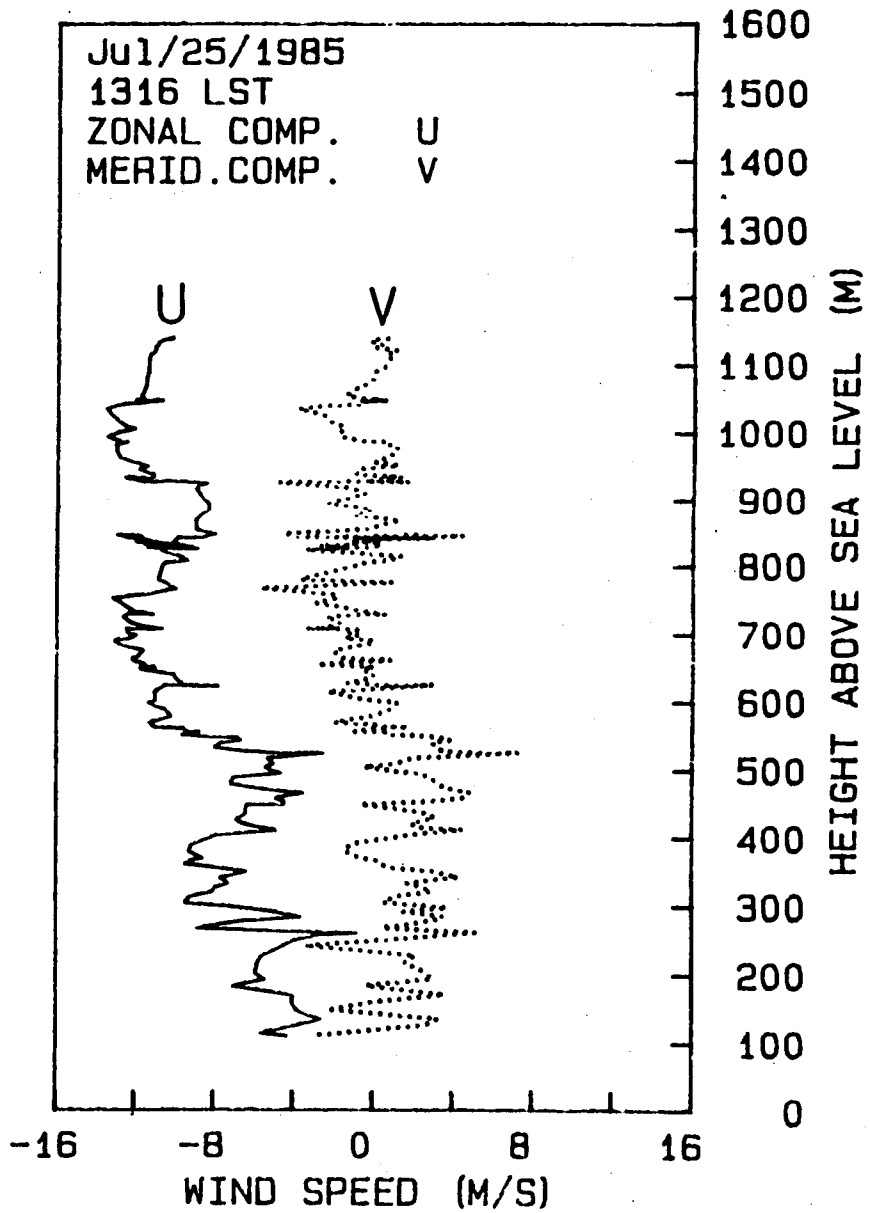
Jul/25/1985
1316 LST
ZONAL COMP. U
MERID.COMP. V
U
V
1600
1500
1400
1300
1200
1100
1000
900
800
700
600
500
400
300
200
100
0
HEIGHT ABOVE SEA LEVEL (M)
-16
-8
0
8
16
WIND SPEED (M/S)

Fig. 3c

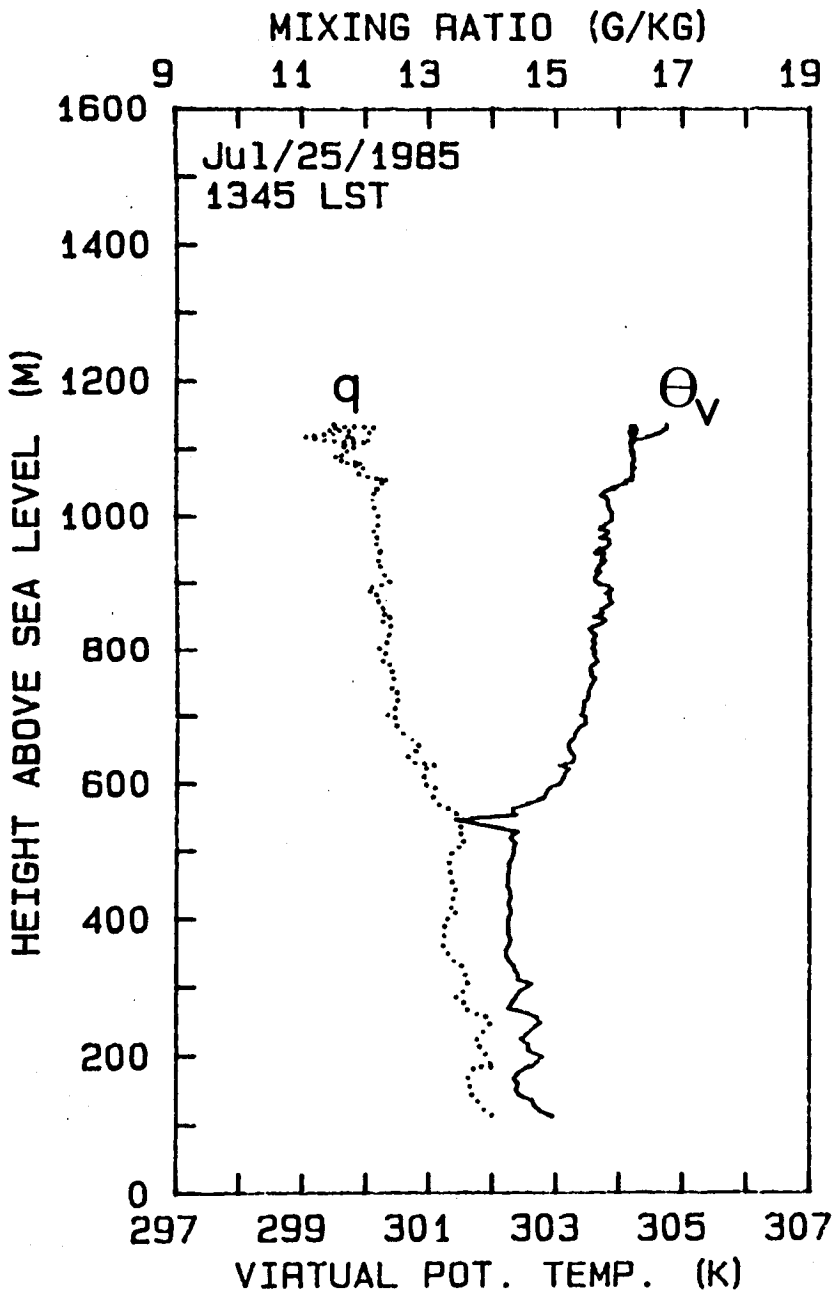
MIXING RATIO (G/KG)
9
11
13
15
17
19
Jul/25/1985
1345 LST
q
θ_v
HEIGHT ABOVE SEA LEVEL (M)
1600
1400
1200
1000
800
600
400
200
0
297
299
301
303
305
307
VIRTUAL POT. TEMP. (K)

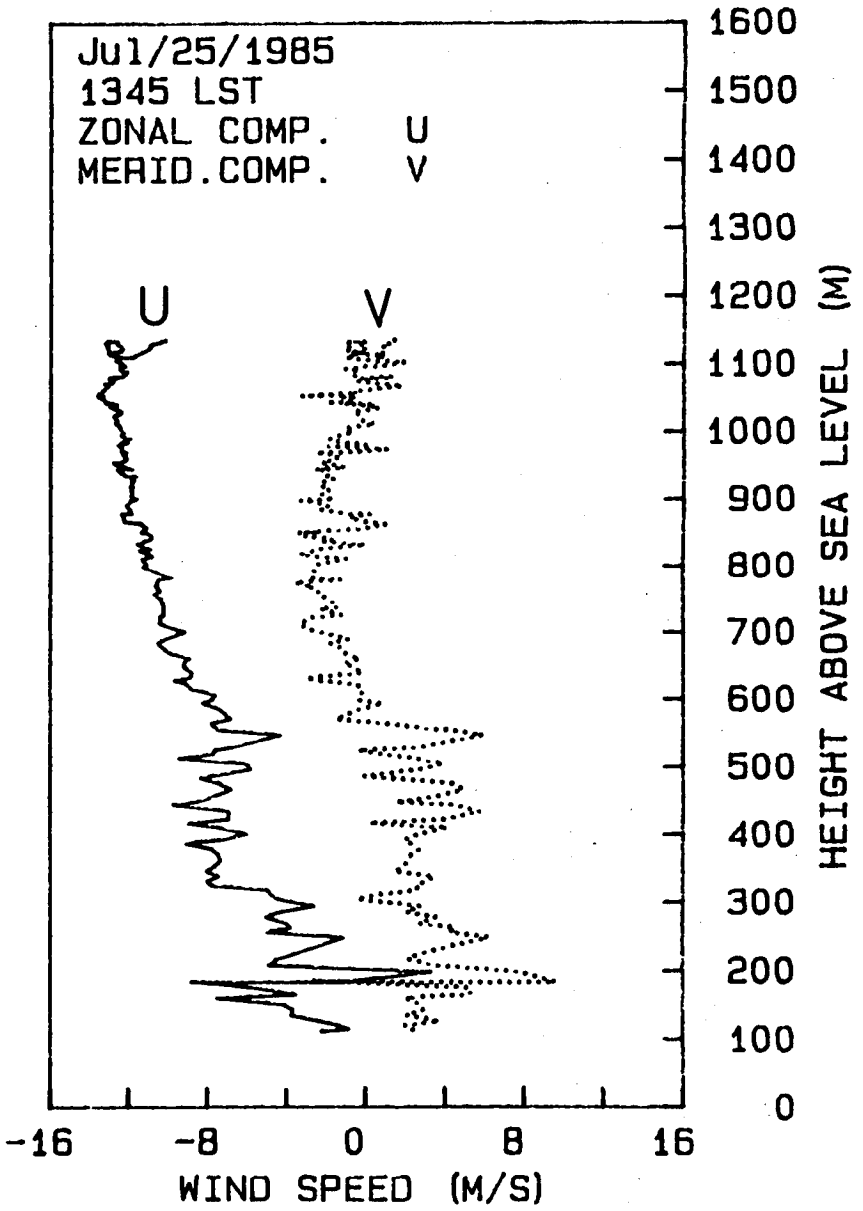
Jul/25/1985
1345 LST
ZONAL COMP. U
MERID.COMP. V
U
V
1600
1500
1400
1300
1200
1100
1000
900
800
700
600
500
400
300
200
100
0
HEIGHT ABOVE SEA LEVEL (M)
-16
-8
0
8
16
WIND SPEED (M/S)

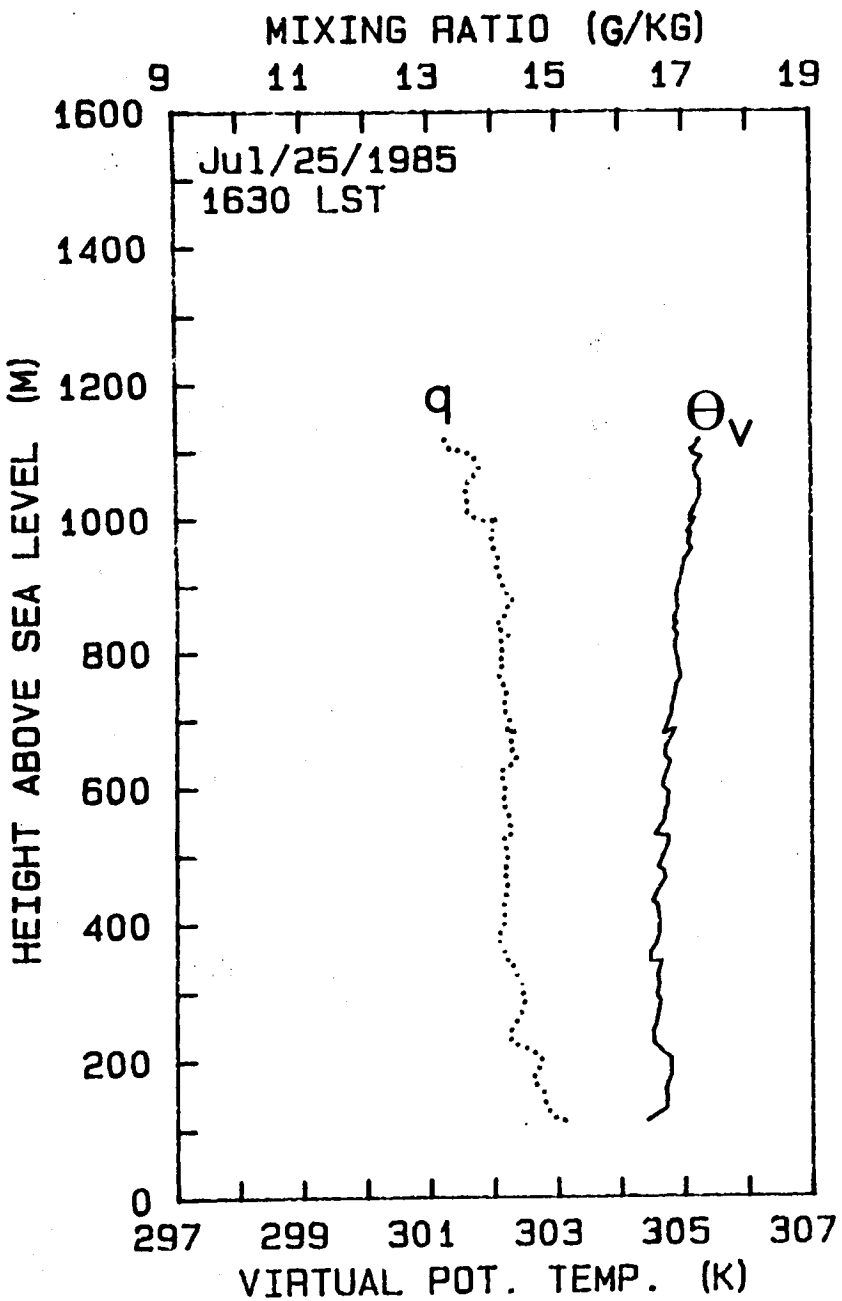
MIXING RATIO (G/KG)
9
11
13
15
17
19
Jul/25/1985
1630 LST
q
θ_v
HEIGHT ABOVE SEA LEVEL (M)
0
200
400
600
800
1000
1200
1400
1600
297
299
301
303
305
307
VIRTUAL POT. TEMP. (K)

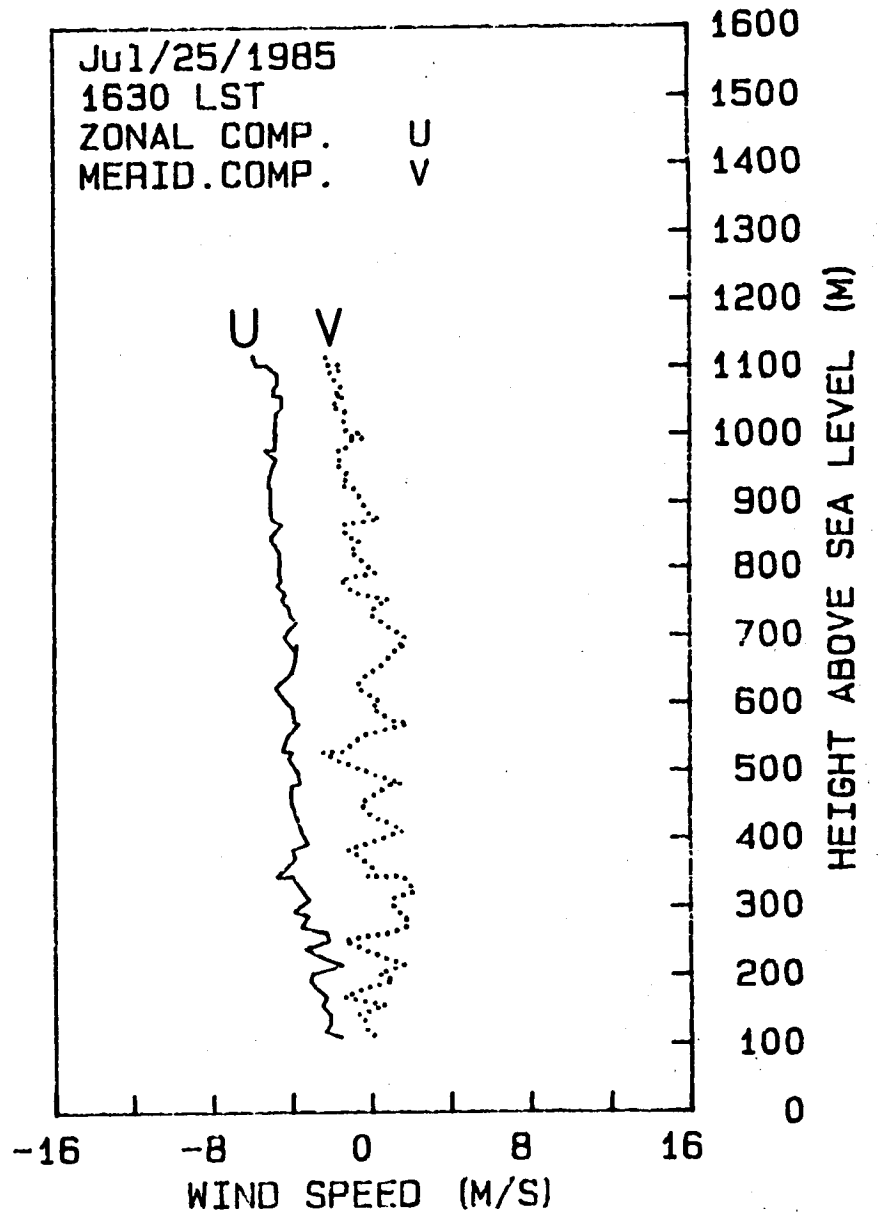
Jul/25/1985
1630 LST
ZONAL COMP. U
MERID.COMP. V
U
V
HEIGHT ABOVE SEA LEVEL (M)
0
100
200
300
400
500
600
700
800
900
1000
1100
1200
1300
1400
1500
1600
-16
-8
0
8
16
WIND SPEED (M/S)

Fig. 3e

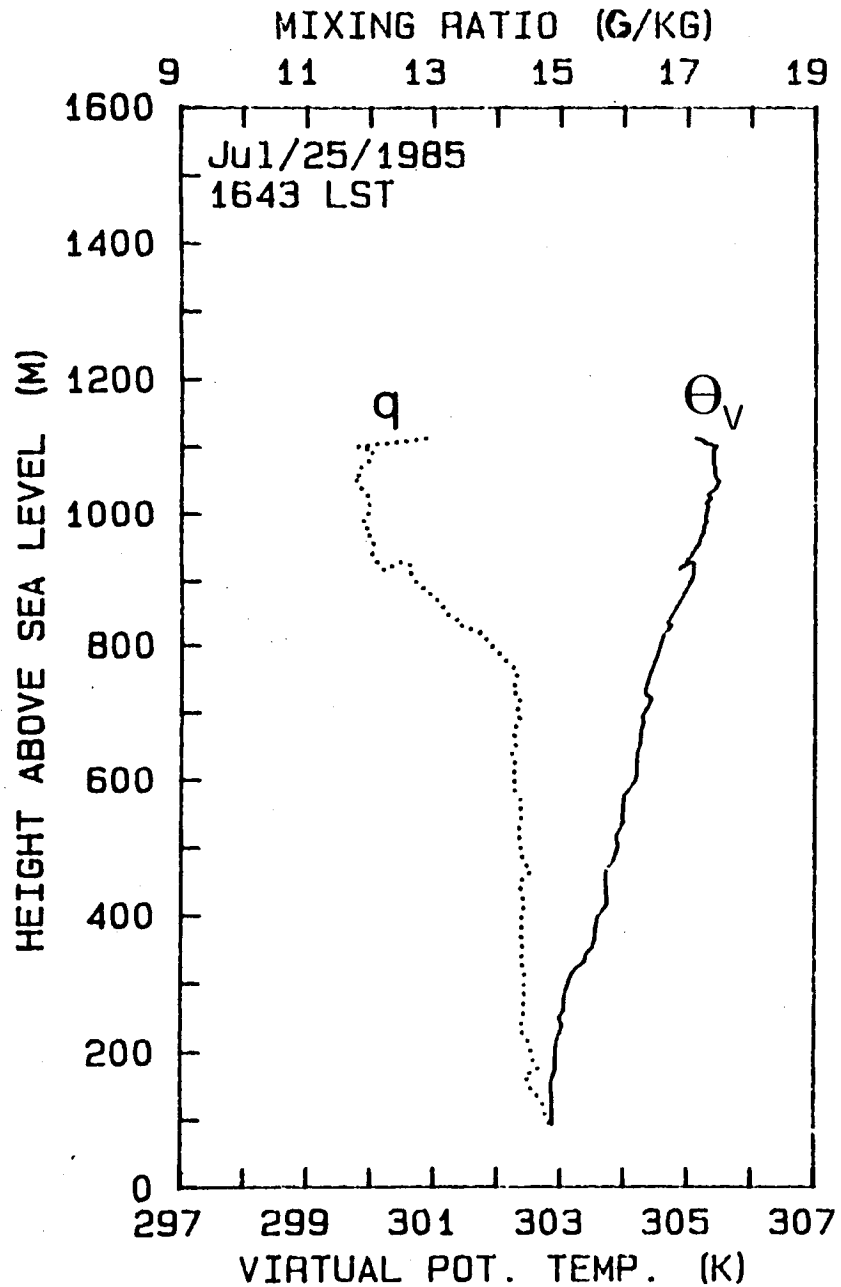
MIXING RATIO (G/KG)
9
11
13
15
17
19
Jul/25/1985
1643 LST
q
Θ_V
HEIGHT ABOVE SEA LEVEL (M)
1600
1400
1200
1000
800
600
400
200
0
297
299
301
303
305
307
VIRTUAL POT. TEMP. (K)

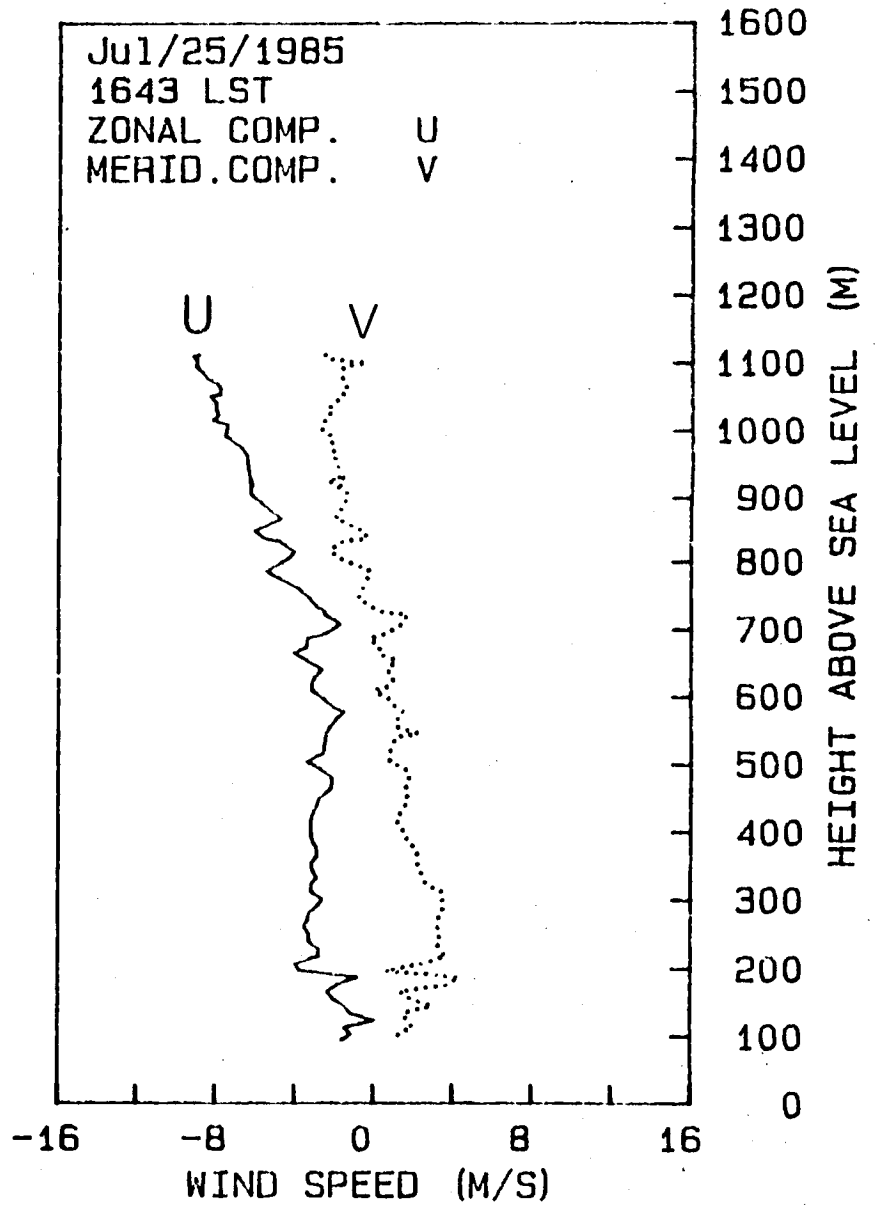
Jul/25/1985
1643 LST
ZONAL COMP. U
MERID.COMP. V
U
V
1600
1500
1400
1300
1200
1100
1000
900
800
700
600
500
400
300
200
100
0
HEIGHT ABOVE SEA LEVEL (M)
-16
-8
0
8
16
WIND SPEED (M/S)

Fig 3f

HEIGHT ABOVE SEA LEVEL (M)
1300
1200
1100
1000
900
800
700
600
500
400
300
200
100
25/07/85
θ_v(°K)
303.0
304.0
303.0
T (°C)
26
24
q (g/kg)
17
15
RAIN (mm)
1
0
T
q
R_s
R_n
$\overline{w't'}$
$\overline{w'q'}$
SR
SS
TIME (LST)
R_s & R_n (w/m²)
600
300
0
$\overline{w'q'}$ (w/m²)
400
200
0
$\overline{w't'}$ (w/m²)
200
0

Fig. 4

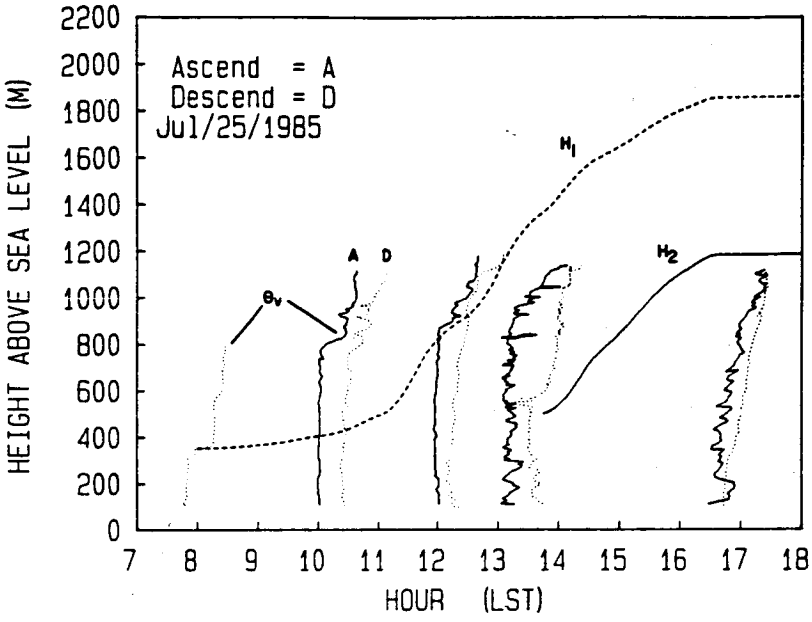
Ascend = A
Descend = D
Jul/25/1985
HEIGHT ABOVE SEA LEVEL (M)
HOUR (LST)
H_1
H_2
θ_v
A
D

(a)

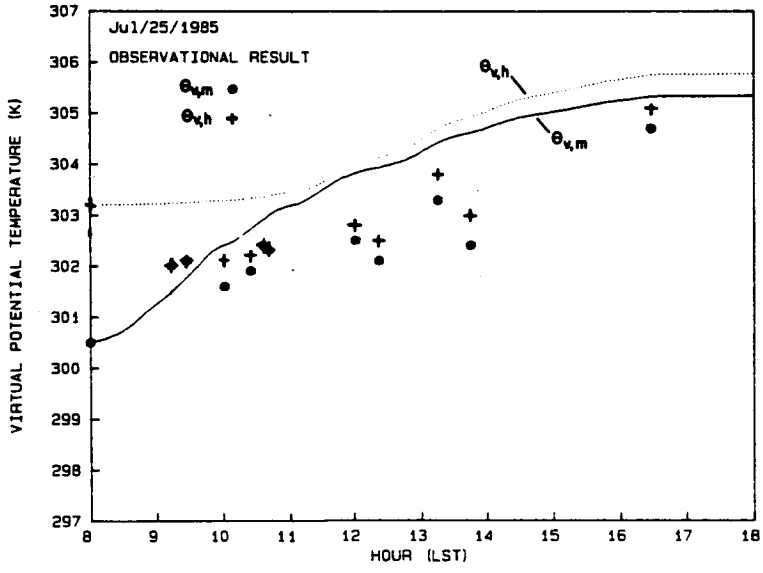
Jul/25/1985
OBSERVATIONAL RESULT
$\theta_{v,m}$
$\theta_{v,h}$
VIRTUAL POTENTIAL TEMPERATURE (K)
HOUR (LST)

(b)

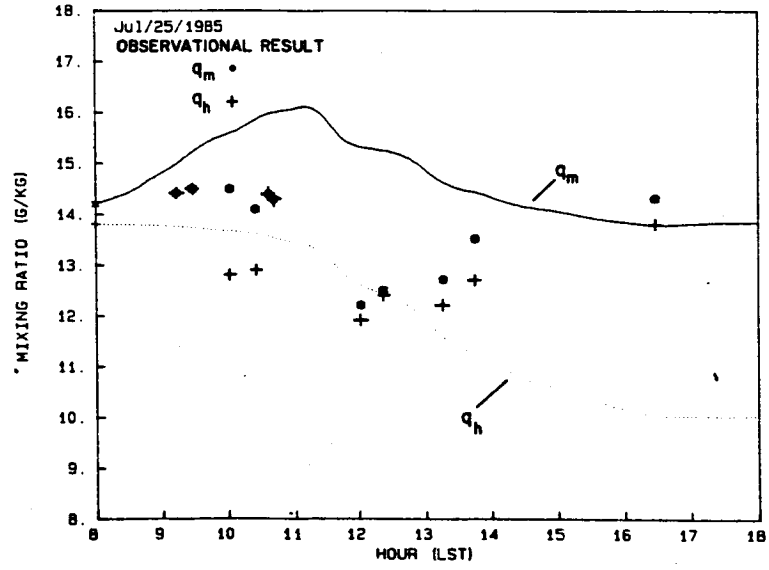
Jul/25/1985
OBSERVATIONAL RESULT
q_m
q_h
MIXING RATIO (G/KG)
HOUR (LST)

(c)

Fig 5

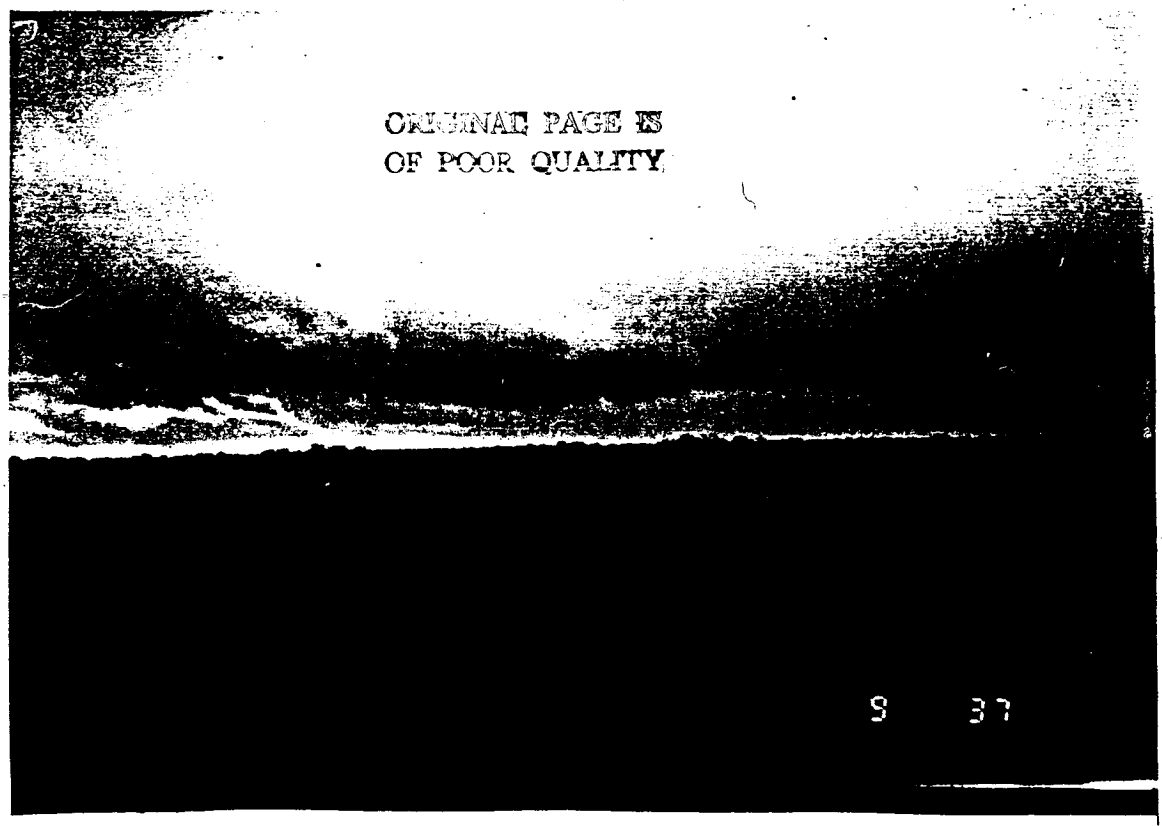

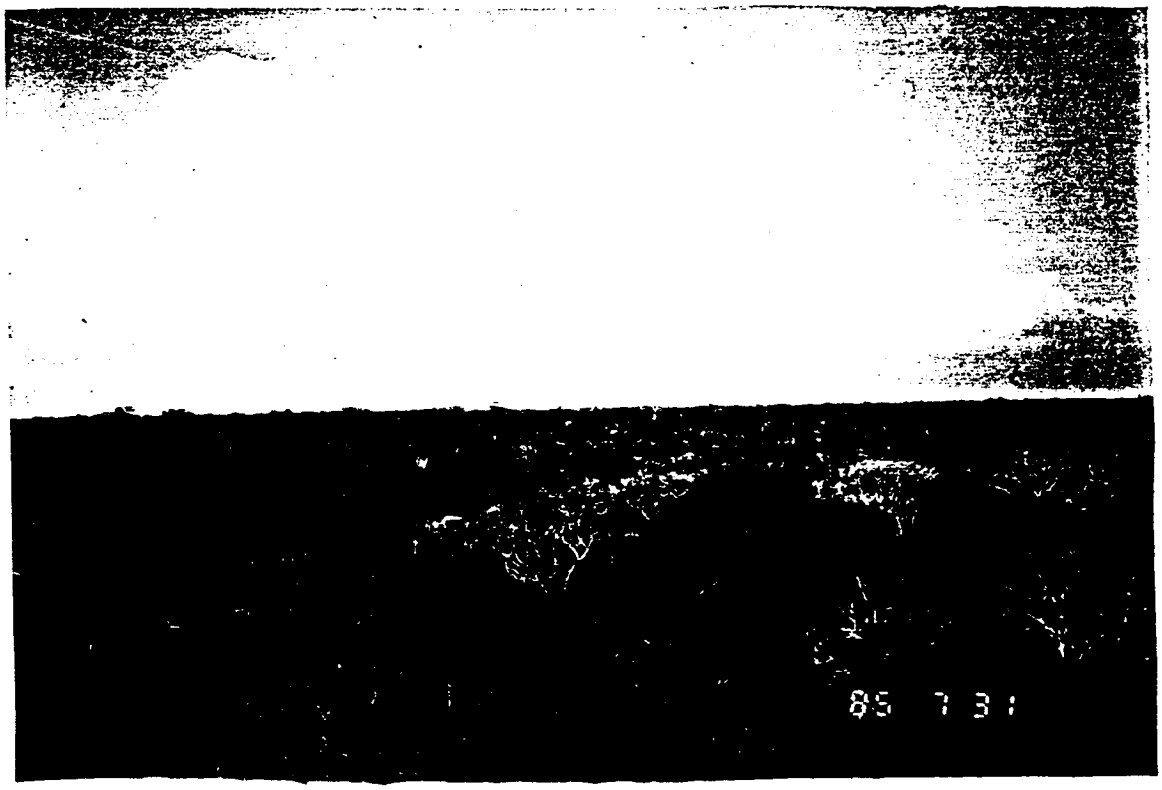

Fig 6

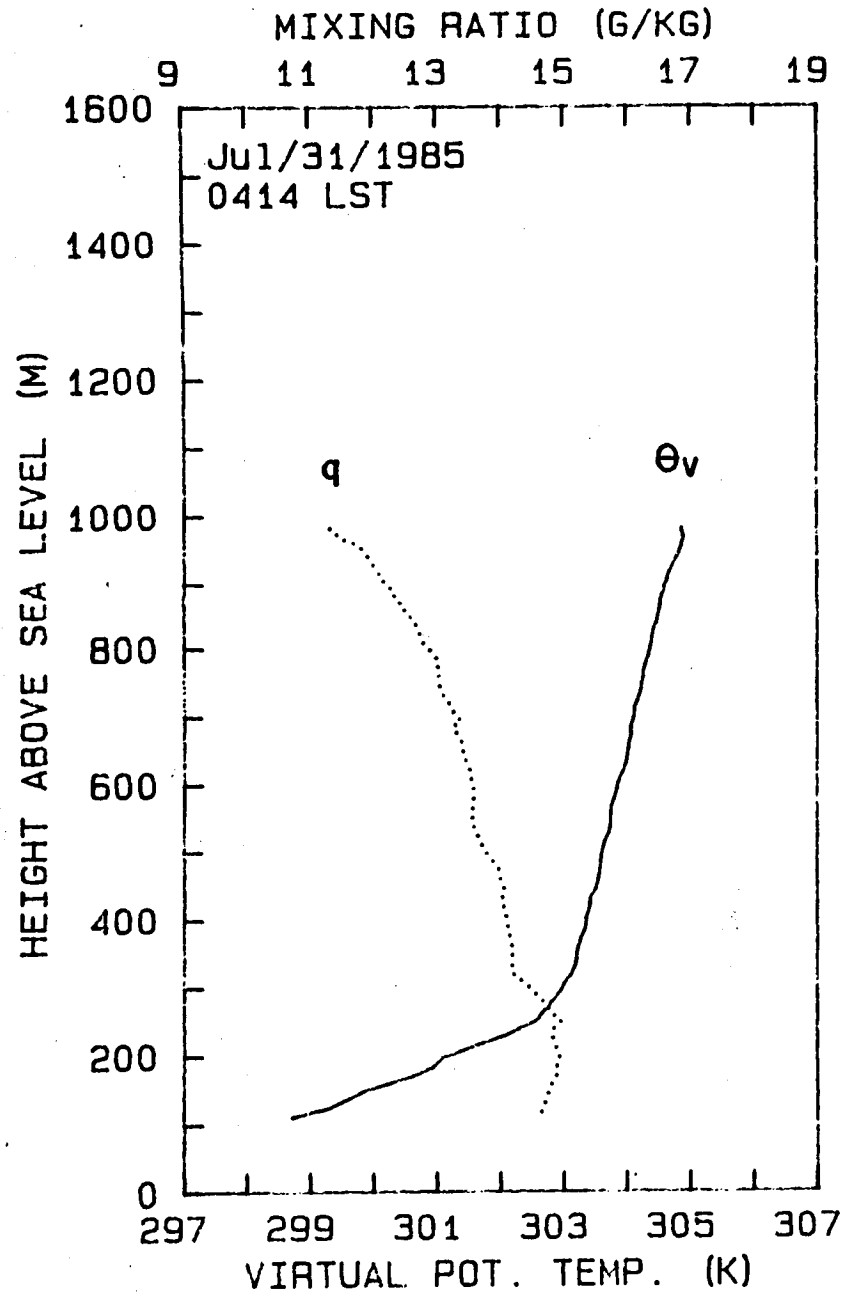
MIXING RATIO (G/KG)
9
11
13
15
17
19
Jul/31/1985
0414 LST
q
θv
HEIGHT ABOVE SEA LEVEL (M)
1600
1400
1200
1000
800
600
400
200
0
297
299
301
303
305
307
VIRTUAL POT. TEMP. (K)

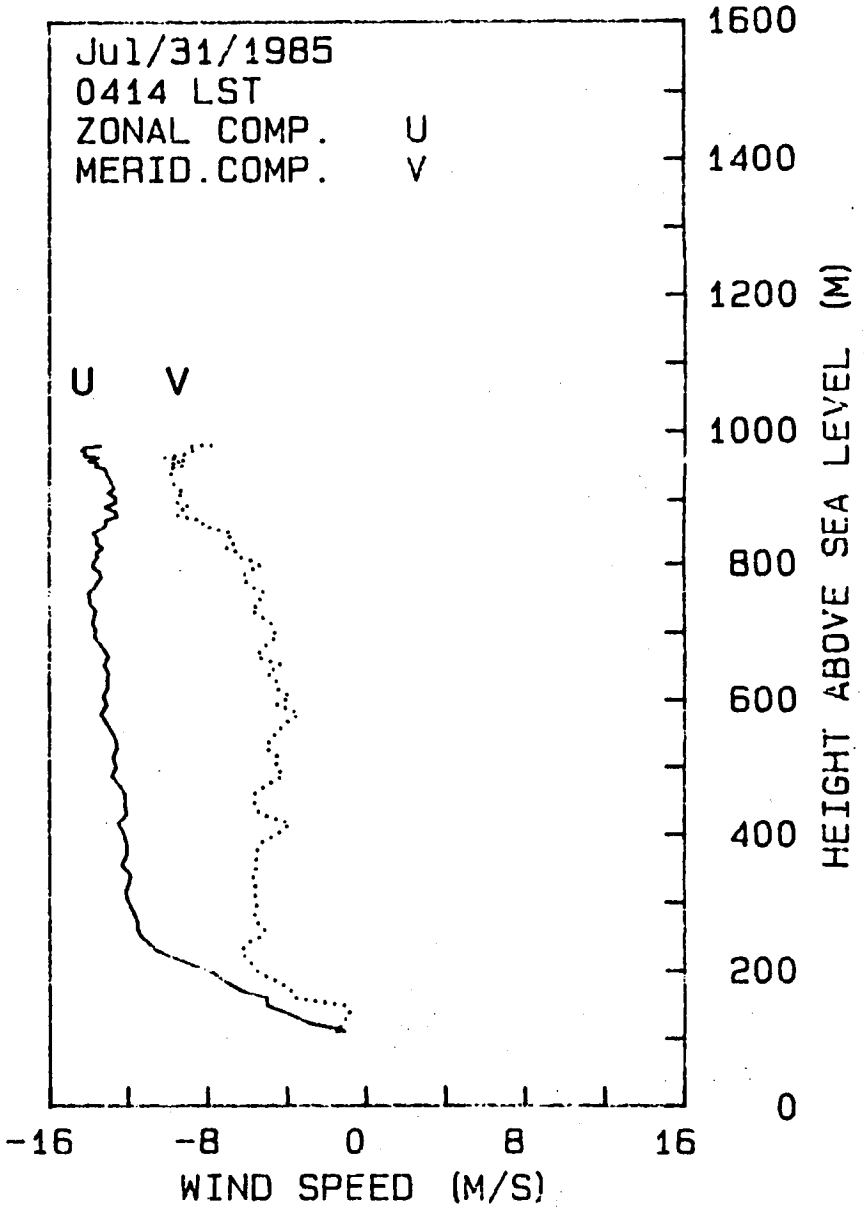
Jul/31/1985
0414 LST
ZONAL COMP. U
MERID.COMP. V
U
V
1600
1400
1200
1000
800
600
400
200
0
HEIGHT ABOVE SEA LEVEL (M)
-16
-8
0
8
16
WIND SPEED (M/S)

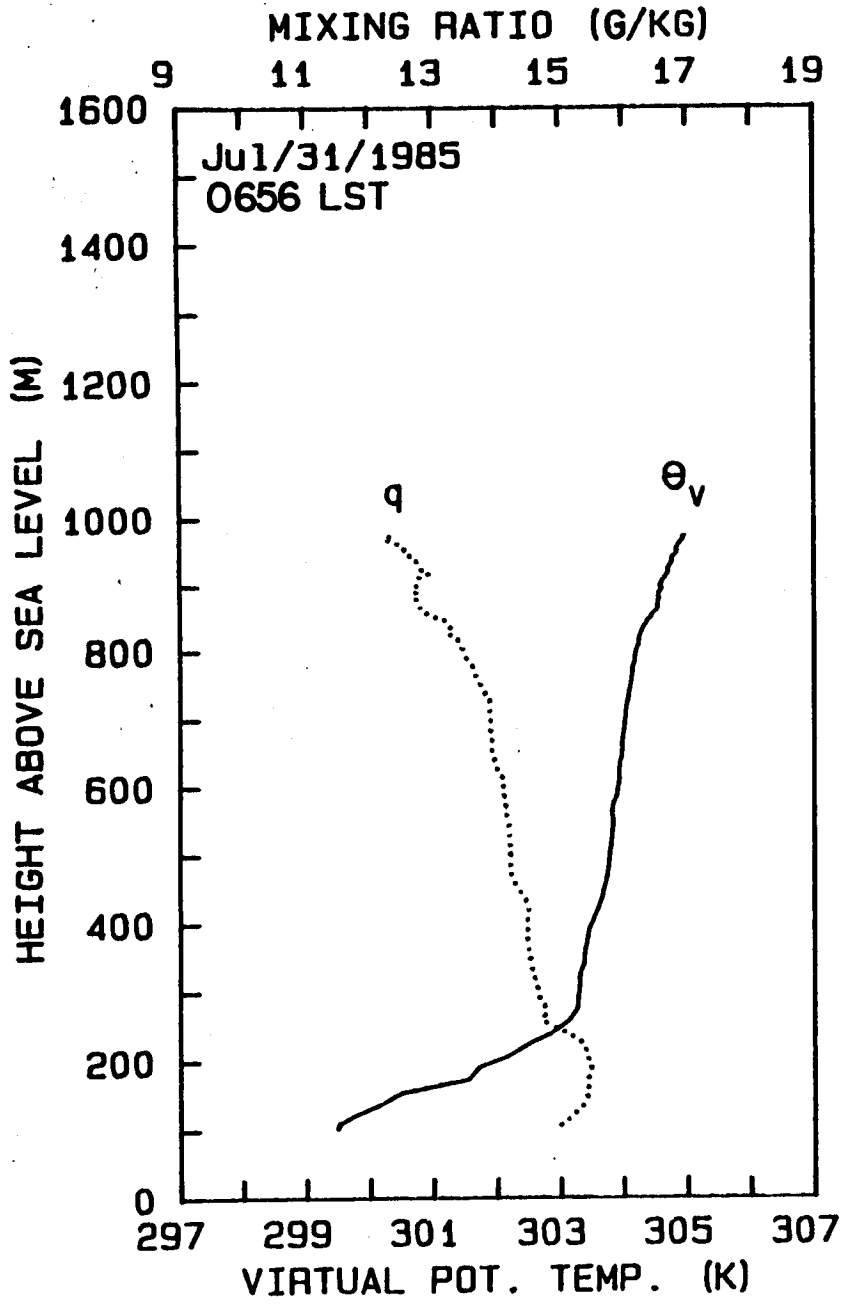
MIXING RATIO (G/KG)
9
11
13
15
17
19
Jul/31/1985
0656 LST
q
θ_v
HEIGHT ABOVE SEA LEVEL (M)
1600
1400
1200
1000
800
600
400
200
0
297
299
301
303
305
307
VIRTUAL POT. TEMP. (K)

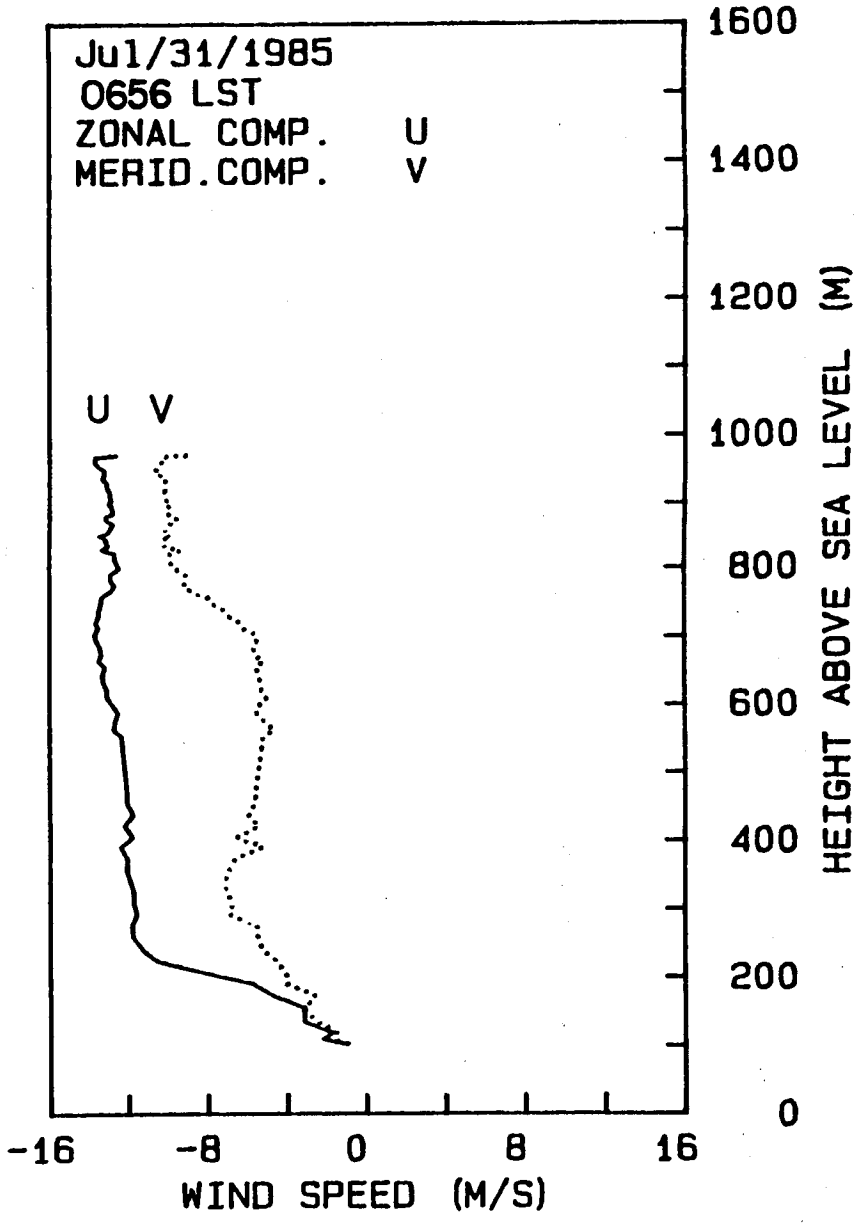
Jul/31/1985
0656 LST
ZONAL COMP. U
MERID.COMP. V
U
V
1600
1400
1200
1000
800
600
400
200
0
HEIGHT ABOVE SEA LEVEL (M)
-16
-8
0
8
16
WIND SPEED (M/S)

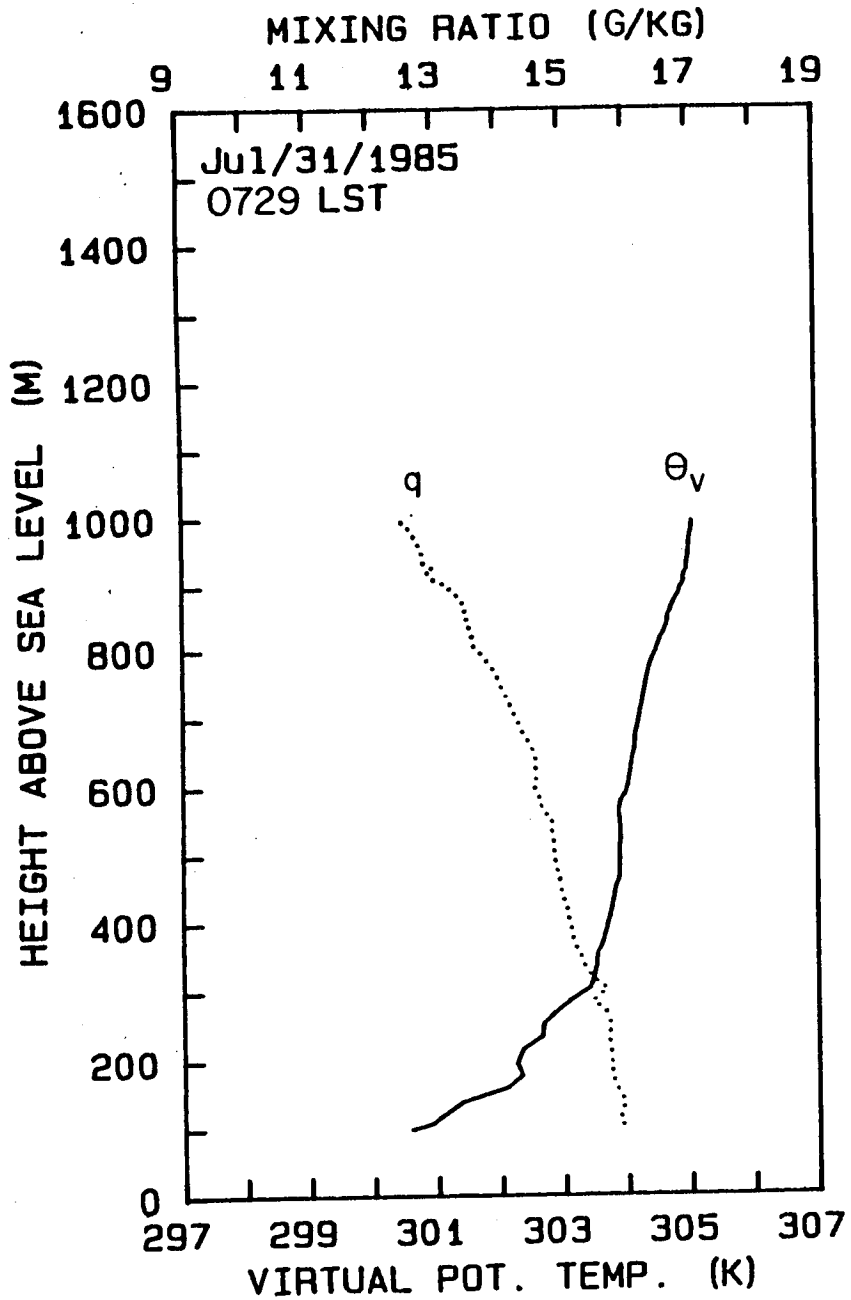
MIXING RATIO (G/KG)
9
11
13
15
17
19
Jul/31/1985
0729 LST
q
Θ_v
HEIGHT ABOVE SEA LEVEL (M)
0
200
400
600
800
1000
1200
1400
1600
297
299
301
303
305
307
VIRTUAL POT. TEMP. (K)

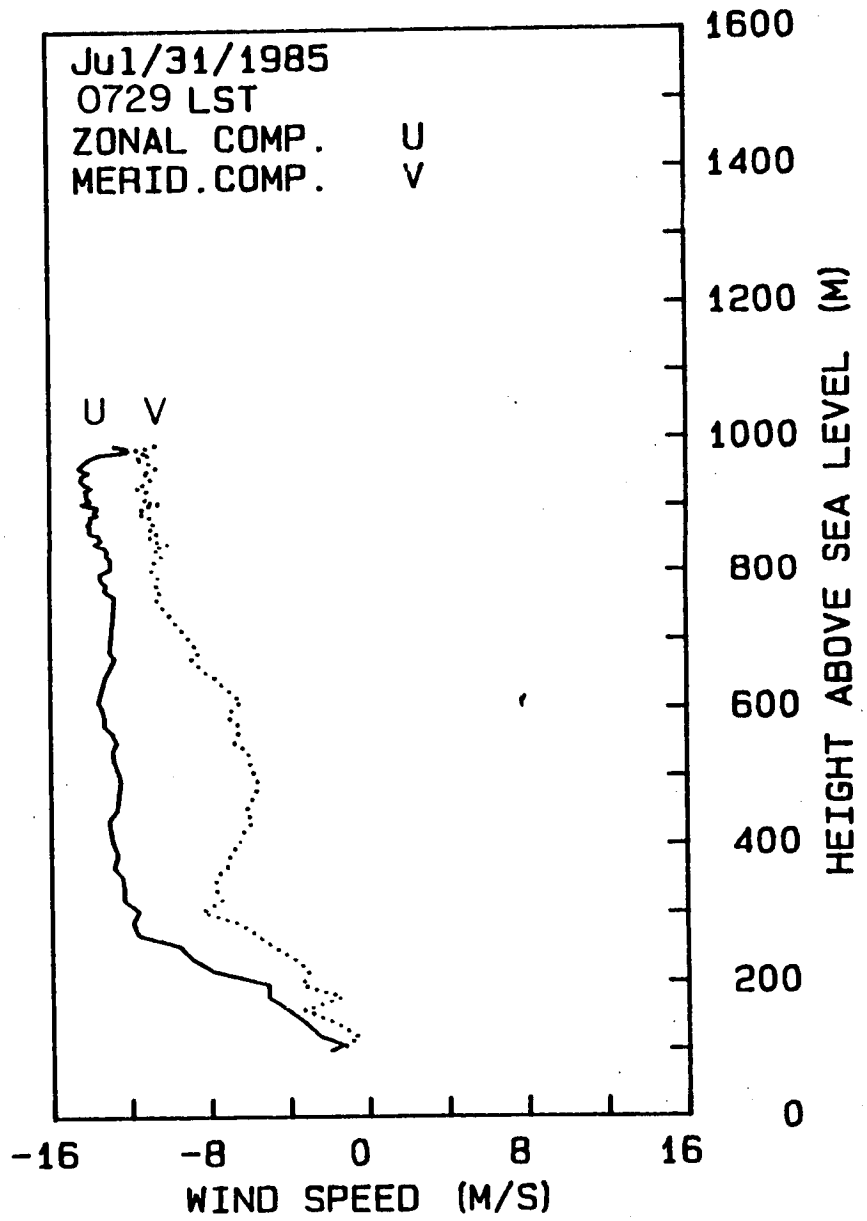
Jul/31/1985
0729 LST
ZONAL COMP. U
MERID.COMP. V
U
V
HEIGHT ABOVE SEA LEVEL (M)
0
200
400
600
800
1000
1200
1400
1600
-16
-8
0
8
16
WIND SPEED (M/S)

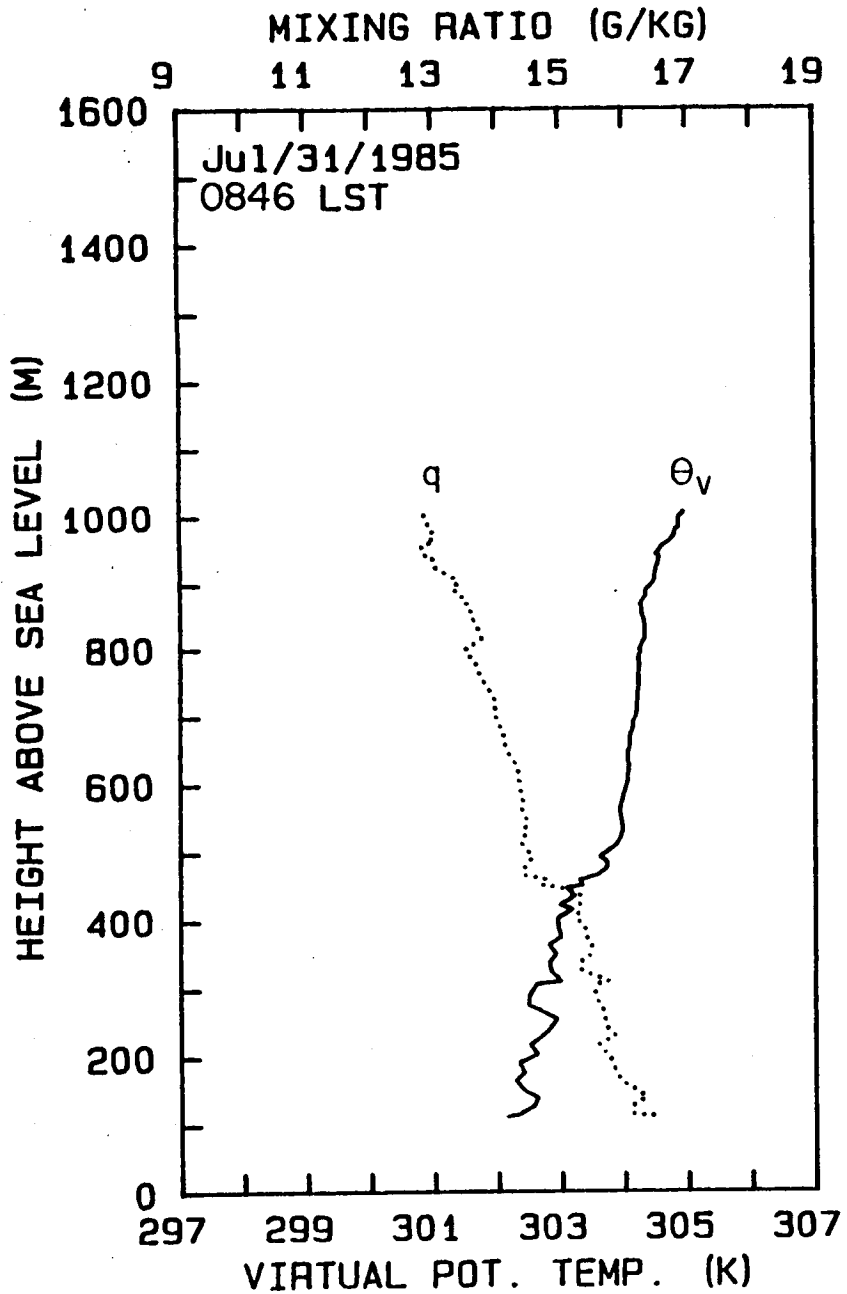
MIXING RATIO (G/KG)
9
11
13
15
17
19
Jul/31/1985
0846 LST
q
Θ_v
HEIGHT ABOVE SEA LEVEL (M)
1600
1400
1200
1000
800
600
400
200
0
297
299
301
303
305
307
VIRTUAL POT. TEMP. (K)

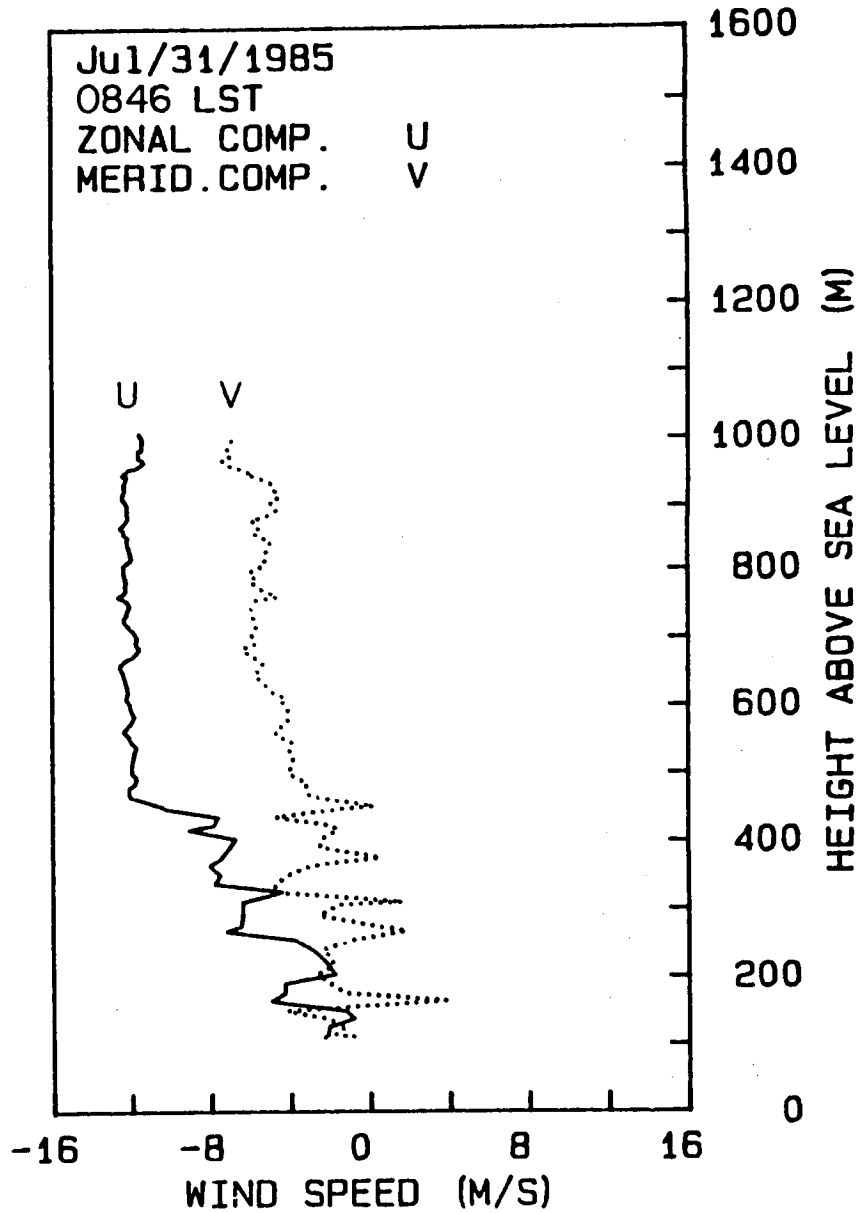
Jul/31/1985
0846 LST
ZONAL COMP. U
MERID.COMP. V
U
V
1600
1400
1200
1000
800
600
400
200
0
HEIGHT ABOVE SEA LEVEL (M)
-16
-8
0
8
16
WIND SPEED (M/S)

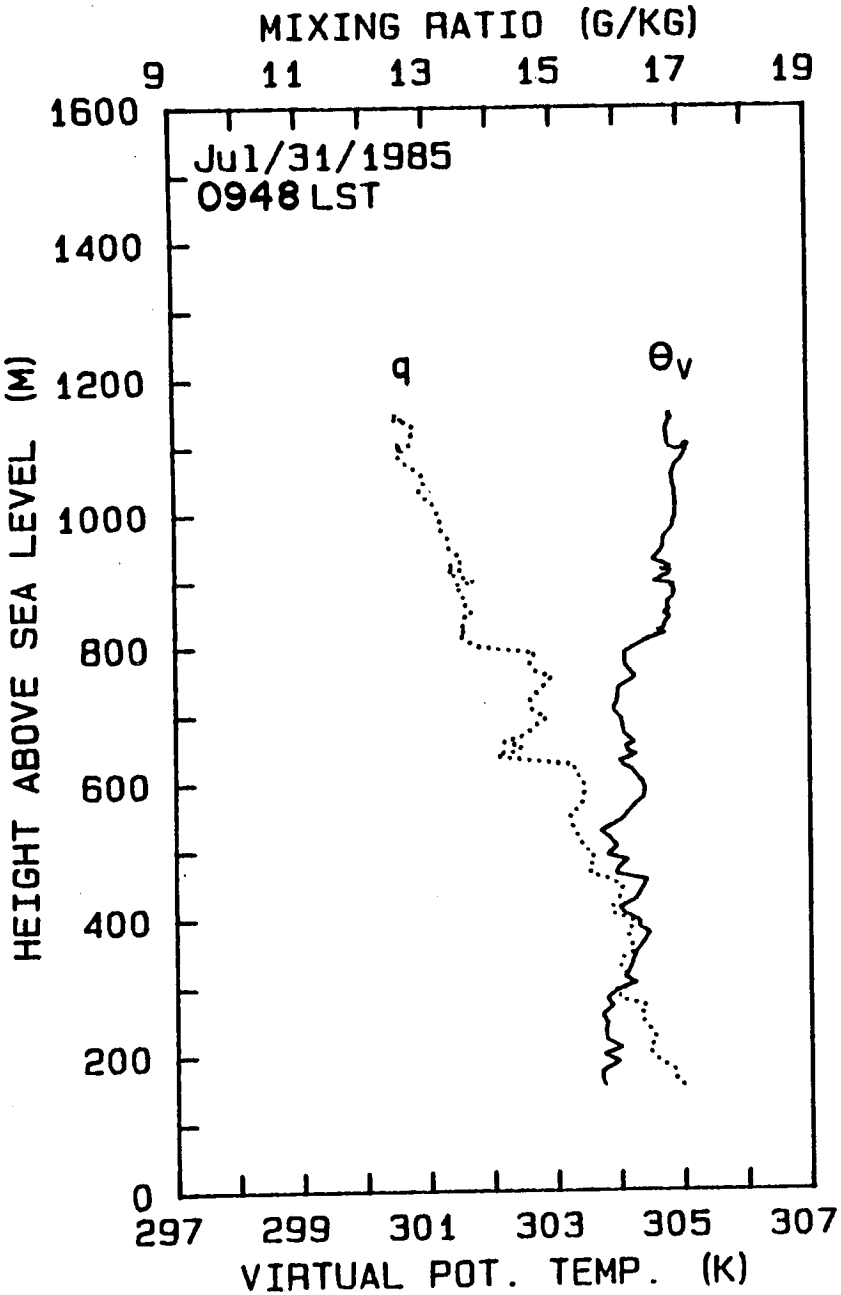
MIXING RATIO (G/KG)
9
11
13
15
17
19
Jul/31/1985
0948 LST
q
θ_v
HEIGHT ABOVE SEA LEVEL (M)
1600
1400
1200
1000
800
600
400
200
0
297
299
301
303
305
307
VIRTUAL POT. TEMP. (K)

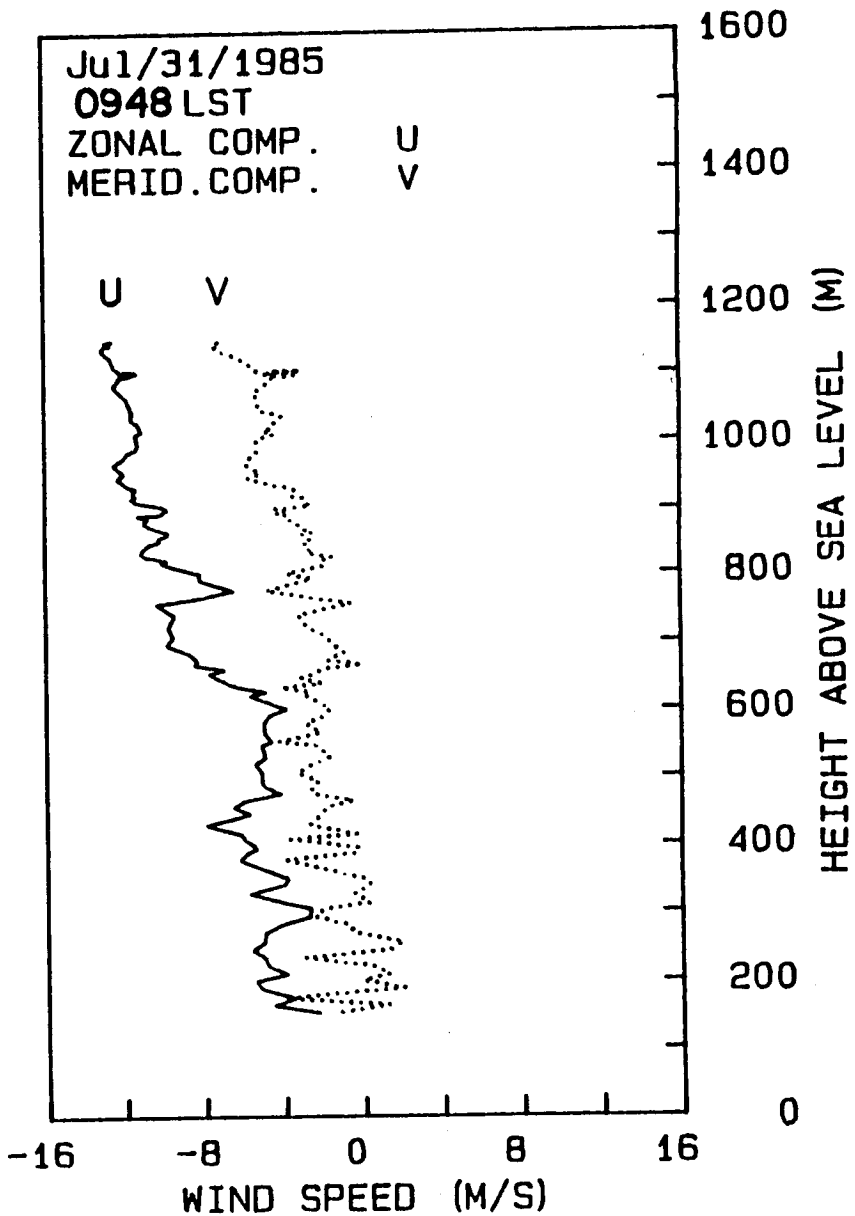
Jul/31/1985
0948 LST
ZONAL COMP. U
MERID.COMP. V
U
V
1600
1400
1200
1000
800
600
400
200
0
HEIGHT ABOVE SEA LEVEL (M)
-16
-8
0
8
16
WIND SPEED (M/S)

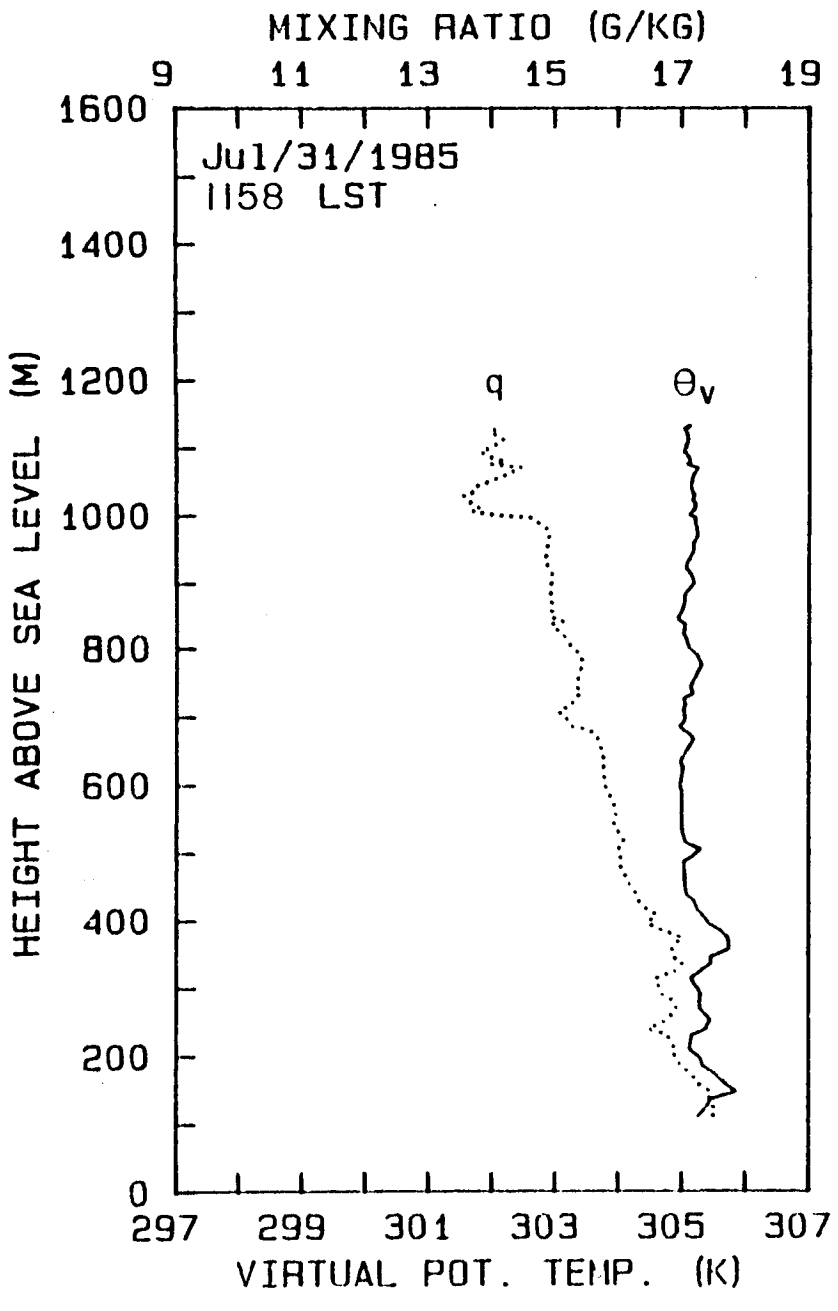
MIXING RATIO (G/KG)
9
11
13
15
17
19
Jul/31/1985
1158 LST
q
θ_v
HEIGHT ABOVE SEA LEVEL (M)
0
200
400
600
800
1000
1200
1400
1600
297
299
301
303
305
307
VIRTUAL POT. TEMP. (K)

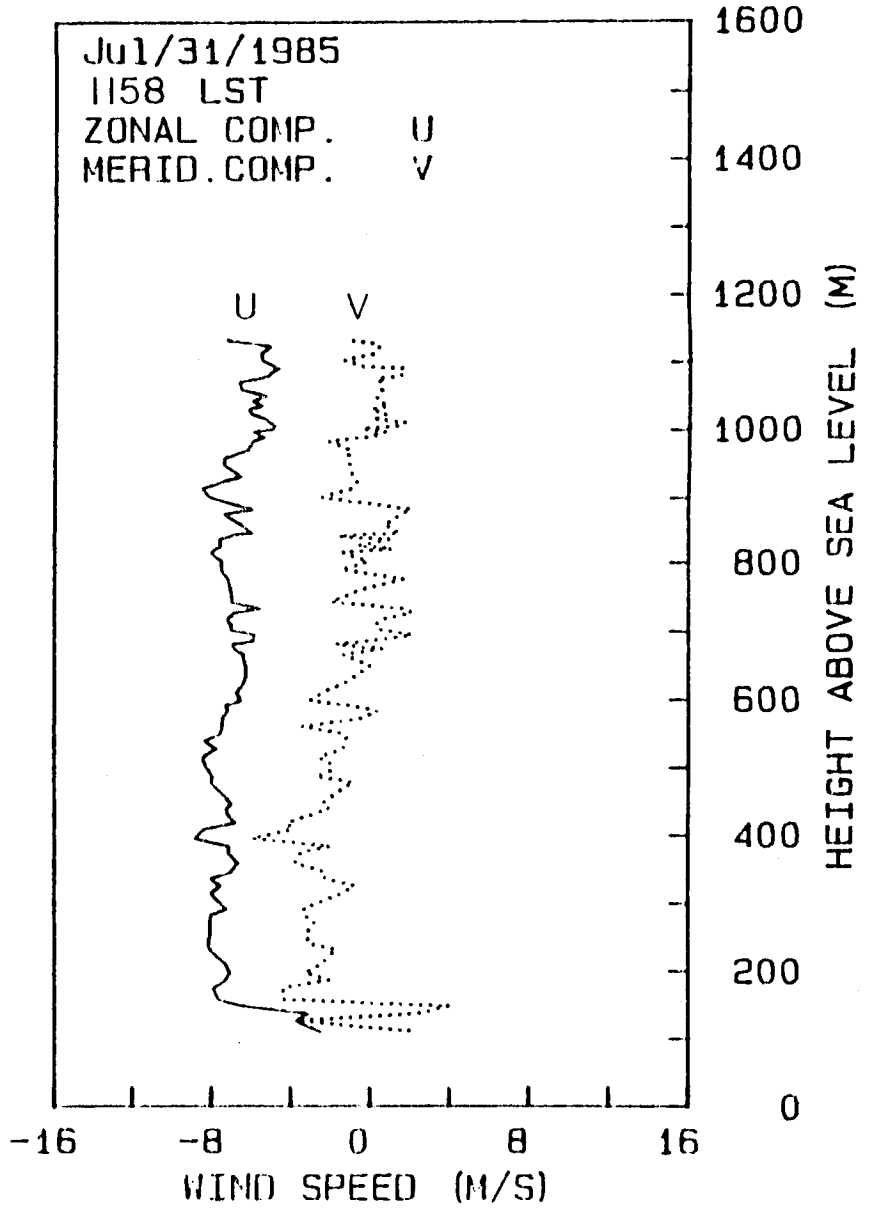
Jul/31/1985
1158 LST
ZONAL COMP. U
MERID.COMP. V
U
V
HEIGHT ABOVE SEA LEVEL (M)
0
200
400
600
800
1000
1200
1400
1600
-16
-8
0
8
16
WIND SPEED (M/S)

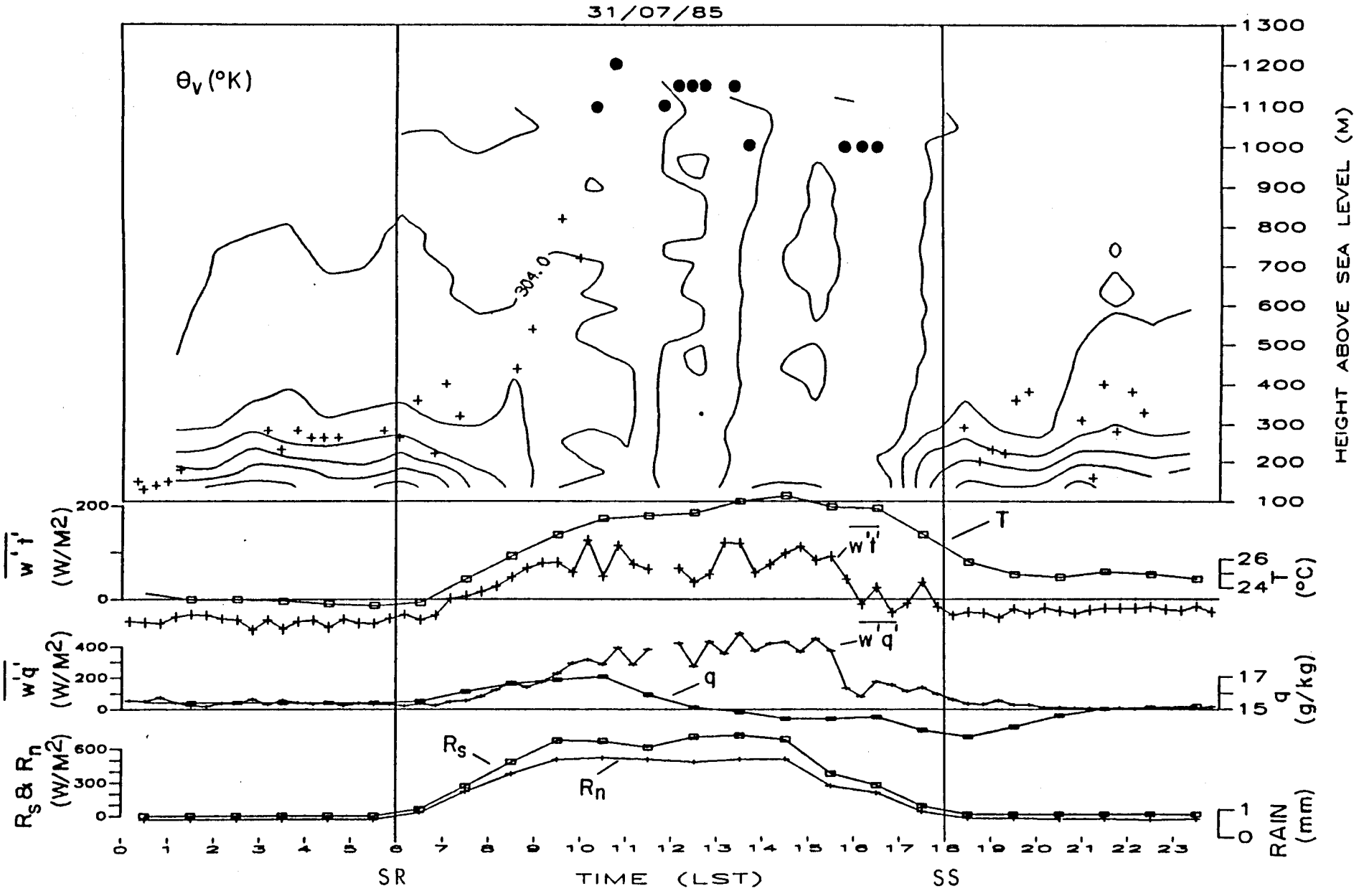
31/07/85
θv (°K)
304.0
HEIGHT ABOVE SEA LEVEL (M)
1300
1200
1100
1000
900
800
700
600
500
400
300
200
100
w'T' (W/M2)
200
0
T
w'T'
26
24
T (°C)
w'q' (W/M2)
400
200
0
w'q'
q
17
15
q (g/kg)
Rs & Rn (W/M2)
600
300
0
Rs
Rn
1
0
RAIN (mm)
0 1 2 3 4 5 6 7 8 9 10 11 12 13 14 15 16 17 18 19 20 21 22 23
SR
TIME (LST)
SS

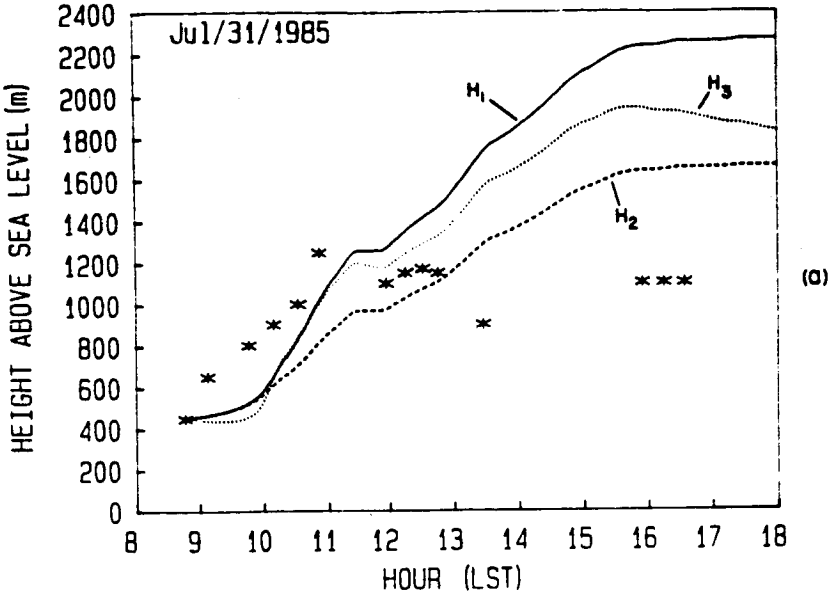
Jul/31/1985
HEIGHT ABOVE SEA LEVEL (m)
HOUR (LST)
H_1
H_3
H_2
(a)

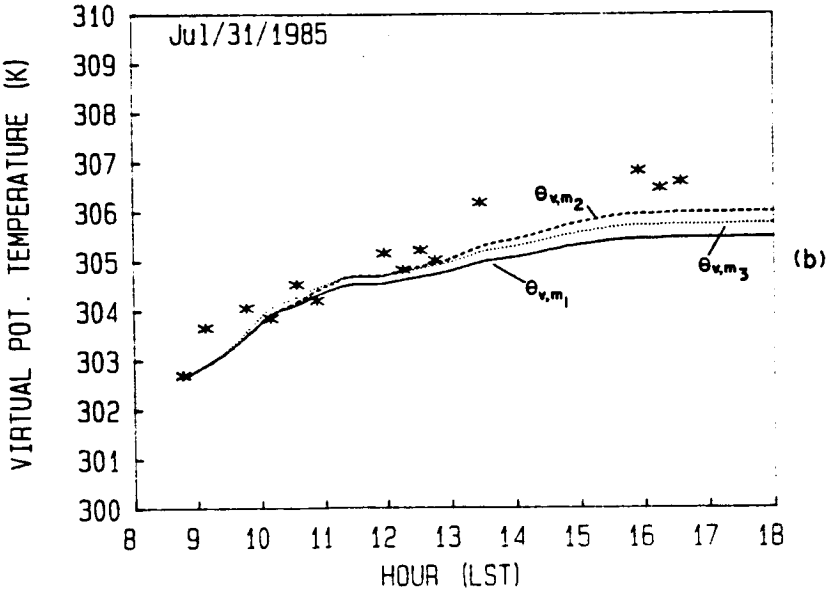
Jul/31/1985
VIRTUAL POT. TEMPERATURE (K)
HOUR (LST)
θ_{v,m_2}
θ_{v,m_3}
θ_{v,m_1}
(b)

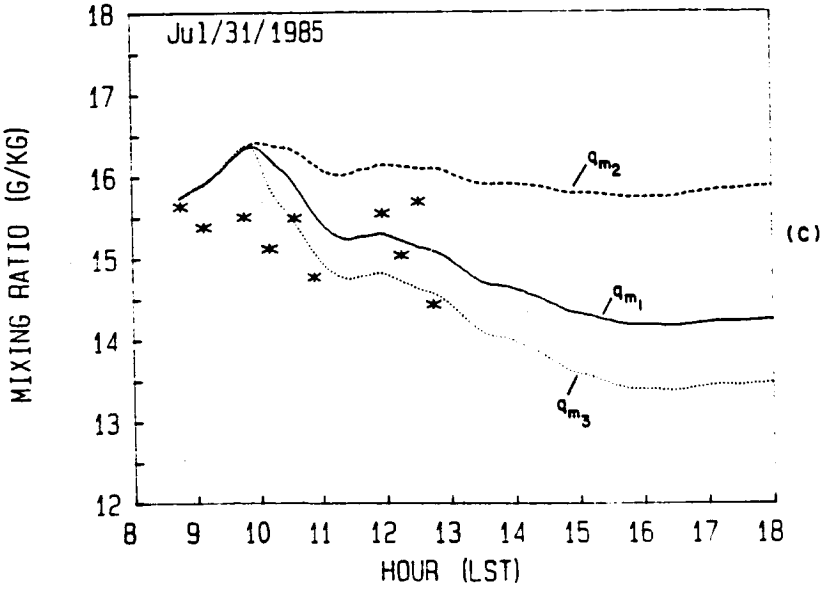
Jul/31/1985
MIXING RATIO (G/KG)
HOUR (LST)
q_{m_2}
q_{m_1}
q_{m_3}
(c)

31 JULY 1985

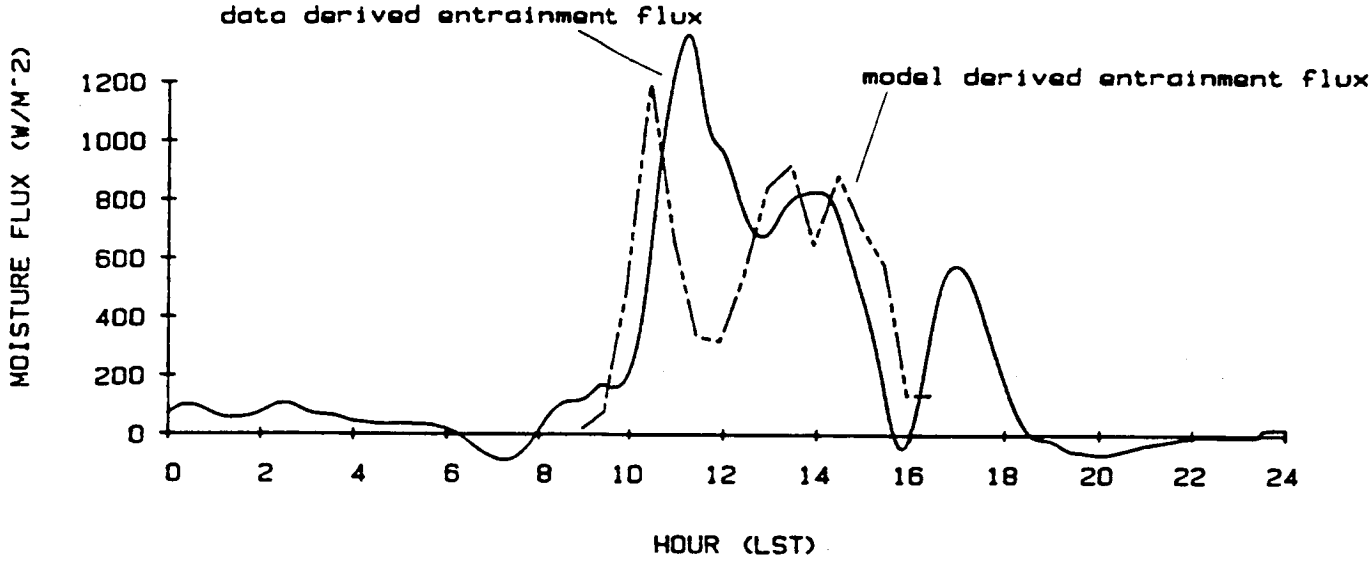

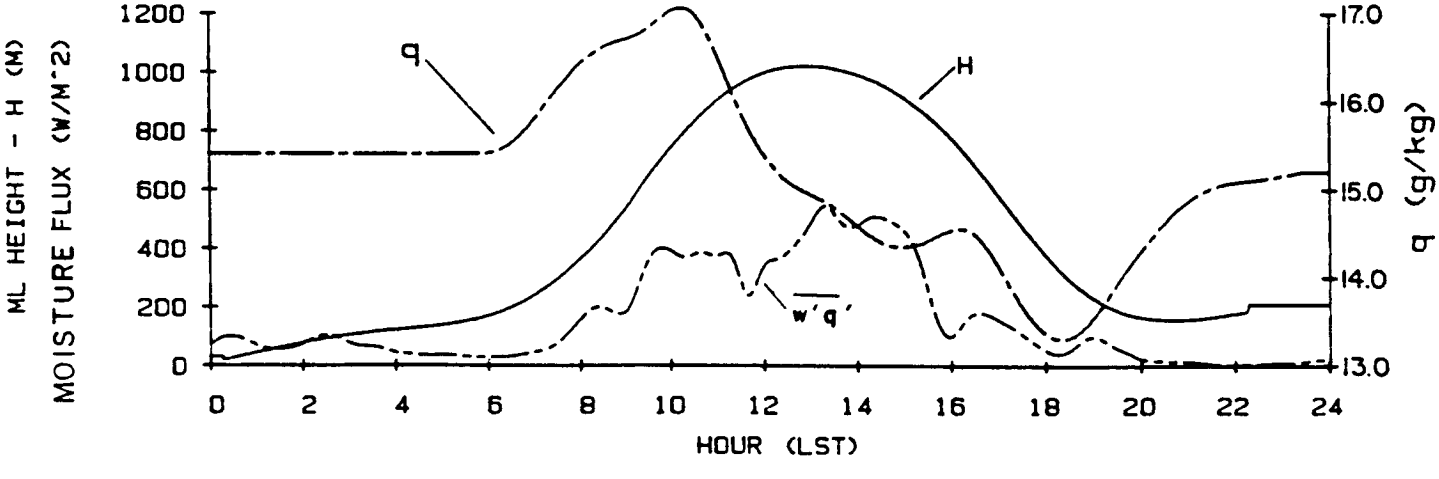

Fig 10

HEIGHT ABOVE SEA LEVEL (M)
1300
1200
1100
1000
900
800
700
600
500
400
300
200
100
26/07/85
θ_v(°K)
304.0
303.0
302.0
301.0
302.0
303.0
304.0
T
$\overline{w'T'}$
q
$\overline{w'q'}$
R_s
R_n
RAIN
(mm)
1
0
q
(g/kg)
17
15
T
(°C)
26
24
R_s & R_n
(W/m^2)
600
300
0
$\overline{w'q'}$
(W/m^2)
400
200
0
$\overline{w'T'}$
(W/m^2)
200
0
SR
SS
TIME (LST)
0 1 2 3 4 5 6 7 8 9 10 11 12 13 14 15 16 17 18 19 20 21 22 23

Fig 11a

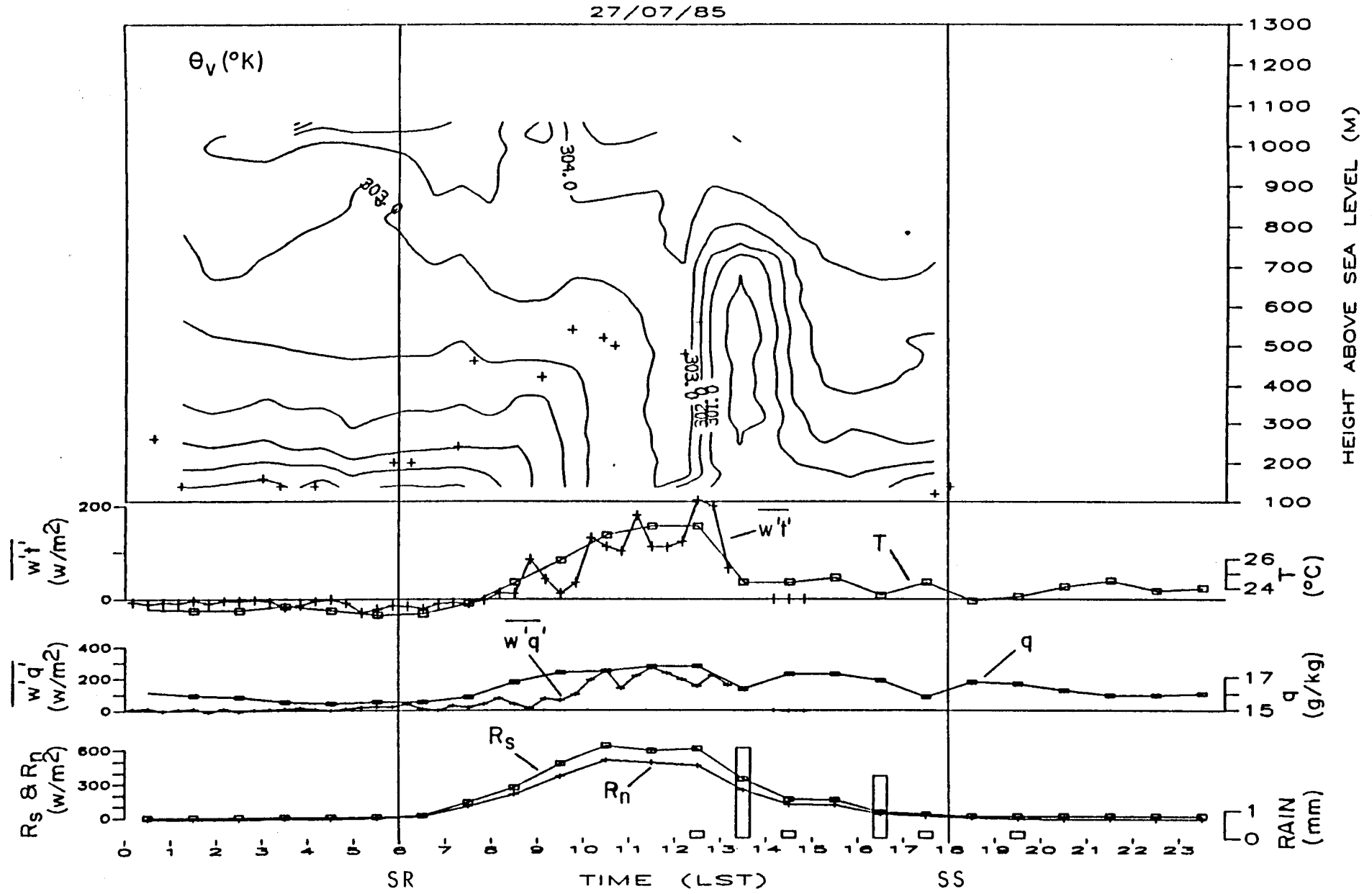
27/07/85
θv (°K)
303.0
304.0
302.0
301.0
HEIGHT ABOVE SEA LEVEL (M)
1300
1200
1100
1000
900
800
700
600
500
400
300
200
100
w'T' (w/m2)
200
0
w'T'
T
26
24
T (°C)
w'q' (w/m2)
400
200
0
w'q'
q
17
15
q (g/kg)
Rs & Rn (w/m2)
600
300
0
Rs
Rn
1
0
RAIN (mm)
0 1 2 3 4 5 6 7 8 9 10 11 12 13 14 15 16 17 18 19 20 21 22 23
SR
TIME (LST)
SS

911 fr

02/08/85
θ_v (°K)
304.0
305.0
306.0
HEIGHT ABOVE SEA LEVEL (M)
1300
1200
1100
1000
900
800
700
600
500
400
300
200
100
T (°C)
26
24
q (g/kg)
17
15
RAIN (mm)
1
0
R_s
R_n
$\overline{w'T'}$
$\overline{w'q'}$
$\overline{w'T'}$ (w/m²)
$\overline{w'q'}$ (w/m²)
R_s & R_n (w/m²)
200
0
400
200
0
600
300
0
SR
SS
TIME (LST)
0 1 2 3 4 5 6 7 8 9 10 11 12 13 14 15 16 17 18 19 20 21 22 23

Fig 11c

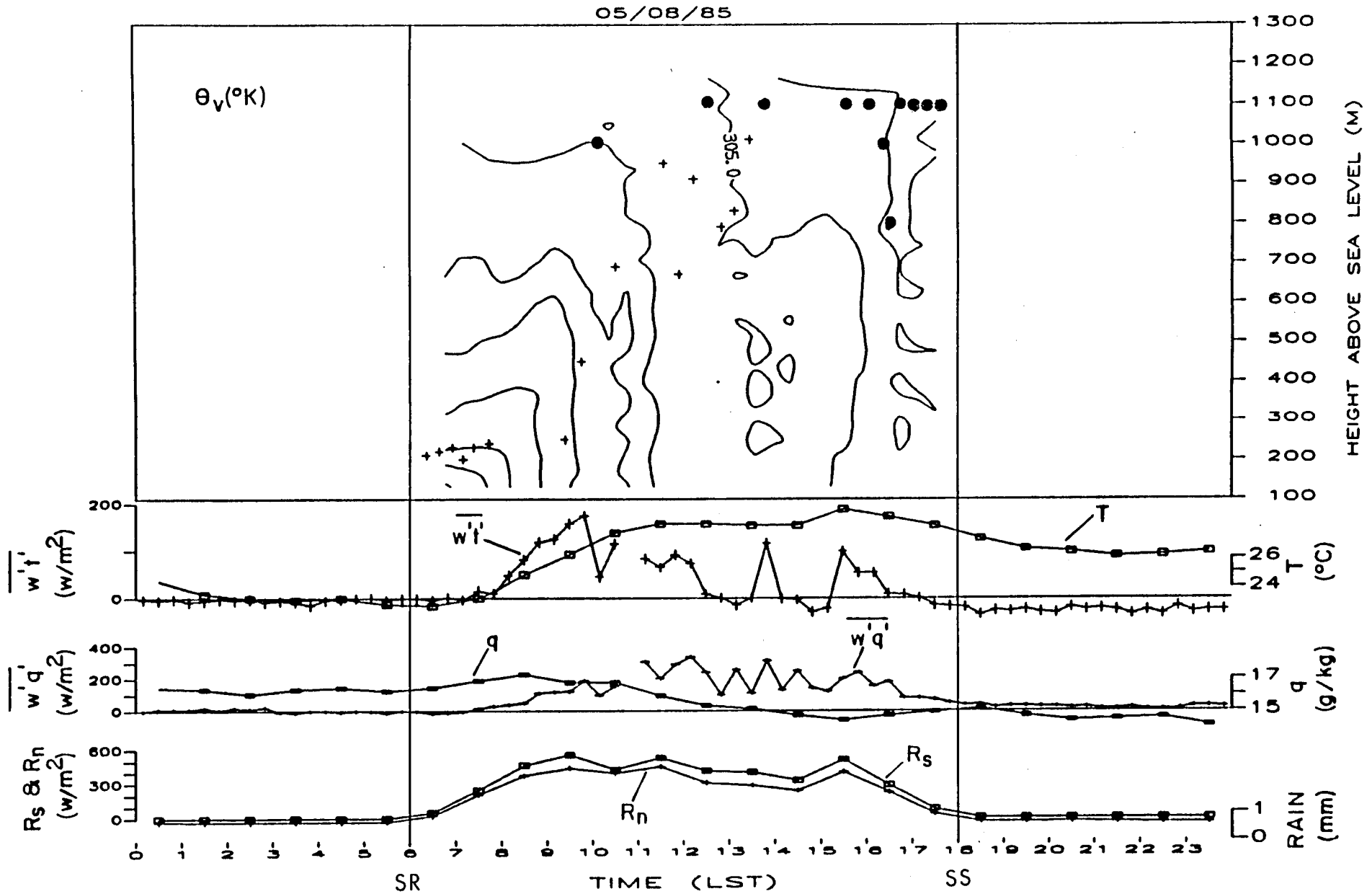
05/08/85
θ_v(°K)
305.0
HEIGHT ABOVE SEA LEVEL (M)
1300
1200
1100
1000
900
800
700
600
500
400
300
200
100
$\overline{w'T'}$ (w/m²)
200
0
$\overline{w'T'}$
T
T (°C)
26
24
$\overline{w'q'}$ (w/m²)
400
200
0
q
$\overline{w'q'}$
q (g/kg)
17
15
R_s & R_n (w/m²)
600
300
0
R_s
R_n
RAIN (mm)
1
0
0 1 2 3 4 5 6 7 8 9 10 11 12 13 14 15 16 17 18 19 20 21 22 23
SR
TIME (LST)
SS

COMPOSITE
θ_v(°K)
305.0
304.0
HEIGHT ABOVE SEA LEVEL (M)
1300
1200
1100
1000
900
800
700
600
500
400
300
200
100
T (°C)
26
24
q (g/kg)
17
15
T
$\overline{w'T'}$
$\overline{w'q'}$
q
Rs
Rn
$\overline{w'T'}$ (w/m2)
200
0
$\overline{w'q'}$ (w/m2)
400
200
0
Rs & Rn (w/m2)
600
300
0
SR
SS
TIME (LST)
0 1 2 3 4 5 6 7 8 9 10 11 12 13 14 15 16 17 18 19 20 21 22 23

Fig 12

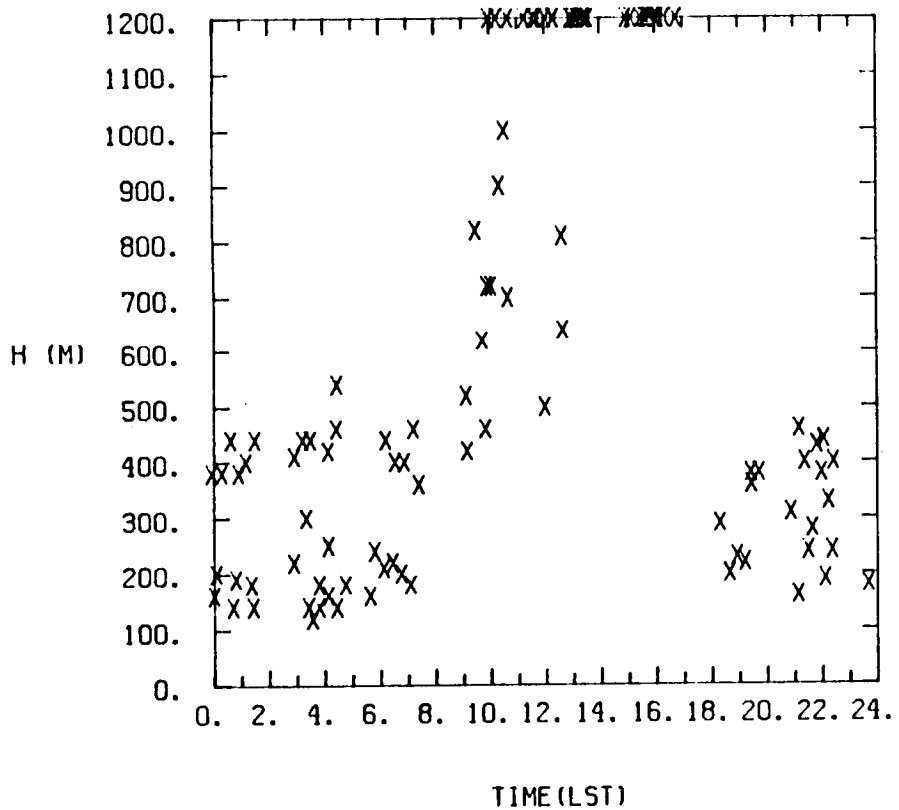
1200.
1100.
1000.
900.
800.
700.
600.
500.
400.
300.
200.
100.
0.
H (M)
0. 2. 4. 6. 8. 10. 12. 14. 16. 18. 20. 22. 24.
TIME(LST)

a

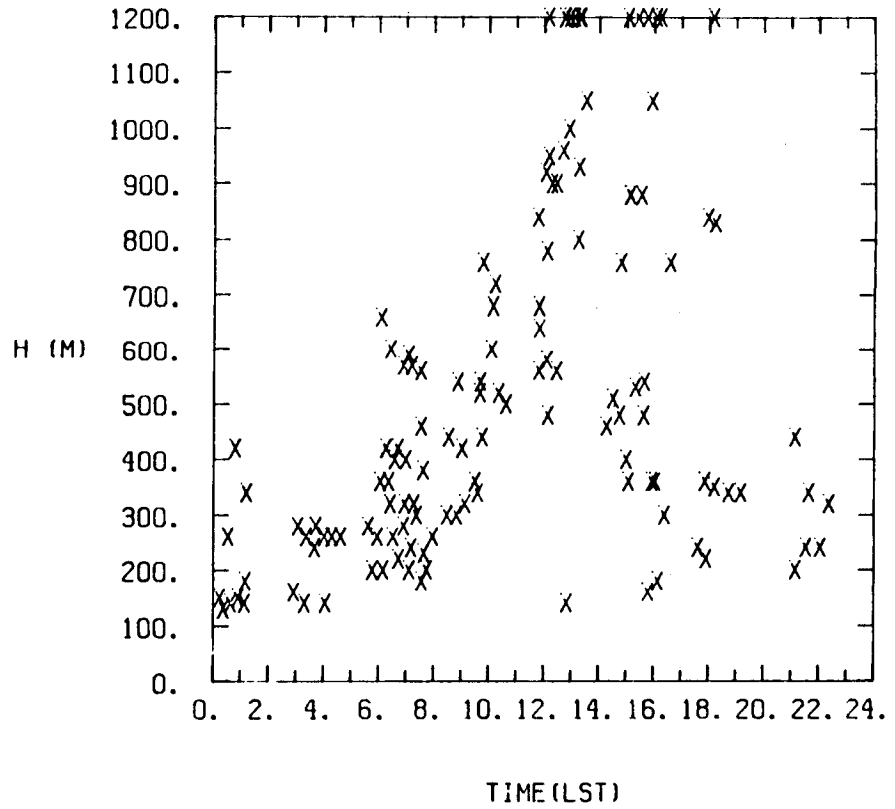
1200.
1100.
1000.
900.
800.
700.
600.
500.
400.
300.
200.
100.
0.
H (M)
0. 2. 4. 6. 8. 10. 12. 14. 16. 18. 20. 22. 24.
TIME(LST)

b

Fig 13

(a)

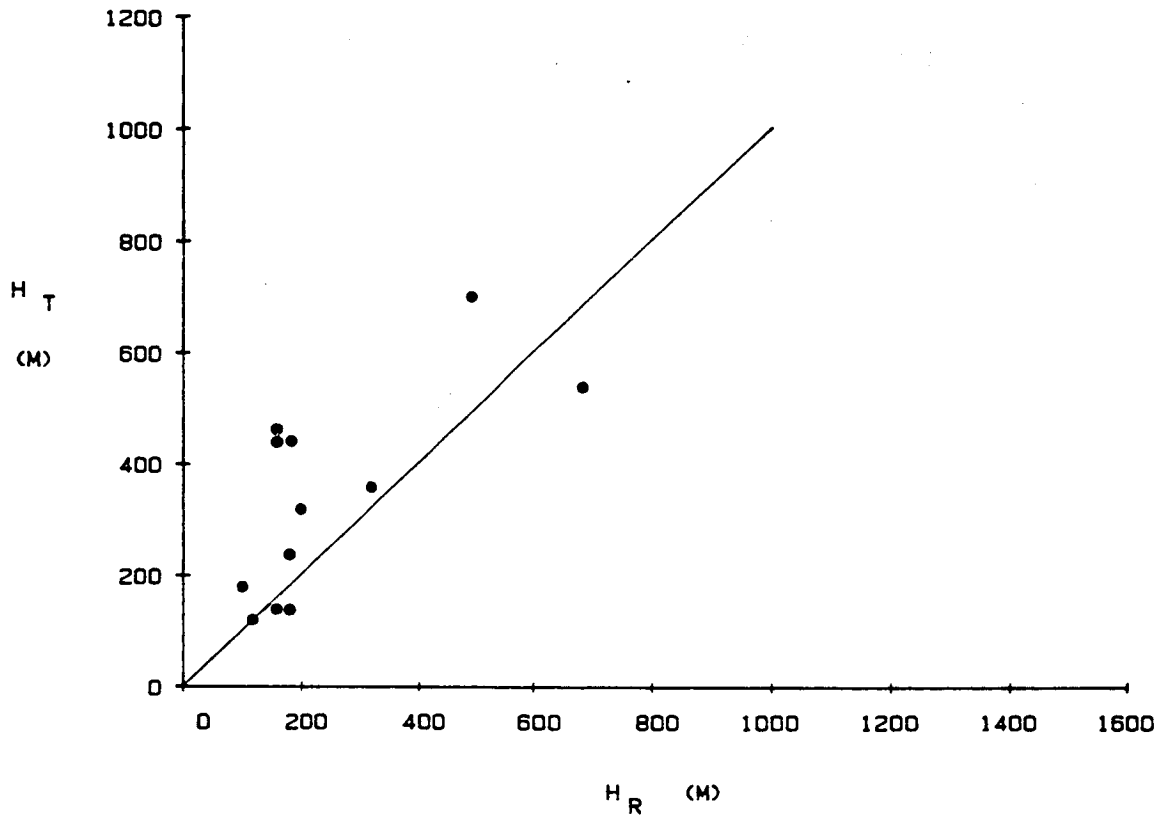
1200
1000
800
600
400
200
0
H T
(M)
0
200
400
600
800
1000
1200
1400
1600
H R (M)

(b)

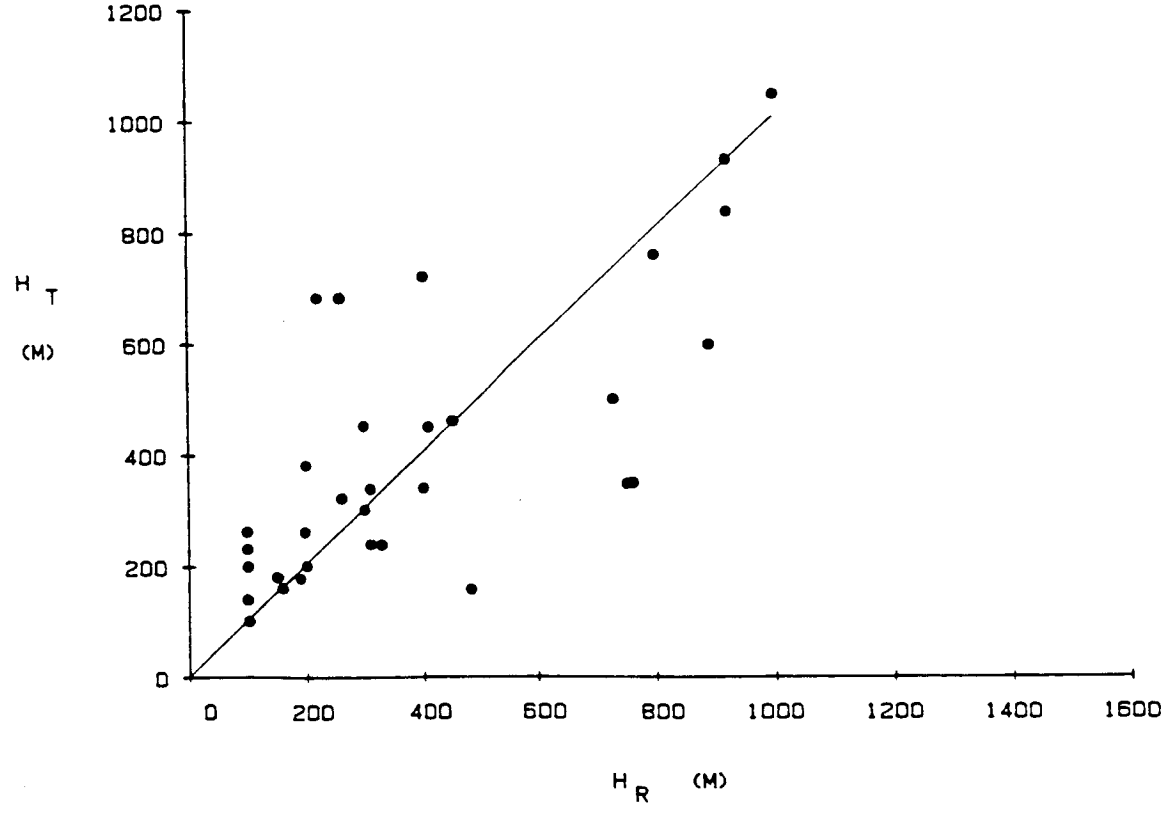
1200
1000
800
600
400
200
0
H T
(M)
0
200
400
600
800
1000
1200
1400
1600
H R (M)

Fig 14

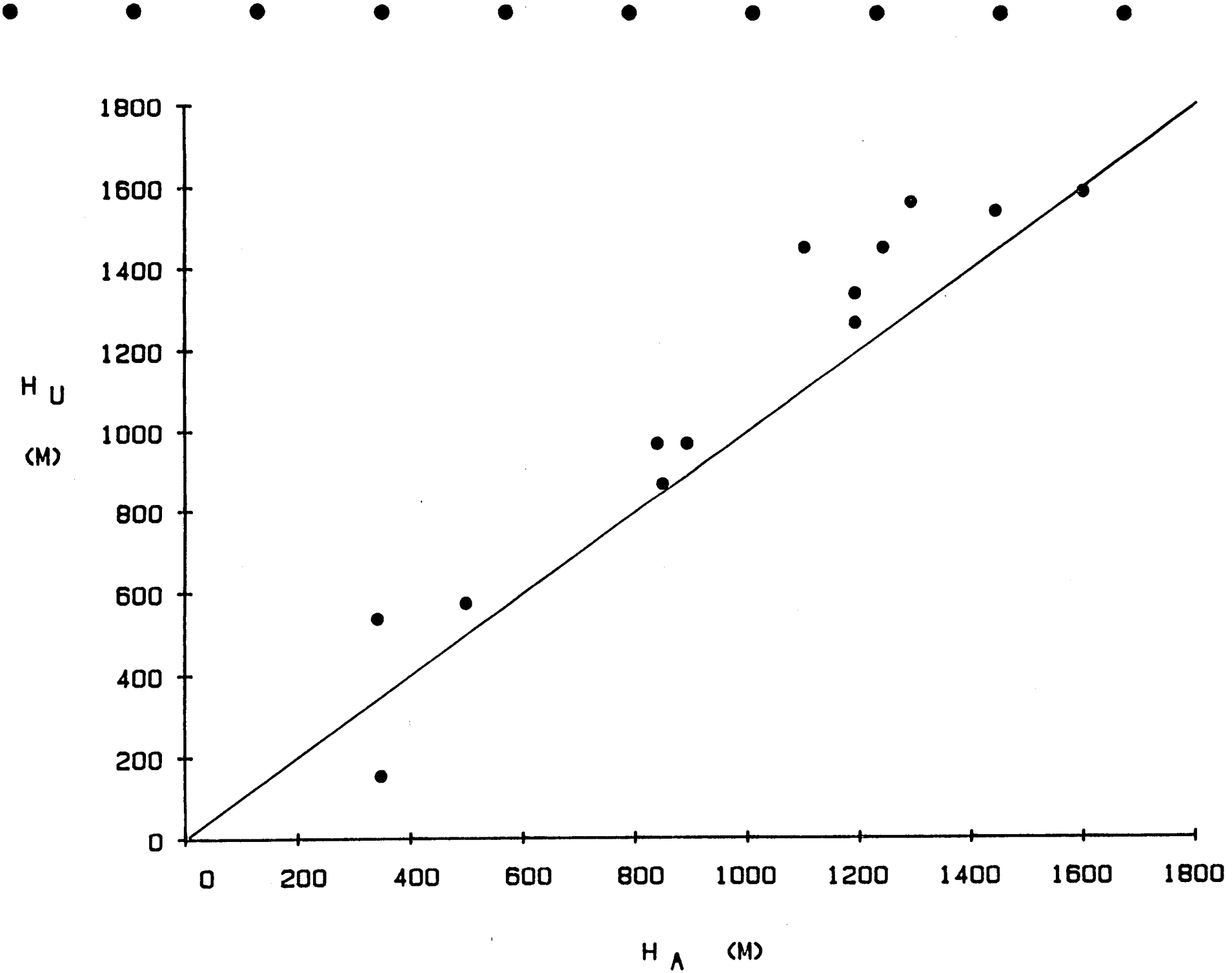
1800
1600
1400
1200
1000
800
600
400
200
0
H U
(M)
0
200
400
600
800
1000
1200
1400
1600
1800
H A (M)

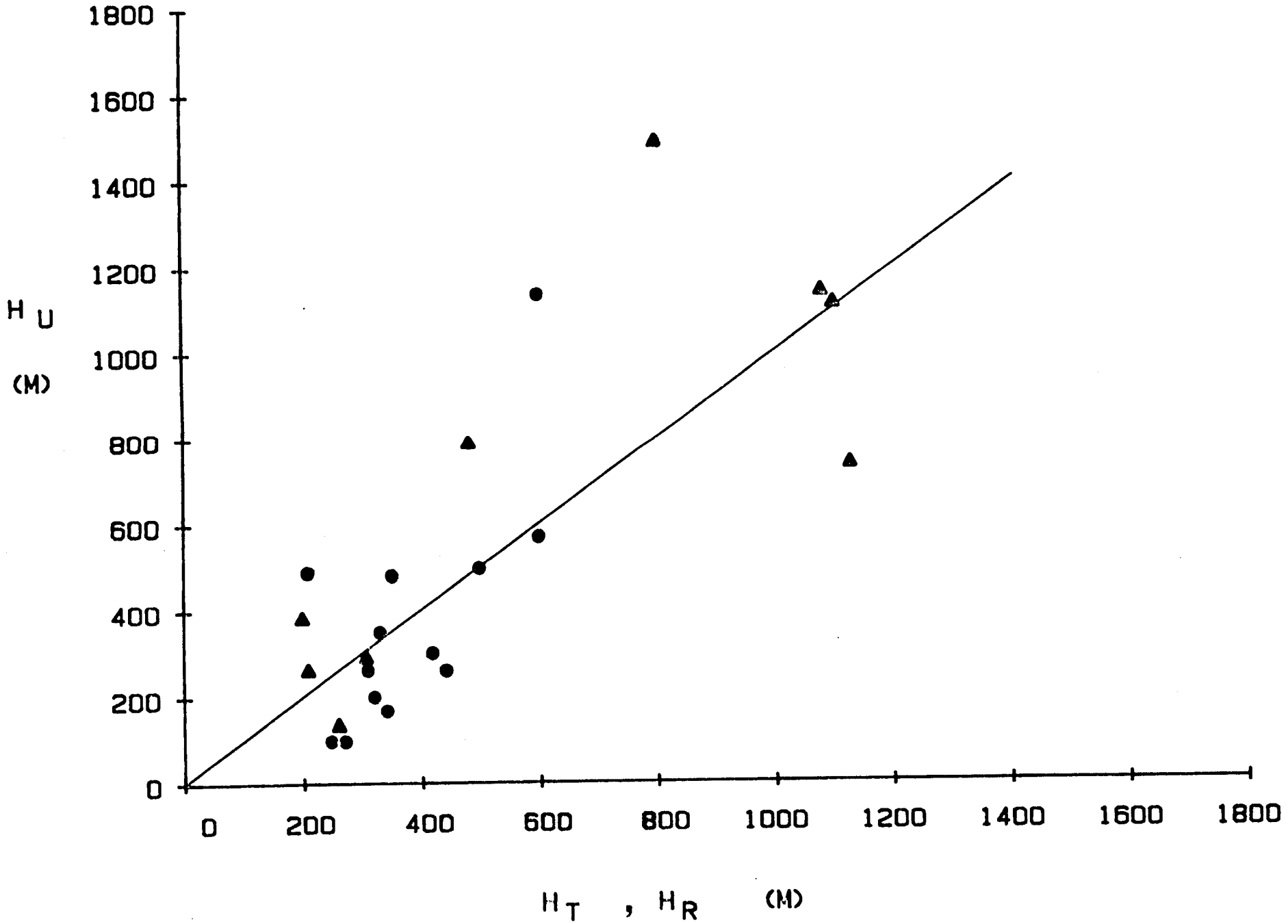
1800
1600
1400
1200
1000
800
600
400
200
0
H_U
(M)
0
200
400
600
800
1000
1200
1400
1600
1800
H_T , H_R (M)

F?
6

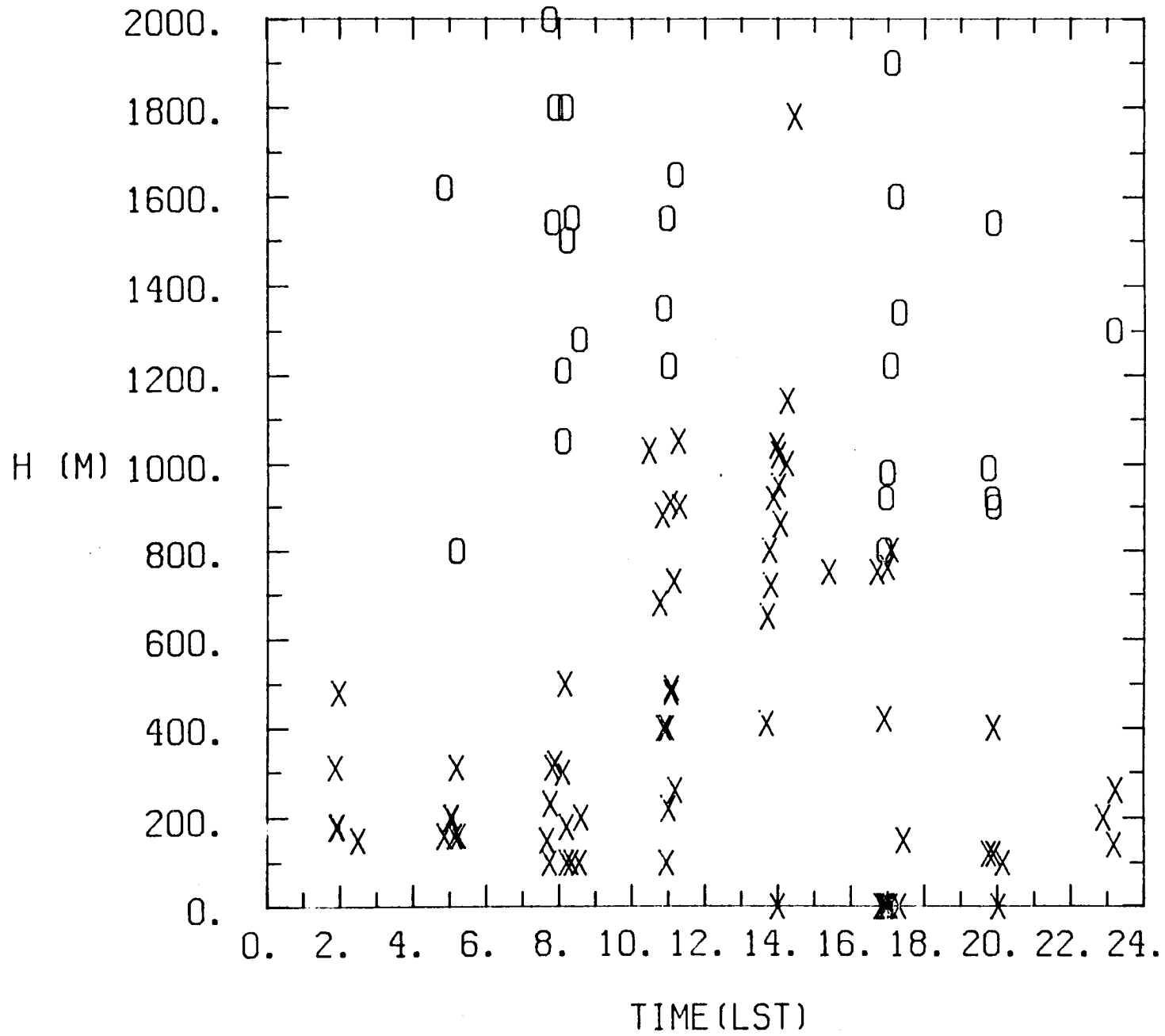
2000.
1800.
1600.
1400.
1200.
1000.
800.
600.
400.
200.
0.
H (M)
0. 2. 4. 6. 8. 10. 12. 14. 16. 18. 20. 22. 24.
TIME(LST)

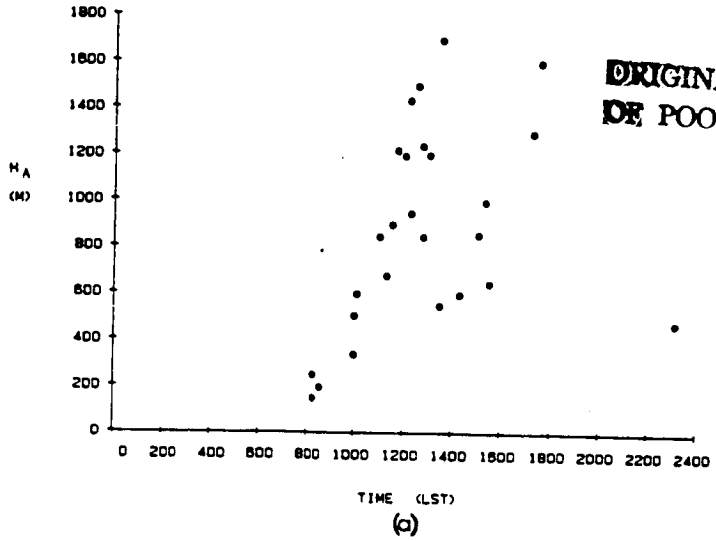

(a)

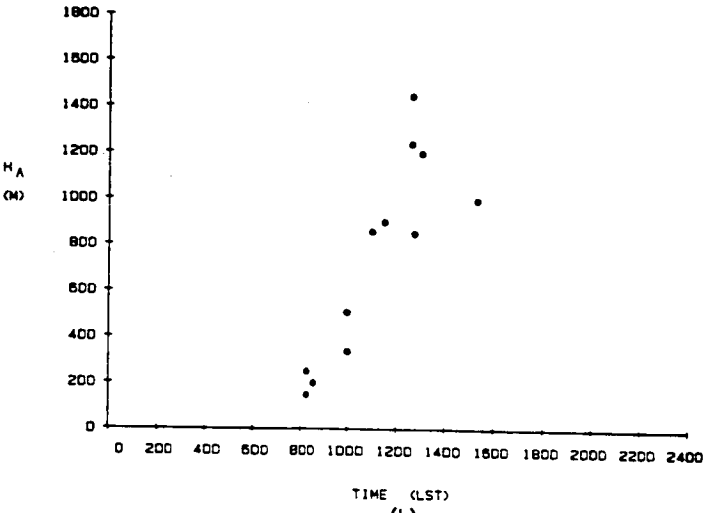

(b)

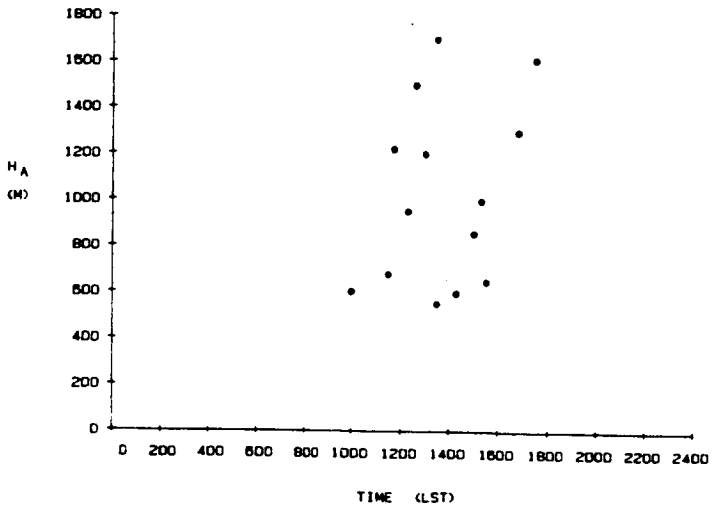

(c)

Fig 18

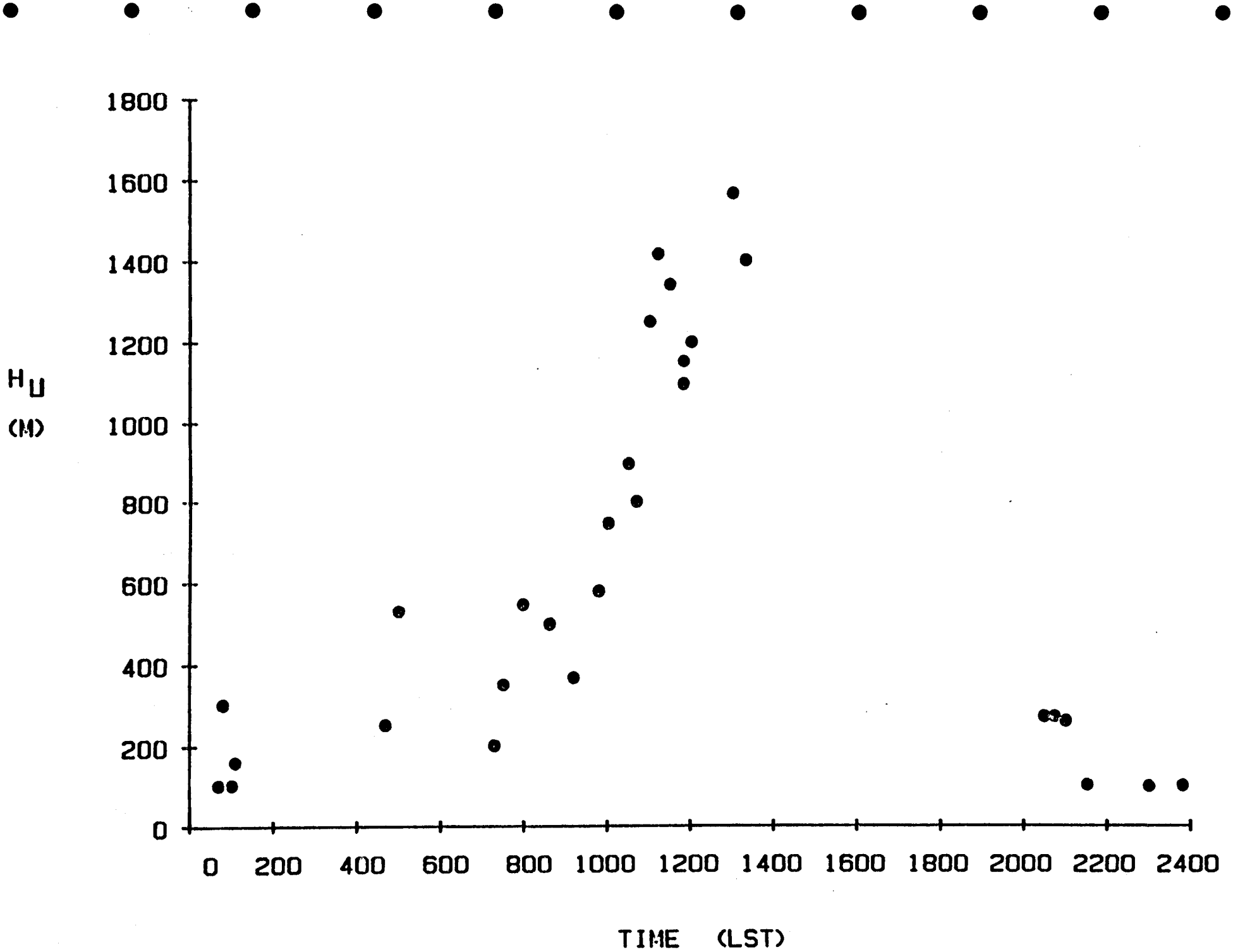
1800
1600
1400
1200
1000
800
600
400
200
0
H_U
(M)
0
200
400
600
800
1000
1200
1400
1600
1800
2000
2200
2400
TIME (LST)

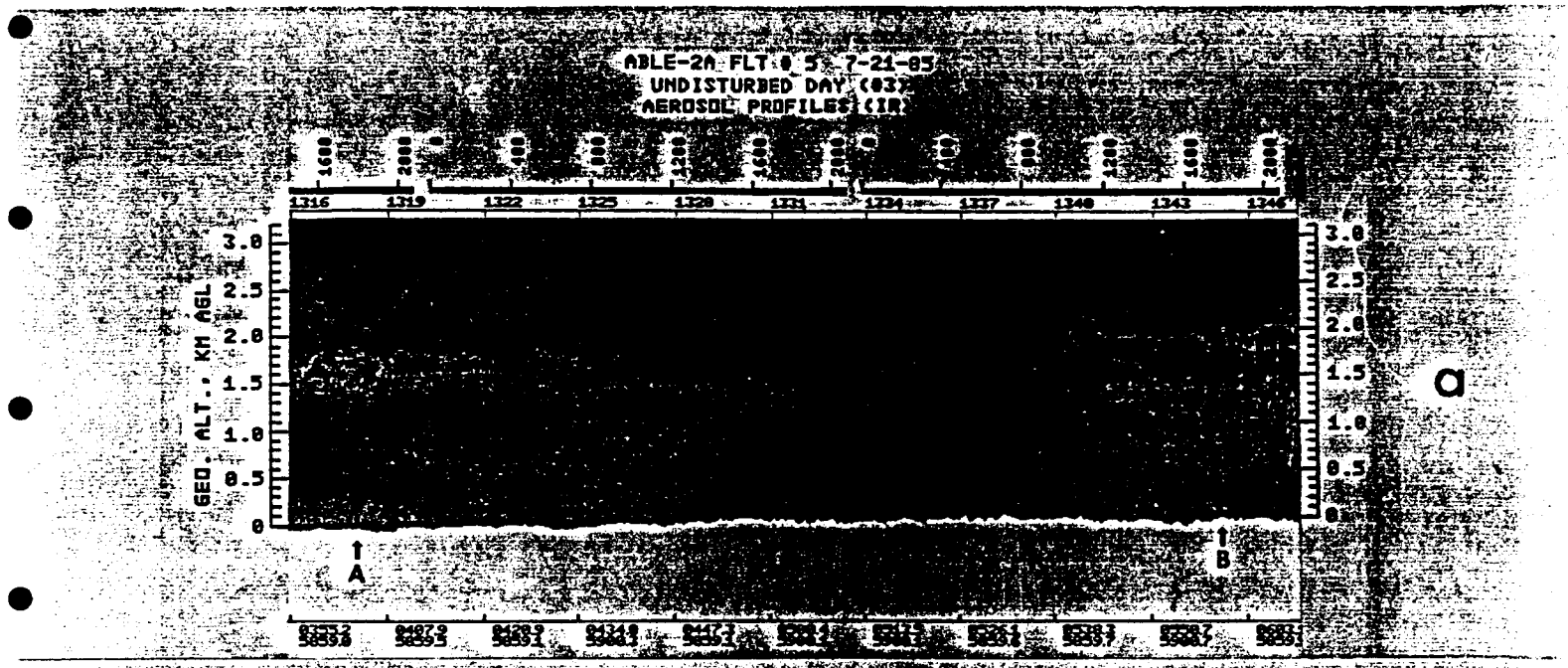

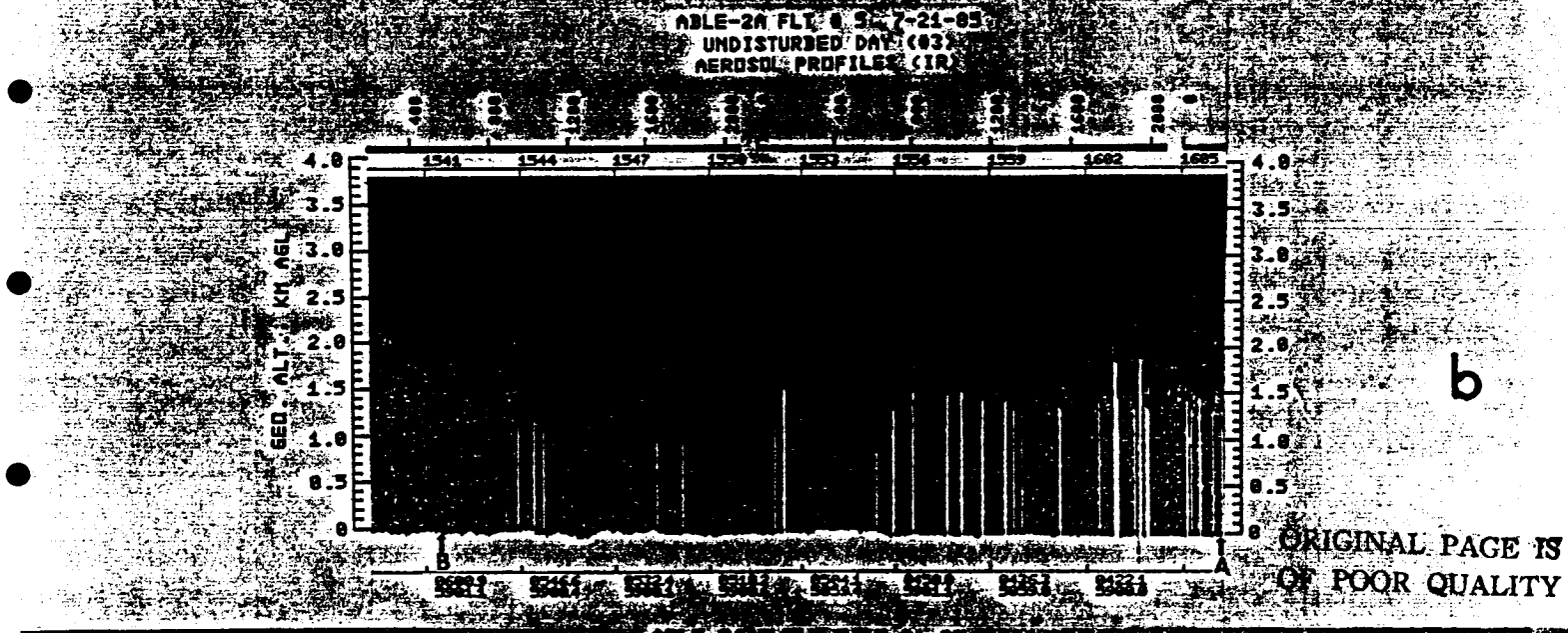

ORIGINAL PAGE IS
OF POOR QUALITY

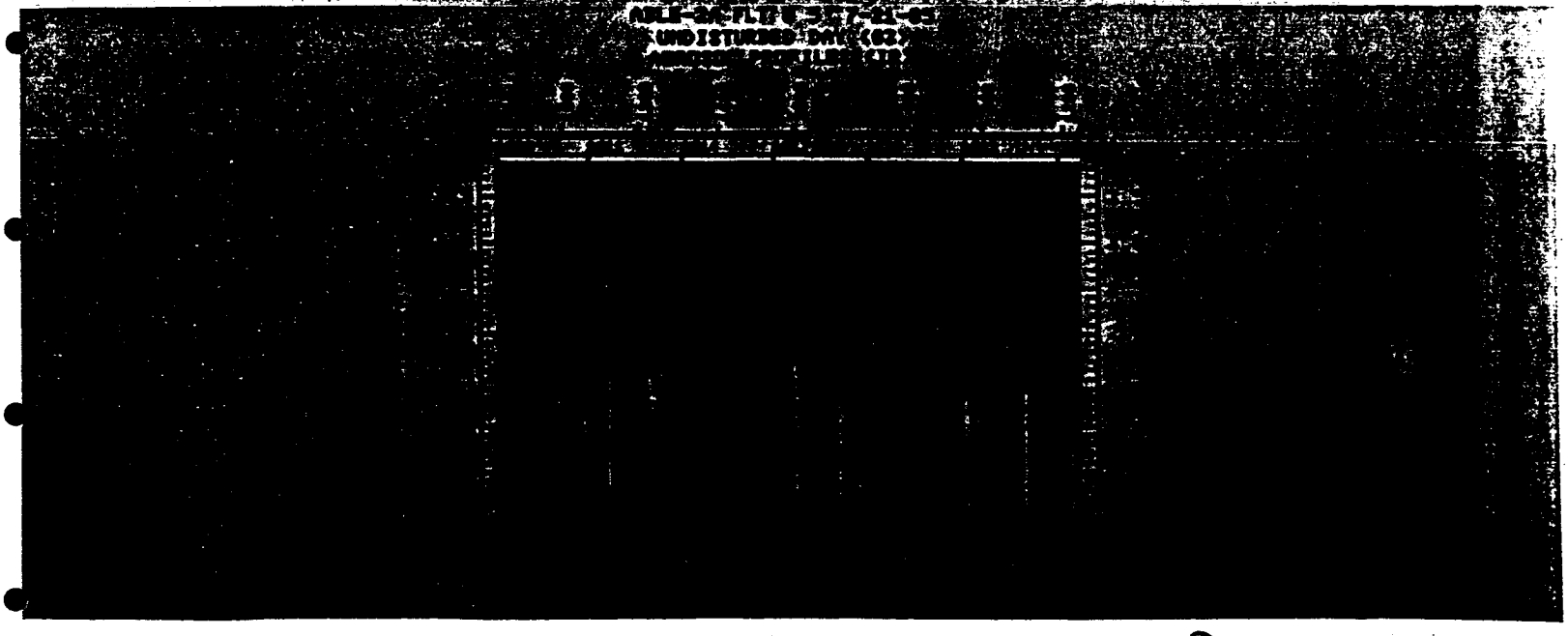

Fig 20

4.2.1 Invited paper presented at the Spring Meeting of the American Geophysical Union.

Growth and Decay of the Atmospheric Boundary Layer over a Tropical Rain Forest

MICHAEL GARSTANG (Department of Environmental Sciences, University of Virginia, Charlottesville, VA 22903)
DAVID FITZJARRALD (ASRC/SUNY, Albany, N.Y. 12205)
SAMUEL HOUSTON (Simpson Weather Associates, Inc., Charlottesville, VA 22902)
CHARLES MARTIN (Simpson Weather Associates, Inc., Charlottesville, VA 22902)
DEBORAH MARTIN (Simpson Weather Associates, Inc., Charlottesville, VA 22902)

Frequent soundings, with high vertical resolution to 1000 m above a given location in the Amazonian rain forest, demonstrate that the atmospheric mixed layer decays rapidly once the net radiative balance above the canopy goes negative. Very strong static stability is established above the canopy creating a two-layered fluid structure. The rough daytime boundary of the forest canopy is replaced by a nearly frictionless interface, allowing the air above this interface to accelerate from velocities of typically 5 mps to as high as 20 mps. Marked velocity shear in the horizontal wind results creating a large increase in mechanical turbulence. The stratified conditions are rapidly destroyed by daytime solar heating with the mixed layer growing through buoyant mixing at a rate of 5 to 10 cm per second.

The diurnal stratification and regrowth of the boundary layer have significant implications to chemical transports into and out of the tropical rain forest.

Paper presented at the Second International Conference on Southern Hemisphere Meteorology, December 1986, Wellington, New Zealand.

4.2.2

TRACE GAS EXCHANGES AND TRANSPORTS OVER THE AMAZONIAN RAIN FOREST

Michael Garstang, Steve Greco and John Scala
Department of Environmental Sciences
University of Virginia
Charlottesville, Virginia 22903

Robert Harriss, Edward Browell and Glenn Sachse
NASA/Langley Research Center
Hampton, Virginia 23665

Joanne Simpson and Wei-Kuo Tao
NASA/Goddard Space Flight Center
Greenbelt, Maryland 20771

and

Arnold Torres
NASA/Wallops Flight Facility
Wallops Island, Virginia 23337

1. INTRODUCTION

The Amazon Basin not only contains the world's largest rain forest but limbs of two major global circulations, the Hadley and Walker circulations, are centered over this basin. Variations in the Southern Oscillation and Pacific and Atlantic warming events influence the intensity of the circulations over the Basin and communicate effects of this circulation to the global atmosphere.

The forests and wetlands of the Amazon Basin supply a significant percentage and a great range of trace gases to the atmosphere (Gregory et al., 1986). Of these gases some, such as, carbon dioxide and methane, are greenhouse gases. Others, of the nitrogen and sulphur species, together with heavy and light hydrocarbons, interact to create ozone, haze layers and acid rain. Man's activities, particularly in the clearing burning of the forests, have a marked impact upon these processes.

Deep cumulus convection not only provides the link between sources of trace gases at the forest canopy and in the upper tropsophere and lower stratosphere but this convection is indeed the unsteady but essential element of the circulation systems themselves (Riehl and Malkus, 1958; Augstein et al., 1980). Understanding of the convective transports therefore serves the dual role of aiding in understanding the transport of chemical species and in understanding the larger scale circulations.

Our purpose in this paper is to present early findings of a sustained effort to understand deep convective transports of chemical species. To reach this goal we believe that direct observations of the thermodynamic, dynamic and chemical characteristics of convective clouds and their surrounding environment must be coupled with numerical modeling of these cloud and chemical processes.

The observations reported on in this paper were obtained during the NASA Global Tropospheric Experiment (GTE) Amazon Boundary Layer Experiment (ABLE II(a)) conducted in July and August 1985. The model calculations were carried out at the NASA/Goddard Laboratory for Atmospheric Science.

2. MEASUREMENT PROCEDURE

Figure 1 shows the experiment location. Cloud transport processes were studied in the two shaded regions. This paper will present results from the mission north of the Rio Negro. The NASA Wallops Electra aircraft used during this experiment is equipped with a range of chemical and meteorological instrumentation (Gregory et al., 1986). Ozone, carbon monoxide, nitric oxide, temperature and water vapor will be of primary concern in this paper. An airborne ultraviolet differential absorption lidar (UV-DIAL) system was used to remotely sense both ozone and aerosols. Aerosols along the lidar path with a spatial resolution of 15 m in the vertical and 20 m in the horizontal were used to determine the vertical structure of the atmosphere (Browell et al., 1983). Horizontal and vertical resolution of the UV-DIAL ozone measurement is 1000 m and 100 m, respectively. Two separate, in situ, measurements of O_3 were made by C_2H_4 chemiluminescence and UV absorption (Gregory et al., 1983, 1984). The in situ measurements on the aircraft profiles can be compared with previously remotely obtained UV-DIAL O_3 measurements. The O_3 measurements are accurate to 5 parts per billion by volume (ppbv) or 5% whichever is greater.

Carbon monoxide was measured in situ using the differential absorption carbon monoxide (DACOM) instrument which utilizes a tunable diode laser detection technique. The precision is 1% or 1 ppbv with a time response of 1 sec.

Nitric oxide was measured by a chemiluminescence technique with an accuracy of better than 20% giving a precision of 3 pptv for a 30 sec integration.

Temperature and moisture measurements were made on the aircraft by standard techniques (Rosemont 102E4A1 temperature sensor and EG&G 137 and 300 dew point hygrometers). Atmospheric soundings were made from the surface to 400 mb every three hours from 1200 GMT to 2100 GMT at a point 150 km southeast of the mission location and to 50 mb every 6 hours, at a point 165 km southeast of the mission location.

Figure 2 shows the aircraft flight tracks and altitudes relative to the N/S cloud line. Flight altitudes were kept constant within $\pm$ 10 m, altitude being determined by a radar altimeter as well as a presure altimeter. Soundings were made at the corners of the box and prior to entering the environment of the cloud system.

GOES imagery was used to locate the cloud system and determine its movement and general organization. The satellite imagery shows that the cloud system being examined propagated steadily from E to W across the Basin over the 24 h preceding sampling. When sampled the cloud system consisted of a 500 km N/S line 100 km wide with E/W organized elements embedded in the line.

3. CLOUD MODEL CALCULATIONS

A two-dimensional version of the 3-D cloud model described by Tao and Soong (1986) was used to simulate convection on the 3 August 1985 mission. The model uses small amplitude random temperature fluctuations at the low levels to simulate thermals. The random thermals are superimposed upon a uniform canopy temperature. The model is initialized using the atmospheric sounding closest in time to the start of the mission. The sounding, representative of the undisturbed atmosphere, is well removed from the influence of the convective activity being sampled. The large scale vertical velocity (-5 cm sec^{-1}) field is superimposed, together with horizontal advection of temperature and moisture and radiative cooling. The model incorporates fairly complete microphysics including ice-processes.

In the two-dimensional form the y-axis lies along the cloud line. The x-axis is thus normal to the cloud line and the cloud structure and circulation is depicted in the x,z plane.

4. RESULTS

Figure 3 shows the equivalent potential temperature field with height for the model generated cloud at 40 min after initialization. The u-w velocity field confirms the downward extension of the low mid-tropospheric values of θ_e while the upward motion coincides with high surface θ_e values extending upwards. The model cloud height at this time is near 8 km, with maximum cloud top reaching 12 km. Photogrammatic calculations based upon airborne images place the maximum observed cloud top at 13 km.

Analysis of the satellite images shows that the cloud system was moving westward at the time of sampling at 28 kmph or less.

Combining model simulation with observations we consider Fig. 3 to be a useful guide, suggesting inflow and upward motion on the western side of the line responding to the gust front. Downward motions originating near 3 or 4 km penetrate to the surface from the east. The eastern side would thus represent the wake of the storm while the western side consists largely of undisturbed conditions near the surface but modified air in the middle troposphere ($\sim$ 600 mb).

Horizontally averaged values of O_3 concentrations for the undisturbed atmosphere and for the eastern and western sides of the cloud system are shown in Fig. 4. On the eastern side considerable O_3 enhancement is seen with O_3 concentrations between 1.5 and 2.0 km exceeding 40 ppbv. Ozone values between 1.7 and 3 km are enhanced above any level observed in the mean undisturbed atmosphere. This suggests that the enhanced ozone values may not be due only to downward transports of mid- to upper-tropospheric ozone but may also be due to anthropogenic production. Theta-e values observed between the same levels (Fig. 3) suggest that air descends from levels no higher than 4 km.

On the western side O_3 enhancement is seen below 3 km. Significant depletion, however, is seen above 3 km suggesting upward transport of air originating below 2.5 km. Any marked entrainment or mixing with environmental air in the column during the process of upward transport would require that the air originates at a level substantially below 2.5 km.

Figure 5 shows values of O_3, CO, NO and θ_e along each horizontal flight leg of the aircraft box shown in Fig. 2.

At the 5 km flight level on the eastern side (A to B), O_3 is generally depressed below the undisturbed value of 40 ppbv for that altitude. Ozone, carbon monoxide and nitric oxide concentrates are all high near A suggesting that these high values are due to anthropogenic sources probably in the form of an elevated haze layer. At B, O_3 versus CO and NO are inversely correlated, with very depressed values of O_3 and elevated values of NO. This suggests that at this location the aircraft is in the region of upward transports.

Examination of the θ_e values at the 5 km level clarifies the situation. Very low values of θ_e (near 330°K) at 5 km near A are indicative of mid-tropospheric air. Since the θ_e values suggest descent we can conclude that any upward transport which formed the haze layer originated at a point remote from this convective system. Gradual increases in θ_e towards B implies some upward motion. Thus θ_e confirms that high values of O_3 observed both in Fig. 4 and near A on the eastern side can be of dual origin, i.e., mid-

troposphere as well as anthropogenic.

The 150 m flight level on the eastern side of the system shows pronounced correlations between all three trace gases. Nitric oxide is elevated above levels at which photochemical production of O_3 can occur. The equivalent potential temperature shows a marked drop from A to B at 150 m suggesting that by B at the lower level we are embedded in the wake of the system.

On the western side of the cloud system, O_3 is generally depressed especially at the lower level except near D' where it reaches values (24 ppbv) only slightly above undisturbed conditions. The equivalent potential temperature shows the uniformly high values of the boundary layer at the lower level indicating undilute boundary layer inflow. The equivalent potential temperature at 5 km is everywhere well above the mid-tropospheric minimum of 330°K. High values of CO, NO and θ_e near D' at the 150 m level suggests that this air is of surface origin.

5. CONCLUSIONS

The interpretation of trace gas chemistry in the vicinity of deep convection can benefit from

a) the measurement of other thermodynamic quantities, particularly quantitites with quasi-conservation characteristics such as θ_e.

b) cloud model simulations which can provide a framework for the interpretation of the observations.

c) Conversely, chemical species provide tracers which can help in the interpretation and validation of cloud model calculations.

A combination of measurements of temperature and humidity, chemical species and model calculations are needed to interpret the chemical observations. Chemical observations by themselves would not have suggested a remote anthropogenic source for the concentrations measured near 5 km on the eastern side of the system.

An awareness of the relatively large changes in specie concentrations which convection can effect through both upward and downward transports would seem to require the increasing use of cloud models. These models must ultimately incorporate chemical production and destruction. Caution would have to be used in interpreting observations of species over a number of hours in a framework of convective transports which occur over time scales of tens of minutes.

6. REFERENCES

Augstein, E., M. Garstang and G.D. Emmitt, 1980: Vertical mass and energy transports by cumulus clouds in the tropics. Deep Sea Res., Spec. Vol., 9-21.

Browell, E.V., A.F. Carter, S.T. Shipley, R.J. Allen, C.F. Butler, M.N. Mayo, J.H. Siviter, Jr. and W.M. Hall, 1983: NASA multipurpose airborne DIAL system and measurement of ozone and aerosol profiles. Appl. Opt., 22, 522-534.

Gregory, G.L., C.H. Hudgins and R.A. Edahl, Jr., 1983: Laboratory evaluation of an airborne ozone instrument which compensates for altitude/sensitivity effects. Envir. Sci. and Tech., 17.

_____, S.M. Beck and J.A. Williams, 1984: Measurements of free tropospheric ozone: An aircraft survey from 44° north to 46° south latitude. J. Geophy. Res., 89, 9642-9648.

_____, R.C. Harriss, R.W. Talbot, R.A. Rasmussen, M. Garstang, M.O. Andreae, R.R. Hinton, E.V. Browell, S.M. Beck, D.I. Sebacher, M.A.K. Khalil, R.J. Ferek and S.V. Harriss, 1986: Air chemistry over the tropical forest of Guyana. J. Geophys. Res., 91, 8603-8612.

Riehl, H. and J. Malkus, 1958: On the heat balance of the equatorial trough zone. Geophys., 6, 503-535.

Tao, W-K. and S-T. Soong, 1986: A study of the responses of deep tropical clouds to mesoscale processes: 3-D numerical experiments. Submitted to J. Atmos. Sci.

7. ACKNOWLEDGEMENT

We wish to acknowledge the broad support of NASA in the GTE/ABLE program. We particularly wish to recognize the contributions of the NASA Electra aircrew and technicians. The work done at the University of Virginia was supported under NASA contract NCC1-95. We thank Mary Morris and Deborah Martin for the typing and drafting.

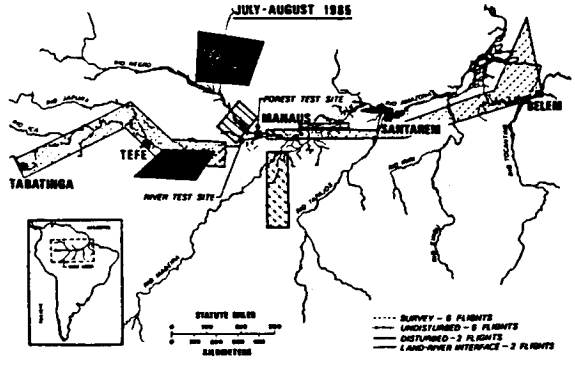

Figure 1. Study area over Amazon Basin (insert) together with flight tracks of missions. The cloud complex described in this paper is within the shaded region to the north of the Rio Negro.

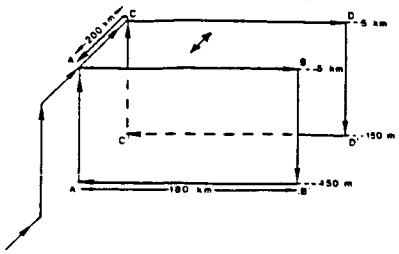

Figure 2. Flight tracks and vertical soundings around the cloud complex. The upper level tracks A to B and C to D on the eastern and western sides of the cloud were flown at about 5 km, the lower level tracks B' to C' and D' to C' at 150 m. The cloud line extends northward out of the open end of the box with a mean width of 100 km shown by the double-headed arrow.

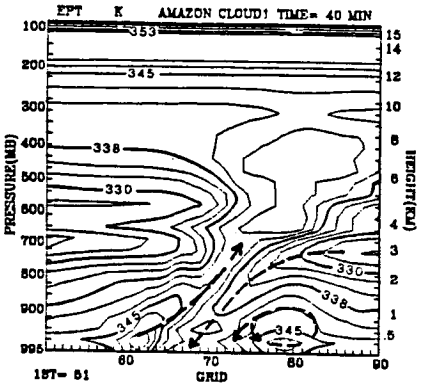

Figure 3. Two-dimensional cloud model output at 40 mins after initialization. Equivalent potential temperature contours in °K are shown together with heavy dashed lines approximating the u-w vectors. North is into the page. Cloud top height reaches 400 mb.

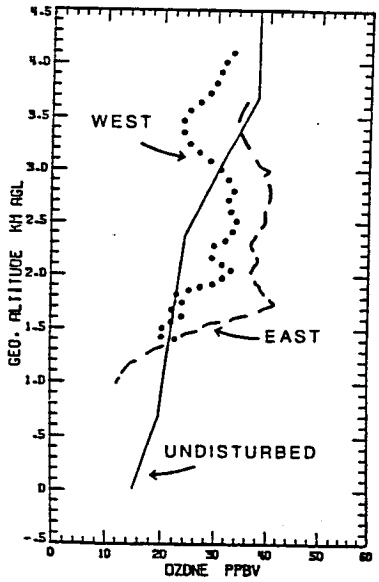

Figure 4. Vertical profiles of O_3 spatially averaged along the eastern (dashed) and western (dotted) sides of the cloud complex compared to the mean vertical profile of O_3 for the undisturbed equatorial atmosphere (solid).

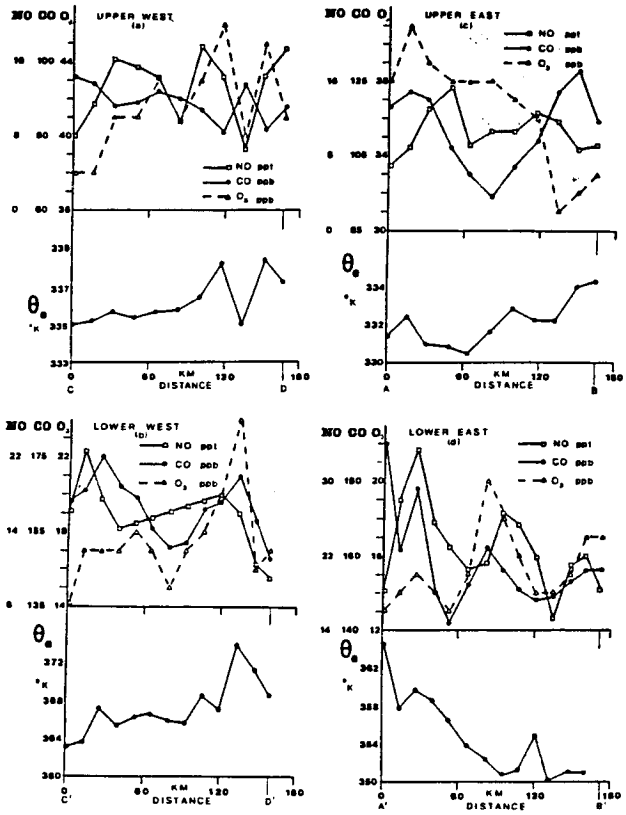

Figure 5. Values of O_3, CO, NO and θ_e along each leg of flight box around the cloud complex.

a) Upper traverse on western side.
b) Lower traverse on western side.
c) Upper traverse on eastern side.
d) Lower traverse on eastern side.